

Constraining the marine environments of
the Cambrian metazoan radiation

Thesis submitted for the degree of
Doctor of Philosophy
at the University of Leicester

by

Thomas William Wong Hearing

School of Geography, Geology and the
Environment

University of Leicester

September 2018

Abstract

Constraining the marine environments of the Cambrian metazoan radiation

Thomas William Wong Hearing

Major advances have been made in understanding the biological aspects of the Proterozoic/Phanerozoic transition, but Earth's physical environment over this interval is poorly constrained. In particular, there are no quantitative constraints on early Cambrian sea temperatures. The stable oxygen isotope ratio ($\delta^{18}\text{O}$) from fossil biominerals is a widely used proxy for ocean temperatures, but a dearth of Cambrian biomineral $\delta^{18}\text{O}$ data has left a substantial data gap coinciding with the evolution of animal-rich ecosystems.

Carefully selected phosphatic 'small shelly fossil' (SSF) taxa from three coeval sites in the UK, Morocco, and Canada were examined as potential sources of early Cambrian biomineral $\delta^{18}\text{O}$ data. A rigorous protocol for assessing the isotopic preservation of SSF biogenic phosphate was established that considered the microstructural, ultrastructural and chemical preservation of visually distinct SSFs. Subsets of SSFs identified as pristine or altered, distinguishable under optical microscopy, were found to be isotopically distinct, with pristine SSFs isotopically heavier than altered SSFs. Well-preserved SSFs yielded $\delta^{18}\text{O}$ values consistent with geological evidence for a Cambrian greenhouse world, similar to Mesozoic and Cenozoic hothouse climates. Specifically, these data suggest that early Cambrian high latitude (Avalonian) sea surface temperatures (SSTs) were approximately 23 °C and low latitude (Laurentian) SSTs approximately 35 °C. These data provide the first quantitative constraints on early Cambrian sea surface temperatures.

These isotopic SSTs were used to calibrate FOAM general circulation model (GCM) simulations set up to test a range of Cambrian $p\text{CO}_2$ levels and continental configurations. The calibrated GCM simulations were compared to a new database of climatically sensitive lithologies, with data/model agreement scored according to the environmental conditions required for particular lithologies to form. This study places first-order quantitative constraints on Cambrian ocean temperatures from both proxy data and climate modelling approaches, and lays the groundwork for interrogating Cambrian environments with greater precision.

Acknowledgements

Producing this thesis has been one of the hardest tasks I have ever undertaken. That it has reached this stage is thanks in no small part to many colleagues, friends, and family. I would first like to acknowledge NERC (CENTA studentship NE/L0022493/1) and the BGS (BUFI S266) whose funding made this research possible. The isotope work in this thesis was supported by NIGF grants IP-1530-0515 and IP-1667-1116, and EIMF grant IMF-567-1015.

I have been fortunate to have a broad and engaged supervisory team, who have all contributed substantially to my intellectual development over the last four years. Dr Tom Harvey, Prof Mark Williams, Prof Sarah Gabbott, Dr Phil Wilby, and Prof Mel Leng have all also contributed valuable scientific insights throughout the production of this thesis. Tom Harvey and Mark Williams are particularly thanked for their generous open-door style of supervision.

There are many people to whom I am grateful for practical and theoretical technical support that was instrumental in this work. From the University of Leicester: Helen Booth-Wynne, Dr Annika Burns, Graham Clark, Colin Cunningham, Dr Tom Knott, Nick Marsh, Lin Marvin, and Vinay Patel are thanked for help with chemical and SEM analyses, and producing thin sections and polished blocks. From the British Geological Survey: John Fletcher, Dr Angela Lamb, Louise Neep, Dr Jeremy Rushton, Hilary Sloane, and Dr Andi Smith are thanked for help with preparing samples, and supporting SEM, chemical and isotope analyses. Dr Sam Hammond, Open University, is thanked for help with EPMA work. I am deeply indebted to Dr John Craven and Mike Hall, from the Edinburgh Ion Microprobe Facility, for extensive support and practical help in preparing for and running SIMS analyses, and dealing with unexpected interruptions to data collection.

I am very grateful to Dr Alexandre Pohl and Prof Yannick Donnadieu for useful discussions and practical help with running the climate model simulations used in this work. In particular, Alexandre Pohl is thanked for initiating the climate simulations and building the model files. Dr Pierre Sepulcre kindly shared his R code which forms the basis of the code used to convert model and lithological data into Köppen-Geiger climate classifications. Dr Christopher Scotese kindly supplied PALEOMAP data, including palaeotopographic and palaeobathymetric data, which formed one of the base maps tested here. Azizi Abdelfattah, Dr Khadija El Hariri, Francesca Hearing, Prof

Duncan McIlroy, and Matthew Saker-Clark are thanked for their help organising and conducting field work. Dr Adrian Rushton is thanked for valuable discussions on the Comley Limestones and the lower Cambrian strata of Britain.

The moral and practical support of current and former colleagues at University of Leicester has been invaluable in surviving, and occasionally thriving, through my PhD. In particular: Dr Thomas Clements, Dr Tom Fletcher, Dr Rob Goodall, Ryan Hunt, Dr Leah Nolan, Dr Tom Potter, Phil Smith, Tara Stephens, and Dr James Wheeler. You have all helped, in various ways, to keep me more or less cheerful.

None of this would have happened without support and encouragement throughout my life from my parents, Jill and Trevor. To this day, they still put up with every trip to the beach resulting in more ‘interesting’ rocks coming home and, more often than not, staying there! Finally, I am most grateful to my wonderful wife, Sherri, for her unceasing love and support, and for resisting a state of perpetual exasperation with my (too) often (too) long hours. You have always helped me realise what is truly important in life.

Table of Contents

Abstract.....	i
Acknowledgements.....	ii
Table of Contents.....	iv
List of Tables.....	viii
List of Figures.....	ix
List of Abbreviations.....	xiv
Chapter One: Introduction.....	1
1.1. The Cambrian climate and marine environments.....	1
1.2. The oxygen isotope palaeothermometer.....	4
1.3. Marine environments and the Cambrian metazoan radiation.....	5
1.4. Scope of the thesis.....	7
1.4.1. Aims.....	7
1.4.2. Objectives.....	7
1.5. Thesis summary.....	8
Chapter Two: Geological settings.....	10
2.1. Chapter summary.....	10
2.2. Introduction.....	10
2.2.1. The Comley Limestones – a priority target.....	10
2.2.2. Early Cambrian geography.....	11
2.3. Materials and Methods.....	12
2.4. Samples from the Comley Limestones, Shropshire, UK.....	13
2.4.1. Petrography of samples used in this thesis.....	16
2.4.2. Depositional setting of the Comley Limestones.....	22
2.5. Samples from the Cambrian of the High Atlas Mountains, Morocco.....	23
2.6. Samples from the Forteau Formation, Newfoundland and Labrador, Canada.....	27
2.7. Discussion.....	30
2.7.1. Resolving climatically important timescales.....	30
2.7.2. Correlations and time slab definitions.....	31
2.8. Conclusions.....	33
Chapter Three: Identifying alteration of bioapatite.....	35
3.1. Chapter summary.....	35
3.2. Introduction.....	35
3.3. Limitations of the current $\delta^{18}\text{O}$ record.....	37
3.3.1. Whole rock samples.....	37
3.3.2. Biogenic samples.....	38
3.3.3. Sources of isotopic alteration.....	40
3.3.4. Potential Cambrian biominerals for isotopic analysis.....	41
3.3.5. Carbonate versus phosphate.....	41
3.4. Finding suitable fossil biominerals.....	43

3.4.1. Cambrian ‘Small Shelly Fossils’	43
3.4.2. A note on sampling constraints from isotope analysis protocols	44
3.4.3. Taxon selection criteria	45
3.5. Selected taxa	47
3.5.1. Linguliformean brachiopods	47
3.5.2. Rhombocorniculum Walliser 1958	49
3.5.3. Torellella laevigata Linnarsson 1871	50
3.6. Materials	51
3.6.1. Bulk limestone processing	51
3.6.2. Microfossil preparation	51
3.7. Methods: Assessing the preservation state of biogenic phosphate	53
3.7.1. Gross morphology	55
3.7.2. Microstructure	57
3.7.3. Ultrastructure.....	59
3.7.4. Elemental chemistry	60
3.7.5. Isotopic composition	63
3.8. Results: Preservation of biogenic phosphate in the Comley Limestones	63
3.8.1. Gross morphology	63
3.8.2. Microstructure	68
3.8.3. Ultrastructure.....	73
3.8.4. Elemental composition.....	76
3.9. Beyond the Comley Limestones	84
3.9.1. West Gondwana	84
3.9.2. Laurentia	87
3.10. Conclusions.....	91
3.10.1. A protocol to assess the preservation of phosphate biominerals.....	91
3.10.2. Preservation hypotheses to be tested using isotope data.....	93
Chapter Four: Early Cambrian phosphate oxygen isotope data	94
4.1. Chapter summary	94
4.2. Introduction.....	94
4.2.1. Hypotheses to be tested with $\delta^{18}\text{O}$ data.....	96
4.2.2. The rationale for using different $\delta^{18}\text{O}$ sampling techniques	96
4.3. Materials and Methods.....	98
4.3.1. Samples	98
4.3.2. Bulk isotope analyses	100
4.3.3. Ion microprobe analyses	101
4.4. Results.....	103
4.4.1. Silver phosphate analyses	103
4.4.2. SIMS analyses	108
4.5. Discussion.....	119
4.5.1. Testing the efficacy of the preservation protocol.....	119
4.5.2. Tissue-specific variability	120
4.5.3. Inter-specimen variability	122

4.5.4. Comparing analytical techniques: silver phosphate outperforms SIMS for ancient brachiopods.....	124
4.5.5. A palaeolatitudinal $\delta^{18}\text{O}$ gradient.....	125
4.6. Conclusions.....	125
Chapter Five: Early Cambrian sea surface temperatures.....	127
5.1. Chapter summary.....	127
5.2. Introduction.....	127
5.3. Phosphate oxygen temperature equations.....	127
5.4. The oxygen isotopic composition of Cambrian seas.....	130
5.4.1. Secular variation.....	130
5.4.2. Local variation.....	136
5.5. Early Cambrian sea surface temperature calculations.....	138
5.6. Palaeoenvironmental implications.....	142
5.7. Conclusions.....	143
Chapter Six: Modelling early Cambrian climates.....	145
6.1. Chapter summary.....	145
6.2. Introduction.....	145
6.2.1. The Cambrian greenhouse world?.....	145
6.2.2. Aims, objectives and rationale.....	146
6.3. Methods in modelling early Cambrian climate.....	148
6.3.1. The Fast Ocean Atmosphere Model (FOAM).....	148
6.3.2. Model boundary conditions.....	149
6.3.3. Palaeotopographic and palaeobathymetric maps.....	152
6.4. Early Cambrian climate model results.....	157
6.4.1. Map A.....	160
6.4.2. Map B.....	161
6.4.3. Map C.....	162
6.4.4. Map D.....	162
6.4.5. Model calibration.....	165
6.5. Methods in early Cambrian data–model comparison.....	170
6.5.1. Climate classification.....	171
6.5.2. Lithological data.....	173
6.5.3. Calculating data–model agreement.....	180
6.6. Results of early Cambrian data–model comparisons.....	181
6.6.1. Early Cambrian modelled Köppen-Geiger classification.....	181
6.6.2. Data/model comparison.....	186
6.7. Discussion.....	188
6.7.1. Models, geological data and isotopic temperatures.....	188
6.7.2. Irreconcilable differences?.....	189
6.7.3. Deep ocean circulation perspectives on oxygen and phosphate.....	190
6.7.4. Early Cambrian glaciation on Avalonia?.....	191
6.7.5. Early Cambrian climate and biodiversity.....	192
6.7.6. Biodiversity, Konservat-Lagerstätten and Cambrian climates.....	193

6.8. Conclusions.....	195
Chapter Seven: Conclusions	197
7.1. Thesis aims.....	197
7.2. Assessing phosphate oxygen isotopic preservation in deep time	197
7.3. The Cambrian $\delta^{18}\text{O}$ record and temperature estimates	198
7.4. The early Cambrian marine environment	198
7.5. Future work.....	199
Bibliography	201
Appendices.....	233
Appendix A.....	233
Appendix B	233
Appendix C	234
Introduction	234
Data processing	234
Data and figures	235
References cited in Appendix C.....	243
Appendix D.....	244
Appendix E	244
Appendix F.....	244
Appendix G.....	244
Appendix H.....	244
Appendix I	244

List of Tables

Table 2-1. Sedimentology and depositional environments of the Comley Limestones.	20
Table 2-2. Time slab definitions.	33
Table 3-1. Taxon selection criteria.	47
Table 4-1. Early Cambrian silver phosphate oxygen isotope data.	107
Table 4-2. Summary of SIMS analyses.	115
Table 5-1. Published phosphate oxygen isotope temperature equations.	129
Table 5-2. Cambrian SST estimates from each of the six equations.	141
Table 6-1. Orbital parameters for the FOAM climate simulations.	152
Table 6-2. Altitude categories for palaeogeographic reconstructions.	155
Table 6-3. Model calibration using Avalonian isotopic sea temperatures.	168
Table 6-4. Thresholds of Köppen-Geiger climate classification scheme.	172
Table 6-5. Formation conditions of climatically sensitive lithologies.	176
Table 6-6. Scoring agreement of lithological occurrences and Köppen-Geiger climate zones	185
Table 6-7. Data/model agreement scores calculated for all “Lower Cambrian” deposits	186
Table 6-8. Data/model agreement scores calculated for all deposits with depositional ages between 510 Ma to 520 Ma.	187

List of Figures

Figure 1-1. The Palaeozoic biomineral carbonate and phosphate $\delta^{18}\text{O}$ records.	2
Figure 1-2. The Neoproterozoic/Palaeozoic transition.	3
Figure 1-3. The Cambrian metazoan radiation.	5
Figure 2-1. A typical view of early Cambrian palaeogeography.	11
Figure 2-2. Cambrian and Tremadocian strata and major Palaeozoic tectonic structures of southern Britain.	13
Figure 2-3. Lower/middle Cambrian stratigraphy of Comley, Shropshire, UK.	15
Figure 2-4. Phosphate nodules from the Comley Limestones.	16
Figure 2-5. Thin sections from the Comley Limestones.	18
Figure 2-6. Thin section images of the Comley Limestones hardground.	19
Figure 2-7. Geopetal structures in the Comley Limestones.	22
Figure 2-8. Geographical and geological maps of Ait Iyou, Morocco.	25
Figure 2-9. Lower/middle Cambrian stratigraphy of Ait Iyou, Morocco.	26
Figure 2-10. Geographical and geological setting of the Forteau Formation, Great Northern Peninsula, western Newfoundland, and southern Labrador, Canada.	28
Figure 2-11. Lower/middle Cambrian stratigraphy of western Newfoundland and southern Labrador, Canada.	29
Figure 2-12. Correlation of the time slabs used in this thesis.	34
Figure 3-1. The conodont colour alteration index (CAI).	36
Figure 3-2. Small shelly fossils (SSFs) from the Comley Limestones.	43
Figure 3-3. Protocol for assessing the isotopic preservation of biogenic phosphate.	54
Figure 3-4. Light-coloured linguliformean brachiopods from the Comley Limestones.	64
Figure 3-5. Dark-coloured linguliformean brachiopods from the Comley Limestones.	64
Figure 3-6. The ornament of <i>Rhombocorniculum</i>	65
Figure 3-7. Light- and dark-coloured <i>Rhombocorniculum</i> specimens.	65
Figure 3-8. Stained <i>Rhombocorniculum</i> specimens.	66

Figure 3-9. <i>Torellevella</i> specimens from the Comley Limestones.	67
Figure 3-10. Stained <i>Torellevella</i> specimens.	68
Figure 3-11. Laminar microstructure Comley Limestones brachiopods.	69
Figure 3-12. Detail of Comley Limestones brachiopods microstructure.....	70
Figure 3-13. Botryoidal fabrics in Comley Limestones brachiopods.	70
Figure 3-14. Microstructure of <i>Rhombocorniculum</i>	71
Figure 3-15. Phosphatised tubules in <i>Rhombocorniculum</i>	72
Figure 3-16. Laminated walls of <i>Torellevella</i>	72
Figure 3-17. Aberrations in the walls of <i>Torellevella</i>	73
Figure 3-18. Comley Limestones light-coloured brachiopod ultrastructure.....	74
Figure 3-19. Comley Limestones dark-coloured brachiopod ultrastructure.....	74
Figure 3-20. Ultrastructure of <i>Rhombocorniculum</i>	75
Figure 3-21. Ultrastructure of <i>Torellevella</i>	76
Figure 3-22. Principal components analysis of all Comley Limestones SSF EPMA data.	77
Figure 3-23. Principal components analysis of all Comley Limestones SSF EPMA data grouped by taxon and colour.	77
Figure 3-24. EDS maps of Comley Limestones brachiopods.....	79
Figure 3-25. Principal components analysis of all Comley Limestones brachiopod EPMA data grouped by colour.	80
Figure 3-26. EDS maps of Comley Limestones <i>Rhombocorniculum</i> specimens.	81
Figure 3-27. Principal components analysis of all Comley Limestones <i>Rhombocorniculum</i> EPMA data grouped by colour.....	82
Figure 3-28. EDS maps of Comley Limestones <i>Torellevella</i> specimens.....	83
Figure 3-29. Principal components analysis of all Comley Limestones <i>Torellevella</i> EPMA data grouped by horizon and colour.	84
Figure 3-30. General morphology of brachiopods from Ait Iyou, Morocco.....	85

Figure 3-31. Recrystallisation of Ait Iyou brachiopods.	85
Figure 3-32. Recrystallised microstructure of Ait Iyou brachiopods.	86
Figure 3-33. Recrystallised ultrastructure of Ait Iyou brachiopods.	86
Figure 3-34. Principal components analysis of all Moroccan and Comley Limestones SSF EPMA data grouped by horizon and colour.....	87
Figure 3-35. Dark-coloured brachiopod from the Forteau Formation with well-preserved gross morphology but lacking clear lamination.....	88
Figure 3-36. Light-coloured brachiopod from the Forteau Formation with well- preserved gross morphology and some evidence of biogenic lamination.	89
Figure 3-37. Light-coloured brachiopod from the Forteau Formation, with well- preserved gross morphology but massive in cross section.	90
Figure 3-38. Fractured section through a specimen of the bivalve <i>Pojetaia runnegari</i> . 90	
Figure 4-1. Bulk isotope data from the Comley Limestones.....	104
Figure 4-2. Bulk isotope data from the Forteau Formation.	105
Figure 4-3. Histogram of SIMS measurements on Comley Limestones brachiopods..	109
Figure 4-4. Boxplot of all Comley Limestones brachiopod SIMS measurements by tissue type.	110
Figure 4-5. Comley Limestones Ad light-coloured brachiopods SIMS data.	111
Figure 4-6. SIMS $\delta^{18}\text{O}$ data from the compact laminae of pristine and altered Comley Limestones brachiopods.	111
Figure 4-7. Histogram of SIMS analyses of linguliformean brachiopods from AI-202a.	113
Figure 4-8. Boxplots of SIMS measurements on AI-202a brachiopods.....	114
Figure 5-1. Phanerozoic carbonate biomineral $\delta^{18}\text{O}$ record.	130
Figure 5-2. The Palaeozoic phosphate $\delta^{18}\text{O}$ record.	131
Figure 5-3. Modelling $\delta^{18}\text{O}_{\text{sw}}$ over Earth history.....	133
Figure 5-4. Variability of $\delta^{18}\text{O}_{\text{sw}}$ in the modern surface ocean.	137
Figure 5-5. Comparing Cambrian, Mesozoic, and Cenozoic SST proxy data.....	142

Figure 6-1. Four contrasting views of the early Cambrian world.....	147
Figure 6-2. Comparison of FOAM-modelled SST and present day measured conditions.	149
Figure 6-3. Modelled $p\text{CO}_2$ over the Phanerozoic Eon.	151
Figure 6-4. Topographic and bathymetric base maps used in the climate model simulations.	153
Figure 6-6. Zonal annual precipitation under different model conditions.	158
Figure 6-5. Zonal average sea surface temperatures (SSTs) under different model conditions.	159
Figure 6-7. Cross plot of modelled mean annual surface air temperature against $p\text{CO}_2$ for each palaeocontinental and orbital configuration.	160
Figure 6-8. Cross plot of mean annual precipitation against $p\text{CO}_2$ for each palaeocontinental and orbital configuration.	161
Figure 6-9. Deep ocean circulation simulated by the CONVEC2 parameter.	162
Figure 6-10. Temperature depth profiles through the modelled oceans of each map under PD 32 conditions.	164
Figure 6-11. Isotopic temperature/model calibration points.	165
Figure 6-12. Palaeolatitudinal distribution of climatically sensitive lithologies under each palaeocontinental configuration.	178
Figure 6-13. Frequency distribution of climatically sensitive lithologies in the database by palaeocontinent.	179
Figure 6-14. PD 32 Köppen Geiger classification maps for each palaeocontinental configuration.	183
Figure 6-15. Frequency distribution of Köppen-Geiger climate classes for each basemap from PD 32 simulations.	184
Figure 6-16. Data/model agreement scores calculated for all deposits dated as "Lower Cambrian" in age.	186
Figure 6-17. Data/model agreement scores calculated for all deposits dated between 510 Ma to 520 Ma.	187
Figure 6-18. The strontium isotope curve for the Neoproterozoic/Phanerozoic transition.	188

Figure 6-19. Stratigraphic and palaeogeographical context of the major Cambrian Konservat-Lagerstätten. 194

List of Abbreviations

- AI – Ait Iyou (locality in the High Atlas Mountains, Morocco)
- BSE – BackScattered Electron mode (SEM)
- CAI – Conodont Alteration Index
- DCA – Detrended Correspondence Analysis
- EDX – Energy-Dispersive X-ray spectroscopy
- EPMA – Electron Probe MicroAnalysis
- FEG-SEM – Field Emission Gun-SEM
- GCM – General Circulation Model
- GNP – Great Northern Peninsula (western Newfoundland, Canada)
- IFM – (Alicona) Infinite Focus Microscope
- Ma – million years ago
- Myr – million years
- PCA – Principal Components Analysis
- REEs – Rare Earth Elements
- RL – Reflected Light
- SE – Secondary Electron mode (SEM)
- SEM – Scanning Electron Microscope
- SGGE – School of Geography, Geology and the Environment, UoL
- SIMS – Secondary Ion Mass Spectrometry
- SMNH – Swedish Museum of Natural History
- SSF – Small Shelly Fossil
- SST – Sea Surface Temperature
- TL – Transmitted Light
- UoL – University of Leicester

DON'T PANIC

— Douglas Adams, 1978

Chapter One: Introduction

1.1. The Cambrian climate and marine environments

The Cambrian Period has long been considered a greenhouse interval in the evolution of Earth's climate (e.g. Boucot *et al.* 2013; Erwin & Valentine 2013; McKenzie *et al.* 2016); a warm cradle of metazoan life nestled between extensive Neoproterozoic glaciations (Zhu *et al.* 2007; Halverson *et al.* 2009; Mills *et al.* 2017) and the Middle to Late Ordovician icehouse (Vandenbroucke *et al.* 2009, 2010; Cooper *et al.* 2012; Ghienne *et al.* 2014). Unlike the rest of the Phanerozoic Eon (Figure 1-1; e.g. Grossman 2012b), Cambrian climates have remained quantitatively unconstrained, with palaeoenvironmental interpretations relying on qualitative geological proxy data. Available geological data, from the distribution of climatically sensitive lithologies (e.g. Boucot *et al.* 2013), to palaeobiogeographic ranges of early animals (e.g. Kerner & Debrenne 2013; Williams *et al.* 2015), and geochemical environmental proxies (Peters & Gaines 2012), are in general agreement that the early Cambrian was a greenhouse world. There is also evidence from the strontium isotope curve (Figure 1-2) of an enhanced hydrological cycle and high continental weathering rates, compatible with a greenhouse climate, peaking around the Neoproterozoic/Palaeozoic transition (Peters & Gaines 2012).

However, the hypothesis of a continuous, stable, greenhouse climate is not unanimously accepted. Evidence of low altitude ice has been reported from both high (Landing & MacGabhann 2010) and low (Runkel *et al.* 2010) palaeolatitudes. There have also been suggestions of cool spells, associated with events in the carbon isotope and fossil record, punctuating a generally greenhouse climate (Saltzman *et al.* 2000, 2004; Elrick *et al.* 2011; Cherns *et al.* 2013).

Unlike much of the rest of the Phanerozoic, the Cambrian Period has also remained relatively untouched by general circulation model (GCM) climate simulations. Although GCM simulations have been used to interrogate Ordovician climates (e.g. Pohl *et al.* 2014, 2016, 2017), only one study has directly examined Cambrian climates (Nardin *et al.* 2011). Other studies, looking at Phanerozoic-scale climate evolution have used GCMs to provide only an average climate state for the whole Earth for two or three Cambrian time slabs, typically summarised by a global temperature estimate

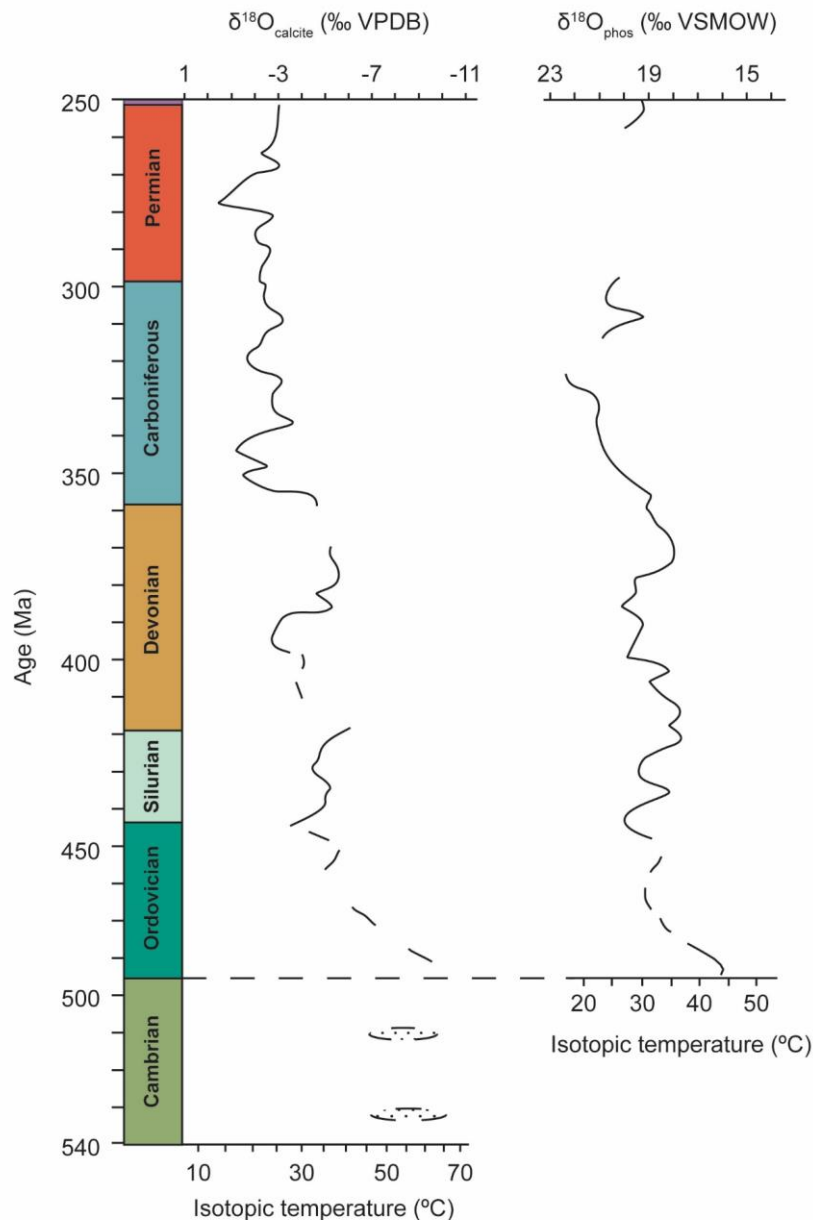
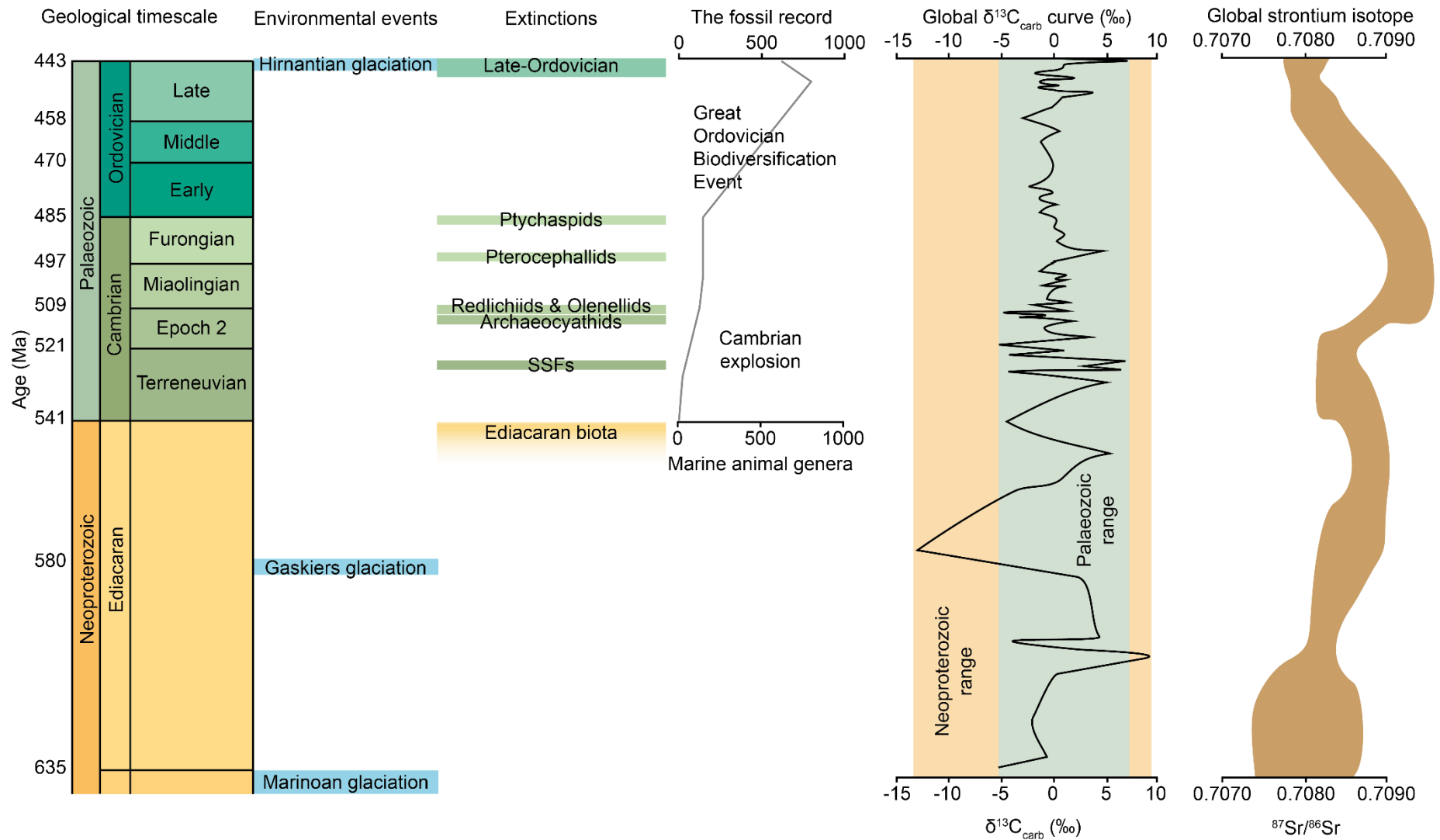


Figure 1-1. The Palaeozoic biom mineral carbonate and phosphate $\delta^{18}\text{O}$ records are broadly comparable, but lack reliable values for the Cambrian Period. Modified after Grossman (2012b).

(Goddéris *et al.* 2012, 2014; Royer *et al.* 2014). Currently, early Cambrian climates await detailed investigation by either quantitative proxy data or GCM simulations.

Constructing an accurate and precise global picture of Cambrian environments has been hampered by loose age constraints on much of the available data (Boucot *et al.* 2013), different interpretations of Cambrian palaeogeography (see Chapter Six), and conflicting proxy evidence. In particular, Cambrian ocean temperatures remain quantitatively unconstrained, despite the importance of this first-order climate parameter in controlling environments and ecosystems. This thesis aims to address the palaeoclimate data gap at the beginning of the Phanerozoic Eon.



3 Figure 1-2. The Neoproterozoic/Palaeozoic transition. There are multiple extinction events against the backdrop of a general metazoan radiation during the Cambrian Period. Extinction events after Cooper *et al.* (2012) and Peng *et al.* (2012). Marine animal genera after Alroy *et al.* (2008). Carbonate $\delta^{13}\text{C}$ from Saltzman & Thomas (2012). Strontium isotope data from Peters & Gaines (2012).

1.2. The oxygen isotope palaeothermometer

The stable oxygen isotope ratio palaeothermometer is one of the most widely used methods for quantitatively reconstructing past climate states (e.g. Grossman 2012a; Pearson 2012). Established by Harold Urey (1947; Urey *et al.* 1951), the technique uses the thermodynamic relationship between the ratio of stable oxygen isotopes ^{16}O and ^{18}O in a mineral and the temperature at which the mineral precipitated (Urey 1947). The stable oxygen isotope ratio is typically expressed using delta notation:

$$\delta^{18}\text{O} (\text{‰}) = 1000 * \left(\frac{\left(\frac{^{18}\text{O}}{^{16}\text{O}} \right)_{\text{sample}}}{\left(\frac{^{18}\text{O}}{^{16}\text{O}} \right)_{\text{standard}}} - 1 \right)$$

There is an inverse relationship between the $\delta^{18}\text{O}$ value of a mineral and the temperature at which it formed so that, all else being equal, minerals precipitated at higher temperatures will have lower $\delta^{18}\text{O}$ values. However, there is also a dependence on the initial $\delta^{18}\text{O}$ value of the fluid from which the mineral formed that must be accounted for (see Chapter Four). The $\delta^{18}\text{O}$ palaeothermometer is commonly used to interrogate marine temperatures in the geological past, and there are at least first-order quantitative constraints on sea surface temperatures (SSTs) throughout most of the Phanerozoic Eon (Grossman 2012a, b).

Recently, the $\delta^{18}\text{O}$ palaeothermometer applied to data from well-preserved fossil biominerals has helped to constrain Early Ordovician climates (e.g. Trotter *et al.* 2008; Quinton *et al.* 2018; Wheeley *et al.* 2018). However, a dearth of suitable material has hindered the application of this technique in the Cambrian Period (Figure 1-1), as phosphatic euconodonts are not known below uppermost Cambrian strata (Smith *et al.* 2002), and most calcareous fossils of this age have been considered to be diagenetically altered (Grossman 2012b). Diagenesis is a substantial problem for $\delta^{18}\text{O}$ studies and needs to be thoroughly investigated (see Chapter Three).

Recent work on late Cambrian phosphatic brachiopods concluded that the fossils were isotopically altered, with the $\delta^{18}\text{O}$ values reflecting burial, not environmental, conditions (Elrick *et al.* 2011; Bergmann *et al.* 2018). Nevertheless, the proliferation of skeletal metazoans during the Cambrian radiation leaves the tantalising possibility that palaeoclimate proxy data may be found amongst the myriad taxa of the earliest biomineralising animals.

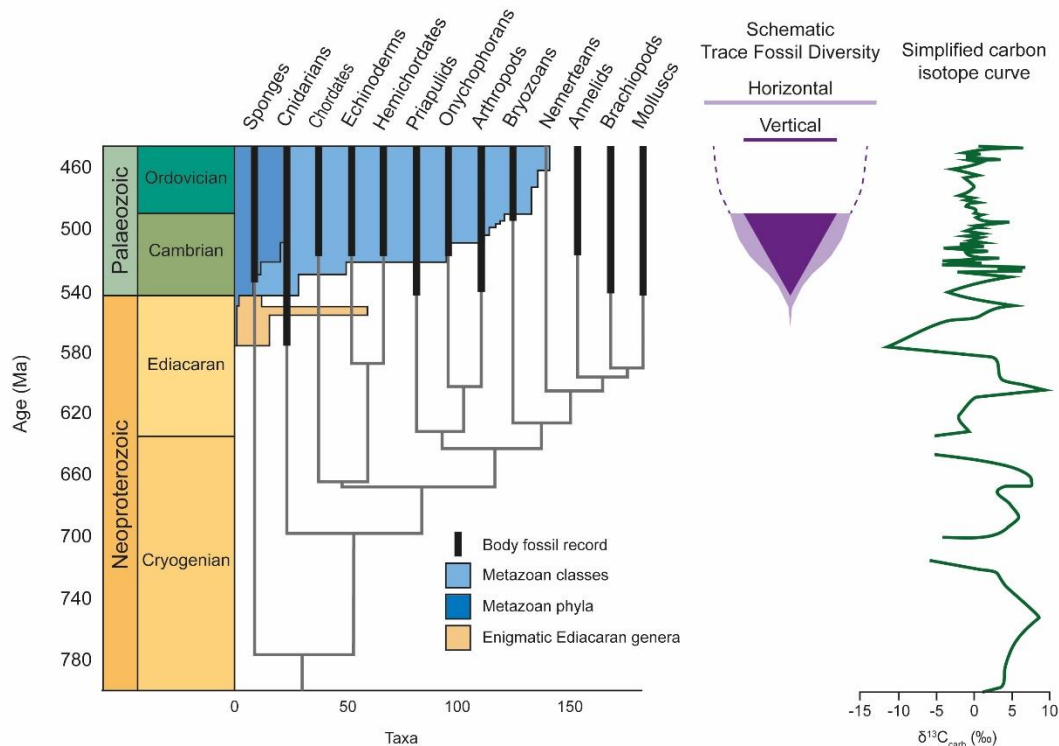


Figure 1-3. The Cambrian metazoan radiation. Diversification in the metazoan body fossil record was broadly coincident with diversification in the trace fossil record and with a step-change in the nature of the carbon cycle at Earth's surface, but these are preceded by an apparently long, cryptic, diversification in the molecular record. Redrawn after Erwin *et al.* (2011), with modifications following Kouchinsky *et al.* (2012), Antcliffe *et al.* (2014), Liu *et al.* (2014), and Van Iten *et al.* (2014). Schematic trace fossil diversity after Marshall (2006). Simplified carbon isotope curve after Saltzman & Thomas (2012)

1.3. Marine environments and the Cambrian metazoan radiation

The Cambrian metazoan adaptive radiation, colloquially called the 'Cambrian explosion', marked a step-change in the evolution of marine life as mobile metazoans replaced the largely sessile benthos that dominated Ediacaran sea floors (e.g. Erwin & Valentine 2013). Most animal phyla appear in the fossil record during the Cambrian radiation (Figure 1-3; Peterson *et al.* 2005; Marshall 2006; Maloof *et al.* 2010b; Sperling *et al.* 2010; Erwin *et al.* 2011), and diversification in the body fossil record is preceded by an equally impressive explosion of trace fossils (Jensen 2003; Jensen *et al.* 2005; Seilacher *et al.* 2005; Oji *et al.* 2018). Trace fossils become increasingly three-dimensional through the Cambrian substrate revolution (Bottjer *et al.* 2000; Bottjer 2012) as complex burrowing habits evolved, increasing the sediment mixed layer depth. The emergence of complex mobile animals and their ecosystems profoundly changed marine environments and geochemical cycles (Smith & Harper 2013) – a change that

marks the Proterozoic/ Phanerozoic eonothem transition (Landing 1994; Brasier *et al.* 1994; Babcock *et al.* 2014).

Discoveries of exceptionally preserved fossils from this interval mean that the biological side of this ecological revolution has been well-studied (Conway Morris 1989; Brooks 2012; Paterson *et al.* 2016; Hou *et al.* 2017). Much work has also gone into understanding changes in the carbon (Brasier *et al.* 1994; Saltzman *et al.* 2000; Maloof *et al.* 2005, 2010a; Zhu *et al.* 2007; Shields 2017, 2018; Boyle *et al.* 2018), sulphur (Strauss *et al.* 2001; Shields *et al.* 2004; Mazumdar & Strauss 2006) and phosphorous (Brasier 1990, 1992b; Cook 1992; Porter 2004; Brasier & Callow 2007; Boyle *et al.* 2014) cycles across the Proterozoic/Phanerozoic transition. However, the physical characteristics of the marine environments which early animals lived in and moulded, such as ocean temperatures, remain poorly constrained.

Nevertheless, some qualitative remarks can be made. The Cambrian radiation occurred during an interval with extensive shallow marine shelf settings, particularly shallow tropical platform environments (Walker *et al.* 2002; Kiessling *et al.* 2003), which generally promote biodiversity (Erwin 2009). Deep ocean oxygen levels were likely low in the early Palaeozoic (Wallace *et al.* 2017; Stolper & Keller 2018), and may have declined during the the early Cambrian (Boyle *et al.* 2014; Wallace *et al.* 2017). There is an emerging picture of highly variable redox conditions in shallow Cambrian seas (Zhuravlev & Wood 1996; Faggetter *et al.* 2017; Wang *et al.* 2018; Wei *et al.* 2018), possibly relating to fluctuating oxygen minimum zones (Hammarlund *et al.* 2017; Guilbaud *et al.* 2018). Nevertheless, terminal Neoproterozoic through early Palaeozoic oceans were sufficiently oxygenated to support metazoan life (Butterfield 2009; Sperling *et al.* 2013; Lenton *et al.* 2014; Mills *et al.* 2014; Erwin 2015), though fluctuating oxygen levels may have contributed to ecosystem instability (Wei *et al.* 2018; Wood *et al.* 2018).

Whilst greenhouse climate intervals are commonly associated with increased biodiversity, warm temperatures are also associated with increased origination and extinction rates (Mayhew *et al.* 2012), though a mechanism to explain this association is not currently known (Clarke 2017). The lower solubility of oxygen in water at higher temperatures may have played an important role in early Palaeozoic marine environments (Peters 2007; Erwin 2009). However, quantitative physical constraints are needed in order to properly evaluate the potential roles of significant environmental parameters on biodiversity.

Some of the earliest skeletal fossils may be able to help tackle this lack of quantitative palaeoclimate proxy data. The term ‘small shelly fossils’ (SSFs) applies to a diverse range of early Cambrian skeletal fossils that represent at least six modern animal phyla and still include many problematica (Bengtson 1992, 2004; Kouchinsky *et al.* 2012). These fossils are the remains of animals that produced skeletons of both carbonate and phosphate, although they are often preserved by secondary phosphate (e.g. Brasier 1990; Porter 2004). However, some SSFs were originally phosphatic and some of these may preserve palaeoenvironmental $\delta^{18}\text{O}$ signals. In this case, the Cambrian explosion could provide a solution to the dearth of earliest Phanerozoic quantitative palaeoclimate data.

1.4. Scope of the thesis

1.4.1. Aims

The primary aim of this study is to quantitatively constrain Cambrian marine environments, with a focus on sea surface temperatures (SSTs) in the earlier part of the Cambrian Period. This may be achieved by using the phosphate oxygen isotope thermometer to estimate SSTs from the $\delta^{18}\text{O}$ data of identifiably well-preserved phosphatic SSFs. To improve confidence in the results, this should be combined with an independent approach, such as general circulation model (GCM) climate simulations. Secondary aims include putting first-order constraints on a Cambrian latitudinal SST gradient and establishing whether current models of palaeocontinental configuration are consistent with global climate patterns expected from climatically sensitive geological data and GCM results.

1.4.2. Objectives

There are several subsidiary objectives to meet in pursuit of the primary aim.

- (a) Identify and sample SSF material from high (Avalonia, West Gondwana) and low (Laurentia) palaeolatitudes that may preserve Cambrian palaeoenvironmental $\delta^{18}\text{O}$ signals (see Chapter Two and Chapter Three).
- (b) Determine and apply criteria for selecting SSF taxa suitable for isotopic analyses (see Chapter Three).
- (c) Establish a protocol for identifying preserved biogenic phosphate in SSFs that distinguished between biogenic and diagenetic material at coarse and fine scales (see Chapter Three).

- (d) Determine and apply the most suitable method for extracting $\delta^{18}\text{O}$ data from well-preserved SSFs (see Chapter Four).
- (e) Use the phosphate oxygen isotope thermometer to estimate early Cambrian SSTs from high and low palaeolatitude $\delta^{18}\text{O}$ data (see Chapter Five).
- (f) Run GCM simulations of early Cambrian climate to test the diverse hypotheses of palaeocontinental configurations and atmospheric CO_2 levels (see Chapter Six).
- (g) Use isotopic temperature estimates to calibrate the GCM simulations (see Chapter Six).
- (h) Compare the distribution of climatically sensitive lithologies to the global climate patterns predicted under different GCM simulations to evaluate the relative performances of different palaeogeographic and atmospheric CO_2 hypotheses (see Chapter Six).

1.5. Thesis summary

Chapter Two details the geographical and geological settings of the materials used throughout the rest of the thesis. Lower Cambrian deposits in Shropshire, UK, the High Atlas Mountains, Morocco, and western Newfoundland and southern Labrador, Canada, were examined. Chapter Two describes the depositional settings and stratigraphical relationships of these sites.

Chapter Three establishes a protocol for assessing the preservation of biogenic phosphate in SSFs. The limitations of the early Palaeozoic stable oxygen isotope ($\delta^{18}\text{O}$) record are addressed, and selected SSFs are considered as candidate material for tackling those limitations. Chapter Three concludes with hypotheses that can be tested with $\delta^{18}\text{O}$ in Chapter Four.

Chapter Four details $\delta^{18}\text{O}$ analyses of early Cambrian SSFs from both bulk and *in situ* measurement techniques. Both inter- and intra-specimen variability are addressed, with particular reference to the hypotheses proposed in Chapter Three.

Chapter Five evaluates the geological and palaeoenvironmental implications of the $\delta^{18}\text{O}$ data presented in Chapter Four. The secular trend in $\delta^{18}\text{O}$ values over time is discussed, and $\delta^{18}\text{O}$ data presented in Chapter Four are used to estimate Cambrian SSTs.

Chapter Six combines palaeoclimate data and GCM simulations to evaluate Cambrian climates. The GCM simulations, calibrated with isotopic temperature estimates from Chapter Five, are compared to a newly compiled database of climatically

sensitive lithologies. The GCM simulations and lithological database are used to evaluate the current diverse hypotheses about early Cambrian continental configuration. Finally, this chapter hosts a broad discussion of some of the palaeoenvironmental and palaeobiological implications of the palaeoclimate data presented in this thesis.

Chapter Seven concludes this work with a summary of the results of the preceding chapters, along with some indications for the direction in which future work might fruitfully travel.

Elements of this thesis, from chapters Three to Six, relating to data from the Comley Limestones, Shropshire, UK, were recently published in Hearing *et al.* (2018).

Chapter Two: Geological settings

2.1. Chapter summary

Chapter Two provides the geological context for the materials used throughout this thesis. Three sites of interest are identified, in the UK, Morocco and Canada, and their sedimentology and depositional environments are briefly described. The samples used throughout this thesis are put in geographical and chronostratigraphical context.

2.2. Introduction

This study aims to place reliable quantitative constraints on early Cambrian climates (see §1.4), and ‘small shelly fossils’ (SSFs) of animals that produced phosphatic skeletons are a potential source of palaeoclimate proxy data. SSFs are found globally in lower and middle Cambrian rocks; however, they are commonly preserved by secondary, i.e. diagenetic, phosphate (Porter 2004). Secondary phosphate is problematic for palaeoclimate work because the diagenetic conditions it formed in may bear no relation to the environment in which the animal lived. It is therefore important to identify Cambrian strata in which SSFs have not been affected by pervasive secondary phosphatisation. In pursuit of this project, three localities with potentially suitable lower Cambrian strata were identified: Shropshire, UK, the High Atlas Mountains, Morocco, and Newfoundland and Labrador, Canada.

2.2.1. The Comley Limestones – a priority target

A pilot project in 2008/9 on phosphatic SSFs from the Comley Limestones yielded promising results. The Comley Limestones have been extensively studied since the early 20th Century work of Edgar Sterling Cobbold (1910, 1911, 1913, 1921, 1927; Cobbold & Pocock 1934). The unit has since become well-known for preserving the soft anatomy of microarthropods (Siveter *et al.* 2001, 2003). The Comley Limestones (Ac2 to Ac5 and Ad of Cobbold 1921) are one of the best-dated early Cambrian rock units in the world. Zircon-bearing bentonite beds in the upper Green *Callavia* Sandstone (Ac1 of Cobbold 1921) and lowermost Quarry Ridge Grits (Ba1 of Cobbold 1921) provided lower and upper radiometric (U-Pb) radiometric age constraints of 514.45 ± 0.36 Ma and 509.10 ± 0.22 Ma, respectively (Harvey *et al.* 2011). These radiometric ages correlate the upper Comley Series of British regional stratigraphy to Cambrian Series 2 Stage 4 of the international chronostratigraphic scheme.

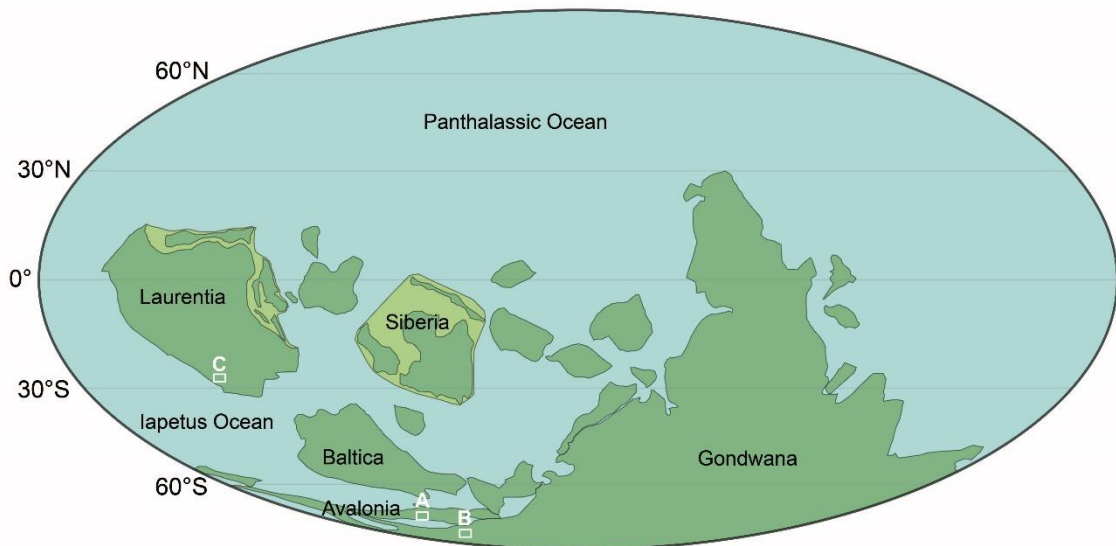


Figure 2-1. A typical view of early Cambrian palaeogeography. A = Shropshire, UK; B = High Atlas Mountains, Morocco; and C = Newfoundland and Labrador, Canada. Adapted after the 520 Ma reconstruction of Torsvik and Cocks (2013, 2016).

The skeletal fauna of the Comley Limestones has been extensively studied (Cobbold 1921, 1931; Brasier 1986; Hinz 1987; Winrow 2015). Strikingly, unlike many deposits of similar age, there is remarkably little secondary phosphatisation of the Comley Limestones microfauna, other than the exceptional preservation of microarthropod soft anatomy that must have occurred very soon after death (Siveter *et al.* 2001, 2003). The Comley Limestones are thought to have been deposited in a shallow marine setting (e.g. Rushton 1974; see §2.4) on the microcontinent Avalonia and are therefore representative of Cambrian sea surface conditions. The tightly-constrained depositional age, shallow marine setting, and lack of pervasive secondary phosphatisation of the microfauna made the Comley Limestones a high priority target for further investigation.

2.2.2. Early Cambrian geography

The distribution of continents, landmasses and oceans exerts a strong control on both local and global climate states. Early Cambrian palaeogeography remains hotly debated, including the positions of some of the major continents (see Chapter Six; e.g. Landing *et al.* 2013b; Torsvik & Cocks 2013, 2016). However, an emerging orthodox view is that there was an ‘antartocentric’ distribution of land, with part of West Gondwana, either South America or North Africa, lying over the South Pole (Figure 2-1). Laurentia is generally considered to have straddled the equator, spanning tropical latitudes. Baltica is thought to have occupied mid-southern latitudes, and Avalonia is generally regarded

as a high latitude peri-Gondwanan continent during the early Cambrian. Initially, this study will operate on the working assumption that the Torsvik and Cocks (2009, 2013, 2016) suite of reconstructions, widely used by lower Palaeozoic researchers (e.g. Vandenbroucke *et al.* 2010; Pohl *et al.* 2014; Servais *et al.* 2014; Williams *et al.* 2015; Martin *et al.* 2016; Paterson *et al.* 2016; Ortega-Hernández *et al.* 2017), most accurately reflects early Cambrian palaeogeography (but see Chapter Six).

2.3. Materials and Methods

Samples of the Comley Limestones were recovered from a trench approximately 200 m south of Comley Quarry in 2009, with over 1,000 kg of rock recovered (see Harvey *et al.* 2011). The Comley Limestones are up to 2 m thick (Rushton 1974), but only approximately 0.8 m thick at the sampled locality. Identification of the horizons within the Comley Limestones in the field is not straightforward and, during collection, samples were given arbitrary labels (A to W), with a small letter used to indicate relative stratigraphic height of different blocks within each sample (a to d). For example, sample Aa is stratigraphically lower than sample Ad, but nothing can be inferred from this relationship about the relative stratigraphic position of sample Bc. At the time of collection, most of this material was thought to be from Ac4 and Ac5 of Cobbald (1921).

Reviews of the published SSF literature suggested two further priority localities for examination. The classic ‘early/middle’ Cambrian boundary section near Ait Iyou, High Atlas Mountains, Morocco, has been subjected to extensive stratigraphic consideration (Geyer 1989, 1990b; Geyer & Landing 1995, 2006; Landing *et al.* 2006; Álvaro & Clausen 2007; Álvaro *et al.* 2014), and calcareous and phosphatic shelly fossils are found alongside each other. Furthermore, during the early Cambrian, North Africa is thought to have been situated at similarly high latitudes to the Comley Limestones (Figure 2-1; Torsvik & Cocks 2013, 2016; but see Landing *et al.* 2013a, b). Samples were collected in April 2016 following the detailed measured logs of Geyer & Landing (1995, 2006), with further high resolution logs produced where necessary.

The lower Cambrian Forteau Formation, Newfoundland and Labrador, Canada, was also identified as a suitable target because its stratigraphy is well known (Knight 2013; Knight *et al.* 2017; Skovsted *et al.* 2017) and the unit has a relatively gentle post-depositional history. Although many taxa can be found preserved in secondary phosphate (e.g. Skovsted & Peel 2007), secondary phosphatisation is not ubiquitous.

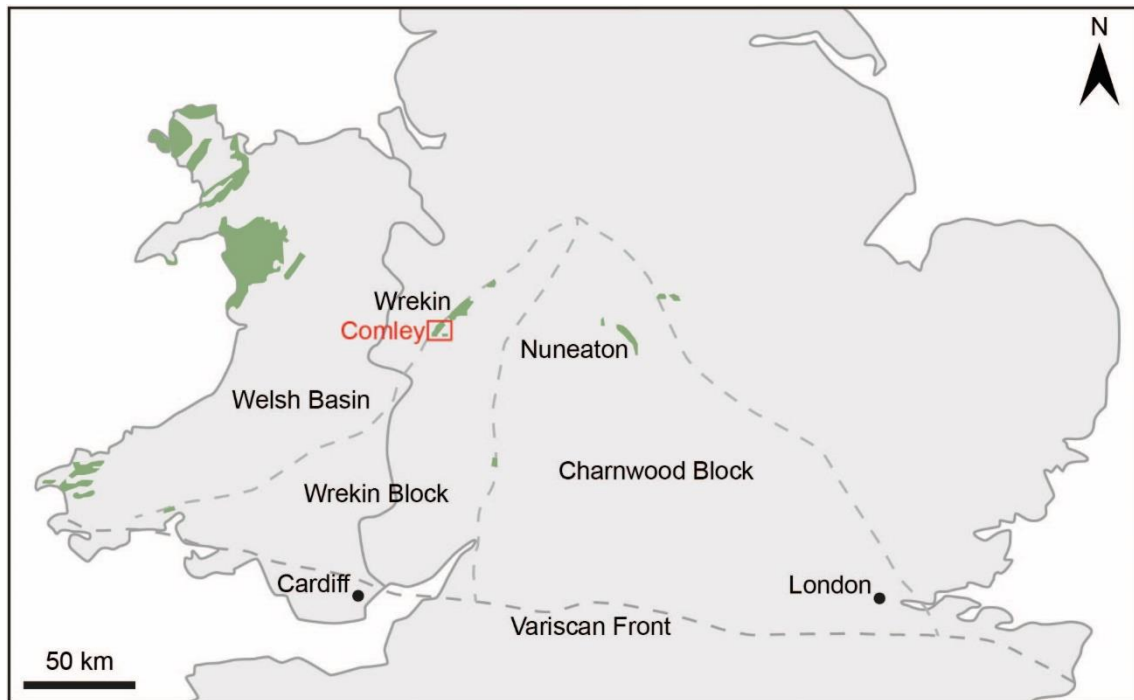


Figure 2-2. Cambrian and Tremadocian (lowest Ordovician) strata (green shading) and major Palaeozoic tectonic structures (dashed lines) of southern Britain. Modified after Brenchley *et al.* (2006), Rushton *et al.* (2011), Harvey *et al.* (2011).

The lower Cambrian rocks of western Newfoundland and southern Labrador were deposited on the palaeo-southern margin of Laurentia and provide a low latitude comparison to the UK and Moroccan strata (Figure 2-1). The Forteau Formation was sampled from western Newfoundland and southern Labrador in July 2017.

2.4. Samples from the Comley Limestones, Shropshire, UK

Cambrian strata crop out across the English Midlands, Welsh Borderlands and Wales (Figure 2-2). The Comley Limestones are found in the Welsh Borderlands and are well known for yielding abundant lower Cambrian SSFs (Brasier 1986; Hinz 1987).

Although the Comley Limestones fauna has been extensively studied (Cobbold 1910, 1911, 1913, 1921, 1931, 1936; Cobbold & Pocock 1934; Brasier 1986; Hinz 1987; Winrow 2015), less attention has been paid to the sedimentology and depositional environment of these rocks. The Comley Limestones stratigraphy was established by Cobbold (1921) on the basis of lithological and faunal differences between horizons, and five subsidiary units were recognised using an alphanumeric scheme (Figure 2-3; Cobbold 1921) which has been adopted with only minor modifications by later authors (Cobbold 1927; Cobbold & Pocock 1934; Rushton 1974, 1999; Siveter *et al.* 2003; Harvey *et al.* 2011; Rushton *et al.* 2011).

Following Cobbold's (1921) divisions (updated by Cobbold 1927; Raw in Cobbold 1931; Cobbold & Pocock 1934), the lithologies of the Comley Limestones were revisited by Rushton (1974) whose descriptions informed most subsequent work (Brasier 1986, 1989; Hinz 1987; Rushton 1999, 2011; Brenchley *et al.* 2006; Harvey *et al.* 2011; Winrow 2015).

The Comley Limestones are a series of laterally discontinuous condensed calcareous horizons separated by discontinuities and sandwiched between two sandstone units (Figure 2-3). The total thickness of the Comley Limestones is something less than 2 m, though the thickness of the subunits varies greatly from one outcrop to another, with some horizons often pinching out altogether (Rushton 1974).

The Green *Callavia* Sandstone (Ac1) is considered to be the uppermost unit of the Lower Comley Sandstone, but is conformable with the overlying Comley Limestones (Rushton 1974). Ac1 is a weakly indurated fossiliferous green sandstone, primarily comprising quartz, feldspar and muscovite with abundant glauconite and very little calcite cement (Raw in Cobbold 1931; Rushton 1974). The fauna is very similar to, though not as rich as, that of the overlying Ac2.

The Red *Callavia* Limestone (Ac2) conformably overlies Ac1 and comprises a richly fossiliferous nodular reddish or purple calcareous sandstone with abundant glauconite, detrital quartz and mica (Raw in Cobbold 1931; Rushton 1974, 1999). Trilobite fragments dominate the calcareous bioclasts and are thickened by the growth of secondary calcite.

The *Eodiscus bellimarginatus* Limestone (Ac3) is somewhat similar to the underlying Ac2 but is a lighter phosphatic sandy limestone (Rushton 1999), with patches of glauconite and detrital material. Towards the top, Ac3 becomes rich in phosphatic clasts (Rushton 1974).

The *Strenuella* Limestone (Ac4) is a red or purple to grey sandy limestone with abundant glauconite and phosphate (Rushton 1974). The detrital component is finer grained and less abundant than that of Ac3, though it may include rounded quartz pebbles (Brasier 1989).

The *Protolenus* Limestone (Ac5) is a pale to dark grey highly fossiliferous limestone that becomes brownish where phosphatic material is most abundant. Ac5 has little arenaceous material, though glauconite is abundant, and primarily comprises calcitic echinoderm plates with a calcitic and ferruginous cement (Rushton 1974).

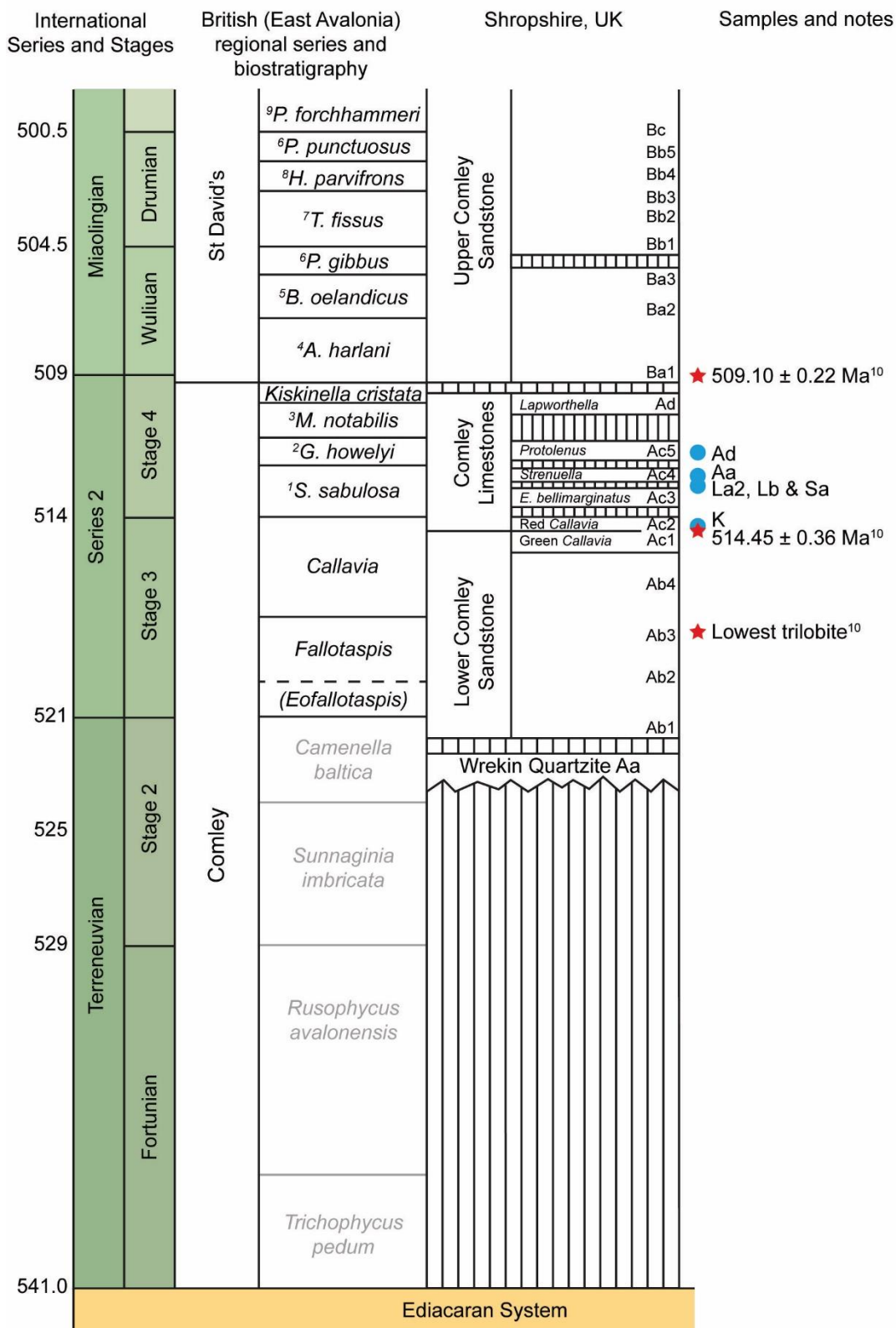


Figure 2-3. Lower/middle Cambrian stratigraphy of Comley, Shropshire, UK. Blue dots denote samples. ¹*Strenuella*; ²*Geyerorodes*; ³*Morocconus*; ⁴*Acadoparadoxides*; ⁵*Baltoparadoxides*; ⁶*Ptychagnostus*; ⁷*Tomagnostus*; ⁸*Hypagnostus*; ⁹*Paradoxides*; ¹⁰*Harvey et al.* (2011). From data in Rushton *et al.* (2011), Harvey *et al.* (2011), Peng *et al.* (2012), and Williams *et al.* (2013).

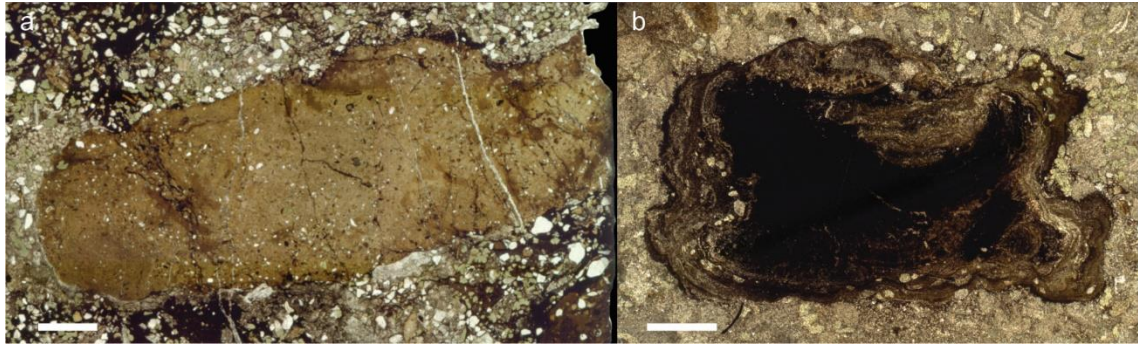


Figure 2-4. Massive (a) and laminated (b) phosphate nodules from the Comley Limestones. Scale bars = 1 mm.

The *Lapworthella* Limestone (Ad) unconformably overlies all of the Comley Limestones horizons and locally transgresses the Lower Comley Sandstone, though it often thins out entirely (Cobbold 1921; Rushton 1974; Brasier 1989). Ad is whitish pink or black, with a high proportion of phosphatic material, abundant glauconite and patches of fine detrital material. Phosphatic material occurs as granules or lumps and may be massive or laminated (Figure 2-4). Mn- and Fe-rich metalliferous nodules are common and are often laminated.

2.4.1. Petrography of samples used in this thesis

Four lithologies were identified in the samples collected for this work (Figure 2-5; Table 2-1). These lithologies were compared to the published descriptions of the the Comley Limestones horizons proposed by Cobbold (1921, 1927) and Raw (in Cobbold 1931) and expanded by Rushton (1974).

Sample K is readily identifiable as Ac2 and is therefore from the lowermost horizon of the Comley Limestones. The lower proportion of detrital material and high proportion of trilobite fragments in sample Aa suggests an assignation of Ac4. The echinoderm hash of sample Ad identifies this as belonging to Ac5.

The phosphatic sandy limestone of samples La2 and Lb are more difficult to place in the established lithostratigraphic scheme. The high proportion of glauconite, phosphate and detrital grains precludes assignment to Ac5 or Ad. The lithology of La2 and Lb most closely match descriptions for either uppermost Ac3, where phosphatic material is more abundant (Rushton 1974), or perhaps lower Ac4 which can include large rounded quartz grains (Brasier 1989).

No unprocessed rock or thin sections remained of sample Sa when this study began in 2014. However, coarse fragments of acid-resistant residue (following acetic acid maceration) bear a close resemblance to samples La2 and Lb, being very sandy

with large, up to pebble-sized, phosphatic and metalliferous nodules. At the time of collection, in 2009, samples La2, Lb and Sa were considered to come from the same horizon.

The interpretation of La2, Lb and Sa as belonging to Cobbold's Ac3 would be contrary to previously published stratigraphies of the trench section that interpreted the majority of the excavated 'middle limestone' as Ac4 or Ac5 (Siveter *et al.* 2003; Harvey *et al.* 2011). It was thought that Ac3 was largely absent from the stratigraphy at this locality. However, from sedimentological data it appears that either the upper Ac3 is preserved here, or that the lower part of Ac4 is lithologically similar to Ac3 and that a revision of the lithological descriptions may be necessary. The sedimentology and stratigraphy of the trench section warrants further detailed study.

The phosphatic horizon near the base of sample K (Figure 2-6) is up to 3 cm deep with an angular upper surface, and it separates two distinct lithologies: an underlying trilobite-rich sandy limestone and an overlying glauconite-rich sandy limestone with few biogenic clasts (Figure 2-6e). The overlying glauconite-rich unit also contains subrounded to angular phosphatic pebble-sized clasts (Figure 2-6d). In places, the uppermost part of the phosphatic horizon includes laminae of glauconite and quartz clasts (Figure 2-6c).

Petrographic observations suggest that the phosphate has an early diagenetic origin, at or close to the sediment/water interface (Glenn *et al.* 1994). These observations include lithological differences between the underlying and overlying units, the irregular upper surface, the preservation of calcareous fossils between the phosphate groundmass, and the fine glauconite and quartz laminae near the top of the horizon. Phosphate precipitation was occasionally interrupted, and the horizon was ultimately exposed to erosion on the sea floor (Figure 2-6f). This horizon is therefore interpreted as an early diagenetic phosphate hardground. Eroded phosphate clasts were eventually incorporated into the overlying lithology, contributing to the phosphate clasts in these overlying horizons. Laminated phosphate clasts in the horizons above the hardground are more readily explained as the result of microbially-mediated precipitation as oncoliths on the sea floor, trapping detrital grains as they grew.

<u>Sample</u>	<u>Description</u>	<u>Cobbold Horizon</u>
Ad	Echinoderm grainstone	Ac5
Aa	Trilobite wackestone to packstone	Ac4
Lb (orientation unknown)	Glaucinite-quartz packstone with phosphatic and metalliferous nodules	Ac4/Ac3
La2		
K	Trilobite-glaucinite packstone	Ac2

Figure 2-5. Plane polarised micrographs of orientated thin sections from the samples examined in this thesis. Sections: Ad.01; Aa.01; Lb.04a; La2.01; K.01. Scale bar = 10 mm.

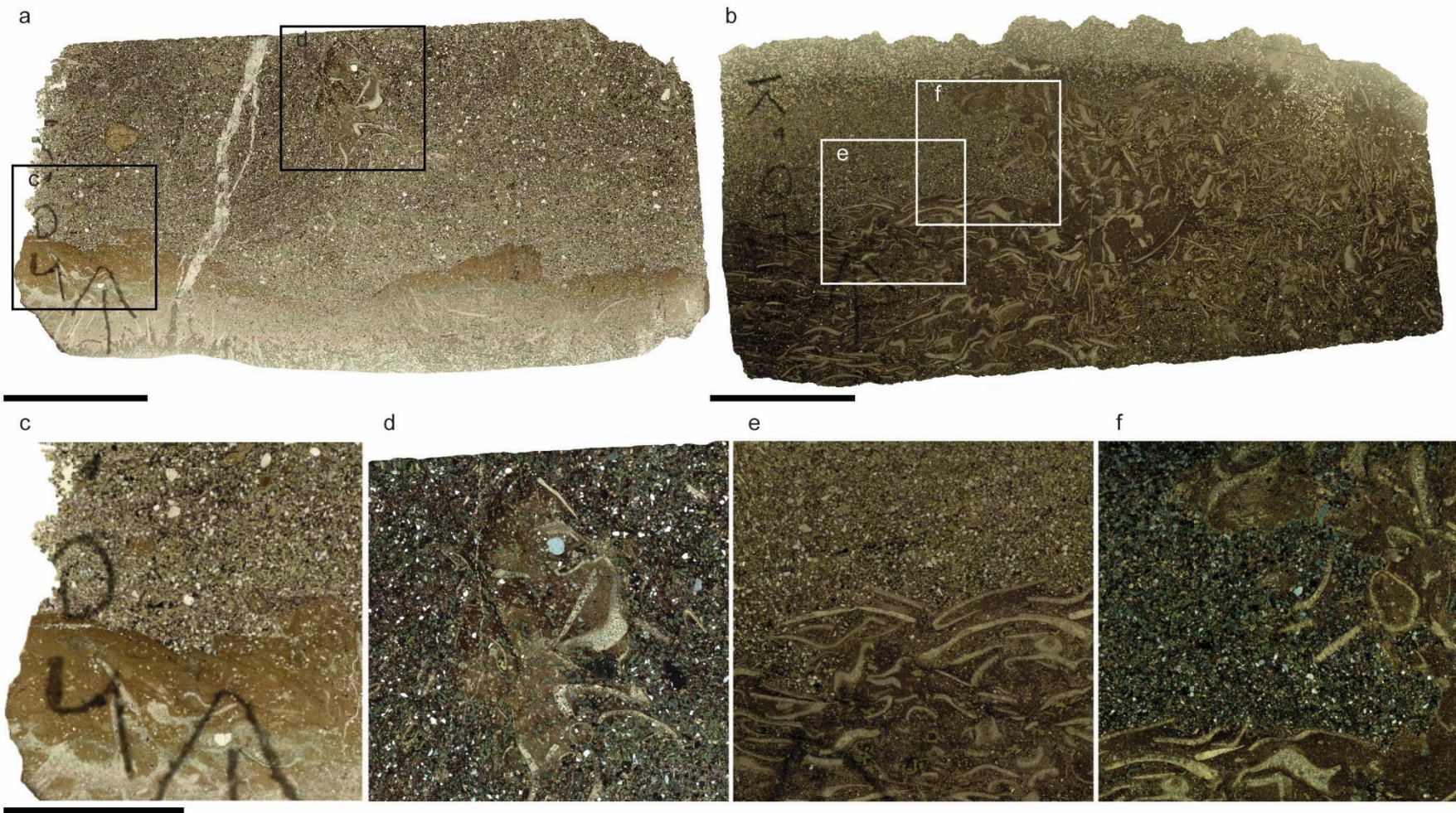


Figure 2-6. Thin section images of the hardground near the base of the Comley Limestones. (a) overview of section K.02. (b) overview of section K.04. (c) top of phosphate horizon. (d) rip-up clast of phosphate horizon in the overlying lithology. (e) sharp contact of phosphatised trilobite-rich limestone with overlying glauconite-quartz sandy limestone. (f) phosphate layer eroded by local undercutting. Scale bars: (a, b) = 10 mm; (c to f) = 5 mm.

Table 2-1. Sedimentology and depositional environments of the Comley Limestones.

Sample	Thin sections	Description	Facies	Cobbold horizons
Aa	01	Reddish-grey trilobitic hash with a micritic matrix, minor glauconite and angular to subangular quartz, and void-filling spar. No evidence of echinoderm fragments. Greenish patches rich in glauconite and quartz, and poor in shelly material. Several geopetal structures evidenced by void-filling sparry calcite.	Trilobite wackestone to packstone	Ac4
Ad	01	Greenish-grey echinoderm hash with abundant glauconite and rarer detrital quartz, lithic fragments, and subangular to rounded massive phosphate clasts. Includes some larger laminated phosphate clasts, trapping quartz and glauconite grains, and often with well-defined edges. Also, some laminated opaque clasts, some with well-defined edges though others are diffuse about a central nodule. Opaque material may pervade adjacent calcite clasts and picks out the stereome structure of echinoderm fragments. No evidence of trilobite fragments.	Echinoderm grainstone	Ac5
K	01 to 04	Irregular phosphate horizon at the base separates two distinct lithologies: underlying trilobite-rich limestone and overlying glauconite- and quartz-rich sandy limestone with minor white mica flecks. Overlying lithology includes some coarser quartz and phosphate grains, up to pebble size. There are no echinoderm fragments.	Trilobite glauconite packstone	Ac2 (with green patches perhaps ripped-up Ac1?)
La2	01	Glauconite-rich microsparite with opaque and phosphate clasts, poorly sorted with abundant angular to rounded quartz grains. Phosphatic fossils are abundant but calcareous fossils are rare. Patches of a rice-like texture that grades between micrite and microspar. Phosphate clasts occur as massive and laminated forms, both types incorporate glauconite and quartz grains. An opaque mineral occurs as massive pervasive patches and well-defined laminated clasts which may trap detrital grains.	Glauconite quartz packstone	Uppermost Ac3 or lower Ac4

Lb	01 to 04	Similar to La2. Heterogeneous glauconite-rich microsparite, poorly sorted, with abundant angular to rounded quartz clasts. Phosphatic fossils are abundant, but calcareous fossils are rare. Patches of rice-textured calcite lacking glauconite, quartz and fossil material. Phosphate clasts occur as massive and laminated forms, resembling oncolites, both types incorporate glauconite and quartz grains. An opaque mineral occurs as massive pervasive patches and well-defined laminated clasts which may trap detrital grains.	Glauconite quartz packstone	Uppermost Ac3 or lower Ac4
Sa	NA	No thin section. Only fragments of acetic acid-resistant residue remain. Sandy limestone with pebble-sized phosphate and red/purple nodules. Comparable to samples La2 and Lb.	NA	Uppermost Ac3 or lower Ac4

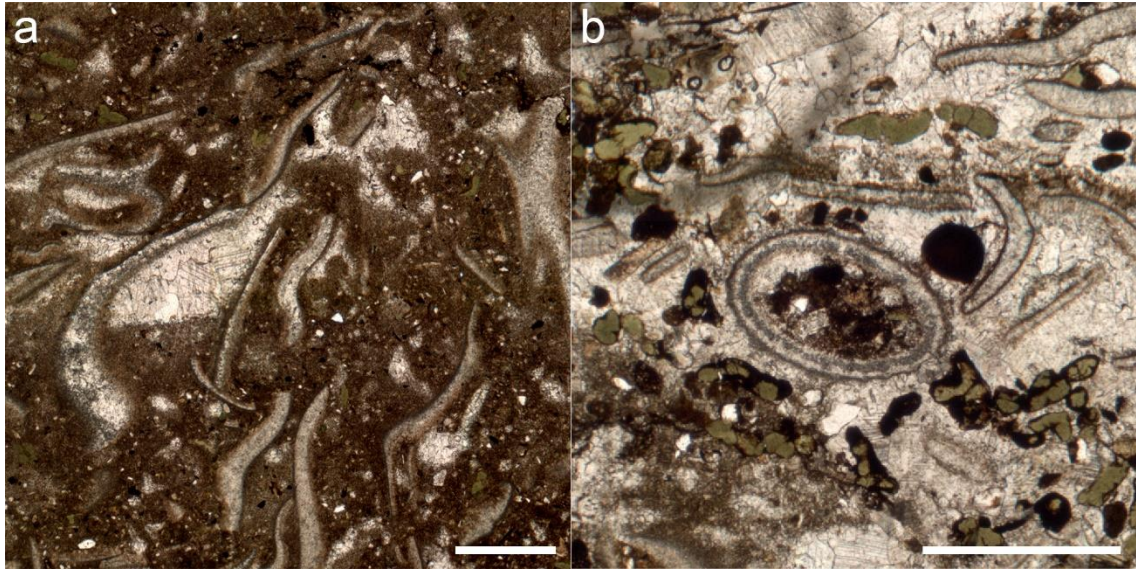


Figure 2-7. Geopetal structures in sample Aa indicate way-up and pre-compaction cementation. (a) A trilobite shell creates a space that was part-filled by lime mud, with the remaining space filled by sparry calcite cement. (b) A calcareous tube (*Coleoides?*) part-filled with mud and detrital grains. Scale bars = 1 mm.

2.4.2. Depositional setting of the Comley Limestones

The contact between the Comley Limestones and the Upper Comley Sandstone is unconformable, recording uplift and tilting of the lower Cambrian Lower Comley Sandstones and Comley Limestones before deposition of middle Cambrian strata (Cobbold 1925; Brasier 1989). The uplift and tilting are compatible with fault block rotation in an extensional, early rift, regime (Rees *et al.* 2014). The Comley Limestones were deposited in a high energy shallow marine setting, with deposition and erosion finely balanced and controlled by local fault activity (Rushton 1974; Brasier 1989; Landing 1996; Rees *et al.* 2014).

The matrix observed in some of the Comley Limestones horizons has been recrystallized but is likely to be neomorphic after micrite following deposition as a lime mud. Phosphate and glauconite grains, abundant throughout the succession, require low background sedimentation rates to form – a condition supported by the relative paucity of clastic material versus the abundance of skeletal grains.

Laminations in some of the phosphatic and metalliferous nodules, which may trap detrital grains, indicate microbially-mediated precipitation on the sea floor. Oncolite formation also requires low background sedimentation rates and periodic overturning of the oncolites. Most of the skeletal grains are fragmentary, implying a high energy current-washed setting. Void-filling spar preserved geopetal structures in some beds (Figure 2-7), suggesting early diagenetic, pre-compaction, calcite cementation. Ripped-

up phosphate clasts in the overlying strata show that this was a highly erosive setting, with episodic deposition and lithification before the next erosive interval.

There are abundant younger strata to which the depositional environment of the Comley Limestones could be compared, such as the Jurassic ‘Snuff Box’ Bed of the Inferior Oolite Formation, or the ‘Junction Bed’ or Beacon Limestone Formation (Gatrall *et al.* 1972; Jenkyns & Senior 1991). However, a temporally closer analogue is the Brèche à *Micmacca* Member of the Jbel Wawrmast Formation, lower/middle Cambrian boundary of southern Morocco. The basal beds of the Brèche à *Micmacca* Member in the Lemdad Syncline in southern Morocco are a succession of condensed trilobitic, glauconitic and phosphatic sandy grainstones to wackstones, containing ferruginous ooids (Landing *et al.* 2006). These beds are interpreted as having been deposited in deepening-upwards settings from subtidal to proximal inner shelf environments (Landing *et al.* 2006). A similar depositional setting is likely for the Comley Limestones.

The Comley Limestones were likely deposited in a proximal inner shelf environment, above storm wavebase, and therefore any palaeoenvironmental signals will reflect sea surface conditions. Secondary phosphatisation is not pervasive throughout the succession, but instead is limited to a hardground horizon near the base, and further up to oncolitic nodules. The Comley Limestones’ SSFs are therefore a high priority target to investigate for early Cambrian environmental proxy data.

2.5. Samples from the Cambrian of the High Atlas Mountains, Morocco

An early Palaeozoic sedimentary cover sequence was deposited on Pan-African Orogen basement rock during the Cambrian marine transgression (Destombes *et al.* 1985; Geyer & Landing 1995, 2006). Lower through upper Cambrian strata crop out in the Anti-Atlas and High Atlas mountains, Morocco, representing a range of depositional settings from fluvial to offshore marine environments (Geyer 1989; Geyer & Landing 1995, 2006; Álvaro *et al.* 2014). The oldest shelly fossils are recorded from the Igoudine Formation in the Anti-Atlas region, and shelly taxa appear only slightly higher in the coeval Lemdad Formation in the High Atlas region (Geyer & Landing 1995, 2006; Álvaro *et al.* 2014). The reported preservation quality of SSFs in the Anti-Atlas region is poor and secondary phosphatisation is abundant. However, the few reports on SSFs from the Lemdad Syncline region of the High Atlas Mountains, where calcitic and

phosphatic fossils occur alongside each other, suggest that skeletal preservation may be much better (Geyer & Landing 1995, 2006).

In the Lemdad Syncline, a thick fossiliferous succession of mixed siliciclastic and carbonate rocks, with archaeocyathan bioherms and condensed phosphatic and glauconitic limestone beds, crops out near the village of Ait Iyou (Figure 2-8; e.g. Geyer 1989; Geyer & Landing 1995, 2006). The stratigraphy of this section is well-studied and has been correlated across the region and internationally using trilobite biostratigraphy (Geyer 1989, 1990b; Geyer & Landing 1995, 2006; Álvaro *et al.* 2014; Sundberg *et al.* 2016). Samples of limestone and carbonate-cemented lithologies were recovered from this succession during field work in April 2016 (Figure 2-9).

The Lemdad Formation is the lowest unit of interest in the area, hosting the oldest skeletal biota of this region. Only the upper ~60 m were examined in this study. The Lemdad Formation is a dominantly siliciclastic sequence of marlstones and siltstones, with thick limestone and dolostone units, archaeocyathan bioherms, and volcanoclastic beds, confined to the High Atlas Mountains region (Geyer 1989, 1990a; Geyer & Landing 2006; Álvaro & Clausen 2007). Oolitic limestones, archaeocyathan reefs, and wave-generated sedimentary structures suggest that the Lemdad Formation was deposited in a generally shallow marine environment (Geyer & Landing 2006; Álvaro & Clausen 2007). A radiometric (U-Pb) age of 515.56 ± 1.16 Ma (Landing *et al.* 1998; recalculated by Maloof *et al.* 2010a) was determined from an ash band in the upper Lemdad Formation, *Antatlasia guttapliviae* Zone, close to the lowest horizon examined in this study.

The Issafen Formation (Geyer 1989) conformably overlies the Lemdad Formation and comprises rhythmically colour banded fine-grained siliciclastic units with a few nodular calcareous horizons (Geyer & Landing 1995, 2006; Álvaro & Clausen 2007; Álvaro *et al.* 2014). In the Lemdad Syncline, the Issafen Formation is thinner than in the Anti-Atlas Mountains, and thins out to the east of Ait Iyou, likely due to erosion (Geyer & Landing 1995, 2006; Álvaro & Clausen 2007). The Issafen Formation lies within the *Sectigena* Zone (Geyer 1989; Geyer & Landing 1995, 2006; Álvaro *et al.* 2014).

The base of the Tatelt Formation (also known as the 'Asrir' Formation) is an erosive contact cutting down through the top of the Issafen Formation and directly overlying the Lemdad Formation in the east of the Lemdad Syncline. A recent summary of the Tatelt Formation was provided by Ortega-Hernández *et al.* (2017). The Tatelt Formation thins northwards from approximately 55 m in exposures in the Anti-Atlas

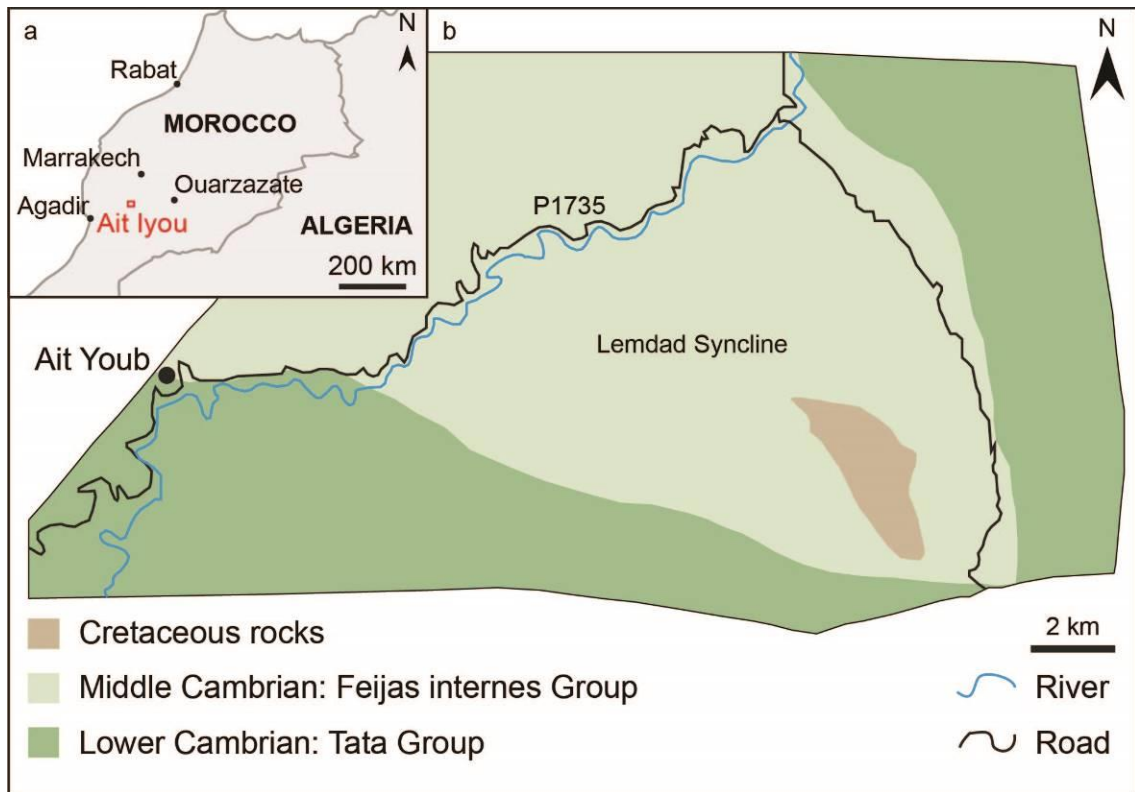


Figure 2-8. Geographic and geological maps of the Moroccan strata examined in this study. (a) Geographic position of Ait Iyou in southern Morocco. (b) Geological map of the Lemdad Syncline, modified after Geyer & Landing (2006) and Ortega-Hernández *et al.* (2017).

Mountains to 13 m to 18 m in the Lemdad Syncline, in concert with a transition from distal to more proximal facies (Geyer & Landing 2006; Landing *et al.* 2006). The more proximal facies of the High Atlas Mountains succession are dominated by fine- to coarse-grained sandstones with intercalated grey-green tuff and ash beds, but also include shale and conglomeratic layers (Geyer & Landing 1995, 2006; Landing *et al.* 2006). The upper Tatelt Formation includes bidirectional trough cross-stratification and is interpreted as being deposited in a near-shore subtidal environment, with occasional intervals of deeper, or more quiescent, deposition (Geyer & Landing 1995, 2006). The Tatelt Formation spans the *Sectigena*, *Hupeolenus* and *Morocconus notabilis* zones of Moroccan trilobite biostratigraphy (Geyer 1990b; Geyer & Landing 1995, 2006; Geyer & Vincent 2015).

An abrupt lithological change to the condensed carbonate-cemented horizons of the basal Brèche à *Micmacca* Member, Jbel Wawrmast Formation, marks the top of the Tatelt Formation, within the *Morocconus notabilis* Zone. These condensed carbonate units are comparable to the Comley Limestones, though the Moroccan strata certainly include younger units than the *Lapworthella* Limestone (Ad). In the Lemdad Syncline,

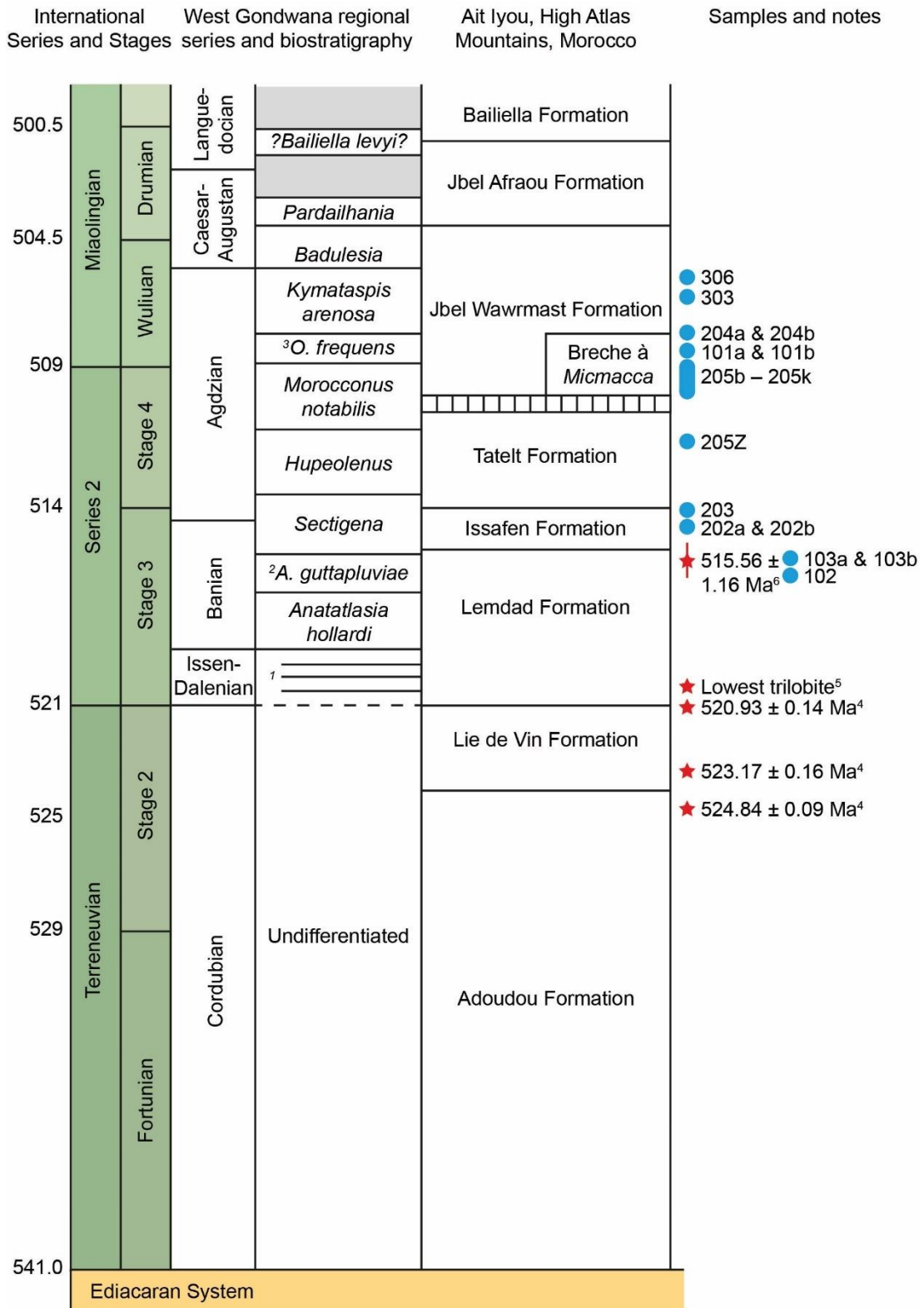


Figure 2-9. Lower/middle Cambrian stratigraphy of Ait Iyou, Morocco. Blue dots denote samples. ¹*Eofallotaspis*, *Fallotaspis tazemmourtensis*, *Choubertella*, and *Daguinaspis* zones; ²*Antatlasia*; ³*Ornamentaspis*; ⁴Maloof *et al.* (2010b). ⁵Geyer & Landing (2006); ⁶Landing *et al.* (1998), updated by Maloof *et al.* (2010a). From data in Geyer & Landing (2006) and Peng *et al.* (2012).

the basal Brèche à *Micmacca* Member comprises at least nine beds of arenaceous fossiliferous nodular limestones with abundant phosphatic and glauconitic matter. Above the condensed limestone units, the Brèche à *Micmacca* Member comprises green shales with infrequent horizons of calcareous nodules. Only the lower ~40 m of the Jbel Wawrmast Formation, all within the Brèche à *Micmacca* Member, were investigated in this study.

In summary, the lower to middle Cambrian strata of the Lemdad Syncline record an interval of shallow marine deposition and occasional erosion in sea water with normal salinity and teeming with life. Although there is some secondary phosphatisation, calcareous fossils are found alongside phosphatic fossils, suggesting that this secondary phosphate precipitation was not pervasive. Therefore, the SSFs of the Lemdad Syncline should also be investigated as potential repositories of early Cambrian palaeoenvironmental proxy data.

2.6. Samples from the Forteau Formation, Newfoundland and Labrador, Canada

The lower Palaeozoic strata of Laurentia have been extensively studied, including the lower Cambrian strata of western Newfoundland and southern Labrador which are known to be highly fossiliferous, preserving phosphatic SSFs alongside calcareous fossils (Skovsted & Peel 2007; Skovsted *et al.* 2017). The Cambrian strata of western Newfoundland and southern Labrador comprise three formations in the Labrador Group, the Bradore, Forteau and Hawke Bay formations, which record a deepening-upwards sequence (e.g. Knight *et al.* 2017; Skovsted *et al.* 2017). In southern Labrador and northwest Newfoundland, on the Great Northern Peninsula (GNP), the Labrador Group strata are gently dipping (Figure 2-10), becoming more severely deformed towards southwestern Newfoundland.

The Forteau Formation conformably overlies the Bradore Formation which comprises fluvial to marginal marine deposits. In southern Labrador and the GNP, the Forteau Formation is wholly marine and comprises three distinct but conformable members. The Devils Cove Member is a 3 m to 8 m thick carbonate unit at the base of the formation, and in places is intercalated with the underlying Bradore Formation sandstones. The Devils Cove Member passes up into the Middle Shale Member which is dominated by fine-grained siliciclastic rocks, interspersed with skeletal and sparry limestones and archaeocyathan bioherms. This middle member is extensively bioturbated, indicative of an open shelf but generally quiescent depositional setting. The

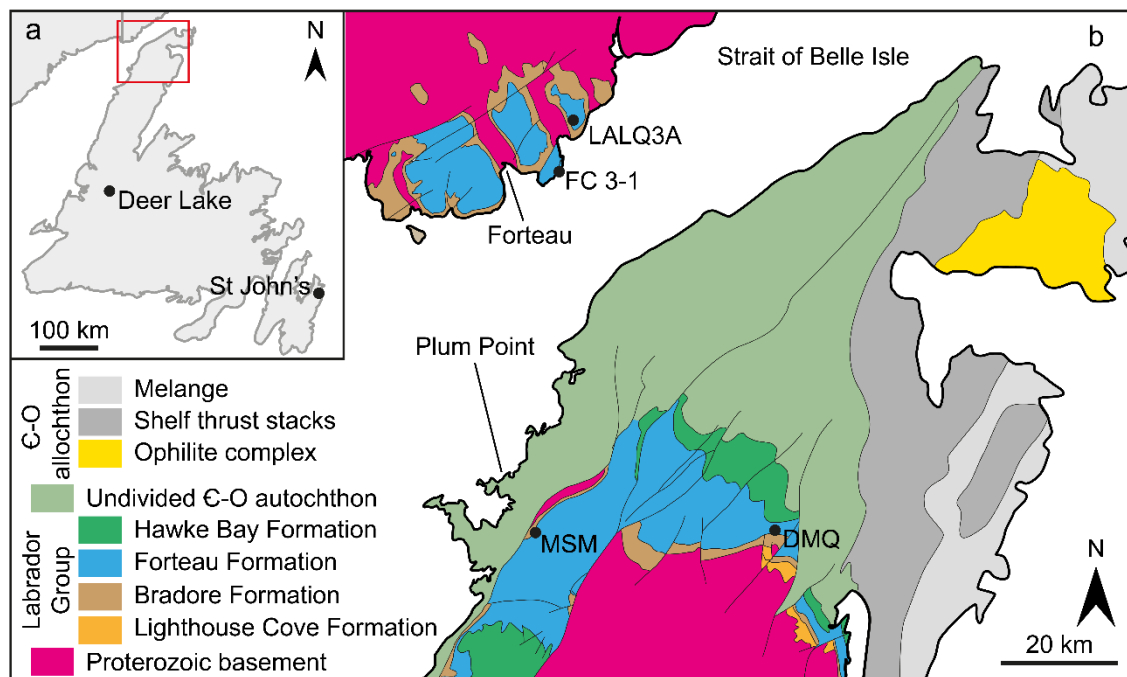


Figure 2-10. Geographical and geological setting of the Forteau Formation on the Great Northern Peninsula, western Newfoundland, and southern Labrador. (a) Geographical setting; red box indicates area of (b). (b) Simplified geological map of the sampling area. Black spots indicate sampling locations. Modified after Knight *et al.* (2017) and Skovsted *et al.* (2017).

Upper Limestone Member is characterised by a basal archaeocyathan biostrome, locally with oolitic, oncolitic and skeletal limestones.

There are no radiometric dates of chemostratigraphic constraints on the Forteau Formation; instead, trilobite biostratigraphy correlated to the rocks of western Canada and the Great Basin, USA, provide the primary age constraints. Trilobites diagnostic of the *Bonnia–Olenellus* Zone constrain the Forteau Formation in the GNP and southern Labrador to the late early Cambrian, Series 2 Stage 4 (James *et al.* 1989). Recent work has refined this assignment to within the middle and top thirds of the *Bonnia–Olenellus* Zone by correlation of sub-zonal trilobite occurrences between the Forteau Formation and the Great Basin Sekwi Formation (Knight *et al.* 2017).

Samples of the Forteau Formation were collected in June 2017 from outcrops and quarries in the GNP and southern Labrador (Figure 2-10). In addition to the materials collected in June 2017, sample FC 3-1 was kindly provided by Christian Skovsted (SMNH) and corresponds to sample FC 3-1 in Skovsted *et al.* (2017, fig. 3) from the upper part of the Middle Shale of the Forteau Formation which crops out in Fox Cove.

Sample MSM was collected from a prominent limestone horizon in a small quarry about 300 m north of Mount St Margaret's Quarry. This archaeocyathan-rich limestone

International Series and Stages Laurentian regional series and biostratigraphy Western Newfoundland and southern Labrador, Canada Samples and notes

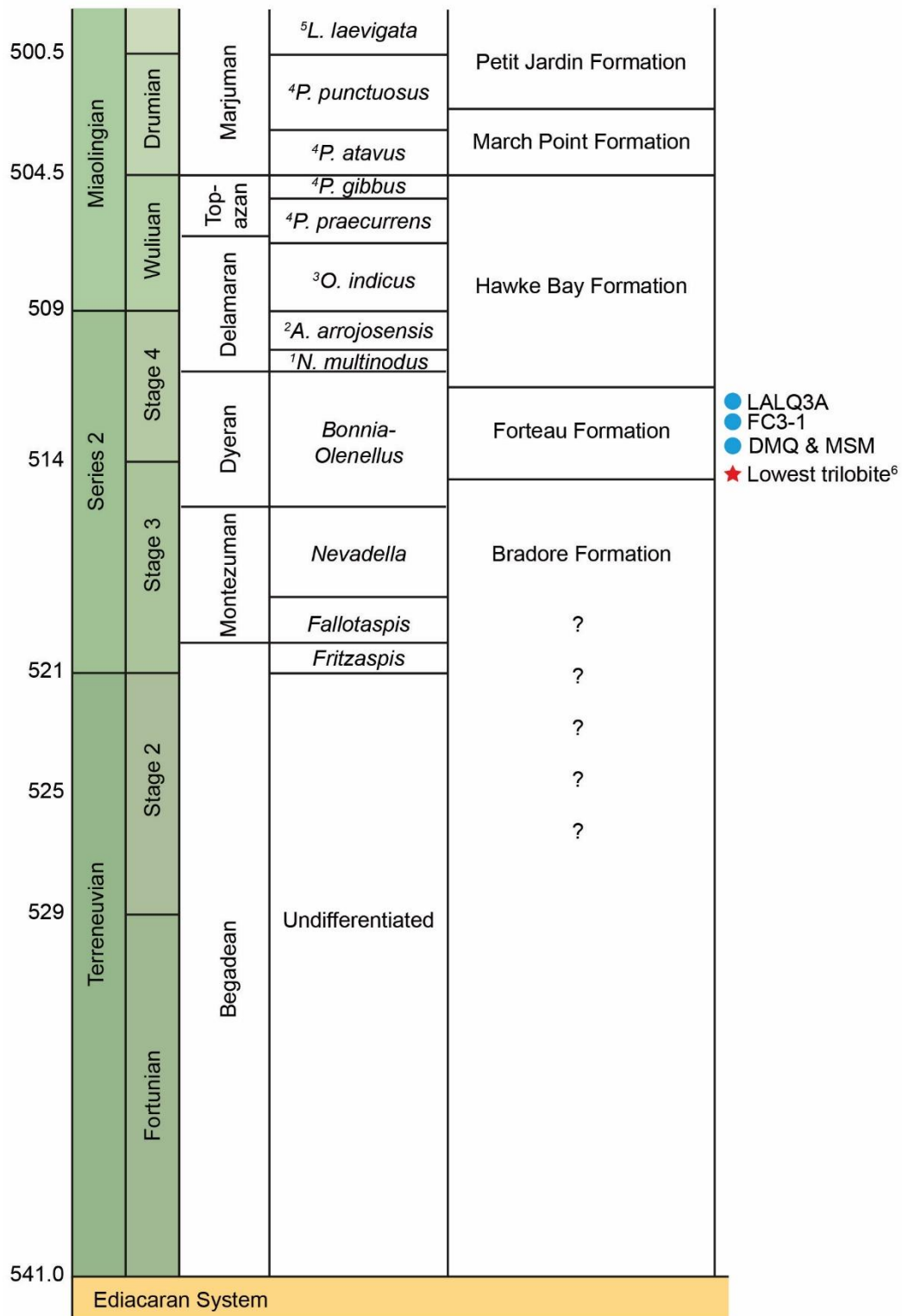


Figure 2-11. Lower/middle Cambrian stratigraphy of western Newfoundland and southern Labrador, Canada. Blue dots denote samples. ¹*Nephrocephalus*; ²*Amecephalus*; ³*Oryctocephalus*; ⁴*Ptychagnostus*; ⁵*Lejopyge*. From data in Peng *et al.* (2012), Knight *et al.* (2017), and Skovsted *et al.* (2017).

horizon likely represents the top of the Devils Cove Member of the Forteau Formation and is the stratigraphically lowest sample from the Forteau Formation.

Sample DMQ was collected from a prominent limestone horizon about 1 m above the local base of the quarry at R432-10 in Knight *et al.* (2017) and Skovsted *et al.* (2017), in the southeast corner. The precise stratigraphic position of the rocks in this quarry is uncertain, with correlation complicated by nearby faults but it is considered to be approximately in the middle of the Middle Shale Member (Knight *et al.* 2017).

Sample LALQ3A was collected from a 60 cm thick interval of interlaminated fossiliferous sandy siltstone and limestone beds, approximately 4.5 m above the base of the quarry, between an underlying archaeocyathan limestone and a prominent overlying red limestone. This horizon is just above the basal archaeocyathan bioherms of the Upper Limestone Member and is the stratigraphically highest sample from the Forteau Formation.

2.7. Discussion

2.7.1. Resolving climatically important timescales

The aim of this work is to investigate Cambrian climates, and so consideration needs to be given to the temporal resolution that can be achieved when investigating climates 500 million years ago. Three partially overlapping timescales are important when considering climate and climate states – trends, rhythms and aberrations (Zachos *et al.* 2001). Climatic trends operate on 10^5 to 10^7 years, and would characterise the general climate state, whether greenhouse or icehouse. Climatic trends are predominantly controlled by geological processes including plate tectonics and continental distribution (Zachos *et al.* 2001). Climatic rhythms operate on 10^4 to 10^6 years, and are primarily controlled by orbital forcing, i.e. regular variations in Earth's orbit, tilt and rotation. Aberrations are fast-acting but geologically short-lived changes to Earth's climate state, operating on timescales of 10^3 to 10^5 years (Zachos *et al.* 2001). Aberrations temporarily kick the climate into a different or more extreme state before reverting to, or assuming a new, background state when the source of the aberration is removed. The best-constrained hypotheses of Cambrian continental configurations are averaged over approximately 5 Myr intervals (e.g. Torsvik & Cocks 2013, 2016), limiting resolution achievable when considering variations in regional climates. Lithological data suggest that the Cambrian Period could be broadly characterised as a greenhouse climate (Boucot *et al.* 2013). Temporal and stratigraphic resolution make detecting

rhythms in Cambrian strata difficult, although cyclostratigraphy has been applied to Cambrian strata (Montanez & Osleger 1993; Osleger 1995). Although climatic rhythms are very likely to be preserved in some Cambrian strata (Hinnov & Hilgen 2012), the signals so far recovered have been ambiguous (Osleger 1995), and research in this area has slowed (Hinnov & Hilgen 2012). Climatic aberrations have been noted in the Cambrian carbon isotope record (Saltzman *et al.* 2000; Zhu *et al.* 2006; Saltzman & Thomas 2012), and may go some way to explaining some of the cold, potentially icehouse, conditions suggested for limited intervals during the Cambrian (Landing & MacGabhann 2010; Runkel *et al.* 2010; Cherns *et al.* 2013). However, loose age constraints on geological data and palaeocontinental configurations hampers any precise correlation of such events.

2.7.2. Correlations and time slab definitions

Following correlation of the localities detailed above (Figure 2-12), six regional time slabs were defined (summarised in Table 2-2). The depositional age of the Comley Limestones is tightly constrained by U-Pb dates of 514.45 ± 0.36 Ma and 509.10 ± 0.22 Ma (Harvey *et al.* 2011). Diagenetic alteration of the bulk carbonate $\delta^{13}\text{C}$ and $\delta^{18}\text{O}$ values of the Comley Limestones (Harvey *et al.* 2011) precludes insights from chemostratigraphic correlation. However, the well-established trilobite biostratigraphy through this succession (Cobbold 1921, 1927) can be correlated through more expanded sections elsewhere in Avalonia (e.g. Rushton *et al.* 2011; Williams *et al.* 2013). The older radiometric date, from just below the base of the Comley Limestones, lies within the upper *Callavia broeggeri* Zone. The lower bed of the Comley Limestones, Ac2, is separated from the overlying Ac3 bed by an unconformity that also marks the boundary between the *C. broeggeri* and *Stenuella sabulosa* zones. Collectively, Ac3, Ac4 and Ac5 span the *S. sabulosa* and *Geyerorodes* (formerly *Orodes*, see Özdikmen 2009) *howelyi* zones. The uppermost unit of the Comley Limestones, Ad, is separated from the underlying units by a substantial unconformity and falls within the upper *Morocconus* (formerly *Cephalopyge*) *notabilis* and lower *Kiskinella cristata* zones. In the Hanford Brook Formation, southeast Newfoundland, the *M. notabilis* Zone has been dated to 511 ± 1 Ma (Landing *et al.* 1998; Westrop & Landing 2000), suggesting that the Comley Limestones were deposited between 515 Ma to 511 Ma. Units Ac3 to Ac5 may have been deposited between 513 Ma to 511 Ma, and the lower Ac2 unit between 515 Ma to 514 Ma. Therefore, two Avalonian time slabs were defined:

A₁: *C. broeggeri* Zones, 515 Ma to 514 Ma, and

A₂: *S. sabulosa* to *G. howelyi* zones, 513 Ma to 511 Ma.

In North Africa, Pan-African Orogen basement rocks are unconformably overlain by an early Palaeozoic continental margin sedimentary cover sequence in North Africa (Destombes *et al.* 1985; Geyer & Landing 2006, 1995). Despite several ash horizons, the trilobitic strata of this cover sequence remain poorly constrained by radiometric ages, though the sub-trilobitic strata have been better dated and chemostratigraphically correlated (Maloof *et al.* 2005, 2010a). Samples used in this thesis were collected from rocks in each of the trilobite zones from the *Antatlasia guttapliviae* Zone through *Kymataspis arenosa* Zone (Figure 2-9). An ash band in the upper *A. guttapliviae* Zone of the Lemdad Formation was dated to 515.56±1.16 Ma (Landing *et al.* 1998; recalculated by Maloof *et al.* 2010b), and has been correlated to the Avalonia *C. broeggeri* Zone (e.g. Sundberg *et al.* 2016). There are no stratigraphically higher radiometric ages. The *A. guttapliviae* through *Hupeolenus* zones of West Gondwana are correlated with the *C. broeggeri* through *S. sabulosa* zones of Avalonia (e.g. Geyer 1990b; Geyer & Landing 2004, 2006; Sundberg *et al.* 2016), making them roughly equivalent to the A₁ time slab. The upper *Hupeolenus* to *M. notabilis* zones may be correlable with the Avalonian *G. howelyi* to *M. notabilis* zones (Geyer & Vincent 2015; Sundberg *et al.* 2016) and could therefore be considered contemporaneous to the A₂ time slab (Figure 2-12). These two Avalonia/West Gondwana paired time slabs are followed in the Moroccan succession by the condensed limestone strata of the Brèche à *Micmacca* Member, Jbel Wawrmast Formation, within the *M. notabilis* through *K. arenosa* zones. Three time-slabs are defined for the Moroccan succession:

G₁ – *A. guttapliviae* to *Hupeolenus* zones, 516 Ma to 512 Ma,

G₂ – upper *Hupeolenus* to *M. notabilis* zones, 512 Ma to 509 Ma, and

G₃ – upper *M. notabilis* to *K. arenosa* zones, 509 Ma to 506 Ma.

The depositional history of the Forteau Formation is well constrained by biostratigraphic correlation with other Laurentian strata (Knight *et al.* 2017). The Forteau Formation lies within the Laurentian *Bonnia–Olenellus* Zone (James *et al.* 1989) which spans Cambrian stages 3 and 4, and the whole of the Laurentian regional Dyeran Series. Sub-zone correlation with trilobite-bearing strata of the Great Basin implies that the Forteau Formation was deposited in middle and upper third of the *Bonnia–Olenellus* Zone (Knight *et al.* 2017). In particular, the occurrence of *Elliptocephala logani* Walcott 1910 throughout the Forteau Formation implies

Table 2-2. Time slab definitions.

Slab	Start	End	Units	Samples
A ₁	515 Ma	514 Ma	Ac1 to Ac2	K
A ₂	513 Ma	511 Ma	Ac3 to Ac5 and Ad	Aa, Ad, Sa (La2, Lb?)
G ₁	516 Ma	512 Ma	Lemdad, Issafen and Tatelt formations	102, 103a & b, 202a & b, 203
G ₂	512 Ma	509 Ma	Tatelt Formation and Brèche à <i>Micmacca</i> Member	205b – k & Z
G ₃	509 Ma	506 Ma	Jbel Wawrmast Formation	101a& b, 204a & b, 303, 306
L ₁	513 Ma	511 Ma	Forteau Formation	DMQ, MSM, FC3-1, LALQ3A

correlation to the middle third of the *Bonnia-Olenellus* Zone in the Great Basin Sekwi Formation. (Knight *et al.* 2017). The Forteau Formation was likely deposited during the early part of Cambrian Stage 4, and so a single Laurentian time slab is defined that is broadly equivalent to the A₂ time slab:

L₁: *Bonnia–Olenellus* Zone, 513 Ma to 511 Ma.

2.8. Conclusions

Three localities with lower to middle Cambrian strata were identified as hosting potentially suitable fossil material for this study. The Comley Limestones, Shropshire, UK, were determined to be the highest priority target for extracting phosphatic SSFs. Additionally, SSFs from the lower Cambrian strata of the High Atlas Mountains, Morocco, and Newfoundland and Labrador, Canada, will also be examined. All three localities comprise strata that were deposited in shallow water settings, under normal marine conditions, and include diverse micro- and macrofaunas.

One to three time-slabs were established for each region, based on the distribution of samples across trilobite biozones. The time slabs are all defined at scales at which climatic trends operate (i.e. > 10⁵ years), and therefore the finer-scale climatic rhythms and aberrations will not be detectable in any recovered data. Stratigraphically expanded sections, such as that of Morocco, or western Newfoundland and southern Labrador, may be suitable for future climate studies with greater stratigraphic resolution.

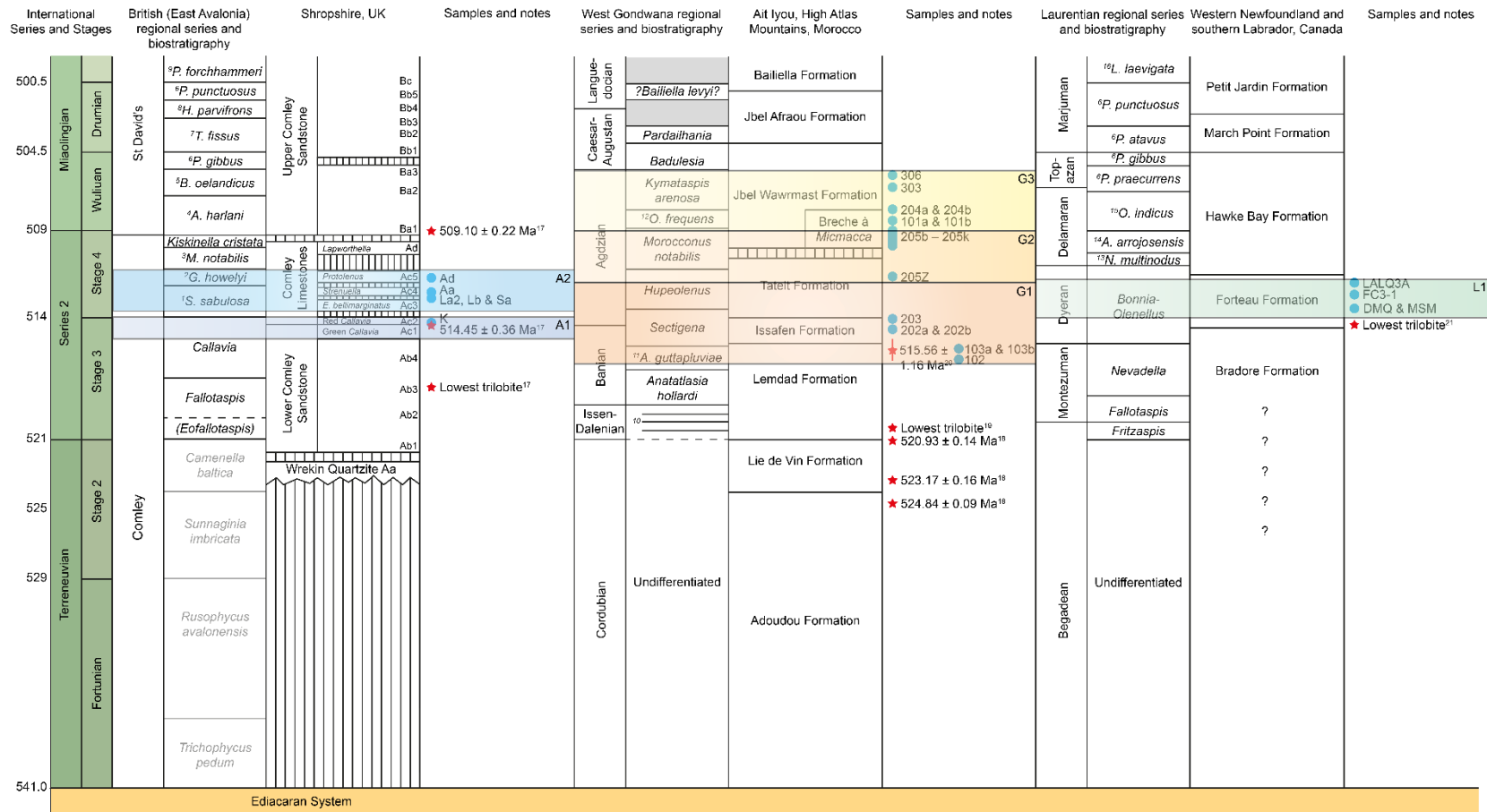


Figure 2-12. Correlation of the time slabs used in this thesis. See text and Table 2-2 for details of time slabs A, G and L. ¹*Strenuella*; ²*Geyerorodes*; ³*Morocconus*; ⁴*Acadoparadoxides*; ⁵*Baltoparadoxides*; ⁶*Ptychagnostus*; ⁷*Tomagnostus*; ⁸*Hypagnostus*; ⁹*Paradoxides*; ¹⁰*Eofallotaspis*, *Fallotaspis tazemmourtensis*, *Choubertella*, and *Daguinaspis* zones; ¹¹*Antatlasia*; ¹²*Ornamentaspis*; ¹³*Nephrolenellus*; ¹⁴*Amecephalus*; ¹⁵*Oryctocephalus*; ¹⁶*Lejopyge*; ¹⁷Harvey *et al.* (2011); ¹⁸Maloof *et al.* (2010b). ¹⁹Geyer & Landing (2006); ²⁰Landing *et al.* (1998), updated by Maloof *et al.* (2010a); ²¹Knight *et al.* (2017). See also Figure 2-3, Figure 2-9, and Figure 2-11. Constructed from data in Geyer & Landing (2006), Rushton *et al.* (2011), Harvey *et al.* (2011), Peng *et al.* (2012), Williams *et al.* (2013), Knight *et al.* (2017) and Skovsted *et al.* (2017).

Chapter Three: Identifying alteration of bioapatite

3.1. Chapter summary

This chapter establishes a protocol for assessing the preservation of ancient biogenic apatite. The limitations of the early Palaeozoic stable oxygen isotope ($\delta^{18}\text{O}$) record are examined. Criteria for selecting early Cambrian ‘small shelly fossil’ (SSF) taxa that may preserve an environmental $\delta^{18}\text{O}$ signal are determined. A protocol for assessing the preservation of biogenic phosphate is proposed and applied to SSFs from the Comley Limestones. The preservation protocol is then applied to SSFs from other strata around the world. This chapter concludes with hypotheses to be tested using $\delta^{18}\text{O}$ data which are examined in Chapter Four. A brief overview of this protocol, applied to selected Comley Limestones SSFs, was recently published in Hearing *et al.* (2018).

3.2. Introduction

Geochemical proxies have been widely applied to reconstruct ancient climates throughout the Phanerozoic. Harold Urey (1947) first determined the “thermodynamic properties of isotopic substances” – the relationship between the stable oxygen isotope ratio ($\delta^{18}\text{O}$) and water temperatures. This was first applied in the geological record when biogenic carbonate from Jurassic and Cretaceous belemnites were analysed for $\delta^{18}\text{O}$ data to determine the temperature of the seawater they lived in (Urey *et al.* 1951). Fossil biomineral and whole rock $\delta^{18}\text{O}$ data has now been used to reconstruct global and local temperature records throughout most of the Phanerozoic Eon (see Chapter Four; e.g. Grossman 2012b). Benthic foraminifera, ubiquitous in deep-sea sediment core records, are probably the most popular source of $\delta^{18}\text{O}$ data for Cenozoic and Cretaceous palaeoclimate work (e.g. Zachos *et al.* 2001; Grossman 2012b), whereas belemnite rostra are favoured in earlier Mesozoic studies for their dense microcrystalline low-Mg calcite composition (Grossman 2012b; Stevens *et al.* 2014). Palaeozoic $\delta^{18}\text{O}$ data are commonly obtained from low-Mg calcitic brachiopods and, increasingly in older strata, phosphatic conodonts (Grossman 2012b). However, there remains a dearth of reliable Cambrian $\delta^{18}\text{O}$ data. This is partly due to the absence of euconodonts below uppermost Cambrian strata, and partly due to the demonstrable diagenetic alteration of most calcareous material of this age (Grossman 2012b).

Diagenetic alteration is a potentially significant problem for all isotopic palaeoclimate studies. Many techniques have been used to try to detect and avoid

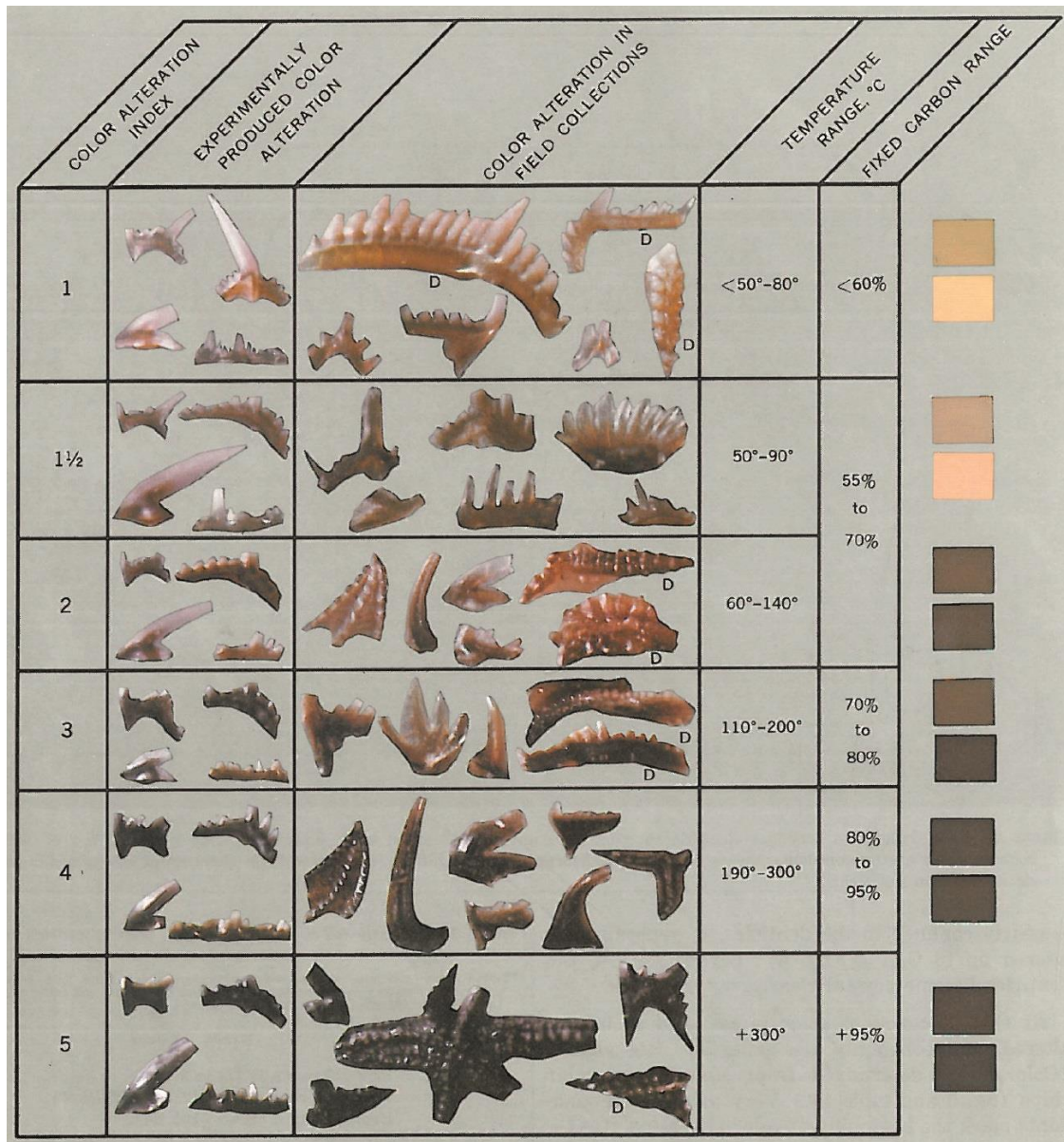


Figure 3-1. The conodont colour alteration index (CAI). Epstein *et al.* 1977, fig. 5.

diagenetic alteration in carbonate biomineral samples. However, there is no silver bullet and the best approach remains to use as many techniques as money and time allow (Brand *et al.* 2011). Conodont preservation is routinely determined by visual examination with reference to the conodont colour alteration index (CAI; Figure 3-1; Epstein *et al.* 1977; Rejebian *et al.* 1987), often without applying any more detailed analysis. Although the CAI is a valuable tool for assessing the preservation of conodont $\delta^{18}\text{O}$, it is not readily applicable to other fossil groups. There is no established protocol for assessing the preservation state of non-conodont phosphatic microfossils.

Phosphate biomineral $\delta^{18}\text{O}$ values are considered less susceptible to post-mortem alteration than carbonate biominerals (Kolodny *et al.* 1983; Wenzel *et al.* 2000; Grossman 2012b). Phosphatic fossils are therefore a potentially more promising source of Cambrian-age $\delta^{18}\text{O}$ data than calcareous fossils. Because the CAI is not readily applicable to non-conodont fossils, it is necessary to work towards a repeatable reliable protocol for assessing the preservation of other phosphatic fossils if they are to be used as a new source of palaeoenvironmental $\delta^{18}\text{O}$ data.

Not all of the techniques developed for assessing the preservation of calcareous biominerals are suitable for phosphate biominerals (Brand *et al.* 2011), and most of the techniques for examining phosphate preservation have been developed for vertebrate skeletal material – conodont elements, and vertebrate bones and teeth (e.g. Armstrong *et al.* 2001; Trueman & Tuross 2002; Wopenka & Pasteris 2005; Neary *et al.* 2011; Thomas *et al.* 2011; Zougrou *et al.* 2016). However, some of these techniques can be adapted for investigating other phosphate-biomineralising taxa.

Because some $\delta^{18}\text{O}$ analytical techniques require destructive bulk sampling of several tens of individual specimens, any protocol needs to distinguish between well-preserved and altered specimens under binocular microscopy, similar to the CAI. Detailed analysis of the microstructure, ultrastructure and chemistry of individual specimens taken as a subset from the bulk samples is needed in order to have confidence in sample selection at this level. An array of techniques are therefore required, from a visual assessment of whole microfossils to assessing the chemical composition within individual specimens.

The final test of a preservation protocol lies in the isotopic analyses of separate samples of well-preserved and altered fossils. The aim of this chapter is to establish a protocol to assess the preservation state of biogenic phosphate in ancient microfossils to be used in isotopic palaeoenvironmental studies. This chapter will conclude with a set of hypotheses of isotopic preservation that can be tested using $\delta^{18}\text{O}$ analyses.

3.3. Limitations of the current $\delta^{18}\text{O}$ record

3.3.1. Whole rock samples

Stable isotope data are routinely collected from chemically precipitated rocks to study Phanerozoic climates. Carbonates are the most common type of chemically precipitated rock on Earth, and are therefore also the most commonly used to gather stable isotope data, though siliceous and phosphatic rocks are also used (Blake *et al.* 2010; Grossman

2012b). Carbonate rocks undergo a post-depositional lithification process during which the initially precipitated metastable carbonate polymorphs, typically aragonite and high-Mg calcite, recrystallise as more stable polymorphs, typically low-Mg calcite (Veizer *et al.* 1999). The relatively high ratio of oxygen in sediment pore water readily facilitates isotopic exchange between pore water and carbonate minerals. This results in early diagenetic resetting of bulk rock $\delta^{18}\text{O}$ values, typically a 2 to 3 ‰ ^{18}O -depletion with respect to well-preserved biogenic minerals (Mii *et al.* 1999; Veizer *et al.* 1999; Grossman 2012a). The relatively large volume of carbon in lithifying carbonate sediments compared to pore waters means that whole rock $\delta^{13}\text{C}$ data are much less affected by the stabilisation process.

3.3.2. Biogenic samples

Although major trends and long-term climate or isotope systematics patterns can be observed in whole rock $\delta^{18}\text{O}$ data, these values are not suitable for detailed climate reconstructions or for temporally isolated studies. Instead, biogenic sources of $\delta^{18}\text{O}$ data are favoured for palaeoclimate studies, particularly in deep time (e.g. Veizer *et al.* 1999; Giles 2012; Grossman 2012b; Veizer & Prokoph 2015).

Agglutinating foraminifera are known from lower Cambrian rocks (McIlroy *et al.* 2001), but foraminifera with calcareous tests are not known below Ordovician strata and do not become widespread until the Devonian (Harper & Brasier 2005). The Cenozoic climate data source of choice is therefore not available for studying Cambrian climates. Belemnite rostra which are favoured in Mesozoic palaeoclimate studies are also unavailable as belemnites are unknown below Triassic strata (Iba *et al.* 2012).

Low-Mg brachiopod calcite $\delta^{18}\text{O}$ values are often used to reconstruct Palaeozoic climates because of the wide stratigraphic and geographical distribution of suitable fossils, and the resistance of low-Mg calcite to isotopic alteration (Veizer *et al.* 1999; Prokoph *et al.* 2008; Grossman 2012a, b; Veizer & Prokoph 2015). Analyses of calcareous brachiopods have helped to produce a near-continuous middle to upper Palaeozoic $\delta^{18}\text{O}$ record. However, this record is more sparsely populated in the lower Palaeozoic (Veizer *et al.* 1999; Prokoph *et al.* 2008; Giles 2012; Grossman 2012b; Veizer & Prokoph 2015).

The reliability of the calcareous brachiopod $\delta^{18}\text{O}$ record, particularly in the lower Palaeozoic, has been called into question. The data commonly exhibit a wide scatter of values, up to 6 ‰ inside 1 Ma time intervals, and also show a secular trend of

increasingly light $\delta^{18}\text{O}$ values, which may indicate increasingly severe alteration with greater age (Grossman 2012b). However, a scatter of $\sim 6\text{‰}$ is consistent with the modern range of marine $\delta^{18}\text{O}$ values (Schmidt *et al.* 1999; LeGrande & Schmidt 2006). The Phanerozoic-scale trend, up to approximately -1‰ per Myr, is observed in the carbonate, phosphate and silica $\delta^{18}\text{O}$ records, from whole rock and biogenic sources (Veizer *et al.* 1999; Giles 2012; Grossman 2012b; Veizer & Prokoph 2015), but remains at odds with data from carbonate clumped isotope (CCI) analyses (e.g. Finnegan *et al.* 2011; Came *et al.* 2014; Cummins *et al.* 2014; Bergmann *et al.* 2018). See Chapter Five for a full discussion of the secular trend in $\delta^{18}\text{O}$ values.

The above debate notwithstanding, it becomes more difficult with increasing age to find demonstrably isotopically pristine biogenic calcite in brachiopods, or indeed in any taxa. Furthermore, recent work has shown that cryptic recrystallisation may be a substantial problem in otherwise apparently pristine calcite (Bennett *et al.* 2018). The oldest reliable calcareous brachiopod $\delta^{18}\text{O}$ data are of Lower Ordovician age (Shields *et al.* 2003). Cambrian-age calcareous brachiopods for which $\delta^{18}\text{O}$ data have been reported (Wadleigh & Veizer 1992) have poorly investigated and reported preservation, as well as deriving from an unspecified “Laurentian” location and geological setting (Wadleigh & Veizer 1992; Grossman 2012b; Veizer & Prokoph 2015).

Oxygen isotope analyses of conodont phosphate are used for palaeoclimate studies throughout Palaeozoic strata and are often helpful in filling gaps in the brachiopod carbonate $\delta^{18}\text{O}$ record, particularly in the lower Palaeozoic (Grossman 2012b). Palaeozoic sea water temperatures have been reconstructed using conodont apatite for over three decades, and it was predicted to become as influential in understanding of marine environments as foraminifera are later in the Phanerozoic (Luz *et al.* 1984). A recent detailed study of conodonts from one horizon of Lower Ordovician strata at Green Point, western Newfoundland, Canada, found evidence in the $\delta^{18}\text{O}$ data that different conodont taxa inhabited different depths in the water column (Wheeleley *et al.* 2018), demonstrating the high-resolution potential of this group in palaeoclimate studies. However, not all conodont taxa can be used in isotopic palaeoclimate studies. Only euconodonts, the clade possessing well-mineralised hyaline crown tissues, are suitable for palaeoclimate work (Wheeleley *et al.* 2012). Euconodonts are not known from strata below the uppermost Cambrian (Smith *et al.* 2002) and are therefore also not available for tackling problems relating to climates at the beginning of the Phanerozoic Eon. For these reasons, Cambrian ocean temperatures have largely

eluded physical constraint, and a novel alternative source of quantitative palaeoclimate proxy data is needed to interrogate Cambrian marine environments.

3.3.3. Sources of isotopic alteration

The isotopic composition of a mineral can be altered in many ways so that the $\delta^{18}\text{O}$ value no longer reflects the environmental conditions in which the mineral formed. This alteration can occur at any point in a rock's history, from immediate post-mortem changes, through burial, to laboratory processing.

Diagenetic alteration is caused by post-depositional pre-metamorphic pre-weathering processes, including burial compaction and heating (Scholle & Ulmer-Scholle 2003). Deposition can be considered as the initial formation of the material, which could be abiogenic seafloor carbonate precipitation or the growth of phosphatic minerals from the cells of a linguliformean brachiopod. Diagenetic alteration can cause physical and/or chemical changes to a mineral, and it can involve the loss, mutation or addition of material (Scholle & Ulmer-Scholle 2003). Diagenetic alteration can occur very early in the history of a fossil, and so still reflect something of the original environmental conditions; or it can be much later in the burial history of a mineral and eradicate any traces of the original environmental conditions. Metamorphic alteration is essentially a more extreme form of diagenetic alteration.

The $\delta^{18}\text{O}$ value of carbonate and phosphate minerals is susceptible to alteration by contact with diagenetic, metamorphic and meteoric waters, due to the high supply of oxygen from H_2O with respect to mineral oxygen (e.g. Grossman 2012b). Early diagenetic alteration, at or near to the sea floor, is likely to involve pore waters which retain some communication with seawater. Rather than reflecting true marine conditions, minerals altered at this stage would reflect conditions in the upper sediment pile which are perhaps slightly warmer and more reducing than the water column.

Later diagenesis usually relates to increasing temperatures with burial depth and mineral interactions with hydrothermal fluids. Elevated temperatures can cause recrystallisation, which in turn may alter the mineral $\delta^{18}\text{O}$ value (e.g. Blake *et al.* 1997; Zazzo *et al.* 2004). Minerals altered in the presence of hydrothermal fluids are exposed to a new source of abundant oxygen with its own $\delta^{18}\text{O}$ value. Late diagenetic isotopic alteration will gradually drive mineral $\delta^{18}\text{O}$ values away from the original environmental values, eventually to be overprinted by a $\delta^{18}\text{O}$ value that reflects the temperature and $\delta^{18}\text{O}$ conditions at which the alteration occurred (e.g. Grossman

2012b). Meteoric alteration, due to recent weathering, can have a similar impact to late diagenesis in driving any original $\delta^{18}\text{O}$ signal out of a mineral. Weathering haloes in indurated carbonate rocks are visible either as oxidation fronts or as a ‘rotten’ dissolved by slightly acidic meteoric waters. These areas can be avoided by visual inspection.

Wheelely *et al.* (2012) demonstrated that processing techniques can alter the oxygen isotope composition of apatite (but see Quinton *et al.* 2016). Whilst limestone maceration in formic acid alters the $\delta^{18}\text{O}$ composition of phosphatic material within it, buffered acetic acid had no noticeable effect (Wheelely *et al.* 2012). Furthermore, heavy liquid separation, which is widely used in processing microfossil samples, is also known to alter the phosphate $\delta^{18}\text{O}$ values (Wheelely *et al.* 2012). It is important to choose and follow laboratory procedures carefully to avoid causing ruinous isotopic alteration to microfossils at this late stage.

3.3.4. *Potential Cambrian biominerals for isotopic analysis*

The rapid appearance and diversification of skeleton-producing animals in the fossil record in the Cambrian explosion makes the early Cambrian Period the earliest time interval in which biominerals may be widely used as sources of $\delta^{18}\text{O}$ data (but see Cohen *et al.* 2011, 2017). Three anions, carbonate (CO_3^{2-}), phosphate (PO_4^{3-}) and silica (SiO_2), in various mineralogies and polymorphs form the building blocks of most animal skeletons, including those used by the earliest biomineralising animals (Lowenstam 1981; Lowenstam & Weiner 1989; Kouchinsky *et al.* 2012). Carbonate biominerals, particularly aragonite and low-Mg calcite, are the most widely used by animals (Lowenstam 1981). Silica biomineralisation was mostly restricted to sponges during the Cambrian, and is not a taxonomically widespread biomineral (Lowenstam 1981; Kouchinsky *et al.* 2012). Phosphate-biomineralisation is scattered across the animal kingdom, but is probably best-known and has been best-studied in chordate teeth and bone (Lowenstam 1981). Phosphate was a more important skeleton-forming mineral in the early Cambrian than now, particularly for producing the skeletons of many ‘small shelly fossil’ (SSF) taxa (Brasier 1990; Kouchinsky *et al.* 2012). Carbonate and phosphate biominerals may therefore be considered as potential sources of Cambrian $\delta^{18}\text{O}$ data.

3.3.5. *Carbonate versus phosphate*

The $\delta^{18}\text{O}$ values of most lower Palaeozoic biogenic and abiogenic carbonates are widely regarded as being more or less diagenetically altered. Care therefore has to be taken in

determining the preservation state of any fossils used for palaeoclimate isotope analyses (e.g. Brand *et al.* 2011). However, it has recently come to light that cryptic alteration of carbonates, not detectable by most of the commonly applied techniques, may be pervasive throughout the lower Palaeozoic carbonate record (Bennett *et al.* 2018). This recent study demonstrated internally variable and cryptically altered calcite $\delta^{18}\text{O}$ values from trilobite optical calcite and likely rules out the potential of trilobite optical calcite as a repository of Cambrian palaeoclimate data (Bennett *et al.* 2018). Currently, it is best to assume that isotopically pristine Cambrian-age calcareous fossils are in such negligible abundance that they are not available for examining Cambrian climates.

The oxygen isotopic composition of phosphate is thought to be less susceptible to alteration than that of carbonate (e.g. Kolodny *et al.* 1983; Shemesh *et al.* 1983; Luz *et al.* 1984; Sharp *et al.* 2000; Wenzel *et al.* 2000; Zazzo *et al.* 2004; Brand *et al.* 2011; Grossman 2012b). There is a theoretical basis for this, in that the phosphorous—oxygen bond in the phosphate ion (PO_4^{-3}) is substantially stronger than the carbon—oxygen carbonate ion (CO_3^{-2}) bond (e.g. Chenery *et al.* 2010), meaning that more energy is required to induce isotopic exchange. This is supported by comparative $\delta^{18}\text{O}$ analyses on coeval carbonate and phosphate samples, in which the carbonate $\delta^{18}\text{O}$ values are generally lighter and exhibited a greater spread than the phosphate $\delta^{18}\text{O}$ values (e.g. Wenzel *et al.* 2000; Joachimski & Buggisch 2002; Joachimski *et al.* 2004, 2009; Buggisch *et al.* 2008; Grossman 2012b).

Biogenic phosphate approximates to calcium (hydroxyfluor)apatite, which can be expressed as $\text{Ca}_{10}(\text{PO}_4)_6(\text{OH}, \text{F}, [\text{CO}_3]_{0.5})_2$, historically known as francolite (Elliott 2002). Biogenic apatite is also considered to be something of a ‘dustbin mineral’ for its ready acceptance of rare earth elements (REEs) into the crystal lattice post-mortem (Grandjean-Lécuyer *et al.* 1993), though this can occur without recrystallisation or alteration to the mineral’s oxygen isotopic composition (Joachimski *et al.* 2009). Biogenic phosphate $\delta^{18}\text{O}$ values are not affected by low temperature abiogenic recrystallisation of phosphate minerals (Blake *et al.* 1997; Zazzo *et al.* 2004). However, recrystallisation at elevated temperatures, or when microbially mediated, can change biogenic phosphate $\delta^{18}\text{O}$ values (Blake *et al.* 1997; Zazzo *et al.* 2004; Joachimski *et al.* 2009; Wheeley *et al.* 2012). For this reason, the CAI (Figure 3-1) is routinely used to assess the suitability of conodont elements for isotope analysis as it is a proxy for the degree of thermal alteration that conodont elements have been subjected to, either from burial diagenesis or contact metamorphism (Epstein *et al.* 1977; Rejebian *et al.* 1987).



Figure 3-2. Examples of small shelly fossils (SSFs) from the Comley Limestones. Coloured images taken using an Alicona Infinite Focus Microscope (IFM). Grayscale images taken using a scanning electron microscope (SEM).

In summary, biogenic phosphate $\delta^{18}\text{O}$ is more robust to thermal alteration than those carbonate $\delta^{18}\text{O}$ (e.g. Wenzel *et al.* 2000; Joachimski *et al.* 2009; Grossman 2012b). Phosphate biominerals are an abundant component of the Cambrian skeletal fossil record, and therefore may be a suitable target for Cambrian palaeoenvironmental $\delta^{18}\text{O}$ data.

3.4. Finding suitable fossil biominerals

3.4.1. Cambrian 'Small Shelly Fossils'

An alternative source of quantitative palaeoclimate data for the Cambrian Period needs to be found to circumvent the dual problems of diagenetic alteration and the absence of the taxa ordinarily considered suitable. Phosphate-biomineralising taxa are more likely to preserve $\delta^{18}\text{O}$ compositions on geological timescales than carbonate-biomineralising taxa. In this case, Darwin's dilemma of the 'Cambrian explosion' may provide a solution rather than the usual myriad of interesting problems.

'Small shelly fossils' (SSFs) are the skeletal remains of some of the earliest biomineralising animals and were one of the early markers of the 'Cambrian explosion'. They are often studied as isolated phosphatic remains extracted by acid maceration from

limestones (Figure 3-2). The SSFs are an eclectic group of microfossils comprising representatives of at least six modern phyla, alongside many problematic taxa (Bengtson 1992, 2004). SSFs are the result of a multitude of early biomineralisation strategies, with the SSF animals producing calcareous, phosphatic and siliceous skeletal elements (Brasier 1990; Kouchinsky *et al.* 2012) – this is unsurprising given the phylogenetic diversity of this group.

Despite their original diversity of biomineralisation strategies, many early Cambrian SSFs are preserved by secondary phosphate, as steinkerns (internal moulds) or by replacement of the original biomineral (e.g. Brasier 1990; Porter 2004). Indeed, the middle Cambrian crash in SSF abundance and diversity has been linked to the closure of the phosphatisation taphonomic window, rather than purely reflecting a biological event (Porter 2004). Recent work on the Cambrian Series 2/Miaolingian Thornton Limestone, Australia, suggested that skeletal phosphate remobilisation was not required to supply P atoms for secondary phosphatisation; instead, secondary phosphatisation could be achieved by degradation of organic matter in the surrounding sediment (Creveling *et al.* 2014). Pervasive remineralisation is not required to preserve SSFs with secondary phosphate and, consequently, original phosphatic skeletal material could be preserved alongside secondarily phosphatised biogenic carbonates.

Some SSFs undoubtedly produced phosphatic skeletons (Brasier 1990) and some of these biophosphatising taxa may be considered as candidate repositories of isotopic palaeoclimate data. When exceptionally well-preserved SSFs are reported, ‘exceptional preservation’ typically refers to high fidelity replication of originally organic biological structures in secondary phosphate. However, the preservation of original skeletal material rather than of anatomical detail is required if an environmental phosphate $\delta^{18}\text{O}$ signal is to be extracted. This requires a different type of ‘exceptional preservation’ that avoids secondary phosphatisation, and this is examined later in this chapter.

3.4.2. A note on sampling constraints from isotope analysis protocols

Two main techniques are used to extract oxygen isotope data from phosphatic minerals: the silver phosphate bulk method, and *in situ* secondary ion mass spectrometry (SIMS). Each method has merits and drawbacks, though the SIMS method has been favoured in work for more recent studies (Trotter *et al.* 2008; Wheeley *et al.* 2012, 2018). However, these techniques have different, and strict, sample preparation requirements. The

requirements of isotope sampling protocols impact on both the assembly of analytical samples and the types of preservation tests that can be applied to each sample.

The method for bulk isotope analyses follows an analytical protocol adapted after O'Neil *et al.* (1994) that requires an initial, i.e. fossil, sample mass of at least 10 mg. This equates to several tens to a few hundred individual SSF specimens. This method can therefore only be applied to sufficiently abundant fossil taxa. Furthermore, using this method, it is impractical to make a detailed assessment of the preservation state of each individual SSF specimen. Any protocol for assessing the preservation state of biogenic apatite to be analysed via this method needs to be applicable under binocular microscopy, similar to the conodont CAI (Epstein *et al.* 1977; Rejebian *et al.* 1987).

The *in situ* SIMS method analyses ~30 μm diameter spots on polished sections through individual specimens. This removes the large sampling requirements outlined above and allows for much more detailed examination of the preservation state of each analysed specimen. The high spatial precision afforded by SIMS analysis means that a protocol for assessing the preservation state of biogenic apatite to be analysed by this method must be able to identify highly localised alteration that would not be observed in a bulk signal from tens to hundreds of otherwise well-preserved specimens.

Both of these techniques are, however, useful, and may be especially so when combined (see Chapter Four). The analytical uncertainty of SIMS $\delta^{18}\text{O}$ measurements is much greater than that of silver phosphate $\delta^{18}\text{O}$ measurements, and SIMS analyses contain an additional uncertainty as the technique incorporates $\delta^{18}\text{O}$ contributions from all oxygen sources in the analysis spot. In phosphates, this can be particularly problematic given their proclivity for incorporating carbonate and hydroxyl ions within the apatite lattice. The silver phosphate method has the advantage of high $\delta^{18}\text{O}$ measurement precision, and the guarantee of only analysing phosphate-bound oxygen from which all current phosphate $\delta^{18}\text{O}$ – temperature relations are derived (Longinelli & Nuti 1973; Kolodny *et al.* 1983; Lécuyer *et al.* 1996, 2013; Pucéat *et al.* 2010; Chang & Blake 2015). Both techniques are useful, and both are used in this thesis (see Chapter Four), but they exercise constraints on sampling and therefore on the establishment of a preservation protocol.

3.4.3. Taxon selection criteria

It is essential that any analysed fossils come from animals that produced phosphatic skeletons, not skeletons of another mineral subsequently replaced by secondary

phosphate. This is necessary, but not sufficient, to identify fossils that preserve a Cambrian environmental $\delta^{18}\text{O}$ signal. Brasier (1990) presented six criteria for determining which SSF taxa produced phosphatic skeletons. Phosphate-biomineralising SSF taxa will have skeletons that:

- a. are consistently phosphatic across different locations and horizons that otherwise lack widespread phosphate,
- b. are consistently preserved as phosphate alongside other taxa which have skeletons preserved by other minerals,
- c. have similar structures in similar-sized specimens from the same horizon,
- d. preserve consistent microstructure and ultrastructure across different specimens of the same taxon,
- e. have an absence of micro-borings, and
- f. have a consistent chemical composition within and between horizons.

Many Cambrian SSF taxa meet these criteria (Brasier 1990), including the hyolithelminthes, *Torellella* and *Hyolithellus*, the tommotiids including *Sunnaginia*, *Eccentrotheca* and *Lapworthella*, the spinose genus *Rhombocorniculum*, and the linguliformean brachiopods. These criteria will be used to help determine which taxa are suitable candidates for isotopic analysis.

Taxon-specific biological fractionation ('vital effects') in the phosphate oxygen isotope system is thought to be small with respect to analytical uncertainty (Lécuyer *et al.* 1996). However, monotaxic samples should be analysed to avoid mixing any vital effects that do exist. The following criteria were used to select the most suitable SSF taxa for analysis (Table 3-1). Each taxonomic group should:

- a. have precipitated a phosphatic skeleton, determined following the criteria of Brasier (1990);
- b. be abundant in the Comley Limestones, and lower Cambrian rocks more generally, to ensure enough specimens can be assembled for isotopic analyses;
- c. possess a substantial phosphatic skeleton, to maximise potential resistance to chemical alteration, for instance by having a densely crystalline skeleton;
- d. have a well-understood biological microstructure, to distinguish between pristine and altered material;
- e. have stable phylum- and class-level taxonomic assignments, to help determine suitable modern analogue taxa;
- f. have stable genus-level taxonomic assignments, to ensure monotaxic samples;

Table 3-1. Taxon selection criteria. See main text for a full discussion of these criteria. Criteria assessed as passed (1), having possible support (?), or failed (0).

Taxon	a	b	c	d	e	f	g	h
Linguliformean brachiopods	1	1	1	1	1	1	1	1
<i>Rhombocorniculum spp.</i>	1	1	?	1	0	1	1	?
<i>Torellella laevigata</i>	1	1	?	?	0	1	1	1
<i>Hyalithellus cf. micans</i>	1	1	?	?	0	1	1	1
<i>Lapworthella spp.</i>	1	?	?	?	0	1	1	?
<i>Sunnaginia imbricata</i>	1	0	?	1	1	1	1	0
<i>Rushtonites spinosus</i>	1	0	?	1	0	1	1	?

a. originally phosphatic skeleton; b. abundant in Cambrian rocks; c. skeleton potentially robust to alteration; d. well characterised biomineral microstructure; e. high level taxonomic stability; f. generic level taxonomic stability; g. wide palaeogeographic distribution; h. long temporal range.

- g. have a wide palaeogeographic range, to make a globally useful proxy; and
- h. have a long temporal range, to produce a proxy that can be applied throughout the Cambrian Period.

Of the above criteria, the first two, (a) and (b), are essential whilst the rest are desirable. Taxa must be originally phosphatic and occur in sufficient abundance to allow repeat bulk $\delta^{18}\text{O}$ analyses.

3.5. Selected taxa

Of the myriad SSFs from the Comley Limestones, three taxonomic groups were considered suitable for this work (Table 3-1): linguliformean brachiopods, *Rhombocorniculum*, and *Torellella*. The tommotiid *Lapworthella* was also found to be a potentially suitable candidate under the selection criteria but is not sufficiently abundant in the Comley Limestones for bulk isotope analyses, and so is not considered further.

3.5.1. Linguliformean brachiopods

Because of their well-studied extant relatives, the linguliformean brachiopods are the best understood of the SSFs considered here in terms of microstructure, chemistry and lifestyle. This makes them a potentially valuable group to examine as repositories of Cambrian environmental proxy data. Linguliformean brachiopods are probably the most abundant skeletal elements in the Comley Limestones acid-resistant residue.

The linguliformean brachiopods of the Comley Limestones belong to the lingulate orders Lingulida and Acrotretida, and the paterinate order Paterinida (Brasier 1986; Hinz 1987; Cocks 2008; Winrow 2015).

The lingulid brachiopods are represented by the genus *Eoobolus* Matthew 1902 in the Comley Limestones, with at least two species being present: *E. aff. viridis* Cobbold 1921 (synonymised from *Lingulella viridis* by Li & Holmer, 2004) and *E? parvulus* Cobbold 1921 (reassigned from *Obolus* by Cocks, 2008). Three additional *Eoobolus* species were described in a recent PhD thesis (Winrow 2015): *E. davidsoni*, *E. sedgwicki*, and *E. huttoni*. However, as this is not a formal publication under the International Code on Zoological Nomenclature these remain nomina nuda. Winrow (2015) also recommended erection of a new genus for *E.? parvulus* – *Svenjaella* nomen nudum – on grounds of morphology and shell microstructure, though for the present this species remains formally, if tentatively, assigned to *Eoobolus* (Cocks 2008). See Winrow (2015) for detailed discussion of the lingulate brachiopods of the Comley Limestones. The acrotretid brachiopods include *Linnarssonina ophirensis* Walcott 1902, *Acrothyra comleyensis* Cobbold 1921, *Acrothyra cf. sera* Matthew 1902, *Acrothyra signata sera* Matthew 1902, and *Curticia minuta* Bell 1944.

Various species of *Paterina* Beecher 1891 have been described from the Comley Limestones, most notably *P. labradorica* Billings 1861 (Cobbold 1921; Brasier 1986; Hinz 1987; Winrow 2015). The phylogenetic position of the Paterinata remains unresolved; they are possibly deep or basal on the Linguliformea stem, or may in fact be stem Brachiopoda (Holmer 2001; Winrow 2015). However, they are not common in the Comley Limestones, so no paterinate brachiopods were used in this study.

The majority of lingulate brachiopod specimens from the Comley Limestones were lingulids, rather than acrotretids. To avoid mixing potentially different ordinal-level vital effects, only shells from lingulid brachiopod were used in this study. Most brachiopod specimens recovered from the acid-resistant residues were fragments, not identifiable at species-level and sometimes not identifiable at genus-level. However, differences in biological fractionation between the extant lingulid genera, *Lingula* and *Glottidia*, are negligible compared to analytical uncertainty (Lécuyer *et al.* 1996). Therefore, monotaxic samples assembled at the ordinal level, and in any case more likely dominated by the single lingulid genera: *Eoobolus*, are justifiable.

Early Cambrian lingulid brachiopods were epibenthic animals living in shallow marine settings. Their thin shell and small size suggest that they were unable to burrow

as their extant relatives do, but were either attached to the seafloor by a strong pedicle or lived interstitially between sediment grains (Ushatinskaya *et al.* 2001). Therefore, any recorded environmental signal will reflect sea surface conditions.

3.5.2. *Rhombocorniculum* Walliser 1958

Rhombocorniculum is a phosphatic spinous genus with two species (Kouchinsky *et al.* 2015), *R. cancellatum* Cobbold 1921 and *R. insolatum* Missarževskij in Missarževskij & Mambetov 1981, known from worldwide lower Cambrian strata. Only *R. cancellatum* has been reported with confidence from the Comley Limestones (Cobbold 1921; Hinz 1987). Brasier's (1986) report of *R. aff. insolatum* from the Comley Limestones describes it as having a much stronger, more *cancellatum*-like, ornamentation than typical *R. insolatum*. These sclerites may now be considered within the morphological variability of *R. cancellatum* (Kouchinsky *et al.* 2015). In the Comley Limestones, *Rhombocorniculum* co-occurs with the similar, but distinct, phosphatic spinous genus *Rushtonites* Hinz 1987 which is likely a junior synonym of *Mongolitubulus* Missarževskij 1977 (Skovsted & Peel 2001; Kouchinsky *et al.* 2015).

The ornamentation and internal structure of *Rhombocorniculum* is well documented (Landing 1995; Li *et al.* 2003; Kouchinsky *et al.* 2015). The outside of the sclerite is ornamented with a regular rhombohedral pattern that may diminish towards the base. Micron-width rods orientated parallel to the long-axis of the sclerite are visible on the external surface. The sclerite walls comprise hollow tubules separated by narrow phosphatic partitions subparallel to the external edge of the spine. The tubules have an irregular cross section. The thick phosphatic wall surrounds a hollow central lumen.

Rhombocorniculum has been compared to the organic-walled spines of *Hallucigenia* (Caron *et al.* 2013) and to annelid chaetae (Kouchinsky *et al.* 2015), though phylum-level taxonomic classification remains problematic. *Rhombocorniculum* fulfils all the criteria for a phosphate-biomaterialised Cambrian sclerite (Brasier 1990), but there are no known biomaterialised annelid chaetae. Although *Hallucigenia* spines were composed of organic matter, phosphate-biomaterialised lobopodian sclerites are known (Steiner *et al.* 2012; Caron *et al.* 2013; Yang *et al.* 2015b), adding support to the hypothesis of *Rhombocorniculum* as a lobopodian sclerite (Caron *et al.* 2013). Regardless of its phylogenetic affinity, *Rhombocorniculum* was a phosphatic spinous sclerite grown by an animal with a likely benthic ecology. *Rhombocorniculum* is

palaeogeographically widespread and abundant, with well-documented microstructure, and can be used in this study.

3.5.3. *Torellevella laevigata* Linnarsson 1871

Phosphatic tubes are abundant in early Cambrian acid-resistant residues, including those of the Comley Limestones. Cambrian phosphatic tubular fossils are grouped under Order Hyolithelminthida Fisher 1962 (phylum and class uncertain) which comprises two families: Hyolithellidae Walcott 1886 and Torellevellidae Holm 1893. The hyolithellids are characterised by a tube with a circular cross section whereas the torellevellids have an oval cross section; additionally, the torellevellids typically have much thicker phosphatic walls than the hyolithellids. The torellevellids are therefore likely to be more robust to diagenetic alteration than the hyolithellids. Hyolithelminths are known to have had benthic attached epifaunal and shallow infaunal ecologies in shallow marine habitats, with specimens having been found preserved in life positions (Vinn 2006; Skovsted & Peel 2011). The high-level biological affinity of the hyolithelminthes remains unresolved, but they have been compared to both cnidarians (e.g. Vinn 2006) and annelids (e.g. Skovsted & Peel 2011).

Two torellevellid genera, *Torellevella* Holm 1893 and *Rushtonella* Cobbold & Pocock 1934, have been described from the Comley Limestones (Cobbold & Pocock 1934; Brasier 1986), though *Rushtonella* is now considered to be a junior synonym of *Torellevella* (Landing 1988). *Torellevella* specimens from the Comley Limestones are considered to belong to *T. laevigata* Linnarsson 1871 (*sensu lato* pending revision) due to the continuous morphological variation between described species (Landing 1988).

Torellevella microstructure is not well characterised in the literature, but it is thought to have been composed of phosphatic laminae (Vinn 2006). This is consistent with other hyolithelminths which have a laminated microstructure. Crystallites in alternate laminae of *Hyolithellus* are arranged in different orientations, producing a plywood structure (Bengtson *et al.* 1990; Skovsted & Peel 2011), though no such structure has been reported from *Torellevella*. In summary, *Torellevella* was a benthic, phosphate-biomineralising organism that produced a thick-walled tube, and is potentially suitable for isotopic analyses.

3.6. Materials

3.6.1. Bulk limestone processing

All of the samples used in this study come from strata around the traditional early to middle Cambrian, now Cambrian Series 2/Miaolingian, boundary. The geological and stratigraphic context of these samples is detailed in Chapter Two. The following method was used to process all samples used in this study.

Acetic acid maceration following an adapted form of the standard protocol of Jeppsson *et al.* (1999) was used to recover acid-resistant residues including phosphatic microfossils. This method has a negligible effect on phosphate $\delta^{18}\text{O}$ values, especially by comparison with formic acid maceration which is known to cause isotopic alteration (Wheeley *et al.* 2012; but see Quinton *et al.* 2016). To avoid catastrophic phosphate dissolution that occurs at and below $\text{pH} = 3.6$ (Jeppsson *et al.* 1999), the solution was maintained at or above $\text{pH} = 4$.

Limestone blocks of approximately 1 kg were mechanically broken into 5 cm to 10 cm chunks, using a jaw crusher, to increase rock fragment surface area and reduce the time required to dissolve the samples. The rock chips were immersed in a pre-prepared solution comprising 700 ml concentrated (80 %) acetic acid, diluted in 5000 ml warm water and buffered with 2400 ml acetate buffer (spent acetic acid). The initial run was buffered to $\text{pH} > 4$ using powdered sodium acetate. For smaller rock samples, half volumes were used. Samples in the acetic acid solution were thoroughly rinsed, and the acid solution refreshed, every four to six weeks. However, longer exposure times to the solution is not thought to affect phosphate oxygen isotope composition (Wheeley *et al.* 2012). Acid-resistant residues were collected between 1000 μm and 125 μm sieves, and thoroughly rinsed with deionised water before being gently oven-dried ($T < 50^\circ\text{C}$).

Heavy liquid separation (HLS), commonly used to concentrate microfossils within an acid-resistant residue, was not used for the majority of samples because it is known to affect $\delta^{18}\text{O}$ values of phosphatic microfossils (Wheeley *et al.* 2012). For some samples of the Comley Limestones processed before September 2014, bromoform HLS was used, and both the heavy and light fractions were labelled and kept. These samples have been treated in exactly the same way as samples that were not subjected to HLS.

3.6.2. Microfossil preparation

The rinsed and dried acid-resistant residues were examined using a binocular microscope. SSF specimens were picked out using a brush wetted with deionised water

and placed into labelled microfossil slides. Where necessary, individual specimens were cleaned of additional sediment using a brush wet with deionised water, and fine needle was used to remove larger grains or to break off obstinately dirty portions of the fossils.

Some analyses are best performed on flat highly polished surfaces cut through the fossils, which are also a requirement for SIMS $\delta^{18}\text{O}$ analyses. Individual SSFs were imaged before being orientated, usually horizontally or vertically, and adhered to brown packing tape. Fossil specimens used for SIMS analyses were arranged within 5 mm of the centre of the block, around a central piece of Durango apatite supplied by the EIMF that was used as a $\delta^{18}\text{O}$ standard. Cylindrical 1" diameter plastic moulds were placed around the taped specimens, keeping the Durango standard central, and adhered to the packing tape.

Two types of epoxy resin were used: Buehler's EpoxiCure2 and EpoThin2 epoxy resins; both are suitable for SIMS work (Engwell & Hall 2008). EpoxiCure2 was initially used as it scored highest in the EIMF evaluation of suitable epoxy resins (Engwell & Hall 2008). However, it became apparent during this work that the lower viscosity of EpoThin2 was preferable when working with small fossils that have complex and irregular morphology. Therefore, EpoThin2 was used for later blocks and surface re-impregnation of all blocks.

The epoxy resin and hardener were gently mixed for two minutes in a plastic beaker using a wooden spatula under a fume hood, according to the manufacturer's instructions. The plastic moulds with SSFs adhered to packing tape were placed on a smooth flat glass plate to avoid introducing unwanted topography. The combined resin was gently poured into the plastic moulds covering the fossils to a thickness of approximately 15 mm to 20 mm. If necessary, fossils were carefully re-orientated using a fine needle before the resin cured. The resin blocks were cured for 24 hours under constant pressure of ~2 bar to compress the resin into all accessible cavities and to remove or reduce trapped air bubbles. After 24 hours the resin blocks were removed from the pressure chamber, and the plastics moulds, and left to cure for at least a further 72 hours, until resin was fully hardened and not tacky to touch. In colder temperatures (winter) this could take considerably longer than 72 hours.

The flat face nearest to the fossils was ground by hand using coarse (P600), medium (P800), and fine (P1200) silicon carbide paper on a glass plate and lubricated with water. The blocks were then polished by hand using progressively finer (15 μm , 6 μm , 3 μm , 1 μm and 0.25 μm) equidimensional diamond pastes on separate polishing

cloths. Where analytical techniques demanded a finer polish, γ -alumina paste was used, with automated polishing for 15 minutes. Surface maps of each block were so that specimens could be readily identified during subsequent analyses.

3.7. Methods: Assessing the preservation state of biogenic phosphate

Conodont preservation is routinely determined by reference to the conodont CAI (Epstein *et al.* 1977; Rejebian *et al.* 1987), but this is not widely applicable to other phosphatic fossil groups. In particular, there is no established protocol for assessing the preservation state of Cambrian phosphatic SSFs. It is therefore necessary to establish a repeatable protocol for assessing the preservation of SSF phosphate, if they are to become a reliable new source of palaeoenvironmental $\delta^{18}\text{O}$ data.

The approach recommended for assessing the preservation of carbonate biominerals is to use as many techniques as can reasonably be applied (Brand *et al.* 2011). Not all of the techniques applicable to carbonate biominerals can be used on phosphatic ones, and most of the techniques for examining phosphate preservation have been developed for vertebrate skeletal material – conodont elements, and vertebrate bones and teeth (e.g. Armstrong *et al.* 2001; Trueman & Tuross 2002; Wopenka & Pasteris 2005; Neary *et al.* 2011; Thomas *et al.* 2011; Zougrou *et al.* 2016). However, some of these techniques can be adapted for novel phosphate-biomineralising taxa.

Because some isotope analyses require destructive bulk sampling of several tens of individual specimens, the protocol needs to work at the specimen selection stage, similar to the CAI. To have confidence in this, more detailed analyses are necessary, looking at the microstructure, ultrastructure and chemistry of individual specimens. An array of techniques are therefore needed, including a visual assessment of microfossils along with detailed structural and chemical analyses (Figure 3-3).

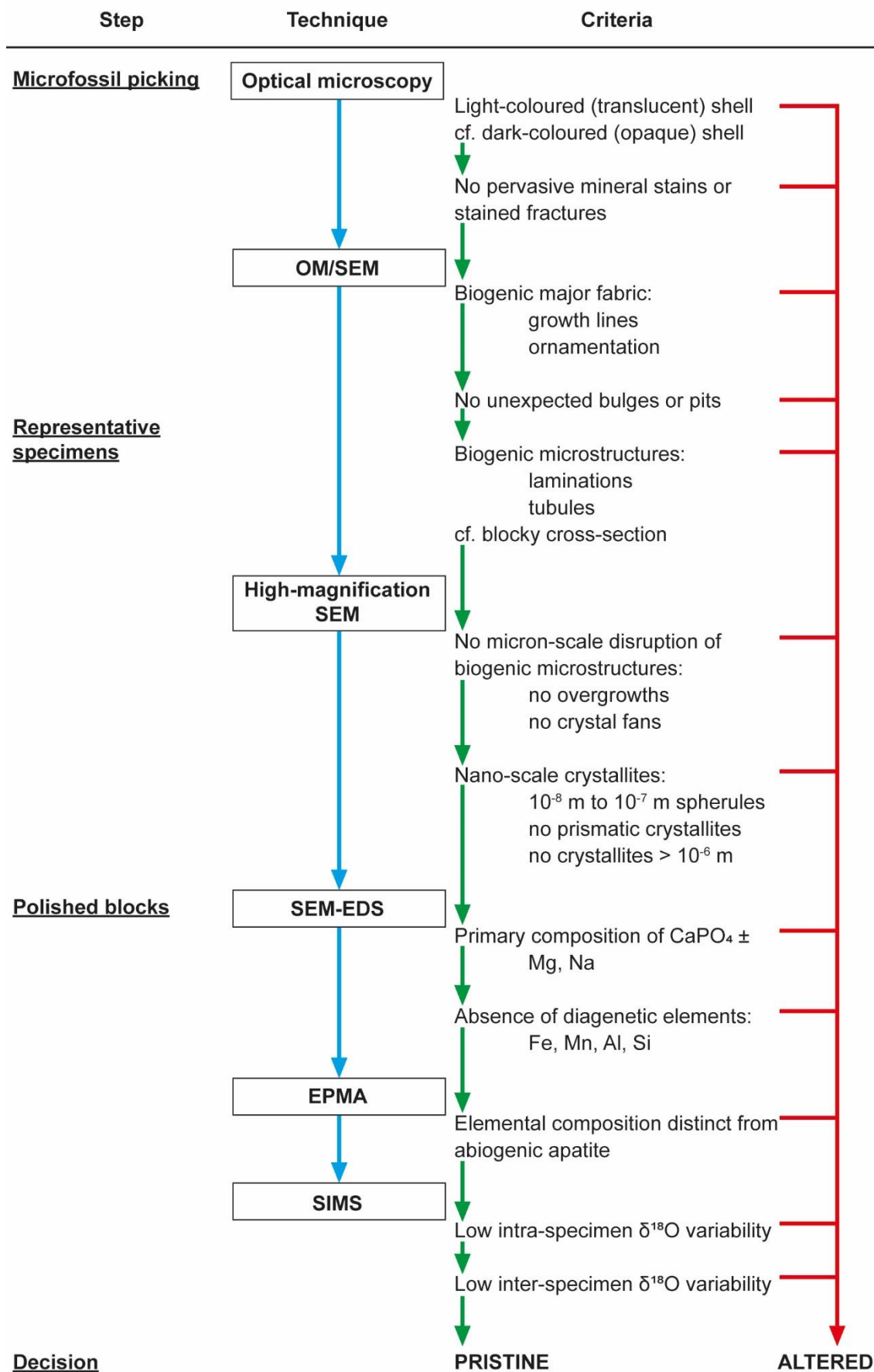


Figure 3-3. Protocol for assessing the isotopic preservation of biogenic phosphate. See discussion in the text.

3.7.1. Gross morphology

The general shape, growth lines, external ornamentation, and colour can be examined using a binocular microscope. This is the step at which any potential alteration needs to be determined, much like the CAI, for this protocol to be applied for bulk isotope analyses. Growth lines and external ornamentation should be well-preserved, with a lack of evidence of physical abrasion. Physical abrasion may indicate a prolonged pre-burial period in which physical erosion could occur, which may increase the potential for chemical alteration. There should be an absence of overgrowths, which may be visible as blocky or globular regions on the skeleton, and an absence of evidence of internal secondary phosphate precipitation, such as bulging of the skeleton or the presence of new material on the surface of the fossil.

Colour is the other main indicator at this scale. Mineral coatings on the surfaces of some SSFs can be readily identified under binocular microscopy as either unexpected colours or textures. The composition and depth of penetration of this type of alteration is variable, but it may indicate pervasive alteration. Generally, there is no reasonable method for removing coatings of iron oxide adhering to the surface of specimens. These SSFs are therefore unsuitable for stable oxygen isotope analyses. Following inferences from the conodont CAI, darkening and eventually bleaching of specimens indicate progressively greater alteration (Epstein *et al.* 1977; Rejebian *et al.* 1987).

Reflected light (RL) imaging was conducted using a Leica M205C binocular microscope and digital camera attachment, at the SGGE, UoL, illuminated by fibre optic lamps. High resolution imaging of individual SSFs required use of an Alicona Infinite Focus Microscope (IFM) G4c, at the SGGE, UoL. The high relief of these fossils makes them tricky to image. The IFM uses horizontal and vertical stitching of stacked images to produce in-focus images and three-dimensional surface models of objects. Only the basic imaging functions of the IFM were used in this work, but it proved to be the best method for high resolution colour imaging of individual SSFs.

A scanning electron microscope (SEM) was used to produce higher resolution greyscale topographic images of individual SSFs. This is the standard method for imaging SSFs in palaeontology. SEM imaging is particularly useful for observing morphological features such as growth lines, pustules, tubercles, and other external ornamentation in fine detail. Specimens prepared for SEM analysis were mounted on aluminium stubs using either adhesive carbon tabs or a solution of one-part PVA glue diluted into seven parts water to facilitate easy removal of the specimens for further

analysis. Prior to SEM analysis, specimens were sputter-coated with a ~30 nm thick layer of carbon or gold. SEM analysis was typically conducted with an accelerating voltage of 15 keV and beam current between 65 nA to 75 nA. Several SEMs, with energy dispersive X-ray spectroscopy (EDS) attachments, were used during this project:

- a. Hitachi S-3600N SEM with Oxford Instruments INCA X-sight EDS attachment; at the SGGE, UoL;
- b. Phenom Pure desktop SEM; SGGE, UoL;
- c. FEI Quanta 650 FEG-SEM; Engineering Department, UoL;
- d. FEI Sirion FEG-SEM; Engineering Department, UoL;
- e. FEI Quanta 600 SEM with Oxford Instruments INCA X-sight EDS attachment; BGS.

Linguliformean brachiopods

The overall morphology of extant and extinct linguliformean brachiopods is well understood. *Eoobolus* species have inequivalved dorsibiconvex shells that are elongate suboval to subcircular in outline, with a deep narrow subtriangular pedicle groove (Williams *et al.* 1997b; Balthasar 2009; Winrow 2015). Both valves have well-developed flexure lines, the shell thickens slightly towards the anterior, and the adult shell has a pustulose ornament and is finely pitted (Williams *et al.* 1997b; Balthasar 2009; Winrow 2015). Note that the post-larval shell of *E. ? parvulus* lacks pustulose ornamentation, and it was on this and other grounds that Winrow (2015) recommended the erection of a new genus for this species.

Rhombocorniculum

The morphology of *R. cancellatum* has been well documented in the literature (Landing 1995; Li *et al.* 2003; Kouchinsky *et al.* 2015). The genus is characterised by an elongate spinous morphology thickening towards the base, with a thick wall and hollow central lumen, the external surface is ornamented with a regular rhombohedral pattern, and the wall comprises thin hollow tubules (Kouchinsky *et al.* 2015). *R. cancellatum* sclerites are typically elongate, slender and narrow, but can have a broader flattened morphology, as well as transitional forms. Sclerites can be twisted and/or curved by up to 90°, though this is relatively rare in the Comley Limestones. In cross section the sclerite can be subcircular, ovate or tear-drop shaped, and the lumen forms a subcircular or ovate central hole that pinches out towards the tip and emerges at the sclerite base.

Torellella laevigata

T. laevigata is a hollow tube tapering towards the base with an elliptical cross section. The phosphatic tube wall is particularly thick compared to other hyolithelminth taxa. The tube wall comprises laminae subparallel to the internal surface, and the external surface has irregular pseudocircumferential lineations. The tube can be gently twisted and/or curved, and can be folded or crushed without cracking the tube, suggesting that it was slightly flexible during life.

3.7.2. *Microstructure*

Examining the preservation of micrometre scale textures is a common initial step in investigating the isotopic preservation of biominerals (e.g. Brand *et al.* 2011; Bennett *et al.* 2018; Bergmann *et al.* 2018). This is a relatively accessible level of detail that can reveal crude recrystallisation or mineral replacement, both of which are indicative of isotopic alteration. Original (biogenic) microstructures include features such as internal continuous laminations, orientated fibres or columns, and are best identified by reference to closely related extant taxa. Recrystallised or replaced microstructures may include blocky protrusions or radiating crystal fans, which can be obvious, or can manifest as disruptions to biogenic fabrics. Microstructural alteration may be detected under binocular microscopy, but generally requires confirmation by higher resolution SEM imaging.

Microstructure can be examined in fractured specimens or on polished surfaces through individual specimens. Some specimens were embedded in resin blocks for examination, whilst others were mounted on SEM stubs. Examining specimens found in lithological thin sections can help to reveal the relationships between individual fossils and the host lithology, for instance if fossils are associated with a particular secondary mineralisation phase.

All of the SEMs listed above (p. 56) were used to investigate and image the microstructure of fractured specimens, fossils found in thin sections and fossils embedded in resin blocks. The SEMs were typically used in secondary electron (SE) mode to image fractured specimens, and backscattered electron (BSE) mode to image specimens with polished surfaces. Preparing specimens for SEM analysis is essentially a destructive process. Therefore, of these specimens, only those embedded in epoxy resin suitable for SIMS analyses can be used to collect $\delta^{18}\text{O}$ data.

Linguliformean brachiopods

The microstructure of modern and ancient linguliformean brachiopods is well characterised in the literature (e.g. Williams *et al.* 1992, 1994, 1997a, 2007; Cusack & Williams 1996; Cusack *et al.* 1999; Williams & Cusack 1999; Schmahl *et al.* 2008). Linguliformean brachiopods comprise a primary layer of phosphatic granules dispersed in amino acids (Williams *et al.* 1994, 1997a; Cusack *et al.* 1999). The primary layer is thin, minimally phosphatic, and only usually preserved by secondary phosphatisation, presumably early, and presumably nucleating on the phosphatic granules within the primary layer.

The linguliformean brachiopod secondary layer comprises alternating compact and porous (organic-rich) stratiform laminae (Williams *et al.* 1994, 1997a; Cusack & Williams 1996; Cusack *et al.* 1999; Williams & Cusack 1999; Schmahl *et al.* 2008). The porous laminae occur with various morphologies, including bacculate, virgose, rubbly, and columnar, and vary with taxonomy and position within the shell. Some porous laminae have no mineral component at all and are completely composed of chitinous organic matter (Schmahl *et al.* 2008). The majority of brachiopods examined in this study were eobolids, the secondary layer of which comprised alternating compact and rubbly or virgose laminae, which seems to be the ancestral state of linguloid brachiopods (Cusack *et al.* 1999).

Rhombocorniculum

The microstructure of *Rhombocorniculum* has been well-characterised in the literature. The sclerite walls are formed by a packed-straws structure of hollow tubules about 1 µm in diameter with thin phosphatic walls (Kouchinsky *et al.* 2015). The tubules do not bifurcate or truncate each other, and are subparallel to the internal surface. The tubules seem to emerge into the lumen at the inner surface of the wall, though this has not yet been conclusively demonstrated. The tubules do not emerge at the outer surface; instead there is a region of densely-packed phosphate at the outer edge of the sclerite wall at least 5 to 10 µm thick. The external surface of the sclerite has fine longitudinal striations ~0.1 µm in width. These striae are an order of magnitude finer than the tubules.

Torellella

Torellella is a somewhat understudied genus, perhaps unsurprisingly given its simple morphology. The tube wall of *Torellella*, like other hyolithelminths, comprises phosphatic laminae, perhaps with a plywood structure, that are visible in cross section

(Vinn 2006; Skovsted & Peel 2011; Kouchinsky *et al.* 2015). These laminae are sub-parallel to the inside of the tube wall and do not truncate each other or bifurcate.

3.7.3. Ultrastructure

The preservation of sub-micrometre scale (sub-micron) textures, or the ultrastructure, of shells and skeletons is also used in skeletal carbonate preservation protocols (Brand *et al.* 2011). However, the cost and time involved in the high-resolution imaging required to discern biogenic or diagenetic ultrastructures mean that ultrastructure examinations are less common than microstructural investigations. Imaging structures <1 µm in size can reveal details of fine-scale recrystallisation and/or mineral replacement which may indicate isotopic alteration. Biogenic apatite ultrastructures include blocky, platelet and spherular morphologies (e.g. Wopenka & Pasteris 2005; Schmahl *et al.* 2008). These are contrasted to the prismatic and acicular morphologies which are typical of synthetic and geological apatites (Wopenka & Pasteris 2005). As with microstructural analyses, extant or better understood younger related taxa can be used to provide a phylogenetic bracket on plausible biogenic ultrastructures that are expected in SSFs.

SSF ultrastructure was examined by high resolution SEM imaging of fractured surfaces of specimens adhered to SEM stubs, and of polished sections through specimens embedded in epoxy resin. Sub-micron resolution could only be achieved with the more recently developed field emission gun (FEG)-SEMs. Ultrastructural imaging was conducted using the FEG-SEMs in the Engineering Department, UoL. Even with these machines, imaging at this resolution is time consuming and could not be applied to every specimen.

Linguliformean brachiopods

The ultrastructure of linguliformean brachiopods has been well characterised in modern and fossil specimens. Linguliformean brachiopod compact laminae comprise densely packed sub-micron (10 nm to 100 nm) apatitic spherules (Cusack & Williams 1996; Williams *et al.* 1997a, 2007; Cusack *et al.* 1999; Schmahl *et al.* 2008). These can recrystallise into prismatic or rod-like morphologies, or anneal into coarser grained tablets during diagenesis (Cusack & Williams 1996; Cusack *et al.* 1999). The phosphatic components of the various porous laminae morphologies, including the baculate and virgose fibres, are also thought to comprise sub-micron phosphatic spherules (Cusack *et al.* 1999).

Rhombocorniculum

The ultrastructure of *Rhombocorniculum* sclerites has not been described. By comparison to extant and other extinct phosphatic taxa, it seems reasonable to assume that platelet and spherulitic morphologies could have characterised the original biomineral, compared with prismatic or acicular crystallite morphologies which would be indicative of diagenetic alteration (e.g. Cusack *et al.* 1999; Wopenka & Pasteris 2005; Schmahl *et al.* 2008; Ferretti *et al.* 2017). Additionally, smaller, sub-micron, crystallites could be considered as biogenic, whereas larger crystallites are more likely the result of recrystallization or secondary mineralisation.

Torellella

Although the ultrastructure of *Torellella* has not been characterised in detail in the literature, that of other hyolithelminths is better known (Skovsted & Peel 2011).

Hyolithellus tubes have a plywood structure in which the crystallites of alternate laminae are arranged orthogonal to each other. Although this plywood structure has been tentatively reported from *Torellella* (Kouchinsky *et al.* 2015), it has not been demonstrably figured. Therefore, there are two possibilities for the biogenic ultrastructure of *Torellella*: a plywood structure, or laminae comprising phosphatic spherules. Recrystallised apatite in *Torellella* is expected to have larger tablet-shaped or prismatic crystallites.

3.7.4. Elemental chemistry

The major, minor and trace element composition of a mineral may be used as a proxy measure of possible isotopic preservation. This is well characterised in and routinely applied to calcareous fossils (Brand *et al.* 2011) but is not so well understood in phosphatic fossils, despite several studies (e.g. Watabe & Pan 1984; Grandjean-Lécuyer *et al.* 1993; Williams *et al.* 1997a, 2007; Armstrong *et al.* 2001; Trueman & Tuross 2002; Trotter & Eggins 2006). Part of the problem is that apatite is a ‘dustbin mineral’ that readily accommodates various monovalent, bivalent and trivalent cations within its open lattice structure (e.g. Nathan 1984; Hughes & Rakovan 2002; Wopenka & Pasteris 2005). Post-mortem, biogenic apatites are particularly accepting of rare earth elements (REEs) and other transition metals (Grandjean-Lécuyer *et al.* 1993) in a variety of ways including adsorption, substitution, diffusion and recrystallisation (e.g. Kohn *et al.* 1999; Armstrong *et al.* 2001; Trueman & Tuross 2002). Post-mortem uptake of REEs by apatites can occur at various stages of diagenesis including very early burial, within the top few centimetres of the sediment column (Chen *et al.* 2015). However, it is notable

that REE (and other element) uptake can happen without affecting the PO_4^{3-} ion site, and without interfering with the phosphorous–oxygen bond. Cation ion substitution can therefore occur without affecting $\delta^{18}\text{O}_{\text{phos}}$ values (Joachimski *et al.* 2009).

Nevertheless, recrystallisation is an efficient method of altering both elemental chemistry and isotopic ratios, especially as coupled substitutions are common in apatites to maintain charge balance (e.g. Trueman & Tuross 2002; Wopenka & Pasteris 2005). Furthermore, carbonate ions (CO_3^{2-}) can substitute into the apatite lattice, either into the phosphate (PO_4^{3-}) site as a coupled substitution involving another monovalent anion (OH^- or F^-) or a trivalent cation substitution for Ca^{2+} , or into the monovalent anion channel site. The topic of elemental composition therefore deserves some attention as it may be useful for detecting extensive coupled substitutions.

Other than their being composed of biogenic phosphate, the primary elemental composition of both *Rhombocorniculum* and *Torellella* is not known. However, the elemental composition of modern linguliformean brachiopods has been fairly well characterised in the literature as a phosphate mineral closely resembling but not identical to francolite, a fluorine- and carbonate-bearing hydroxyapatite (Watabe & Pan 1984; Puura & Nemliher 2001; Williams *et al.* 2007). It is reasonable to assume that ancient phosphate-biomineralising invertebrate taxa produced a skeleton of similar to modern phosphate-biomineralising invertebrate taxa.

Modern linguliformean brachiopod apatite comprises 75% to 94% calcium phosphate, with a variable Mg content (0.3% to 6.7% has been documented) and potentially some Na and Sr (Williams *et al.* 1997a, 2007). Notably, Al, Fe and Mn are not normally incorporated within the crystal lattice of linguliformean brachiopod shells either during life or in early diagenesis at or near to the sea floor, and significant quantities of either are indicative of later diagenesis.

Linguliformean brachiopod hydroxyapatite has a consistent F:Ca ratio of 0.033 ± 0.002 across the calcified layers of its shell (Watabe & Pan 1984). However, the high OH^- content makes biogenic hydroxyapatite moderately unstable and, as a result, F^- ions are commonly incorporated into the apatite lattice during very early diagenesis, beginning on the seafloor. The replacement of larger asymmetrical OH^- ions by smaller spherical F^- ions increases the thermodynamic stability of apatite (Freeman *et al.* 2001; Kohn & Cerling 2002; Trueman & Tuross 2002; Wopenka & Pasteris 2005). Carbonate ion content varies substantially within and between extant linguliformean brachiopod genera, with CO_3^{2-} comprising 1.8 wt% to 2.2 wt% in *Lingula* species and up to 3.6

wt% in *Glottidia* species (Watabe & Pan 1984; LeGeros *et al.* 1985; Williams *et al.* 1997a). Similarly to a high hydroxyl content, high carbonate content of bioapatite results in a lower crystallinity and therefore lower thermodynamic stability, making the material more susceptible to alteration (LeGeros *et al.* 1985).

EDS has recently been employed to good effect in investigating the preservation of biogenic phosphate by analysing major and minor element distribution in ancient phosphatic brachiopods (Lang *et al.* 2015; Bergmann *et al.* 2018). In this study, EDS analyses were performed using Oxford Instruments Inca X-sight systems attached to the Hitachi S-3600N, FEI Quanta 600, and FEI Quanta 650 SEMs. The EDS analyses were not quantitative, but were used to qualitatively map relative abundances of major and minor elements within individual SSFs skeletons. EDS analyses were conducted on specimens embedded in epoxy resin blocks with a 30 nm carbon coat. An accelerating voltage of 15 keV with beam current between 65 nA to 75 nA was used. The working distances were optimised for each machine: 15 mm for the Hitachi S-3600N and 10 mm for the FEI machines.

Electron probe microanalysis (EPMA) was used to quantify the major, minor and some of the trace element chemistry of the SSFs. EPMA was performed over two sessions in October 2016 and May 2017 on the CAMECA SX 100 at the Open University with the assistance of Dr Sam Hammond. EPMA was conducted on SSFs embedded in epoxy resin blocks coated with 30 nm carbon. To mitigate for F mobility during exposure to an electron beam, F was always the first element analysed and a lower accelerating voltage was used (Stormer *et al.* 1993; Stormer & Pierson 1993; Goldoff *et al.* 2012). A focused 10 µm diameter electron beam was used. For F analyses, the accelerating voltage was 10 keV and the beam current 4 nA. For all other elements analysed, the accelerating voltage was 20 keV and the beam current 20 nA. Full analytical settings and standards are reported in Appendix A.

Quantitative EPMA data was sorted and cleaned in Excel to remove analyses that incorporated: (a) a strong resin signal, usually manifest as a low total or low Ca value, or (b) that had a strong signal from interaction with adhering sediment grains, typically manifest as very high Al or Si values. Detrended correspondence analyses (DCAs) were performed on each data set to determine the underlying model of the data, either linear or unimodal. All of the data sets used were found to have an underlying linear model, as expected for most environmental data. Explorative principal component analyses (PCAs) were used to investigate both the overall distribution of the elemental data, and

to reduce the complexity of the data. Selected elements were also examined in more detail for biogenic and diagenetic signals.

3.7.5. *Isotopic composition*

Ultimately, all of the techniques above are only proxy measures of isotopic preservation. Isotopic analyses are needed to test the utility of these techniques and the protocol outline above (Figure 3-3). *In situ* SIMS analyses are particularly useful for this as they can operate a spatial precision of 60 μm (30 μm spot plus 30 μm gap) to reveal intra-specimen variability of isotopic preservation that may relate to particular microstructures, ultrastructures or elemental composition (Wheeley *et al.* 2012).

Inter-specimen isotope analyses have also proven useful in assessing the preservation state of a population of phosphatic microfossils. Joachimski *et al.* (2009) found no substantial isotopic alteration in conodonts with $\text{CAI} \leq 5$ using the bulk silver phosphate analyses. However, Wheeley *et al.* (2012) used *in situ* SIMS analyses to demonstrate increased $\delta^{18}\text{O}$ variance in conodonts with a CAI value > 1 . Therefore, $\delta^{18}\text{O}$ analyses at high spatial resolution are an important addition to the preservation protocol (Figure 3-3).

3.8. Results: Preservation of biogenic phosphate in the Comley Limestones

3.8.1. *Gross morphology*

Linguliformean brachiopods

In general, SSFs from the Comley Limestones have well preserved gross morphology. Growth lines and external ornament such as small pustules are clearly distinguishable on linguliformean brachiopod specimens (Figure 3-4). Most specimens are fragmentary, with whole brachiopod valves extremely rare. Whilst some of this fragmentation may occur during processing, fossils found in thin sections of the Comley Limestones are also commonly broken, suggesting that the shells were broken before deposition in a high energy environment (Rushton 1974). Some of the fragmentary brachiopod specimens appear smoothed and rounded (e.g. Figure 3-4a), rather than having sharp angular edges, indicating a prolonged period of pre-depositional abrasion.

Brachiopod specimens from each horizon can be readily divided into light-coloured translucent specimens and dark-coloured opaque specimens. The light-coloured translucent specimens often exhibit colour differentiation that appears to follow growth bands, as in modern linguliformean brachiopods (Figure 3-4). This type

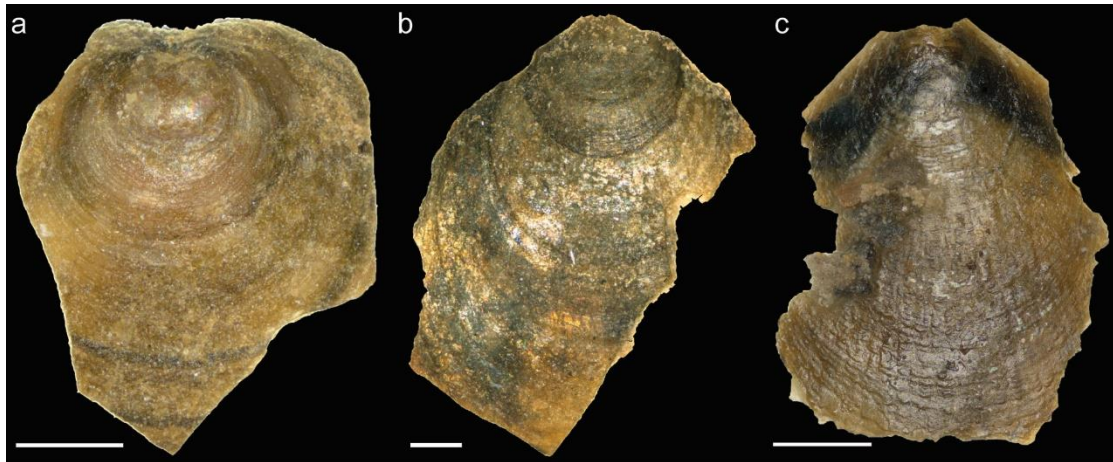


Figure 3-4. Light-coloured linguliformean brachiopods from the Comley Limestones with growth lines and pustulose ornamentation. Specimens (a) SaBrL08; (b) SaBrL02; (c) La2HBr05. Scale bars 200 μ m.

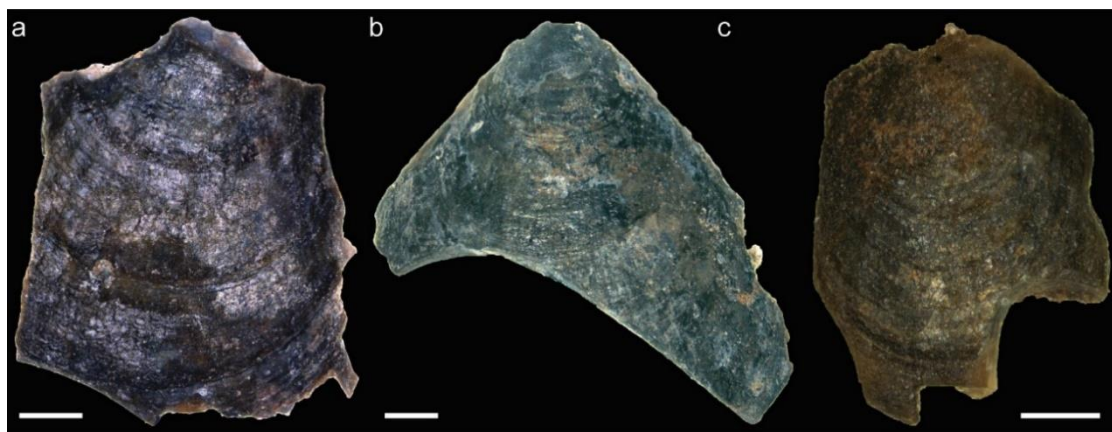


Figure 3-5. Dark-coloured linguliformean brachiopods from the Comley Limestones with growth lines and pustulose ornamentation. Specimens (a) La2BrD0208; (b) SaBrL02; (c) La2HBr05. Scale bars 200 μ m.

of colour variation is normally absent from the dark-coloured specimens (Figure 3-5), which are typically uniformly dark, though occasional specimens display alternating dark/bleached colour variation. Dark to opaque specimens may also have a greasy lustre which may be related to diagenesis of organic matter.

A working hypothesis arises from this: the light translucent brachiopods which display likely growth-related colour banding are better preserved than the dark opaque specimens, including those with alternating dark/bleached banding. This can be tested by more detailed analyses later in the protocol but, if correct, would be the basis for assembling samples for bulk analyses.

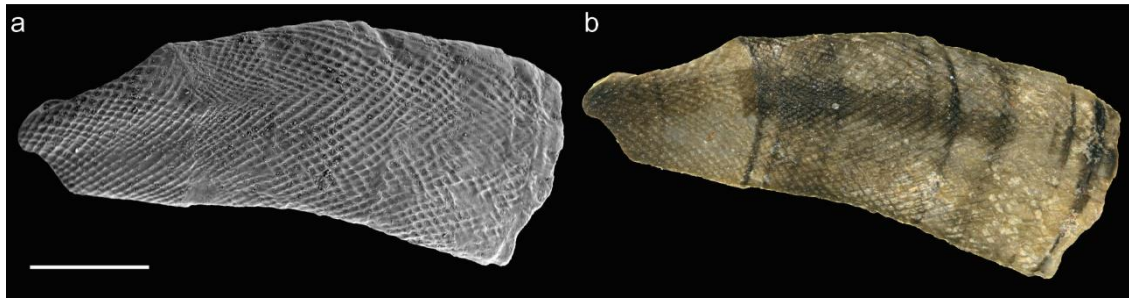


Figure 3-6. The ornament of *Rhombocorniculum* is well-preserved on most specimens from the Comley Limestones. Specimen La2Rh06. (a) SEM image; (b) IFM image displaying colour banding. Scale bar 500 μm .



Figure 3-7. IFM images of light- (a - c) and dark-coloured (d - f) *Rhombocorniculum* specimens. Light-coloured specimens may preserve transverse colour bands. All scale bars 200 μm . Specimens: (a) La2Rh06; (b) La2Rh07; (c) La2HRh01; (d) La2Rh01; (e) La2Rh02; (f) La2HRh22.

Rhombocorniculum

The eponymous rhombohedral ornament of *Rhombocorniculum* is well-developed on most specimens and is readily discernible under a binocular microscope (Figure 3-6). Many of the Comley Limestones *Rhombocorniculum* specimens are also fractured and fragmentary, with both the base and tip frequently missing. Many specimens are sharply fractured and have well-preserved external ornamentation. However, some specimens have rounded fractures and smoothed surfaces which may grade into poorly preserved ornamentation, indicating a prolonged history of pre-burial abrasion on the seafloor.

Rhombocorniculum specimens can also be readily divided into dark- and light-coloured specimens (Figure 3-7). Light coloured *Rhombocorniculum* are typically light to medium grey in colour, whereas the dark specimens vary from dark grey to deep black. Some specimens have transverse colour bands which are orthogonal to the



Figure 3-8. *Rhombocorniculum* specimens stained orange/brown, presumably with iron and/or manganese oxides. Specimens: (a) La2HRh28; (b) La2RhL03. Scale bars = 200 μm

growth direction of the sclerite and may reflect some form of growth banding. Most specimens are dull in lustre, though some of the darkest, black-coloured, specimens have a greasy lustre (Figure 3-7e). Although colour banding is found on both light and dark specimens, it has not been observed on the darkest specimens. The light/dark colouring across *Rhombocorniculum* specimens is inconsistent: some specimens are solely light or dark, whilst others have an outer layer of dark phosphate enclosing light-coloured layer, and *vice versa*. It remains unclear what causes this colour variation.

There is a further subset of specimens which are stained dark orange or light brown (Figure 3-8), likely by iron or manganese oxide precipitates. Stained specimens can still retain evidence of colour banding (Figure 3-8b), perhaps indicating superficial rather than pervasive chemical alteration. Orange/brown staining was also found on internal fractures in some light-coloured specimens (Figure 3-7b), suggesting that fractures act as loci of chemical alteration. A hypothesis to be tested by more detailed analyses in this protocol is that light-coloured *Rhombocorniculum* specimens without a greasy lustre and perhaps displaying transverse colour banding are better preserved than dark coloured and/or stained specimens.

Torellella

Torellella specimens are preserved as thick-walled tubes, pale blue-grey to beige-grey in colour, with near-concentric laminations seen in cross-section picked out by darker



Figure 3-9. *Torelrella* specimens from the Comley Limestones. Note the external transverse lineations (b, d) and internal laminations (c, e). Specimens: (a) LbTo25; (b) SaTo11; (c) La2To01; (d) SaTo02; (e) SaTo07. Scale bars = 200 μ m.

and lighter layers (Figure 3-9). Irregular pseudocircumferential lineations were found on the outside of the tube wall, which are faint but discernible under optical microscopy (Figure 3-9). Both the lineations and internal laminations probably record somewhat irregular growth as a result of laying down thin bands of phosphate at and around the aperture, though the precise relationship these structures bear to *Torelrella* ontogeny remain unresolved. Faint lineations notwithstanding, most specimens have an unornamented exterior surface.

In a similar manner to *Rhombocorniculum* sclerites, *Torelrella* tubes may be stained orange or brown, particularly along internal fractures (Figure 3-10), further suggesting that internal fractures act as loci for diagenetic mineralisation in the Comley Limestones. A few specimens are marred by bulges and/or irregular pits with characteristic sizes of 100s μ m. The bulges may be growth deformities or a diagenetic feature and require further investigation. The pits may be drill-holes from micro-predation that was sometimes successful, and sometimes not. Similar traces are known from specimens of the related hyolithelminth *Hyolithellus*, so this is not a taxon-specific phenomenon.

The majority of *Torelrella* specimens from the Comley Limestones are preserved as thick-walled, internally laminated, light blue-grey tubes or fragments of tubes with regular surfaces, i.e. lacking pits and bulges, and with fine lineations on their external surface (Figure 3-9). These were interpreted as being better preserved than the less



Figure 3-10. *Torelrella* specimens stained orange/brown, presumably with iron and/or manganese oxides. Note the locus of staining along fractures. Specimens: (a) LbTo13; (b) SaTo25. Scale bars = 200 μ m.

common beige-grey specimens which typically have thinner walls. Blue-grey specimens without obvious secondary mineral staining were considered suitable to take forward as candidate well-preserved SSFs.

3.8.2. Microstructure

Linguliformean brachiopods

The thin weakly mineralised linguliformean brachiopod primary layer was not observed in any specimens from the Comley Limestones. Light-coloured translucent specimens preserve couplets of compact and porous laminae (Figure 3-11). The porous laminae of these specimens were either virgose to rubbly or purely non-mineralised layers (c.f. Schmahl *et al.* 2008) which may host clay particles (Figure 3-12). Unequivocal bacculate lamination was not found, consistent with the hypothesis that eobolids characterise the ancestral linguloid brachiopod porous laminae state having rubbly or virgose laminae (Cusack *et al.* 1999).

Dark-coloured specimens of linguliformean brachiopods from the Comley Limestones commonly preserve similar couplets to those seen in translucent specimens (Figure 3-11). Rarely, botryoidal fabrics, appearing brighter under BSE imaging, were observed disrupting both compact and porous laminae (Figure 3-13). Botryoidal fabrics were more commonly found in porous laminae, or at the edges of compact laminae. The variable degree of microstructural preservation in dark-coloured specimens suggests

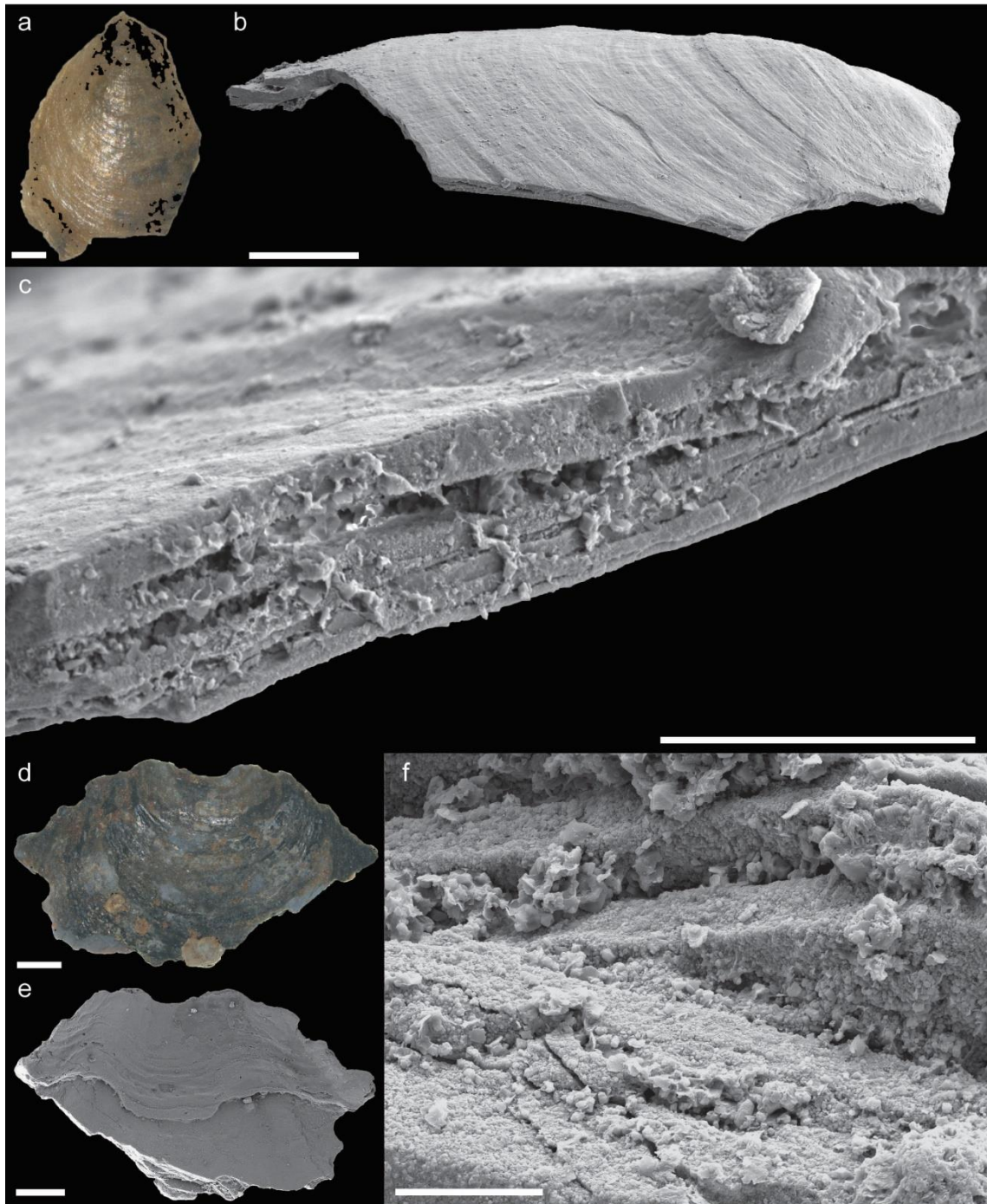


Figure 3-11. Laminar microstructure is preserved in both light- (a to c) and dark-coloured (d to f) brachiopods. Specimens: SaBr04 (a to c); La2Br09 (d to f). Scale bars: (a, b, d, e) = 200 μm ; (c, f) = 20 μm .

that they have been subjected to variable degrees of alteration, in some cases causing coarse recrystallisation and/or the precipitation of secondary phosphate.

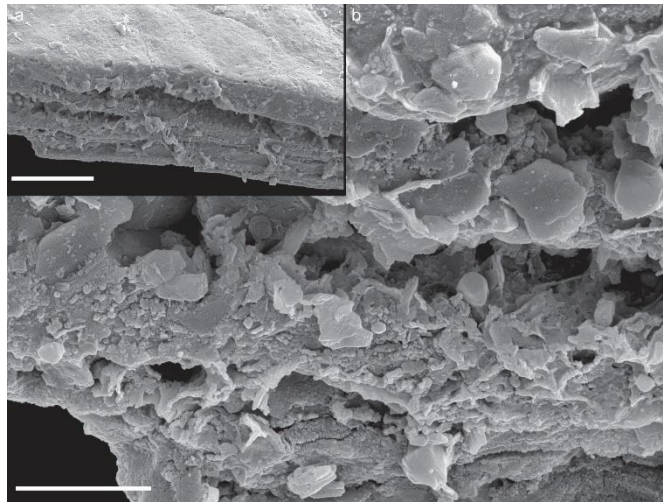


Figure 3-12. (a) Laminar structure. (b) Close-up of (a) showing compact and porous laminae, with large flakes of authigenic clay minerals in porous laminae. Specimen: SaBr04. Scale bars: (a) = 20 μm ; (b) = 5 μm .

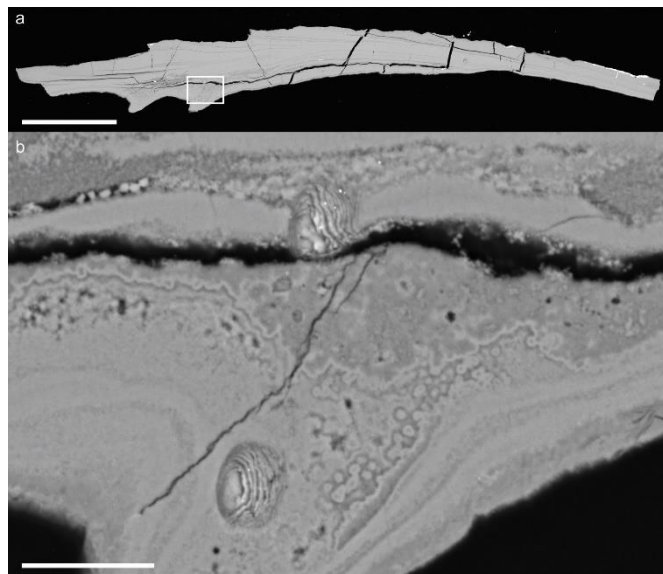


Figure 3-13. Botryoidal fabrics at the compact/porous layer boundary, seen in a specimen embedded in resin. Specimen: AaBrL07. Scale bars: (a) = 200 μm ; (b) = 20 μm .

Rhombocorniculum

All light-coloured, and most dark-coloured, *Rhombocorniculum* specimens from the Comley Limestones that were examined exhibited the packed-straws microstructure typical of the genus (Figure 3-14). These specimens also generally lack evidence for extensive secondary phosphate filling the tubules, which has been documented elsewhere and initially led to mis-interpretation of the microstructure of *Rhombocorniculum* (Kouchinsky *et al.* 2015). However, some of the dark-coloured specimens showed evidence for extensive secondary phosphate infilling the tubules

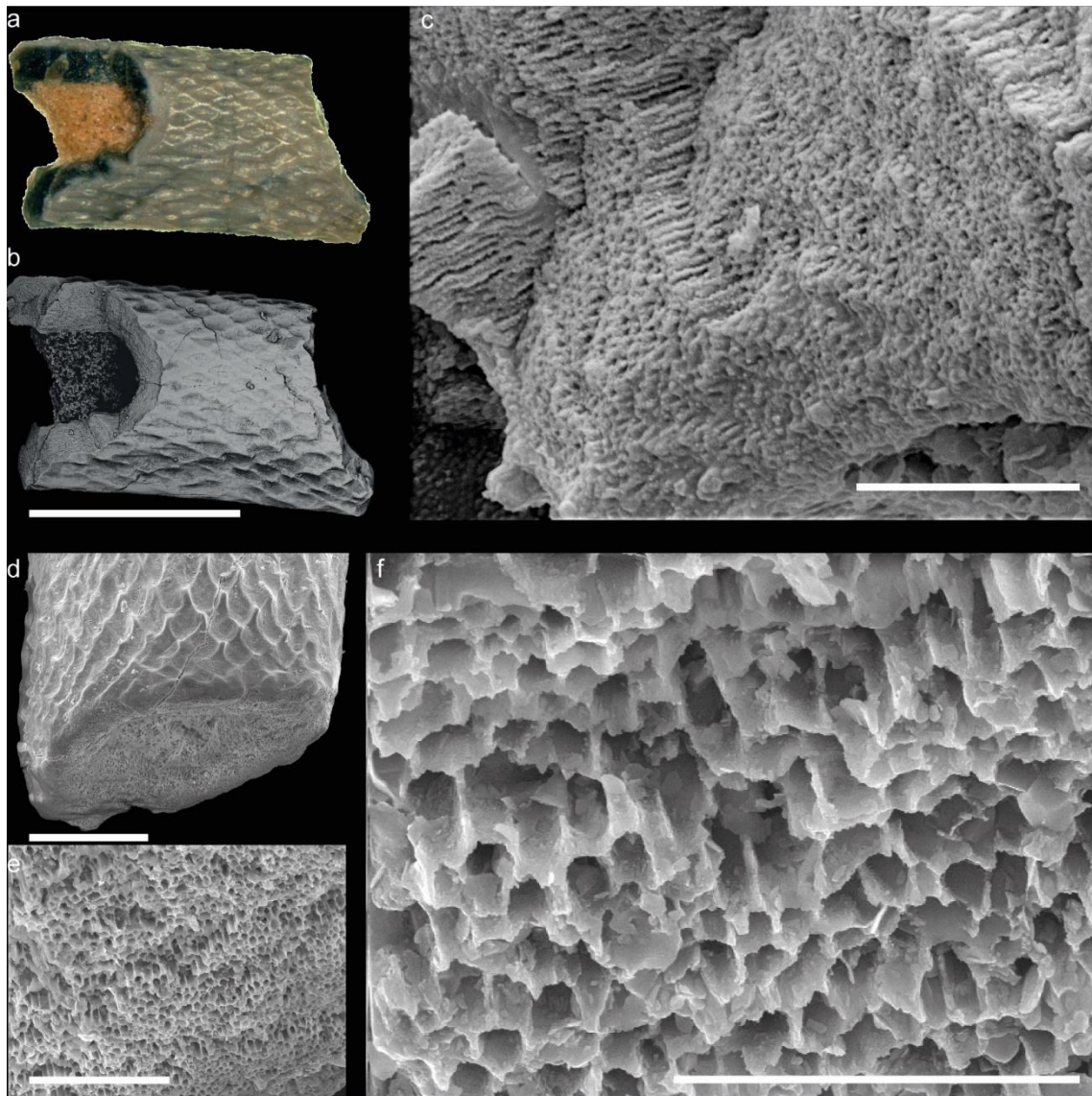


Figure 3-14. Packed-straws structure of *Rhombocorniculum*. (a) IFM colour image; (b) SEM image; (c) close-up of the packed-straws structure in the dark phosphate of the fractured wall of specimen VaRh02. (d to f) SEM images of the tubules in the wall at the base of specimen CCRh02. Scale bars (a, b) = 500 μm ; (c, e) = 20 μm ; (d) = 100 μm ; (f) = 10 μm .

(Figure 3-15). At the microstructural level there are no sample-level differences between the dark- and light-coloured specimens identified by optical microscopy.

Torellella

Optical and SE imaging of *Torellella* revealed laminations in the tube walls of specimens from the Comley Limestones (Figure 3-16). Laminae are less clear under SE than optical imaging, but are particularly well picked out by high-contrast BSE imaging. This suggests that there is little compositional variation between laminae. The observed laminae are sub-parallel to the internal edge of tube walls and do not appear to truncate each other or bifurcate within the tube wall. The internal edge of the tube wall is also

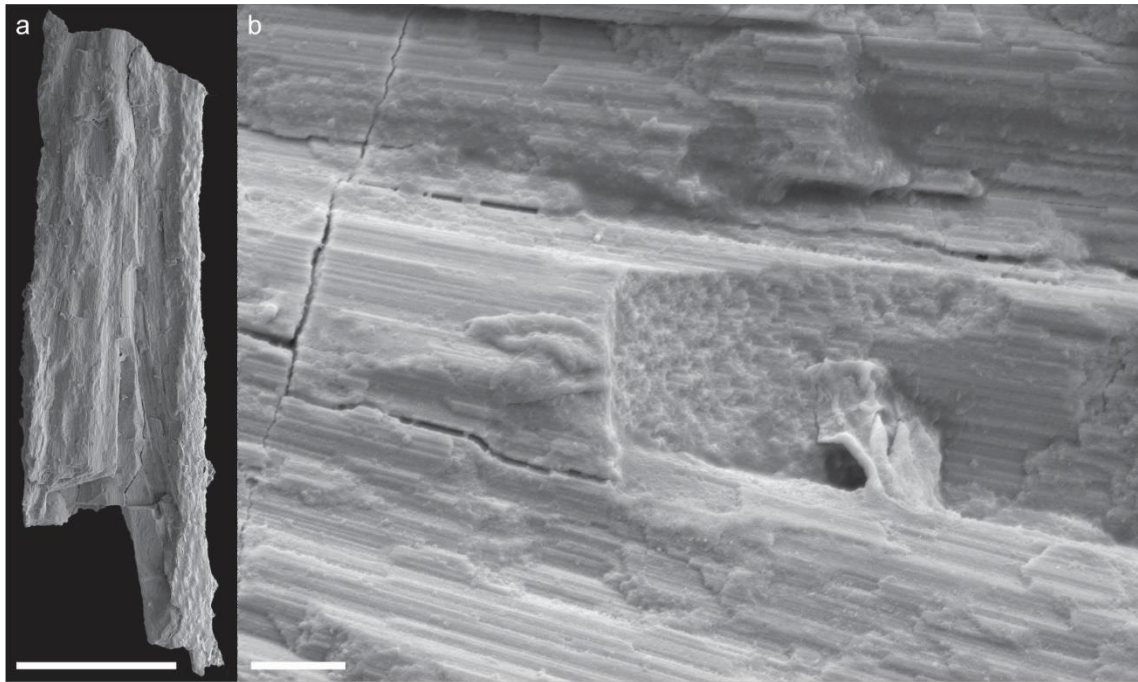


Figure 3-15. Phosphatised tubules of a dark-coloured *Rhombocorniculum* sclerite. The tubules visible in well-preserved specimens have been filled here with secondary phosphate. Specimen La2Rh01. Scale bars (a) = 500 μm ; (b) = 20 μm .

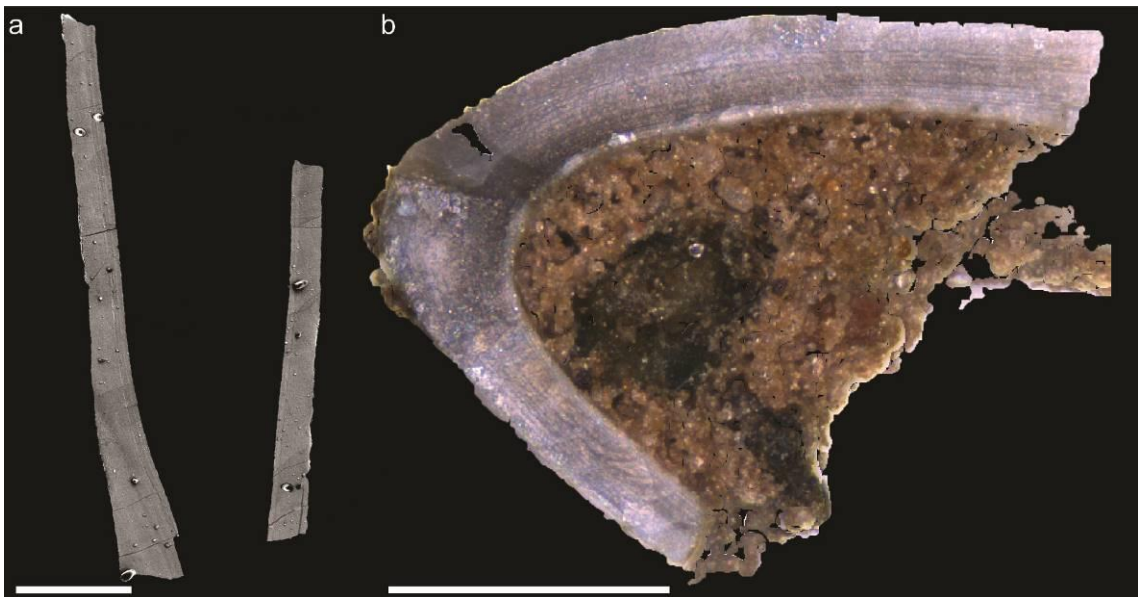


Figure 3-16. Laminations in the walls of *Torelrella* tubes are less clear under SEM analysis (a) than optical microscopy (b). Specimens: (a) La2To06; (b) SaTo07. Scale bars = 200 μm .

slightly more porous than the rest of the wall, and this region is prone to small fractures developing perpendicular to the wall edge (Figure 3-17a, b).

Polished surfaces cut through bulges observed in some *Torelrella* tube walls showed that the cause of bulging was new mineral growth between biogenic laminae (Figure 3-17c, d). The biogenic laminae were plastically deformed around the new phosphate growth, suggesting that the tubes were still flexible when the secondary

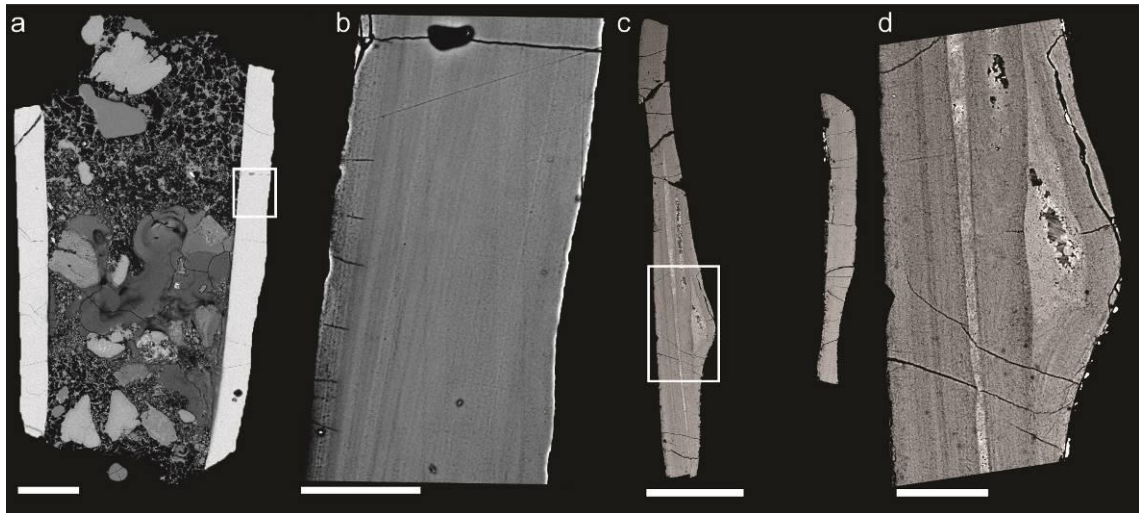


Figure 3-17. BSE images of aberrations in the tube walls of *Torelrella*. (a, b) fracture development in the more porous innermost laminae of the tube wall. (c, d) section through a bulge in the tube wall show growth of brighter secondary phosphate plasticly deforming biogenic laminations. (a, b) LbTo03; (c, d) LbTo44. Scale bars: (a, c) = 200 μm ; (b, d) = 50 μm .

phosphate formed, and therefore that it is likely to be very early diagenetic in origin, at or close to the sea floor. The new phosphate growth is brighter under BSE imaging, indicating a higher degree of crystallinity compared to the biogenic material.

3.8.3. Ultrastructure

Linguliformean brachiopods

High resolution SEM imaging of linguliformean brachiopods from the Comley Limestones showed that the compact laminae of light-coloured brachiopod specimens comprised densely packed spherules 10s nm to 100 nm in diameter (Figure 3-18), and closely resembling the ultrastructure of modern *Lingula* (Schmahl *et al.* 2008). However, where compact/porous laminae couplets were preserved in opaque brachiopods from the Comley Limestones, high resolution SEM imaging showed that the compact laminae comprised micron-scale prismatic and rod-shaped crystallites (Figure 3-19). In one case, sub-micron-scale prismatic crystals were also observed within the compact laminae of translucent specimens. This suggests that some of the translucent specimens may have been subjected to minor, but not pervasive, recrystallisation. There may be an ultrastructural basis for the distinction between translucent and opaque specimens.

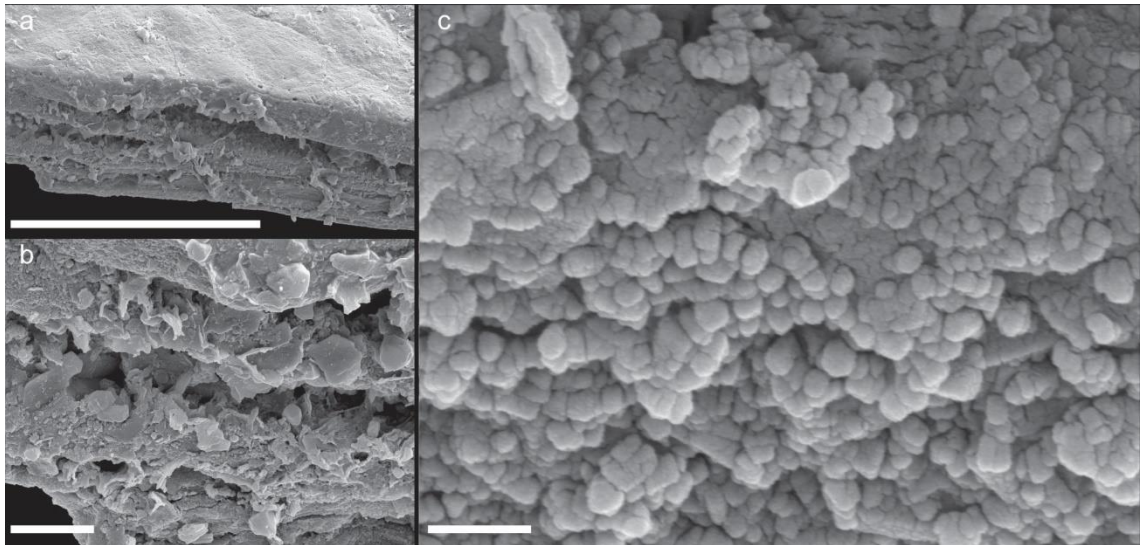


Figure 3-18. Light-coloured linguliformean brachiopods in the Comley Limestones typically preserve compact laminae of densely-packed sub-micron phosphatic spherules. (a, b) Laminar microstructure; (c) spherular ultrastructure. Specimen SaBr04. Scale bars: (a) = 50 μm ; (b) = 5 μm ; (c) = 500 nm.

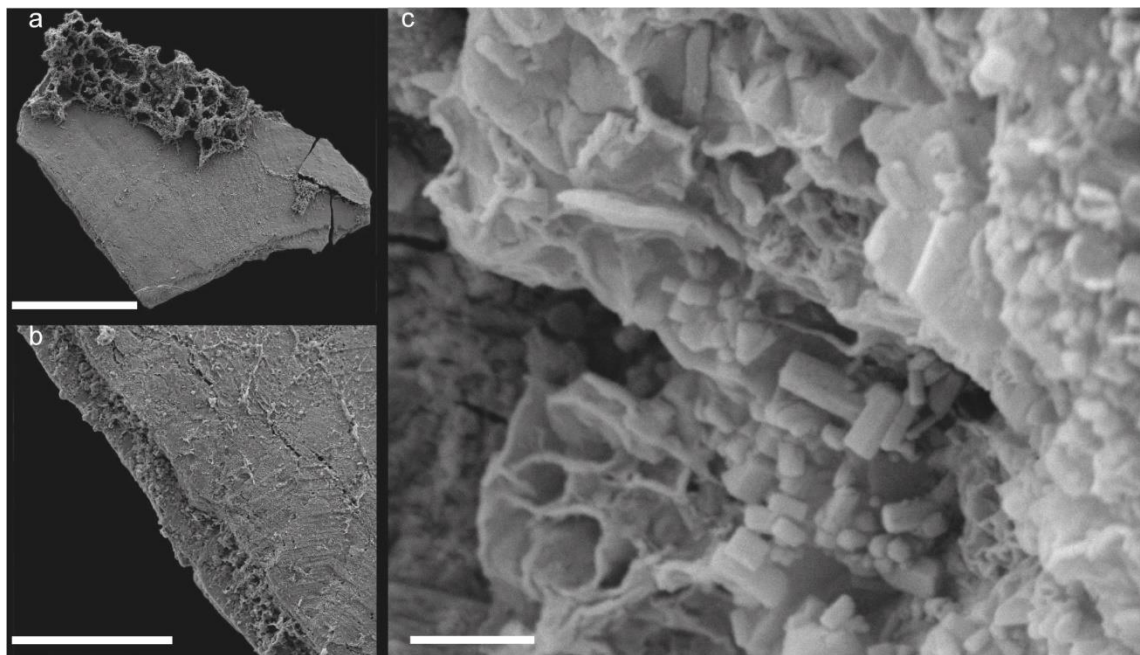


Figure 3-19. Dark-coloured linguliformean brachiopods in the Comley Limestones preserve compact laminae of densely-packed micron-scale prismatic phosphate crystals. (a, b) Laminar microstructure; (c) prismatic ultrastructure. Specimen SaBr78. Scale bars: (a) = 500 μm ; (b) = 100 μm ; (c) = 1 μm .

Rhombocorniculum

The ultrastructure of *Rhombocorniculum* is not well characterised in the literature. The crystallites of the tubule walls have not previously been described. Here, in light-coloured specimens, and dark-coloured specimens with well-preserved microstructure, sub-micron spherulitic crystallites were typically observed in the tubule walls (Figure

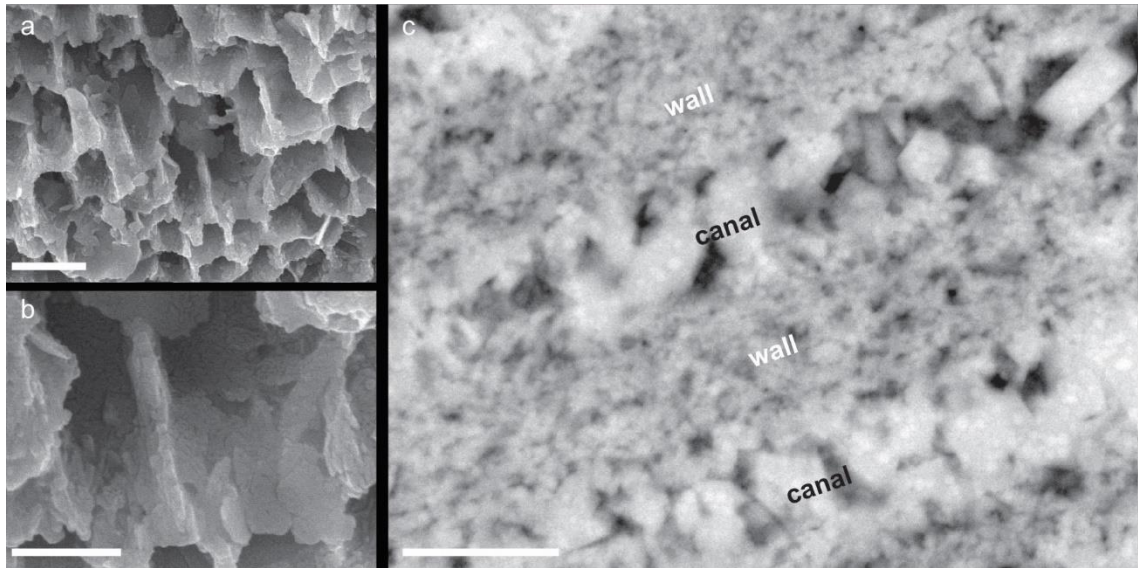


Figure 3-20. Ultrastructure of *Rhombocorniculum* in fractured (a, b) and polished (c) sections. Note the annealing of small crystallites into larger tabelets (b) and the prismatic crystallites precipitated in the canals of the *Rhombocorniculum* tubules. Specimens: (a, b) CCRh02; (c) La2HRh08. Scale bars: (a) = 2 μm ; (b, c) = 1 μm .

3-20). In some specimens these spherular crystallites have been caught in the act of annealing into platelet or tablet morphologies (Figure 3-20b). Strikingly, larger micron-scale prismatic crystals were found within the tubule cavities (Figure 3-20c). These likely formed from post-mortem apatite precipitation locally within the tubules, perhaps as the result of the degradation of organic matter that was hosted there. However, the tubule width of approximately 1 μm makes it unlikely that bacteria could have substantially exploited this organic matter. Therefore, this phosphate may have precipitated from interaction with pore waters and may reflect early diagenetic conditions.

Torellella

Light blue-grey *Torellella* specimens with walls that preserve laminae were found to comprise densely-packed phosphatic spherules (Figure 3-21a–c). The crystallites were comparable in size (50 nm to 100 nm) and morphology to those found in light-coloured linguliformean brachiopods (Figure 3-18) and are not disrupted by either outsized crystallites or crystallites of different morphologies. No evidence of the rod-like crystallites needed to form the plywood structure observed in *Hyolithellus* (Skovsted & Peel 2011) was found.

However, crystallites in the wall of one *Torellella* specimen were found to have recrystallized into randomly orientated prisms and tablets 10 nm to 500 nm in size (Figure 3-21d–f). This recrystallisation may be related to a thick black growth band in

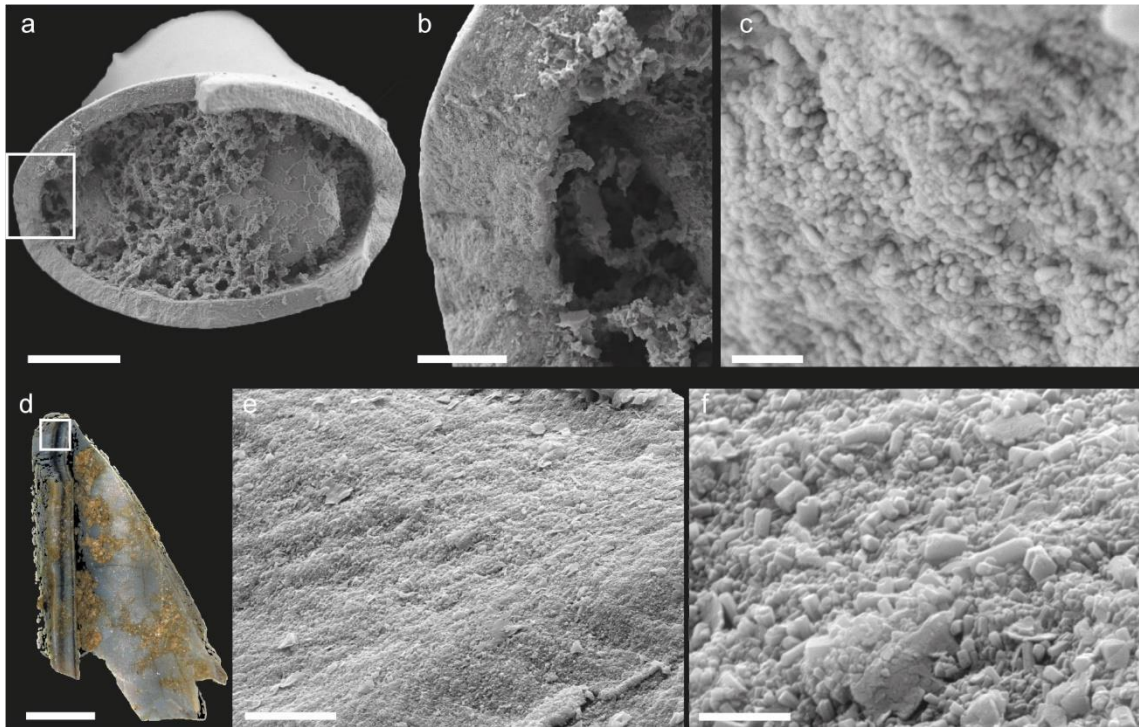


Figure 3-21. Ultrastructure of *Torellella* in fractured sections. Well-preserved apatitic spherular ultrastructure (a to c) and minor recrystallisation into sub-micron prisms and tablets associated with the thick dark layer. Note the very small crystallites in both specimens. Specimens: (a to c) LbTo55; (d to f) La2To01 Scale bars: (a, d) = 100 μm ; (b) = 20 μm ; (e) = 5 μm ; (c, f) = 1 μm .

the middle of the specimen which may have been a more organic-rich region during life and have acted as a catalyst for *in situ* recrystallization post-mortem.

3.8.4. Elemental composition

The results of qualitative EDS elemental analyses, mapping polished surfaces of through SSFs, are taxon-specific and are dealt with below. The taxon-specific results of quantitative EPMA elemental analyses are also presented below, but some general remarks about the whole data set can be made. Principal components analysis (PCA) of the Comley plus Durango data (Figure 3-22; Appendix A) separated specimens from the Comley Limestones and abiogenic Durango apatite along principal component axis 1 (PC1), though there was no significant difference between different samples. PC1 explains 30.5% of the variance, PC2 explains 23.5% of the variance, PC3 explains 11.5% of the variance, and PC4 explains 8.0% of the variance. The greatest separation on PC1 was between the light-coloured SSFs from the Comley Limestones and the abiogenic Durango apatites, and was significant at the 95% confidence interval (Figure 3-23). Whilst dark-coloured SSFs and Durango apatites were also separated along PC1, the 95% confidence ellipses slightly overlapped. When examined by taxon and hypothesised preservation (light or dark), light-coloured specimens of each taxonomic

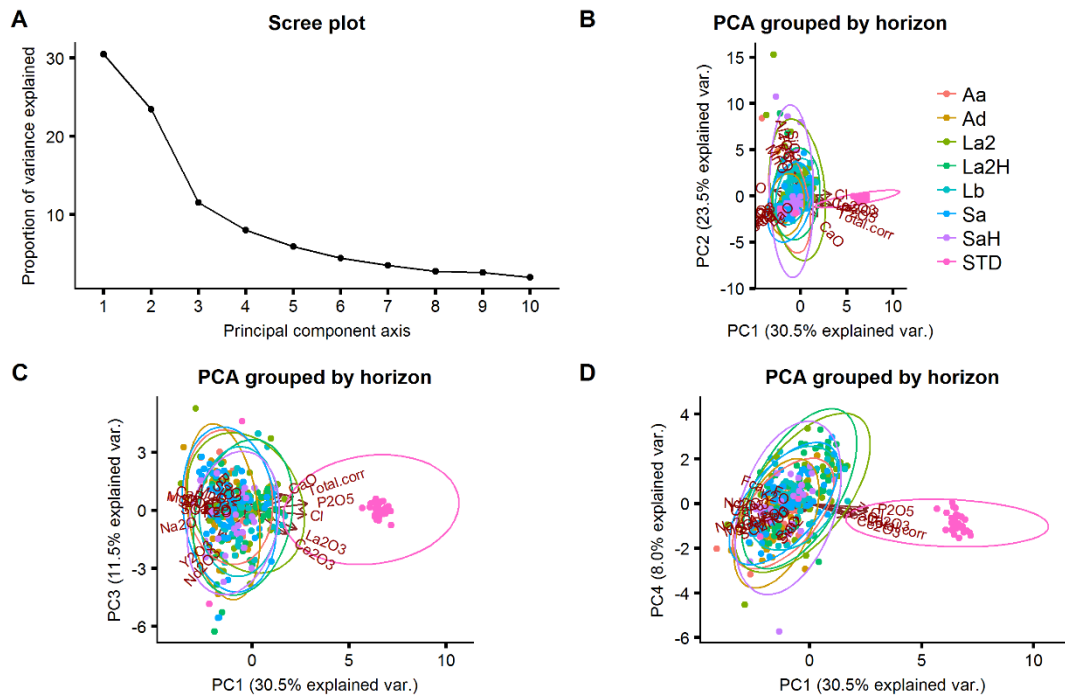


Figure 3-22. Principal components analysis of all Comley Limestones SSF EPMA data. Analysis grouped by horizon; STD = Durango standard apatite.

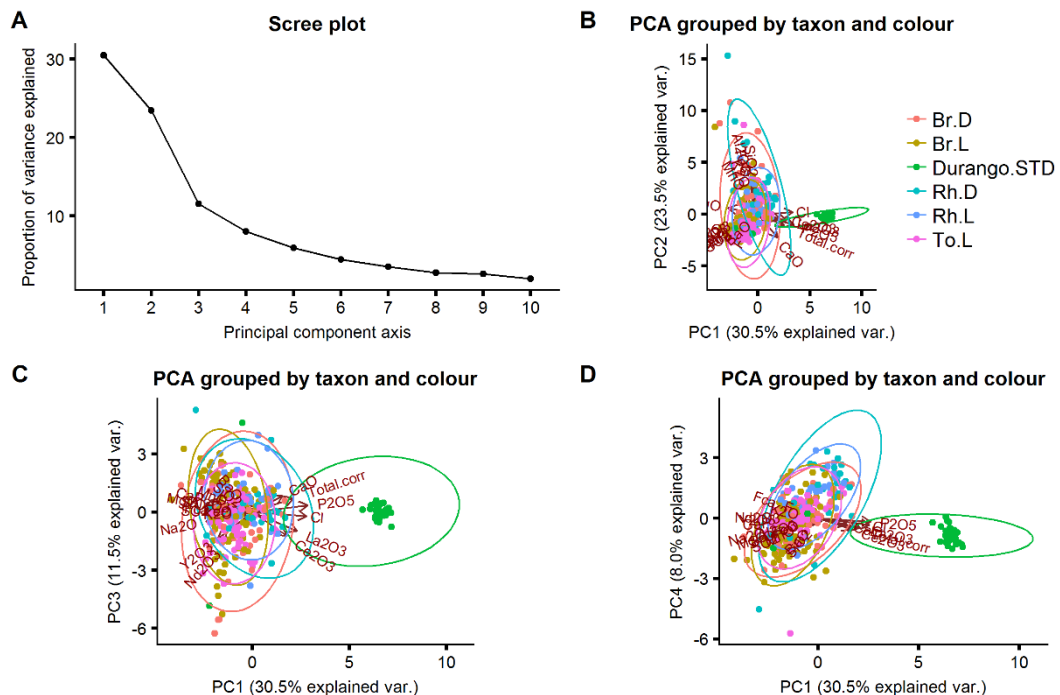


Figure 3-23. Principal components analysis of all Comley Limestones SSF EPMA data grouped by taxon and colour.

group plot in similar PCA space, as overlapping tight-knit groups separated from Durango apatite at the 95% confidence level. All dark-coloured specimens occupied wider areas of PCA space, with much of the additional spread along PC2, and shared a slight overlap at the 95% confidence interval with Durango apatite analyses.

The corrected total value, P₂O₅ wt%, Ce₂O₃ wt%, La₂O₃ wt%, and Cl wt% were strongly positively correlated along PC1, and moderately positively correlated with CaO wt%. These variables were strongly negatively correlated with MgO wt% along PC1, and weakly negatively correlated with Na₂O wt%, Y₂O₃ wt%, and Nd₂O₃ wt%, among other oxides. MgO wt% was strongly negatively correlated with these oxides on PC1. SiO₂, FeO, Al₂O₃, MnO and K₂O were strongly positively correlated on PC2, while F is moderately positively correlated. This suggests that elements indicative of severe diagenetic alteration, particularly Fe and Mn, are not correlated with the main apatite-forming elements and that these may record the growth of new minerals rather than recrystallisation of biogenic apatite in a closed system.

Linguliformean brachiopods

EDS analyses were used to examine the spatial distribution of major and some minor elements, including the distribution of transition metals associated either with uptake from seawater or from later diagenetic or meteoric fluids. EDS maps of the light-coloured linguliformean brachiopods show that elements indicative of diagenetic or meteoric alteration, including iron, silicon and manganese, were restricted to porous laminae and were not found in compact laminae (Figure 3-24a). However, in dark-coloured opaque specimens, minor elements indicative of diagenetic and meteoric alteration could be pervasive throughout both porous and compact laminae (Figure 3-24b). In both light- and dark-coloured specimens, higher concentrations of elements indicative of diagenesis were found around internal fractures, providing further support for these fractures acting as loci for alteration.

A PCA of quantitative elemental EPMA separates linguliformean brachiopods from abiogenic Durango apatites at the 95% confidence interval along PC1 (Figure 3-25). PC1 explained 39.3% of the variance, PC2 explained 21.4% of the variance, PC3 explained 11.1% of the variance, and PC4 explained 5.8% of the variance. Light-coloured brachiopods plotted as a tight cluster within the space occupied by dark-coloured specimens. This suggests that one of the effects of diagenetic alteration is an increase in the variability of chemical compositions across a sample. Interestingly, Ca and Mn were strongly negatively correlated with each other, suggesting that Mn may be replacing Ca in altered specimens. Analyses of the dark-coloured brachiopods were shifted slightly towards the Durango apatite data along PC1 with respect to the light-coloured specimens, but this is not statistically significant.

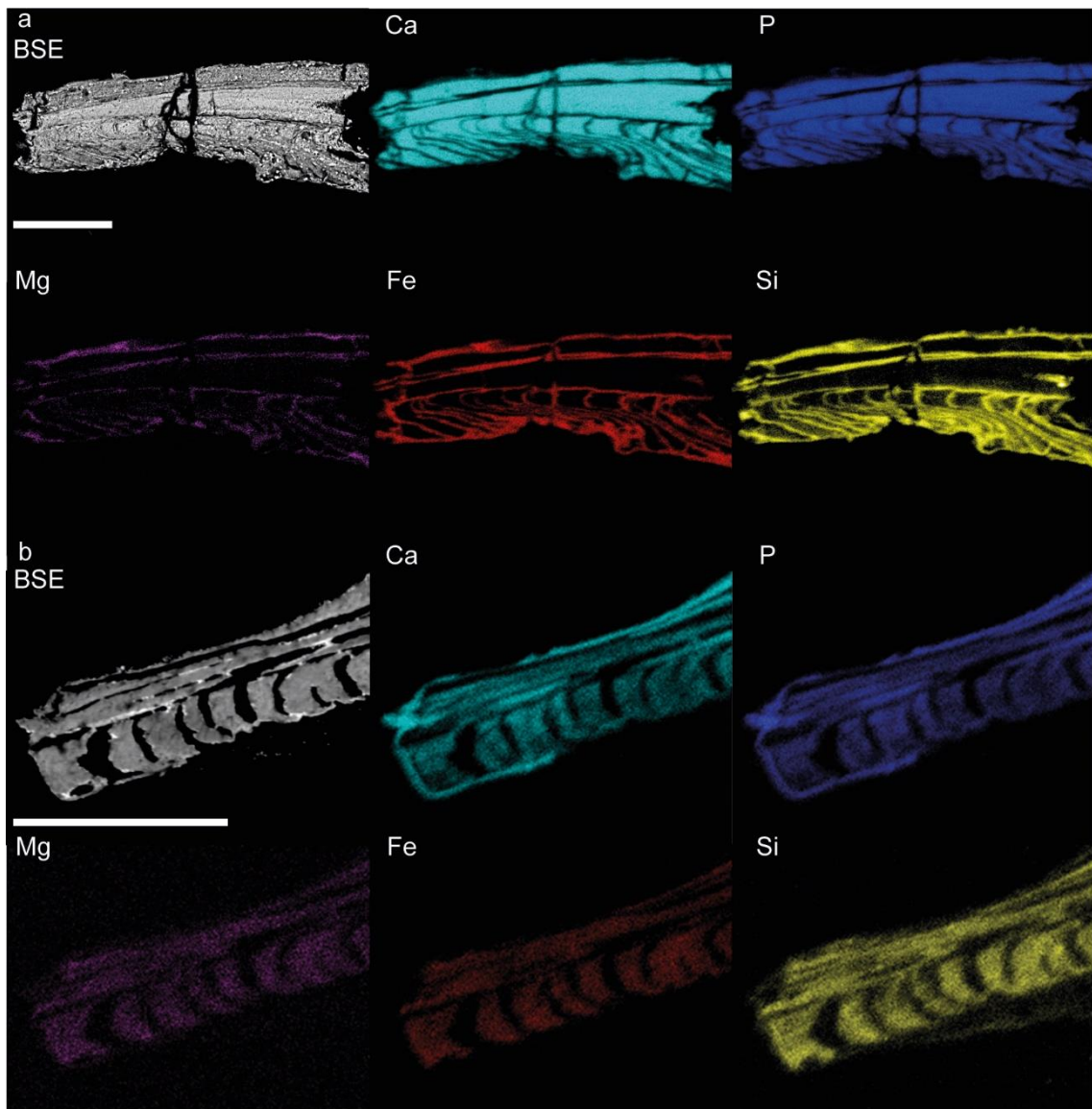


Figure 3-24. EDS maps through the laminar hinge regions of (a) light and (b) dark brachiopods from the Comley Limestones. Specimens: (a) La2Br07; (b) La2HBr08. Scale bars = 50 μm .

In general, compared to dark-coloured brachiopod specimens, light-coloured brachiopods had higher mean concentrations of elements associated with biogenic phosphate, such as Ca, Mg, Na and Sr (see Appendix A). Conversely, the mean values of Fe, Mn, and Ce were lower in light-coloured specimens than dark-coloured specimens. F concentrations were also higher in light-coloured specimens than dark-coloured specimens. These differences were observed in paired samples of light- and dark-coloured brachiopods from the same horizon.

The enrichment of dark-coloured brachiopods in Fe and Mn suggests that they have been subject to a greater degree of chemical alteration during diagenesis than have light-coloured brachiopods. This is also supported by the higher concentration of REEs, particularly Nd and Ce, in dark-coloured specimens. REE uptake is a common feature

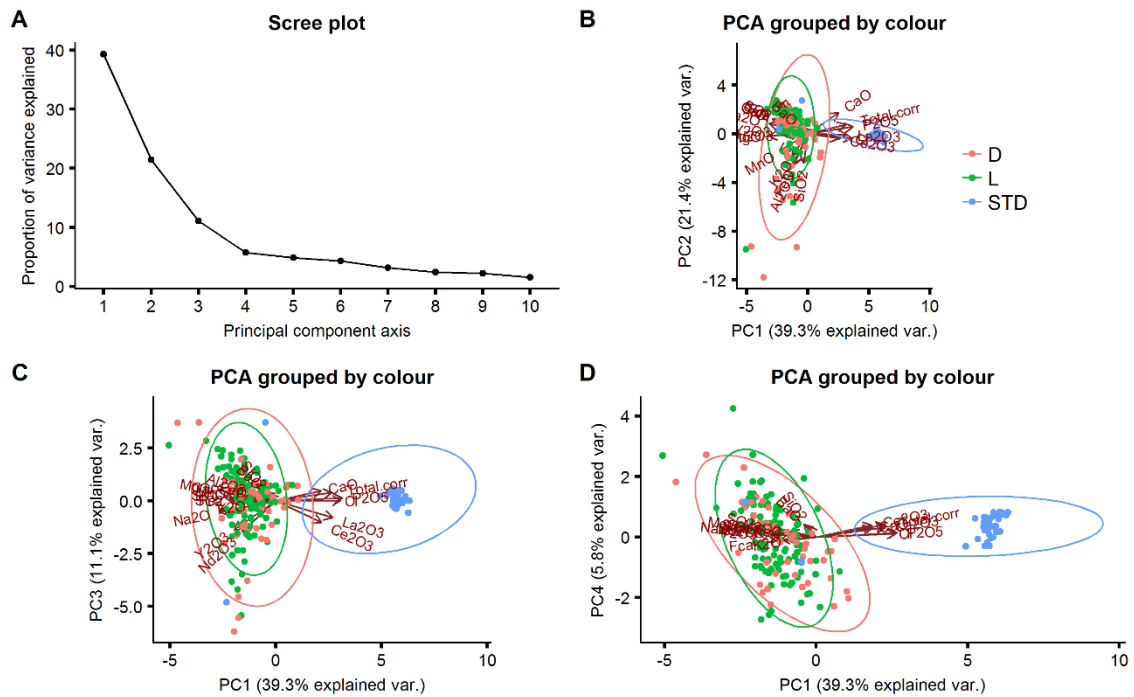


Figure 3-25. Principal components analysis of all Comley Limestones brachiopod EPMA data grouped by colour.

of early diagenetic alteration of phosphates (Grandjean-Lécuyer *et al.* 1993), particularly whilst on the seabed or near the top of the sediment pile.

Rhombocorniculum

EDS analyses were used to examine the spatial distribution of major and some minor elements, including the distribution of transition metals associated either with uptake from seawater or from later diagenetic or meteoric fluids. In most specimens of *Rhombocorniculum* that preserve biogenic microstructures, elements indicative of diagenetic alteration, including Fe, Si and Mn, are focused around fractures through the sclerite walls (cf. Figure 3-7b), and to the material filling the central lumen (Figure 3-26a) which likely derives from the surrounding sediment.

In some *Rhombocorniculum* specimens, the central lumen has a phosphatic infill which was detected under both binocular microscopy and SEM-EDS analysis (Figure 3-26b). SEM-EDS analysis shows that the phosphatic material infilling the central lumen is more highly crystalline and chemically closer to a pure apatite than the phosphatic walls of *Rhombocorniculum*. Specimens with a secondarily phosphatised lumen show signs of more pervasive diagenetic alteration, such as elevated Fe content in the sclerite wall (Figure 3-26b). This phosphatic infill is clearly abiogenic, and is likely to be early diagenetic in origin, precipitating before the sclerite lumen could be

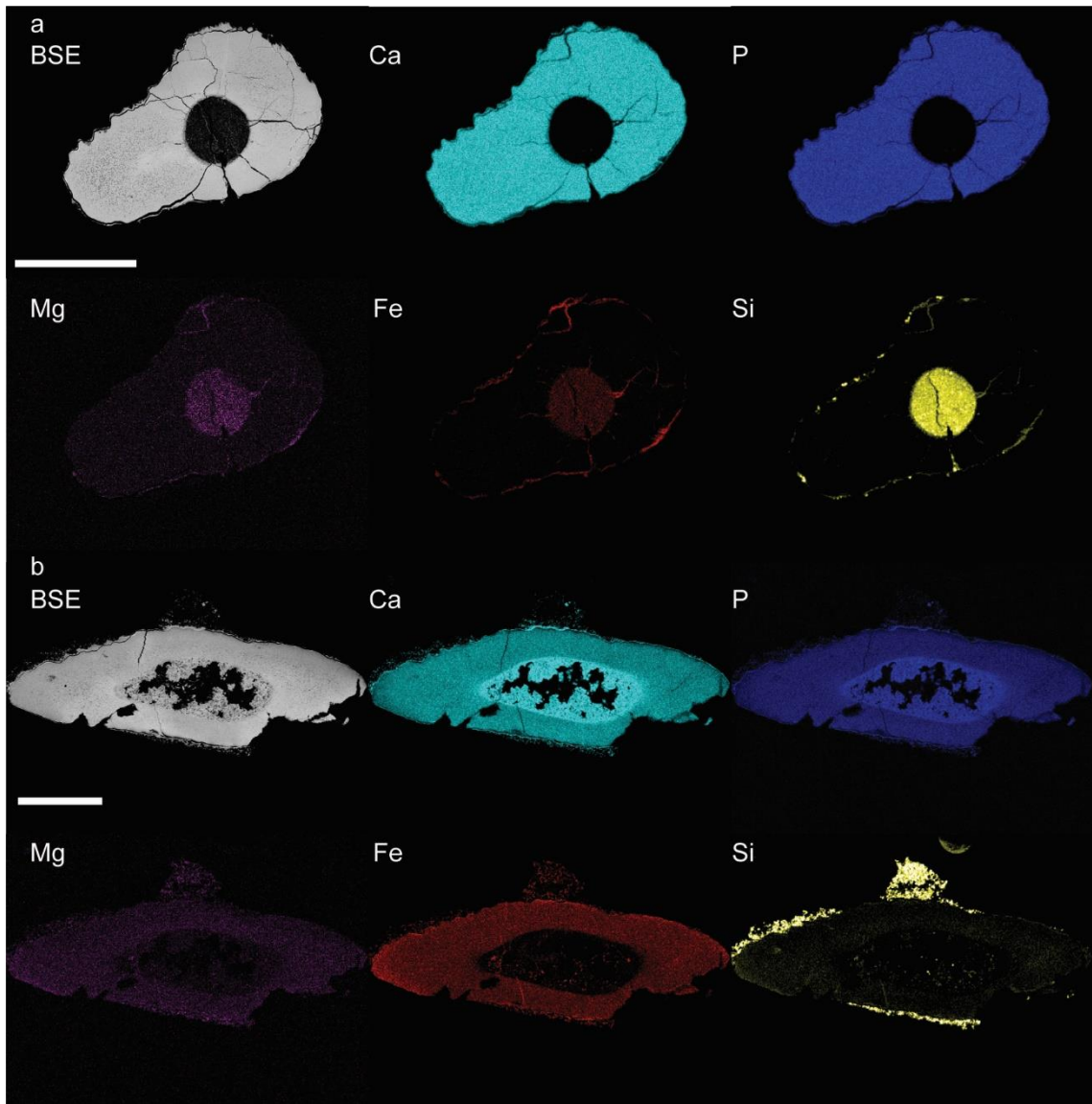


Figure 3-26. EDS maps of cross sections through *Rhombocorniculum* specimens without (a) and with (b) a phosphatised lumen. BSE = backscattered electron image. Specimens: (a) La2HRh12; (b) La2HRh15. Scale bars = 200 μ m.

filled with surrounding sediment. This phosphatic infill may therefore record very early diagenetic conditions and may have formed in contact with Cambrian sea water.

Principal components analysis of *Rhombocorniculum* EPMA data revealed similar patterns to that of the linguliformean brachiopods. Light-coloured *Rhombocorniculum* specimens were separated from abiogenic Durango apatites at the 95% confidence interval along PC1, but there was a slight overlap at the 95% confidence interval of the dark-coloured specimens and abiogenic Durango apatite (Figure 3-27). PC1 explained 43.6% of the variance, PC2 explained 21.2% of the variance, PC3 explained 9.1% of the variance, and PC4 explained 7.3% of the variance. Light-coloured specimens plotted in a tight cluster within the PCA space occupied by dark-coloured specimens. This

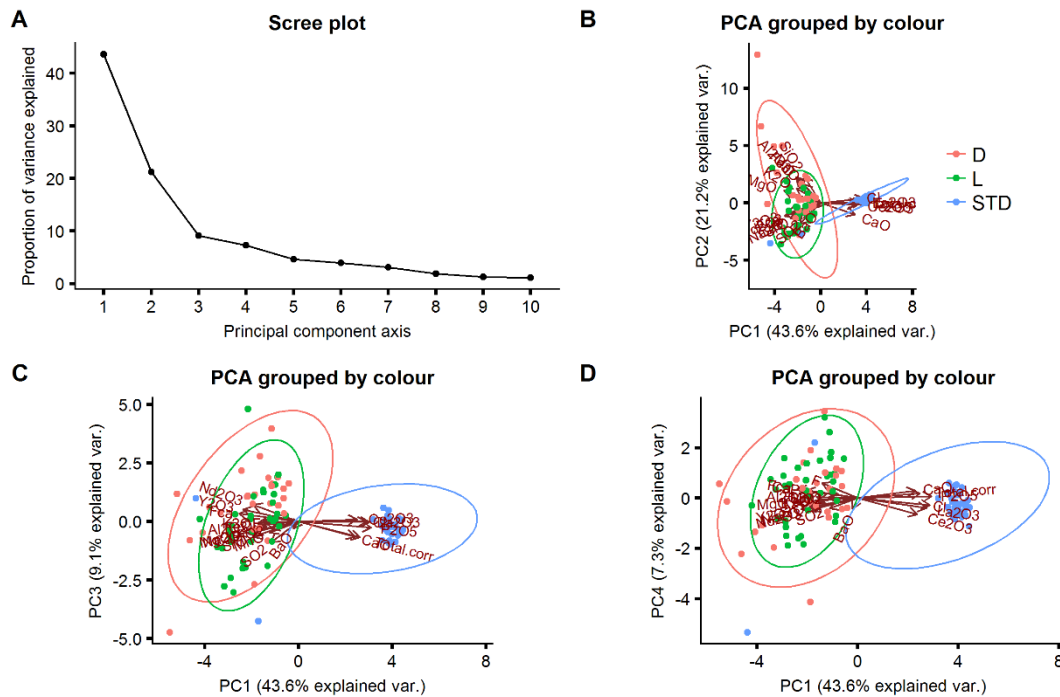


Figure 3-27. Principal components analysis of all Comley Limestones *Rhombocorniculum* EPMA data grouped by colour.

supports the earlier observation that one of the effects of diagenetic alteration is an increase in the variability of chemical compositions across a sample. As with the linguliformean brachiopods, Ca and Mn oxides were strongly negatively correlated with each other, supporting the interpretation that Mn may have replaced Ca in the lattice of altered specimens. Analyses of dark-coloured *Rhombocorniculum* specimens were slightly shifted towards the abiogenic Durango apatite data on PC1.

In general, light-coloured *Rhombocorniculum* specimens had higher Ca:P, Mg:P, Na:P and Sr:P ratios, but lower Al:P, Fe:P and Mn:P ratios than their dark-coloured counterparts from the same horizon (see Appendix A). The exception is that light-coloured specimens from La2 and La2H have lower Mg:P ratios, and light-coloured specimens from La2 and SaH had lower Na:P ratios than their dark-coloured counterparts. This general observation, that elements associated with seawater and biogenic apatite were concentrated in light-coloured specimens and elements associated with diagenesis were concentrated in dark-coloured specimens, further supports the interpretation that these two groups reflect well-preserved and altered biogenic phosphate, respectively.

Torellella

Similar to the *Rhombocorniculum* specimens, EDS analyses of light blue/grey *Torellella* specimens showed that internal fractures were loci of diagenetic or meteoric alteration

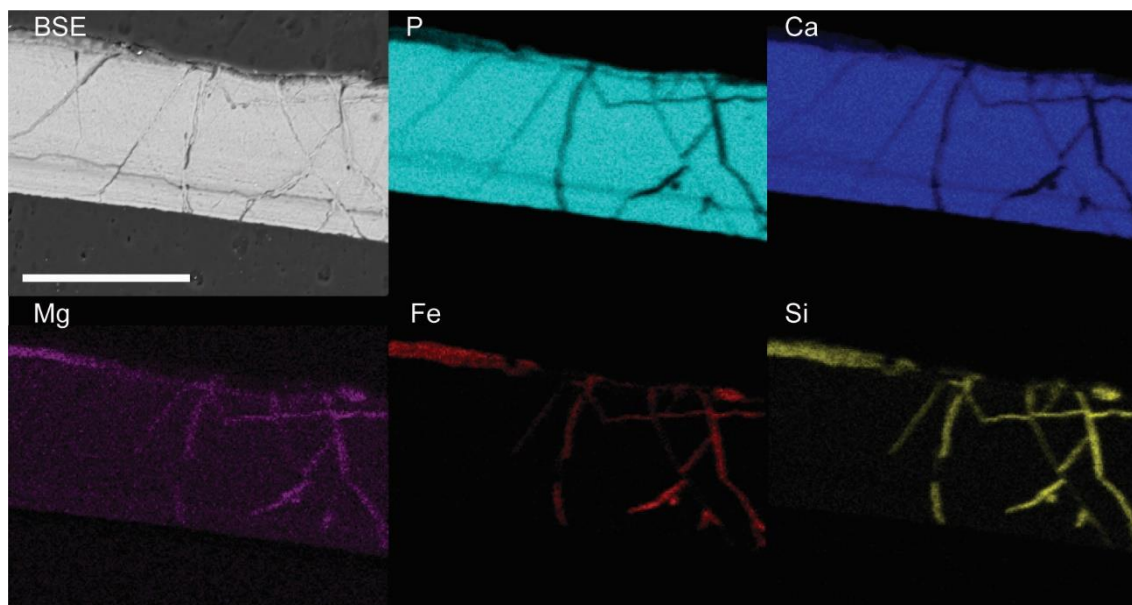


Figure 3-28. EDS maps of a cross section through a *Torelrella* tube. Specimen La2To06. Scale bar = 60 μm . Fractures act as loci for elements indicative of diagenetic alteration.

(Figure 3-28). This is consistent with the patterns of orange and brown staining, focused around internal fractures, which is seen in some of these specimens. Elements indicative of diagenetic alteration, such as Fe and Mn, were not found within main body of the walls.

Quantitative elemental EPMA also demonstrated that the biogenic *Torelrella* specimens are significantly different from the abiogenic apatite standards at the 95% confidence interval (Figure 3-29). PC1 explained 55.9% of the variance, PC2 explained 18.1% of the variance, PC3 explained 6.8% of the variance, and PC4 explained 4.2% of the variance. All *Torelrella* specimens quantitatively analysed were considered to be pristine following the other stages of this protocol. The elemental chemistry of *Torelrella* specimens was similar to that of the pristine brachiopods in PCA space, with no significant separation by horizon (see Appendix A). In particular, *Torelrella* specimens from horizons Aa, Lb, and Sa form very tightly clustered groups that are significantly separated from the Durango standards along PC1. Interestingly, specimens from horizon La2 show the greatest variability along PC1. Some specimens from La2 were found, under ultrastructural analysis, to have undergone minor solid-state recrystallization (Figure 3-20). This may be reflected in the greater elemental variability seen here, as it is for dark-coloured brachiopod and *Rhombocorniculum* specimens.

Specimens from horizon La2 which have been subject to heavy liquid separation (La2H) form a subset within the La2 *Torelrella* data that was chemically offset towards the Durango standards along PC1 and with increased variability along PC2. Specimens

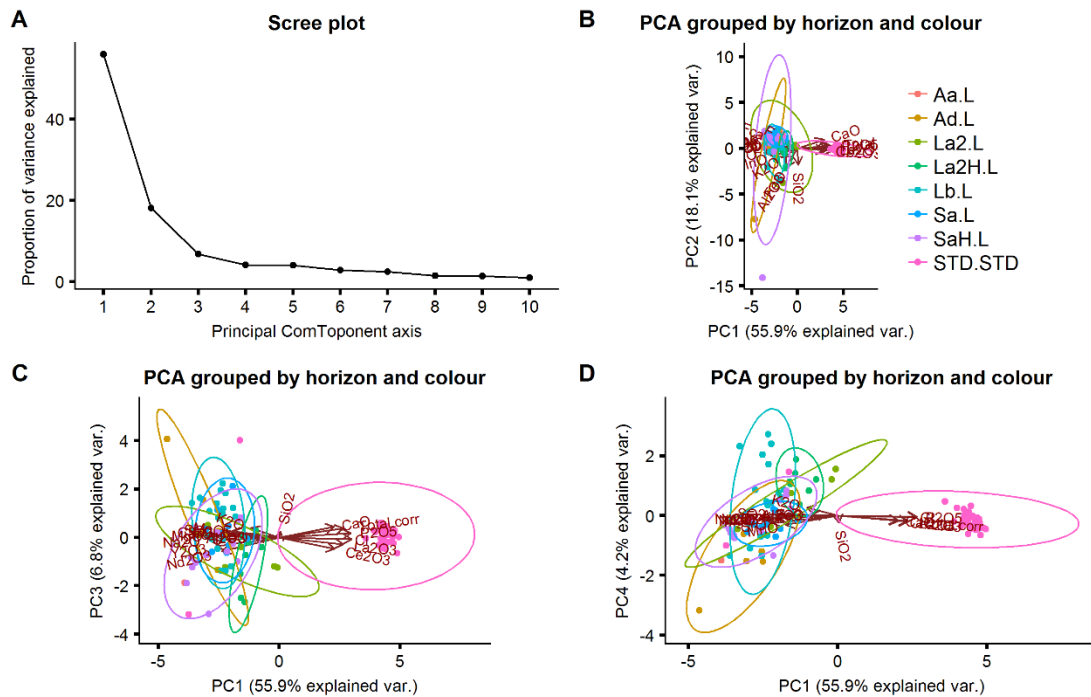


Figure 3-29. Principal components analysis of all Comley Limestones *Torellella* EPMA data grouped by horizon and colour.

from horizon Sa which have been subjected to heavy liquid separation (SaH) also showed increased variability along both PC1 and PC2 compared to Sa specimens that had not been heavy liquid separated (Figure 3-29). This suggests that chemical, as well as $\delta^{18}\text{O}$ (Wheelely *et al.* 2012), alteration occurs during the heavy liquid separation process.

3.9. Beyond the Comley Limestones

3.9.1. West Gondwana

The preservation state of linguliformean brachiopods from Ait Iyou in the High Atlas Mountains, Morocco (see §2.5), was also examined following the protocol outlined above. Similar to the Comley Limestones, the majority of these brachiopod specimens were lingulids, although some acrotretids were also found. Only horizon AI 202-a produced enough brachiopod specimens for isotopic analysis. The majority of these specimens were dark-coloured and opaque with a greasy lustre, although there were enough light-coloured translucent specimens to justify investigating the preservation state of these two optically distinct groups. However, in contrast to brachiopods from the Comley Limestones, the light-coloured specimens from Ait Iyou do not preserve growth lines as alternating light and dark colour bands.

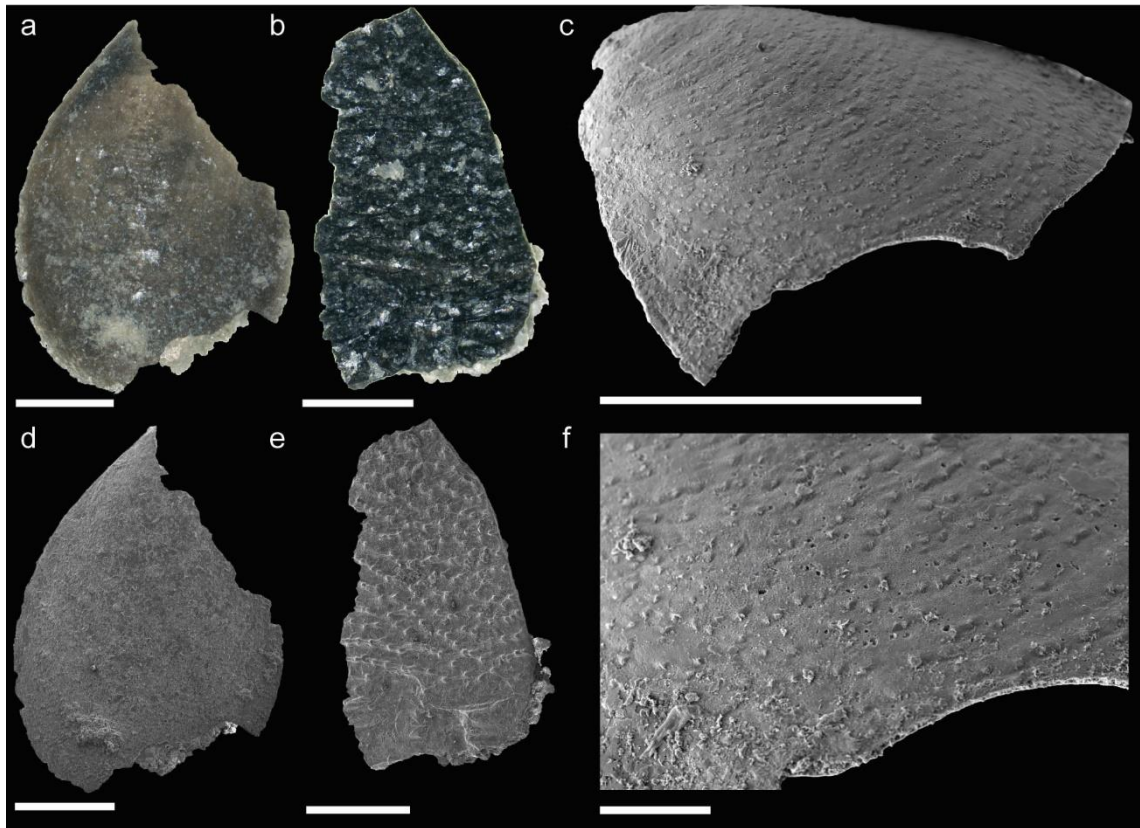


Figure 3-30. General morphology of brachiopods from Ait Iyou. Specimens: (a, d) AI202aBr25; (b, e) AI202aBr20; (c, f) AI202aBr01. Scale bars: (a to e) = 500 μm ; (f) = 100 μm .

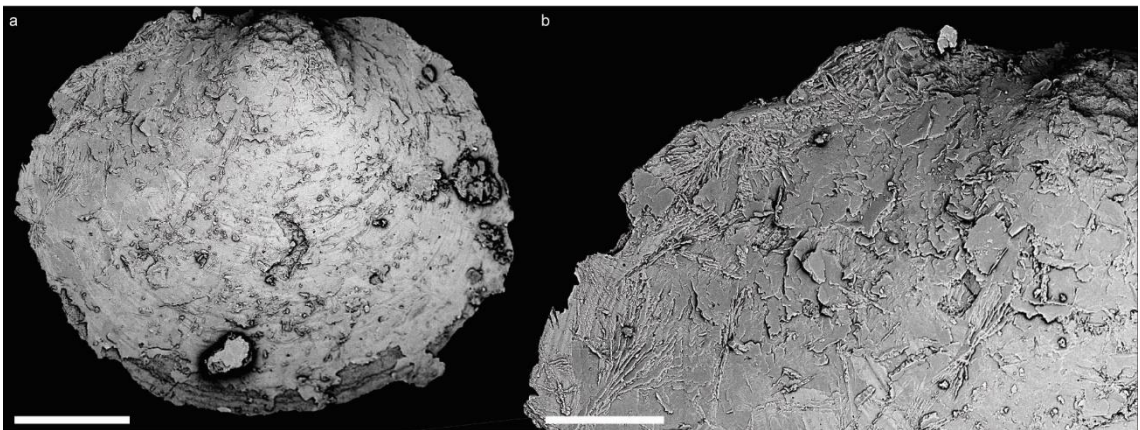


Figure 3-31. Recrystallised phosphatic tablets form the exterior surface of some of the Ait Iyou brachiopods. Specimen AI202aBr02. Scale bars: (a) = 200 μm ; (b) = 100 μm .

The gross morphology of the Moroccan lingulids is generally well preserved and includes growth lines, pustulose ornamentation, and pores in the brachiopod shell (Figure 3-30). Recrystallisation can be pervasive, however, with the external ornamentation of some brachiopod shells obscured by large tablet and blade-like phosphate crystals (Figure 3-31). Alternating compact and porous laminae are preserved in some, but not all, of the Ait Iyou brachiopod specimens (Figure 3-33). In one light-

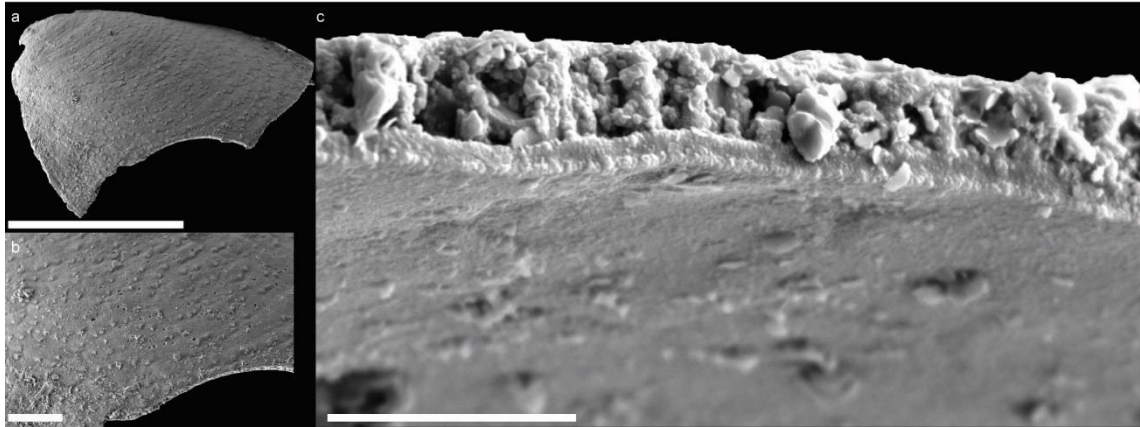


Figure 3-32. Recrystallised columnar microstructure of porous lamina of a brachiopod from Ait Iyou. Specimen AI202aBr01. Scale bars: (a) = 500 µm; (b) = 100 µm; (c) = 20 µm.

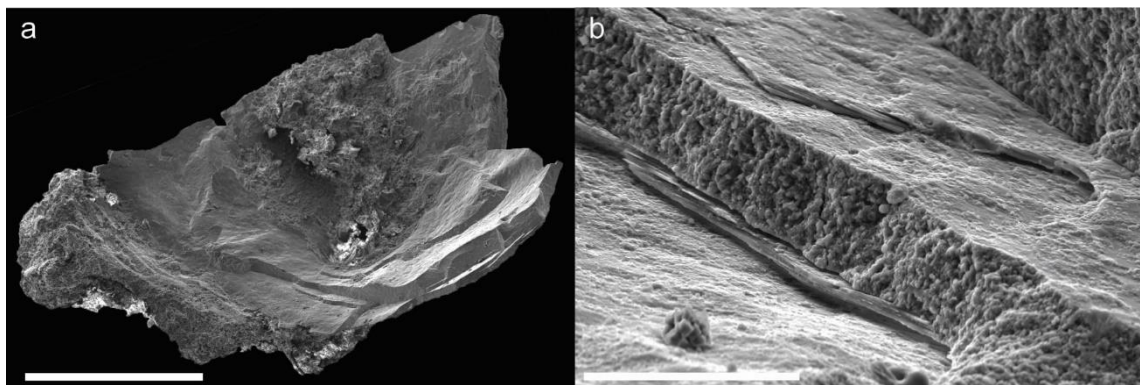


Figure 3-33. Prismatic crystals in the porous laminae of this brachiopods from Ait Iyou. Specimen AI202aBr21. Scale bars: (a) = 500 µm; (b) = 20 µm

coloured translucent brachiopod, a columnar layer between two compact laminae was observed (Figure 3-32), though secondary phosphate can be seen filling in the gaps between columns, almost obscuring the original microstructure in places. However, in the majority of dark-coloured specimens, and in some light-coloured specimens, the shell wall has recrystallised to a thick blocky texture with little or no evidence of biogenic laminations preserved. In the majority of specimens from Ait Iyou, biogenic microstructures have been overprinted by crude recrystallisation. Similarly, biogenic ultrastructure is not preserved in the brachiopod specimens from Ait Iyou. Compact laminae, and where present the columnar textures between compact laminae, comprise prismatic apatite crystallites.

Brachiopod specimens from Ait Iyou are chemically intermediate between abiogenic standard material and specimens from the Comley Limestones. The main separation occurs along PC1, which explained 38.5% of the variance (Figure 3-34). The Ait Iyou lingulid brachiopods overlap in PCA space at the 95% confidence interval with both dark-coloured Comley Limestones brachiopods and the abiogenic Durango apatite,

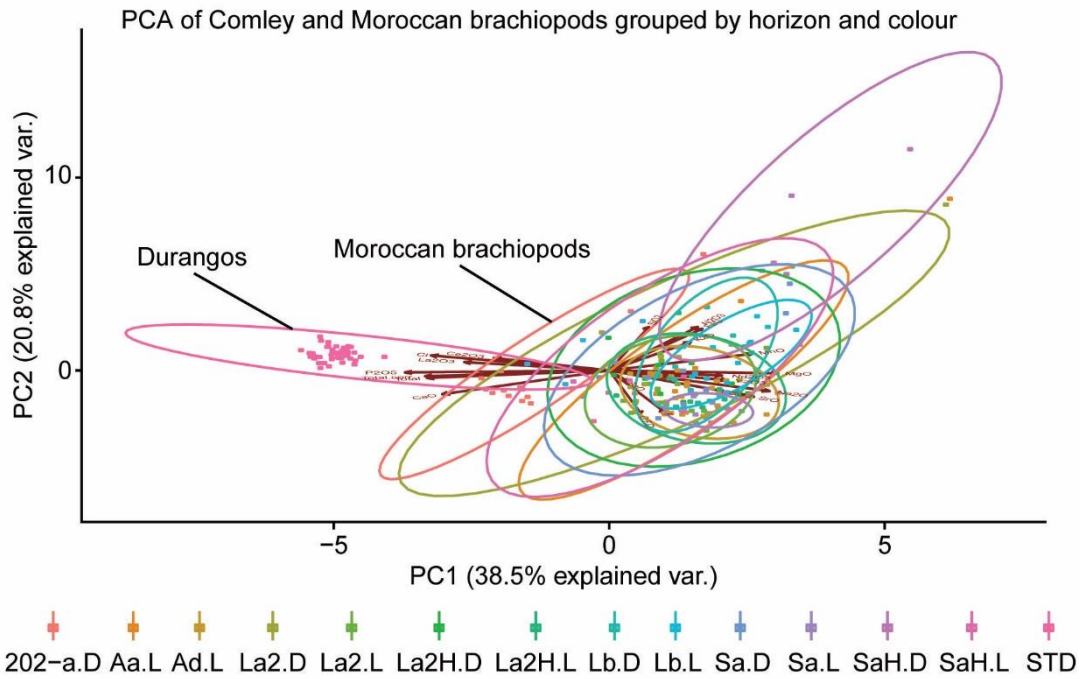


Figure 3-34. Principal components analysis of all Moroccan and Comley Limestones SSF EPMA data grouped by horizon and colour.

but the Ait Iyou specimens are significantly different from light-coloured specimens from the Comley Limestones. These are therefore more severely chemically altered than the dark brachiopods of the Comley Limestones, corroborating the microstructural and ultrastructural observations above.

3.9.2. *Laurentia*

Linguliformean brachiopods were recovered from samples collected in June 2017 from the Forteau Formation, Newfoundland and Labrador, Canada (see §2.6). Specimens from the Forteau Formation were examined following a shortened form of the detailed protocol above as time constraints prevented a more comprehensive investigation. The results for these specimens should therefore be considered preliminary.

The majority of the brachiopods have well-preserved gross morphology, including growth lines and external ornamentation (Figure 3-35a, b; Figure 3-37a; Figure 3-36a, b). Similarly to brachiopods from the Comley Limestones, brachiopods from the Forteau Formation can be subdivided under binocular microscopy on grounds of visual appearance. Visually well-preserved specimens are light-coloured and translucent, whereas visually altered specimens are dark-coloured and opaque, often with a greasy lustre.

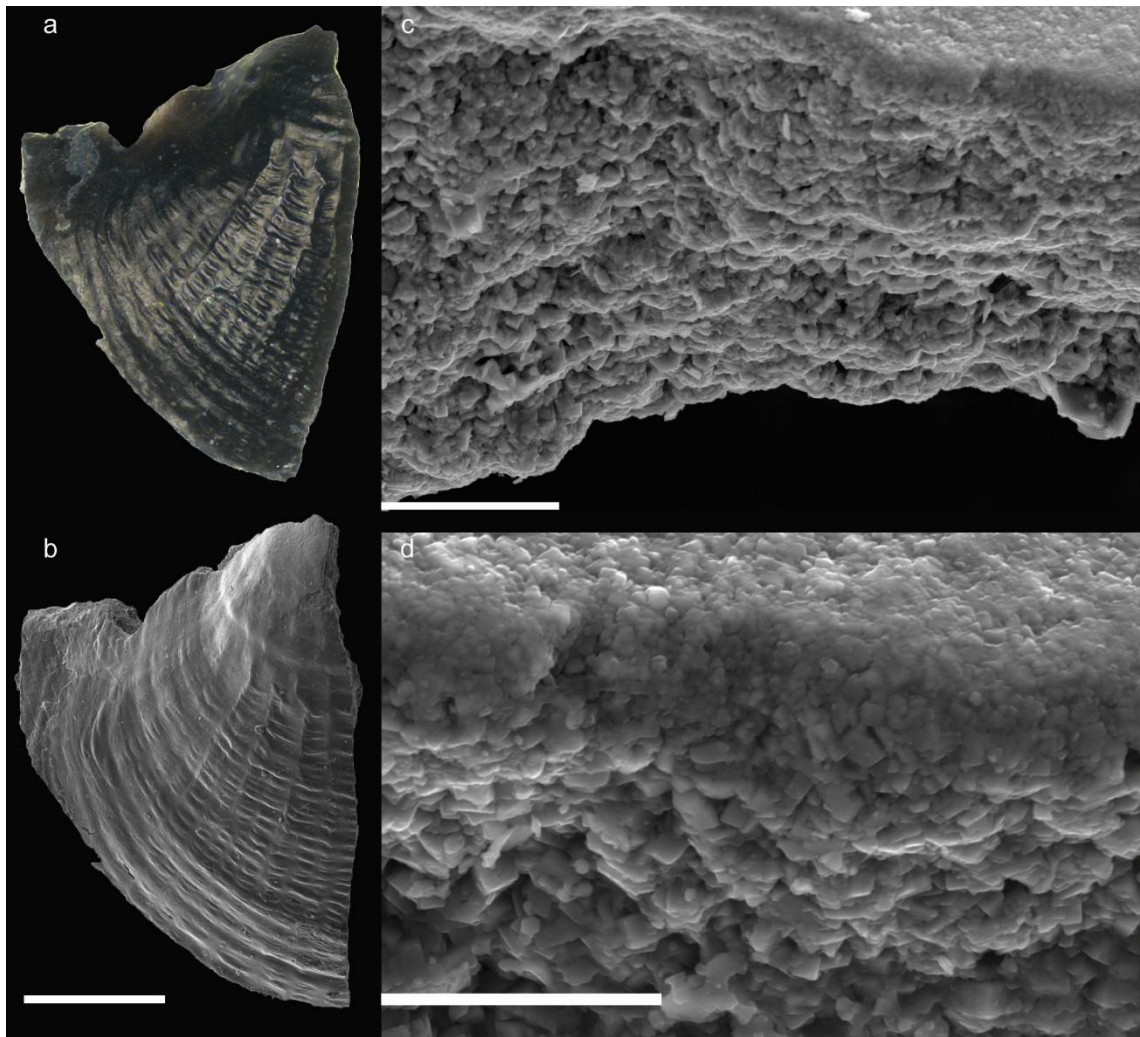


Figure 3-35. Dark-coloured brachiopod from the Forteau Formation, with well-preserved gross morphology (a, b), but lacking clear lamination (c). The shell wall crystallites have begun to recrystallize into micron-scale prismatic apatite, though an upper layer of spherular crystallites remains (d). Specimen DMQBr02. Scale bars: (a, b) = 200 μm ; (c) = 10 μm ; (d) = 5 μm .

Dark coloured brachiopods, hypothesised to be diagenetically altered, do not preserve a laminar microstructure and are commonly blocky in cross-section (Figure 3-35). Unlike in the Comley Limestones, many light-coloured translucent brachiopods from the Forteau Formation are also blocky in cross-section (Figure 3-37), although a few preserve a laminated microstructure (Figure 3-36).

However, there are differences in the ultrastructure of the dark- and light-coloured Forteau Formation brachiopods. Dark-coloured brachiopods typically comprise prismatic crystallites, densely packed and undifferentiated. In contrast, the ultrastructure of the light-coloured specimens is more nuanced. Light-coloured specimens that are blocky in cross-section comprise densely-packed aggregates of micron- or sub-micron-size phosphatic spherules. In laminated light-coloured specimens, the compact laminae comprise densely-packed aggregates of sub-micron phosphatic spherules. Notably, the

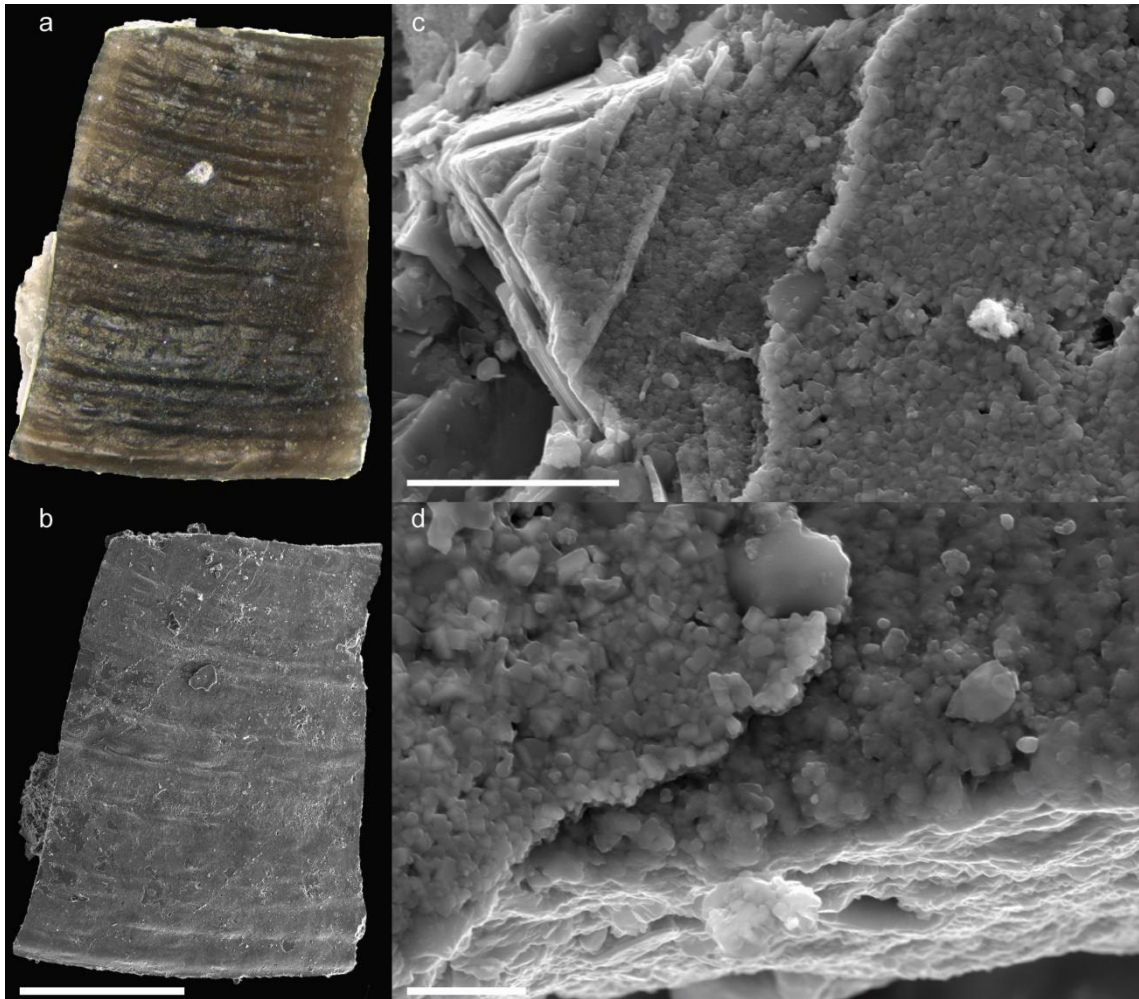


Figure 3-36. Light-coloured brachiopod from the Forteau Formation, with well-preserved gross morphology (a, b), and some evidence of biogenic lamination (c). The shell wall comprises sub-micron spherular crystallites (d). Specimen DMQBr11. Scale bars: (a, b) = 500 μm ; (c) = 5 μm ; (d) = 2 μm .

diagenetic phosphate of the bivalve moulds has a rubbly ultrastructure of angular crystallites up to a few microns in size (Figure 3-38).

In contrast to the application of the preservation protocol to specimens from the Comley Limestones, UK, and the Issafen Formation, Morocco, results from the Forteau Formation, Canada, are more equivocal. Microstructural preservation cannot be wholly assessed by optical microscopy in Forteau Formation specimens, and therefore these SSFs should be treated cautiously. However, at the ultrastructural level, there are consistent differences in crystallite morphology between dark- and light-coloured specimens. The phosphatic spherules of both the blocky and laminated light-coloured specimens are comparable to those found in modern linguliformean brachiopods (Cusack & Williams 1996; Williams *et al.* 2007; Schmahl *et al.* 2008) and in well-preserved specimens from the Comley Limestones (Figure 3-18; Figure 3-21). In

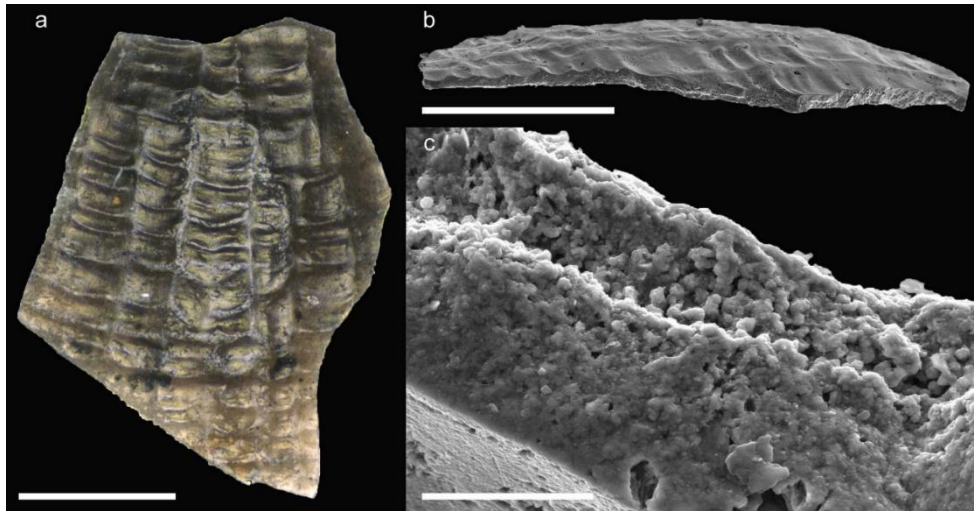


Figure 3-37. Light-coloured brachiopod from the Forteau Formation, with well-preserved gross morphology (a), but with a massive cross section (b, c). The shell wall comprises sub-micron spherular crystallites (c). Specimen DMQBr06. Scale bars: (a) = 200 μm ; (b) = 200 μm ; (c) = 10 μm .

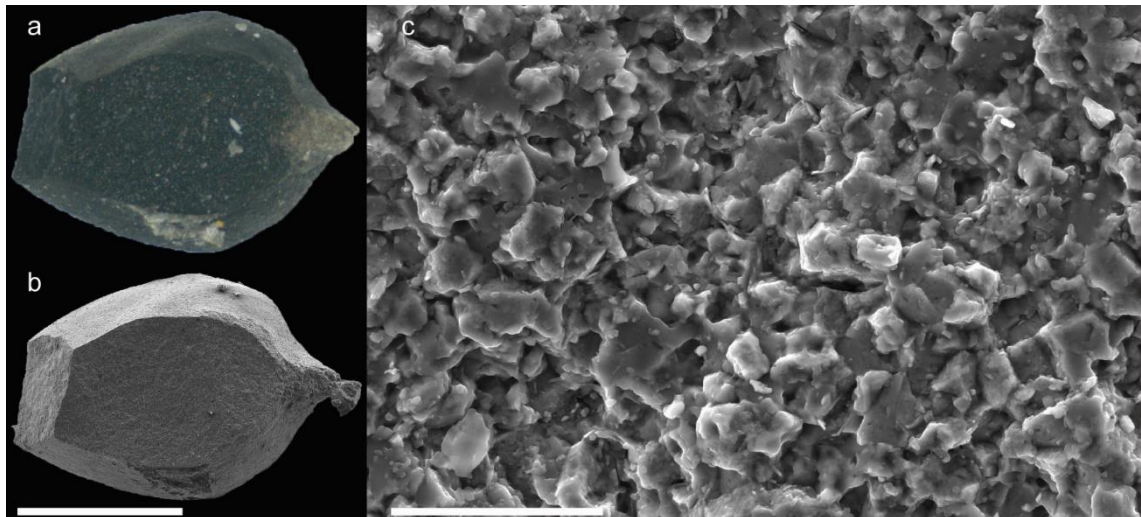


Figure 3-38. Fractured cross section through a specimen of the bivalve *Pojetaia runnegari*, Forteau Formation, Newfoundland, with coarse angular crystallites (c). Specimen DMQ-BIV-02. Scale bars: (a, b) = 500 μm ; (c) = 10 μm .

contrast, the prismatic crystallites of dark-coloured specimens are larger and comparable to those of altered brachiopods from the Comley Limestones (Figure 3-19).

The blocky cross-sections of the light-coloured Forteau Formation brachiopods may reflect minor recrystallisation following collapse and stabilisation of the porous laminae, without affecting the phosphatic crystallites. However, the dark-coloured specimens can be characterised as having undergone more substantial ultrastructural recrystallization. Therefore, the light-coloured Forteau brachiopods may be characterised as ‘minimally altered’, in contrast to the light-coloured Comley Limestones brachiopods, but may still be isotopically pristine. However, as stated

above, analysis of the Forteau Formation specimens requires further work, and these results should be regarded as preliminary.

3.10. Conclusions

3.10.1. A protocol to assess the preservation of phosphate biominerals

The purpose of the protocol detailed in this chapter (Figure 3-3) is to distinguish between isotopically pristine and isotopically altered phosphate biominerals. Paired samples of phosphatic Cambrian microfossils from the Comley Limestones separated under binocular microscopy on the basis of visual appearance show consistent differences in ultrastructure and elemental chemistry. However, most specimens from the Comley Limestones preserve biogenic microstructures, regardless of binocular microscope observations and other indicators of diagenetic or meteoric alteration. In contrast, high-resolution SEM analysis does reveal differences in ultrastructural preservation between these paired samples. This suggests that microstructural preservation is not a sufficient condition for distinguishing between pristine and altered specimens, but that ultrastructural preservation may be.

Chemical analyses were also useful in distinguishing between pristine and altered specimens from the Comley Limestones, and in distinguishing these SSFs from an abiogenic Durango apatite crystal. In particular, the chemistry of altered SSFs from any given horizon was more variable than that of pristine specimens, and the chemistry of both groups in the Comley Limestones was significantly different to that of abiogenic apatite. At whole sample level, the first stage of chemical alteration of phosphatic biominerals, therefore, may be an increase in the variability of the elemental composition of their apatite skeletons. Elemental analysis has shown that REEs and other trace metals can become concentrated in the apatite of SSFs from the Comley Limestones. However, in the case of light-coloured translucent specimens, this has occurred without altering the ultrastructure of the apatite, which is preserved as sub-micron phosphatic spherules; i.e. this is elemental exchange without recrystallisation. Elemental alteration of apatite, particularly involving REEs, can occur without concomitant oxygen isotopic exchange, suggesting that chemical analysis is of limited use when assessing the preservation of phosphatic microfossils (Joachimski *et al.* 2009). Nevertheless, this protocol shows that, applied to a group of fossils, such chemical alteration can be used to assess potential differences in ultrastructural

preservation between visually distinct samples. Whether this elemental alteration of SSF apatite reflects isotopic alteration remains to be tested (see Chapter Four:).

The abbreviated form of this protocol as applied to specimens from the Forteau Formation, Canada, relied solely on SEM analysis. Whilst light- and dark-coloured specimens could be readily separated using binocular microscopy, microstructural alteration was found in specimens of both categories, with light-coloured specimens frequently being blocky in cross-section. However, the colour variation was more closely tied to ultrastructure and crystallite morphology, with light-coloured specimens characterised by sub-micron apatite spherules and dark-coloured specimens by micron-scale prismatic apatite. This suggests that re-organising of the shell microstructure of the light-coloured specimens may have occurred early in the post-mortem history of these brachiopods and without affecting the phosphatic crystallites. Whilst these specimens should be considered cautiously, there is merit in further isotopic examination of separate samples of light- and dark-coloured brachiopods from the Forteau Formation.

The following criteria can be used when examining specimens under a binocular microscope to assemble pristine samples for isotope analyses.

1. Absence of secondary mineral coatings.
2. Absence of secondary mineral precipitation of internal fractures.
3. Clearly defined external morphology and growth structures.
4. Specimen colour not very dark grey to deep black.
5. Lustre is not greasy.
6. Any colour changes orientated in congruence with growth direction.
7. No irregular colour changes.
8. No irregular topography (e.g. bulges).

A subset of representative specimens from each assembled bulk isotope sample should be taken for more detailed investigation following the protocol above (Figure 3-3). To have confidence in the visual separation of groups of microfossils, hypothesised pristine and altered groups should be distinct in the ultrastructural and chemical tests. However, although physical and chemical changes may be indicative of alteration, the final test of the veracity of this protocol lies in isotopic analyses.

3.10.2. Preservation hypotheses to be tested using isotope data

The preservation protocol so far established can consistently distinguish between paired samples from the same horizon, separated by visual observations. The most useful techniques for distinguishing between these paired samples are ultrastructural analyses of individual specimens, and the collective results of chemical analyses of many individual specimens. What remains to be tested is whether these ultrastructurally and chemically distinct paired samples are also isotopically distinct, and whether either or neither preserves a Cambrian $\delta^{18}\text{O}$ signal. Three main hypotheses can be considered, to be tested with $\delta^{18}\text{O}$ data (see Chapter Four):

1. In paired analyses of well-preserved and altered specimens from the same sample, well-preserved specimens will be consistently isotopically heavier than altered specimens.
2. In taxa with compact and porous regions of the skeleton, compact regions will be more resistant to diagenetic alteration than the porous regions.
3. In paired analyses of well-preserved and altered specimens, measurements on well-preserved specimens will have a lower variance than altered specimens.

A fourth hypothesis referring to potential isotopic differences between well-preserved specimens from different palaeogeographic localities can also be considered:

4. Well-preserved specimens from sites at different palaeolatitudes will be isotopically distinct from each other, and in a manner consistent with their relative palaeolatitudinal positions.

These hypotheses will be tested using both *in situ* and bulk $\delta^{18}\text{O}$ analyses, presented in Chapter Four, on samples assembled following the protocol devised in this chapter.

Chapter Four: Early Cambrian phosphate oxygen isotope data

4.1. Chapter summary

Chapter Four presents stable oxygen isotope ($\delta^{18}\text{O}$) analyses of early Cambrian SSFs. Bulk and *in situ* SIMS $\delta^{18}\text{O}$ measurement techniques are described, and the results of analyses of Cambrian SSFs are presented. A discussion of the results follows, and intra- and inter-specimen variability are considered, along with discrepancies between the different techniques. Finally, the hypotheses proposed at the conclusion of Chapter Three are tested.

4.2. Introduction

The stable oxygen isotopic ($\delta^{18}\text{O}$) composition of biominerals is one of the most widely used proxies for Phanerozoic palaeoenvironmental conditions, and it is particularly useful as a deep time palaeothermometer (Grossman 2012b). There is a near-continuous $\delta^{18}\text{O}$ record stretching back to the Early Ordovician Epoch, assembled from analyses of biogenic aragonite, calcite and apatite (e.g. Trotter *et al.* 2008; Grossman 2012b). However, there is a dearth of data for the Cambrian Period. Two recent studies presented phosphate oxygen isotope data from the late Cambrian of Laurentia, but concluded that the $\delta^{18}\text{O}$ values of their specimens were diagenetically altered, based on the isotope values alone (Elrick *et al.* 2011; Bergmann *et al.* 2018). Whereas the first study (Elrick *et al.* 2011) did not investigate the preservation state of their material, the second study considered that only the phosphate $\delta^{18}\text{O}$ ($\delta^{18}\text{O}_{\text{phos}}$) values of their material was altered, and that the specimens were otherwise well-preserved (Bergmann *et al.* 2018). There remains, therefore, a substantial data gap in the $\delta^{18}\text{O}$ record at the beginning of the Phanerozoic.

A protocol for finding suitable well-preserved biominerals to fill the early Cambrian data gap was described in Chapter Three, using biological and geochemical criteria. Three taxonomic groups of phosphatic ‘small shelly fossils’ (SSFs) were considered to meet the necessary criteria to be considered suitable candidate repositories of early Cambrian $\delta^{18}\text{O}$ data: linguliformean brachiopods, *Rhombocorniculum* and *Torellella*. The oxygen isotope systematics of *Rhombocorniculum* or *Torellella* are unknown. However, because vital effects in the $\delta^{18}\text{O}_{\text{phos}}$ systematics of invertebrate taxa are thought to be small (Lécuyer *et al.* 1996), comparisons may be drawn between these extinct taxa and published $\delta^{18}\text{O}$ studies of modern linguliformean brachiopods.

Both modern and fossil linguliformean brachiopods have been reported to have high inter-specimen variability, with *in situ* $\delta^{18}\text{O}$ measurements differing by 3.5 ‰ between three modern *Glottidia palmeri* specimens from one site in Baja California, Mexico (Rodland *et al.* 2003). Vital effects may lie behind the high inter-specimen variability, either during shell growth or via *in vivo* stabilisation of the biogenic hydroxyapatite by substitution of F^- for OH^- ions (Puura & Nemliher 2001; Rodland *et al.* 2003). However, Lécuyer *et al.* (1996) found much lower variability in the $\delta^{18}\text{O}_{\text{phos}}$ values of different specimens of *Lingula anatina* from Asamushi, Japan, and *G. pyramidata* from the Gulf of Nicoya, Costa Rica, with $\delta^{18}\text{O}$ variabilities of 0.4 ± 0.2 ‰ ($n = 4$) and 0.1 ± 0.2 ‰ ($n = 2$), respectively.

Large intra-specimen variability, in excess of 4 ‰, measured using laser ablation mass spectrometry (Sharp & Cerling 1996), has also been reported from modern linguliformean brachiopods (Rodland *et al.* 2003). However, the 500 μm diameter analysis spots on the surface of brachiopod shells:

- a. would have incorporated a substantial $\delta^{18}\text{O}$ contribution from the brachiopod shell primary layer,
- b. may have intersected both compact and porous laminae, sampling different brachiopod shell tissues, and
- c. would have incorporated $\delta^{18}\text{O}$ contributions from all oxygen compounds within the shell.

The linguliformean brachiopod primary layer is an isotopically unknown quantity but comprises a substantial component of organic matter alongside phosphatic crystallites. The isotope systematics of the calcareous brachiopod primary layer is much better understood, and is known to be compromised by vital effects that cause it to be precipitated out of equilibrium with the surrounding sea water (Parkinson *et al.* 2005). It is also conceivable that linguliformean brachiopod compact and porous laminae may have different isotopic signatures, as the different laminae of calcareous brachiopods do (Parkinson *et al.* 2005). Sampling both compact laminae and porous laminae in different proportions may account for some of the $\delta^{18}\text{O}$ variability between the laser ablation pits of Rodland *et al.* (2003).

Nevertheless, $\delta^{18}\text{O}_{\text{phos}}$ values of modern linguliformean brachiopods do seem to correspond to the temperature of the water in which the shells precipitated (Lécuyer *et al.* 1996, 2013). Fossil specimens identified in Chapter Three as isotopically pristine may therefore preserve Cambrian environmental signals in the $\delta^{18}\text{O}_{\text{phos}}$ values of their

shells. However, the preservation tests detailed in Chapter Three are only proxies for the retention of an early Cambrian $\delta^{18}\text{O}$ signal in these fossils. Ultimately, $\delta^{18}\text{O}$ analyses are needed to verify the success or otherwise of the protocol.

Specimens identified following this protocol as either potentially isotopically pristine or isotopically altered were analysed separately, in order to investigate the utility of this protocol. High-precision *in situ* inter- and intra-specimen $\delta^{18}\text{O}$ measurements were used to examine how variability in microstructure, ultrastructure or elemental composition may relate to isotopic preservation.

4.2.1. Hypotheses to be tested with $\delta^{18}\text{O}$ data

Chapter Three concluded with four hypotheses that arise from the preservation protocol and that may be tested with $\delta^{18}\text{O}$ data. These hypotheses are effectively criteria for accepting or dismissing $\delta^{18}\text{O}$ measurements as palaeoenvironmentally informative or diagenetically altered. The hypotheses can be summarised as follows:

H1: Specimens identified as well-preserved will be isotopically heavier than specimens identified as altered, for specimens taken from the same sample.

H2: Within individual specimens, and on average across a sample, brachiopod compact laminae are less susceptible to diagenetic alteration and will be isotopically heavier than porous laminae.

H3: *In situ* $\delta^{18}\text{O}$ analyses of specimens identified as well-preserved will have a lower variance than *in situ* $\delta^{18}\text{O}$ analyses of specimens identified as diagenetically altered, for specimens taken from the same horizon or limestone sample.

H4: Well-preserved specimens sampled from different palaeolatitudes will be isotopically distinct from each other.

4.2.2. The rationale for using different $\delta^{18}\text{O}$ sampling techniques

There are two commonly used techniques for extracting $\delta^{18}\text{O}$ data from phosphatic fossils, and from conodonts in particular: the bulk silver phosphate (Ag_3O_4) method, and the *in situ* secondary ion mass spectrometry (SIMS) approach. Samples for the bulk silver phosphate method only measure the $\delta^{18}\text{O}$ of phosphate-bound oxygen ($\delta^{18}\text{O}_{\text{phos}}$), disregarding other oxygen sources within the mineral, which in biogenic apatite can be substantial (Legeros *et al.* 1967; Watabe & Pan 1984; LeGeros *et al.* 1985; Williams *et al.* 1997a). The ultimate aim of this work is to use $\delta^{18}\text{O}$ values to reconstruct ancient sea temperatures, so it is important to note that all current phosphate oxygen temperature equations are empirically derived from $\delta^{18}\text{O}_{\text{phos}}$ measurements.

The SIMS method has been favoured in more recent studies (Trotter *et al.* 2008; Wheeley *et al.* 2012, 2018) due to the high spatial precision and drastically smaller samples sizes that it affords. This work capitalises on the high spatial precision afforded by SIMS analyses to test H2 that there is tissue-specific differential preservation in brachiopod compact and porous laminae.

However, SIMS analyses are susceptible to variations in the texture and porosity of the analysed material. Both linguliformean brachiopods and *Rhombocorniculum* have regions that are more porous than the crystalline Durango standard material against which results are normalised. SIMS measurements also aggregate $\delta^{18}\text{O}$ contributions from all oxygen sources in a 30 μm analysis spot. In apatite, this can include substantial contributions from structural carbonate ions, and from channel carbonate and hydroxyl ions in the crystal lattice. Differences in porosity, texture and chemical composition between some fossil specimens and the Durango standard are potentially problematic for reconstructing palaeotemperatures from SIMS $\delta^{18}\text{O}$ values.

The bulk and SIMS techniques have shown different responses to the well-understood diagenetic trends in conodont elements, following the conodont colour alteration index (CAI; Epstein *et al.* 1977; Rejebian *et al.* 1987). Using bulk $\delta^{18}\text{O}_{\text{phos}}$ analyses, Joachimski *et al.* (2009) found that conodont elements with $\text{CAI} \leq 5$, indicating a minimum burial temperature of 300 °C (Epstein *et al.* 1977), may be considered isotopically well-preserved. However, Wheeley *et al.* (2012) showed that SIMS analyses detected isotopic alteration, manifest as $\delta^{18}\text{O}$ increased variability, between and within individual conodont elements with $\text{CAI} > 1$, indicating a maximum burial temperature of approximately 80 to 90 °C (Epstein *et al.* 1977). It is therefore conceivable that bulk $\delta^{18}\text{O}$ analyses can mitigate for minor thermal $\delta^{18}\text{O}$ alteration by absorbing the increased variability across a large sample size (Joachimski *et al.* 2009), whilst also masking potentially important alteration that would be revealed by the high spatial resolution of *in situ* SIMS analyses (Wheeley *et al.* 2012). It is also possible that the increased variability of SIMS $\delta^{18}\text{O}$ measurements derives from alteration of the non-phosphate oxygen $\delta^{18}\text{O}$ components. Combining these isotope measurement techniques provides a potentially powerful method for extracting environmentally informative $\delta^{18}\text{O}$ data from specimens that have experienced some minor thermal alteration.

4.3. Materials and Methods

4.3.1. Samples

Phosphatic microfossils were extracted from limestone samples from the lower Cambrian strata of southern Britain, southern Morocco and eastern Canada (Chapter Two) by acetic acid maceration (see §3.6.1). Monotaxic isotope samples were assembled from each limestone block from which sufficient microfossils were recovered. Samples assembled for bulk isotope analysis require at least 10 mg, and preferably 30 mg, of phosphatic fossil material, which equates to several tens to a few hundred individual specimens. A visual assessment of the preservation state of each specimen was made (see Chapter Three), and separate samples of pristine and altered specimens were assembled. Because it was impractical to assess in detail the preservation state of each specimen analysed in a $\delta^{18}\text{O}$ sample, a subset of specimens were subjected to more detailed investigations following the protocol detailed in Chapter Three. This involved examining five specimens, taken at random from each isotope sample, using high resolution SEM analysis, and embedding additional specimens in epoxy resin for EPMA and SIMS analysis (see appendices A, D). This detailed preservation analysis confirmed that there were consistent ultrastructural and chemical differences, and sometimes also microstructural differences, between the samples assembled from a visual preservation assessment. Where possible, sedimentary or diagenetic phosphate samples were also taken in order to provide an independent, non-SSF, oxygen isotope signal against which SSF $\delta^{18}\text{O}$ analyses may be compared.

The Comley Limestones, UK

Five limestone samples from the Comley Limestones were picked for SSFs (see §2.4), and three taxonomic groups were selected for analysis (see §3.5): linguliformean brachiopods, *Rhombocorniculum*, and *Torellella*. Pristine and altered monotaxic samples were assembled from each of the five limestone samples from which sufficient material was recovered (Table 4-1). Subsets of samples La2 and Sa were processed using heavy liquid separation during acetic acid maceration. Because heavy liquid separation has been suggested to affect $\delta^{18}\text{O}_{\text{phos}}$ values, the heavy liquid separated samples were given the suffix “H” (i.e. La2H and SaH) and were treated as distinct samples for isotope analyses.

Intra-specimen variability of the linguliformean brachiopods was investigated, with a focus on tissue-specific variation between compact and porous laminae of the brachiopod shell. Additionally, although the central lumen of most *Rhombocorniculum*

specimens was either hollow or filled with glauconite or detrital grains, the lumens of a few specimens were found to have a phosphatic infill. No sedimentary grains were found in the lumens of *Rhombocorniculum* specimens with phosphate-filled lumens, indicating early phosphate precipitation, before sediment grains could become lodged in the hollow lumen. Interestingly, during SIMS sample preparation, phosphate-filled lumens were only observed in a few of the pristine *Rhombocorniculum* specimens and none were found in altered specimens. The phosphate-infill of the lumen has a low porosity and is highly crystalline, in contrast to the highly porous *Rhombocorniculum* sclerite wall. The lumen infill is therefore more closely matrix-matched to the Durango apatite standard than is the sclerite wall. Analysing porous materials or materials with irregular surfaces can measurably affect the $\delta^{18}\text{O}$ values by a few per mille (Kita *et al.* 2010).

In addition to the fossil samples, two sedimentary phosphate samples from the base of Comley Limestones sample K were analysed (see §2.4). Samples HG-A and HG-B were micro-drilled from sedimentary phosphate exposed at the cut edge of the block. Sample HG-A was microdrilled from an irregular phosphatic horizon near the base of the block, interpreted as an early diagenetic phosphatic hardground. Sample HG-B was microdrilled from a phosphatic pebble a few centimetres above the hardground. Each powdered sample was split into two aliquots, one of which was treated with 15 % acetic acid for 48 hours to remove any carbonate material, and given the suffix “-DC”, while the other aliquot was not treated.

Lemdad Syncline, Morocco

Nineteen limestone samples were collected from the Lemdad Syncline in the High Atlas Mountains, Morocco (see §2.5), of which 11 were processed for phosphatic SSFs. However, only sample AI 202a, from the middle of the Issafen Formation, yielded sufficient phosphatic fossils for successful isotope analysis. Only linguliformean brachiopods could be assembled in sufficient numbers from this unit for isotopic analysis. Specimens identified as visually pristine and visually altered were assembled as separate samples, however closer inspection of these samples following the protocol detailed in Chapter Three showed them all to be chemically and ultrastructurally altered (see §3.9.1). No sedimentary or demonstrably secondary phosphate samples were available from this locality.

The Forteau Formation, Canada

Three samples from the Forteau Formation yielded sufficient SSFs for isotope analysis, and a fourth sample (FC3-1) was kindly donated by Dr Christian Skovsted (see §2.6). These samples were collected in June 2017 and were not available for SIMS analysis which concluded in July 2017. Only brachiopods were recovered from all four of these samples, though MSM also yielded phosphatic tubes similar to *Torellella*. LALQ3A did not yield sufficient brachiopods to assemble a sample of altered specimens. In addition to the biogenic SSF samples, DMQ yielded abundant phosphatised internal moulds of the bivalve *Pojetaia runnegari*. An isotope sample of *P. runnegari* was assembled to provide a diagenetic $\delta^{18}\text{O}$ signal to be compared against pristine and altered phosphatic brachiopod samples from DMQ.

4.3.2. Bulk isotope analyses

All $\delta^{18}\text{O}$ values are reported with respect to Vienna standard mean ocean water (VSMOW; Hornberger 1995). Bulk oxygen isotope analyses were conducted at the NERC Isotope Geoscience Facility (NIGF), BGS, Keyworth, UK, over two sessions in February 2016 and January 2018, supported by NIGF grants IP-1530-0515 and IP-1667-1116. Bulk silver phosphate isotope analyses were conducted following a standard NIGL protocol adapted after O'Neil *et al.* (1994) in which samples were treated to solubilize PO_4^{3-} anions which was then precipitated as silver phosphate (Ag_3PO_4). The wet chemistry of the silver phosphate oxygen isotope method requires samples of several milligrams, or ideally several tens of milligrams. Every SSF sample therefore comprised several tens to a few hundred individual specimens, depending on the size and mass of individual specimens.

Microfossil samples were weighed, placed in labelled beakers and crushed using a glass rod. Concentrated hydrogen peroxide was dispensed into the beakers, which were placed on a hot plate at 50 °C for five days. The H_2O_2 was topped up over the first four days, and the beakers were then evaporated to dryness. Once dry, each sample was dissolved in 2M HNO_3 and transferred to clean polypropylene test tubes. The samples were treated with 2M KOH for neutralization, and then calcium was removed from the solution, precipitated calcium fluoride, by the addition of 2M HF to each sample. Samples were centrifuged and the supernatant dispensed into beakers containing ammonical silver nitrate solution. The beakers were heated gently to slowly precipitate silver phosphate crystals over a few hours. Finally, the silver phosphate crystals were

filtered, thoroughly rinsed, dried, and weighed to $0.300 \pm 0.020 / -0.015$ mg into silver capsules for mass spectrometer analysis.

Oxygen isotope analyses for each sample were measured using continuous flow isotope ratio mass spectrometry (Vennemann *et al.* 2002). A high temperature conversion elemental analyser coupled to a Delta^{Plus} XL isotope ratio mass spectrometer via a ConFlo III interface (Thermo Finnigan, Bremen, Germany) was used to conduct the measurements. All samples were analysed in triplicate. Where there was a large range of triplicate values, the sample was re-run in triplicate. The reference material B2207 (Elemental Microanalysis silver phosphate) was used as an external standard, and has an accepted value of 21.70‰. Standard B2207 had an analytical reproducibility of $< \pm 0.15$ (1 σ) during this set of analyses. The average standard deviation of the triplicate $\delta^{18}\text{O}$ analyses of unknown samples was $\pm 0.15\%$.

4.3.3. Ion microprobe analyses

Ion probe oxygen isotope analyses were conducted at the Edinburgh Ion Microprobe Facility (EIMF), University of Edinburgh, UK, over three sessions in November 2016, January 2017, and July 2017, supported by grant IMF-567-1015. Fragments of a Durango apatite crystal were provided by the EIMF as an isotope standard material for this work. The Durango apatite pieces were fragments of a larger crystal, the phosphate oxygen isotopic composition ($\delta^{18}\text{O}_{\text{phos}}$) of which had been independently characterised as +8.7 ‰ at NIGF before this project began.

Each sample block was made following the method detailed in Chapter Three. Epoxy resins were chosen according to the materials listed by the EIMF (see <https://www.ed.ac.uk/geosciences/facilities/ionprobe/technical/epoxyresins>). For SIMS analysis it is essential to produce a flat surface with low relief, a good polish and no surface air bubbles or gaps between specimens and the resin. Following initial polishing, sample blocks were treated for 24 hours in 30 % H_2O_2 to remove organic matter from the embedded fossils; a treatment which is known not to affect $\delta^{18}\text{O}$ values (Wheeley *et al.* 2012). This treatment removed substantial amounts of organic matter from some of the SSFs and left gaps between fossil material and the surrounding resin. To fill any gaps left by the removal of organic matter, the prepared blocks were surface re-impregnated with a thin layer of resin and again cured under approximately 2 bar pressure before re-grinding with P2400 paper to remove surface resin and re-polishing with 3 μm and 1 μm diamond paste. The blocks were finished off with 10 minutes of

polishing with γ -alumina to produce highly polished surfaces with very low relief that were suitable for SIMS analyses. Prior to SIMS analysis, the sample surface was coated with approximately 30 nm gold to provide a conductive surface.

SIMS measurements were made using the CAMECA IMS-1270 ion microprobe at the EIMF. A primary beam of Cs⁺ ions at 5 nA was focused as a 30 μ m diameter spot on the sample block surface. Secondary ions were extracted at -10 kV, with the ¹⁶O isotope measured at approximately 2×10^9 counts per second (cps) and the ¹⁸O isotope measured at approximately 4×10^6 cps, monitored simultaneously on dual Faraday cups L'2 and H'2. Each spot analysis began with 50 seconds pre-sputtering time, followed by automatic secondary beam and entrance slit centring, with isotope data collected in two blocks of 10 cycles.

At the start of each run, usually at the start of a day, the ion beam was stabilised using $\delta^{18}\text{O}$ measurements on an internal EIMF ilmenite standard. Following stabilisation using the ilmenite standard, the ilmenite standard block was switched for the sample block and 10 measurements were taken from the Durango apatite standard at the centre of the sample block. If the standard deviation of the Durango apatite $\delta^{18}\text{O}$ measurements was ≤ 0.40 ‰ across the 10 measurements, the beam was considered stable enough to move on to analysing unknown samples. If not, further Durango analyses were conducted until the standard deviation of 10 consecutive Durango apatite $\delta^{18}\text{O}$ measurements was ≤ 0.40 ‰.

Once the beam had stabilised, $\delta^{18}\text{O}$ measurements were conducted in alternating blocks of five unknown (SSF) analyses and five standard (Durango apatite) analyses, to monitor instrument drift. When instrument stability was good, with Durango apatite $\delta^{18}\text{O}$ standard deviation < 0.20 ‰, three standard measurements were made for every five unknowns. Linear regressions were applied to each analytical run to correct for instrument drift (Appendix C). Mean external precision was derived from the standard deviation of Durango analyses, following linear regression corrections for long-term instrument drift. This value is reported for each unknown (SSF) analysis and ranges from ± 0.11 to 0.41 ‰.

4.4. Results

4.4.1. Silver phosphate analyses

The Comley Limestones

In total, bulk isotope analyses were performed on 22 samples from the Comley Limestones, including 18 SSF samples and four sedimentary phosphate samples (Table 4-1; see Appendix B). Of the SSF samples, 11 were identified *a priori* as pristine (Colour = L) and seven as altered (Colour = D). Bulk isotope analyses of the pristine SSFs yielded $\delta^{18}\text{O}_{\text{phos}}$ values of 13.30 ‰ to 15.17 ‰, with a mean value of 14.37 ‰, whilst those identified *a priori* as being affected by diagenetic alteration yielded lower $\delta^{18}\text{O}_{\text{phos}}$ values of 12.83 ‰ to 14.31 ‰, with a mean value of 13.57 ‰ (Figure 4-2). Under a Welch two sample t-test, the means of pristine and altered specimens are significantly separated, with a *p* value of 0.0056.

Among the Comley Limestones samples, those from pristine linguliformean brachiopods (*n* = 7) yielded $\delta^{18}\text{O}_{\text{phos}}$ values of 13.30 ‰ to 15.17 ‰, with a mean value of 14.42 ‰, whilst altered brachiopod samples (*n* = 5) yielded $\delta^{18}\text{O}_{\text{phos}}$ values of 12.83 ‰ to 14.31 ‰, with a mean value of 13.62 ‰ (Table 4-1; Figure 4-1). Under a Welch two sample t-test, the means of pristine and altered brachiopod specimens are separated, with a *p* value of 0.0492. Analyses of pristine brachiopods from samples La2 and La2H (denoting heavy liquid separation) yielded $\delta^{18}\text{O}_{\text{phos}}$ values of 13.93 ‰ and 14.26 ‰, respectively. Altered brachiopods from La2 and La2H yielded $\delta^{18}\text{O}_{\text{phos}}$ yielded values of 13.33 ‰ and 13.70 ‰, respectively.

Bulk isotopic analyses of pristine *Rhombocorniculum* specimens from samples La2 and La2H yielded $\delta^{18}\text{O}_{\text{phos}}$ values of 13.88 ‰ and 13.97 ‰, respectively. Altered *Rhombocorniculum* specimens from La2 and La2H both yielded $\delta^{18}\text{O}_{\text{phos}}$ values of 13.45 ‰. Two *Torellella* samples from the Comley Limestones, samples Lb and Sa, were also analysed. These comprised only specimens identified *a priori* as pristine and yielded $\delta^{18}\text{O}_{\text{phos}}$ values of 14.49 ‰ to 14.70 ‰.

The phosphate hardground sample, HG-A, yielded a $\delta^{18}\text{O}_{\text{phos}}$ value of 13.95 ‰ whilst the de-carbonated aliquot, HG-A-DC, yielded a $\delta^{18}\text{O}_{\text{phos}}$ value of 14.07 ‰. The phosphatic pebble, HG-B, yielded a $\delta^{18}\text{O}_{\text{phos}}$ value of 12.77 ‰, and the de-carbonated aliquot, HG-B DC, yielded a $\delta^{18}\text{O}_{\text{phos}}$ value of 12.78 ‰. Treatment with dilute acetic acid to remove any remnant carbonate cement from the sedimentary phosphate samples had no significant effect on the measured isotope values.

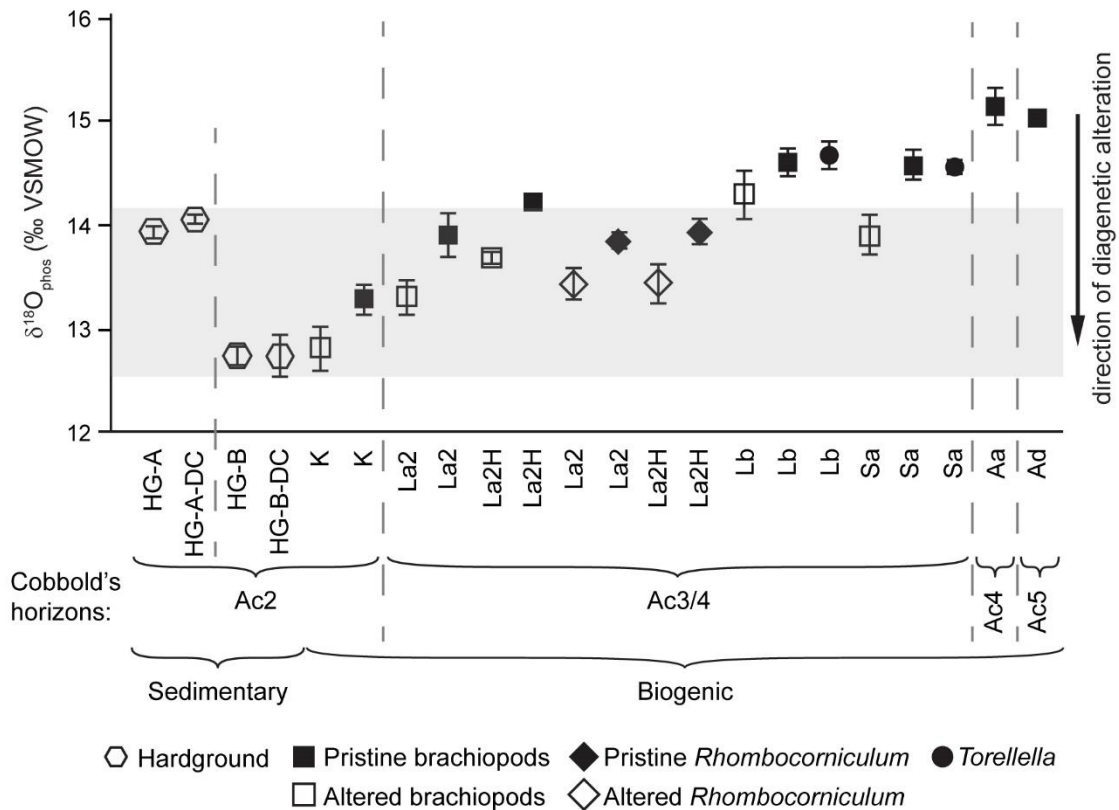


Figure 4-1. Bulk isotope data from the Comley Limestones. Shaded area indicates the $\delta^{18}\text{O}_{\text{phos}}$ range of the sedimentary phosphate. Error bars are one standard deviation of the triplicate isotope analyses. See values in Table 4-1.

Notably, in paired analyses of linguliformean brachiopod and *Rhombocorniculum* specimens from the same sample, $\delta^{18}\text{O}_{\text{phos}}$ values of pristine specimens were consistently heavier than the corresponding $\delta^{18}\text{O}_{\text{phos}}$ values of altered specimens (Figure 4-1). There is also a close correspondence between analyses of *Torellella* specimens and pristine brachiopod and *Rhombocorniculum* specimens, supporting the hypothesis (e.g. Lécuyer *et al.* 2013) that the influence of taxonomy on $\delta^{18}\text{O}_{\text{phos}}$ values (‘vital effects’) in non-tetrapods is negligible. Finally, the $\delta^{18}\text{O}_{\text{phos}}$ values of diagenetically altered linguliformean brachiopod and *Rhombocorniculum* specimens and sedimentary phosphate samples are closely comparable.

SSFs from the High Atlas Mountains, Morocco

Two samples from the early/middle Cambrian transition of the High Atlas Mountains of Morocco were processed for silver phosphate analyses. Paired samples of visually well-preserved and visually altered brachiopods from horizon AI-202a, Issafen Formation, were analysed. The visually well-preserved sample yielded a $\delta^{18}\text{O}_{\text{phos}}$ value of 9.39 ‰, and the visually altered sample had a $\delta^{18}\text{O}_{\text{phos}}$ value of 9.57 ‰ (Table 4-1; see Appendix

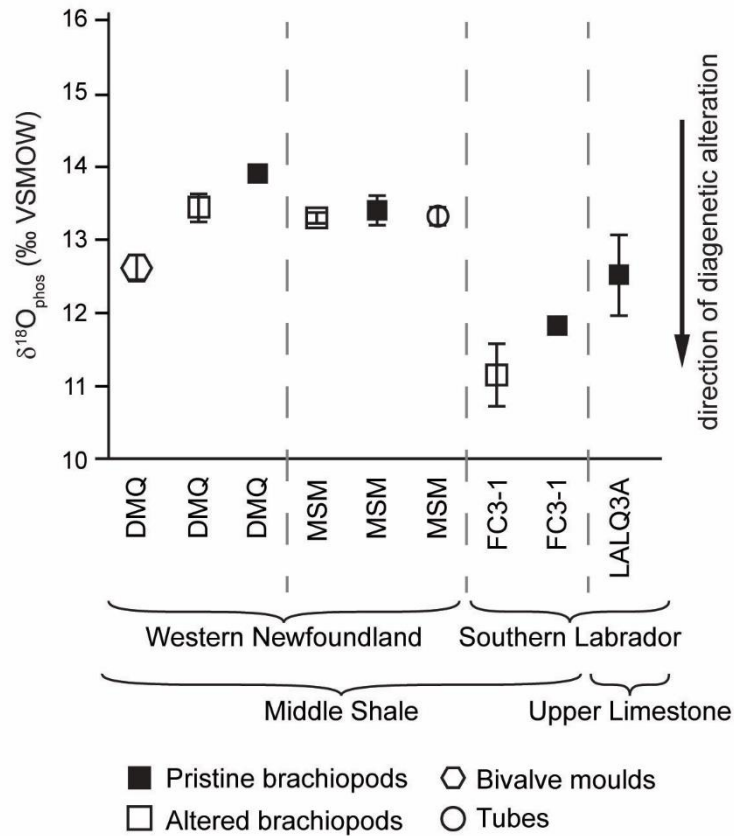


Figure 4-2. Bulk isotope data from the Forteau Formation. Error bars = one standard deviation of the triplicate isotope analyses. See data in Table 4-1.

B). The AI 202a $\delta^{18}\text{O}_{\text{phos}}$ values are within analytical uncertainty of each other and are substantially lighter than values reported from the Comley Limestones SSFs.

SSFs from the Laurentian Forteau Formation

Bulk isotope analyses were conducted on nine samples from Forteau Formation outcrops in western Newfoundland (DMQ and MSM) and southern Labrador (LAL and FC3-1), Canada (see §2.6). Seven of these samples comprised linguliformean brachiopods, one comprised hyolithelminth tubes, and one sample was of phosphatised internal moulds of the bivalve *Pojetaia runnegari*.

Bulk isotope analyses of the Forteau Formation potentially pristine brachiopods (see §3.9.2) yielded $\delta^{18}\text{O}_{\text{phos}}$ values of 11.84 ‰ to 13.90 ‰, with a mean value of 12.91 ‰ (Table 4-1; Figure 4-2; see Appendix B). Bulk isotope analyses of the Forteau Formation altered brachiopods yielded $\delta^{18}\text{O}_{\text{phos}}$ values of 11.15 ‰ to 13.44 ‰, with a mean value of 12.63 ‰. The means of the potentially pristine and altered brachiopod analyses are not significantly separated at the 95% confidence interval by a Welch two sample t-test. The Forteau Formation analyses require more nuanced consideration.

Sample LALQ3A did not yield enough altered brachiopod specimens to analyse. However, in paired analyses of potentially pristine and altered brachiopods from FC3-1, MSM and DMQ, pristine specimens were consistently isotopically heavier than altered specimens. Analyses of pristine and altered brachiopods from sample MSM yielded $\delta^{18}\text{O}_{\text{phos}}$ values of 13.40 ‰ and 13.30 ‰, respectively, implying that either both have some diagenetic overprint or that the diagenetic overprint on the altered specimens is minimal. Analysis of the bleached hyolithelminth specimens yielded a $\delta^{18}\text{O}_{\text{phos}}$ value of 13.31 ‰, comparable to the dark-coloured brachiopod samples.

Sample DMQ produced both potentially pristine and altered brachiopods, and diagenetic phosphate in the form of *P. runnegari* internal moulds. The potentially pristine brachiopods yielded a $\delta^{18}\text{O}_{\text{phos}}$ value of 13.90 ‰, whilst altered DMQ brachiopods yielded a $\delta^{18}\text{O}_{\text{phos}}$ value of 13.44 ‰, and the bivalve moulds yielded a lighter $\delta^{18}\text{O}_{\text{phos}}$ value of 12.62 ‰.

Notably, the potentially pristine brachiopod specimens are consistently isotopically heavier than paired altered fossil samples or secondary phosphate. This is comparable to the separation of pristine biomineral, altered biomineral, and sedimentary $\delta^{18}\text{O}_{\text{phos}}$ values observed in the Comley Limestones. Samples from the MSM locality demonstrate a similar though less pronounced trend between potentially pristine brachiopods and altered brachiopods and hyolithelminth. The Labrador samples, FC3-1 and LALQ3A, yielded lighter values than the Newfoundland samples MSM and DMQ. This may be a primary signal attributable to original palaeoenvironmental differences, and a nuanced approach is required in the environmental interpretation of these data.

Table 4-1. Early Cambrian silver phosphate oxygen isotope data. Mean and standard deviation values are calculated from triplicate $\delta^{18}\text{O}_{\text{phos}}$ measurements (see Appendix B).

ID	Label	Location	Sample	Taxon	Preservation	$\delta^{18}\text{O}_{\text{phos}}$ (‰) ¹	
						Mean	1 S.D.
B001	AaBrL	Comley	Aa	Brachiopods	Pristine	15.17	0.18
B002	AdBrL	Comley	Ad	Brachiopods	Pristine	15.06	0.03
B003	La2BrD	Comley	La2	Brachiopods	Altered	13.33	0.17
B004	La2BrL	Comley	La2	Brachiopods	Pristine	13.93	0.22
B005	La2RhD	Comley	La2	<i>Rhombocorniculum</i>	Altered	13.45	0.14
B006	La2RhL	Comley	La2	<i>Rhombocorniculum</i>	Pristine	13.88	0.08
B007	La2HBrD	Comley	La2H ²	Brachiopods	Altered	13.70	0.06
B008	La2HBrL	Comley	La2H ²	Brachiopods	Pristine	14.26	0.00
B009	La2HRhD	Comley	La2H ²	<i>Rhombocorniculum</i>	Altered	13.45	0.18
B010	La2HRhL	Comley	La2H ²	<i>Rhombocorniculum</i>	Pristine	13.97	0.12
B011	LbBrD	Comley	Lb	Brachiopods	Altered	14.31	0.23
B012	LbBrL	Comley	Lb	Brachiopods	Pristine	14.63	0.14
B013	LbTo	Comley	Lb	<i>Torella</i>	Pristine	14.70	0.14
B014	SaBrD	Comley	Sa	Brachiopods	Altered	13.94	0.18
B015	SaBrL	Comley	Sa	Brachiopods	Pristine	14.62	0.15
B016	SaTo	Comley	Sa	<i>Torella</i>	Pristine	14.59	0.07
B017	HG-A	Comley	A	Hardground	NA	13.95	0.05
B018	HG-A-DC ³	Comley	A	Hardground	NA	14.07	0.03
B019	HG-B	Comley	B	Pebble	NA	12.77	0.09
B020	HG-B-DC ³	Comley	B	Pebble	NA	12.78	0.20
B024	AI202aBrD	AI	202a	Brachiopods	Altered	9.57	0.48
B025	AI202aBrL	AI	202a	Brachiopods	Pristine ⁴	9.39	0.40
B026	DMQ-BIV	Forteau	DMQ	Bivalve moulds	NA	12.62	0.17
B027	DMQBrD	Forteau	DMQ	Brachiopods	Altered	13.44	0.19
B028	DMQBrL	Forteau	DMQ	Brachiopods	Pristine	13.90	0.07
B029	FC3-1BrD	Forteau	FC3-1	Brachiopods	Altered	11.15	0.43
B030	FC3-1BrL	Forteau	FC3-1	Brachiopods	Pristine	11.84	0.04
B031	KBrD	Comley	K	Brachiopods	Altered	12.83	0.21
B032	KBrL	Comley	K	Brachiopods	Pristine	13.30	0.14

B033	LALBrL	Forteau	LALQ3A	Brachiopods	Pristine	12.52	0.55
B034	MSMBrD	Forteau	MSM	Brachiopods	Altered	13.30	0.09
B035	MSMBrL	Forteau	MSM	Brachiopods	Pristine	13.40	0.21
B036	MSMTu	Forteau	MSM	Tubes	Bleached	13.31	0.12

¹Mean and standard deviation of triplicate measurements. ²Suffix 'H' denotes heavy liquid separation. ³Suffix 'DC' denotes acetic acid treatment to remove potential carbonate contamination. ⁴Potentially pristine under visual examination though shown to be altered following the preservation protocol (see Chapter Three).

4.4.2. SIMS analyses

In addition to bulk isotope analyses, individual specimens were analysed using SIMS in order to:

- a. test the compatibility of different isotope measurement techniques,
- b. investigate inter-specimen variability within samples, and
- c. investigate intra-specimen variability.

Durango apatite standards

In total, 323 SIMS measurements were made on seven fragments of Durango apatite embedded in the centre of each epoxy resin block. The accepted $\delta^{18}\text{O}$ value of Durango apatite is 8.7 ‰ (Wheelely *et al.* 2012). Analytical uncertainty was determined from the standard deviation of the Durango measurements bracketing each set of specimen analyses. The mean of the regression-corrected SIMS $\delta^{18}\text{O}$ analyses of all Durango fragments was 8.67 ‰ and the standard deviation was 0.28 ‰, with standard deviations in each run ranged from 0.07 ‰ to 0.42‰ (see Appendix C).

SSFs from the Comley Limestones

In total, 343 SIMS measurements were made on 129 SSF specimens from the Comley Limestones (see Appendix D). SIMS measurements that could be seen by visual inspection to incorporate a contribution from epoxy resin and measurements where $\delta^{18}\text{O} \leq 0$ ‰ were discarded from further analysis as these measurements may be up to 100 % resin. This initial screening reduced the data set to 324 analyses of 126 specimens: 76 brachiopod specimens, 39 *Rhombocorniculum* specimens, 11 *Torellella* specimens, and a single *Hyolithellus* specimen. Of these, 214 measurements were made on pristine specimens (Colour = L), following the protocol described in Chapter Three, and 110 on altered specimens (Colour = D; see Appendix D).

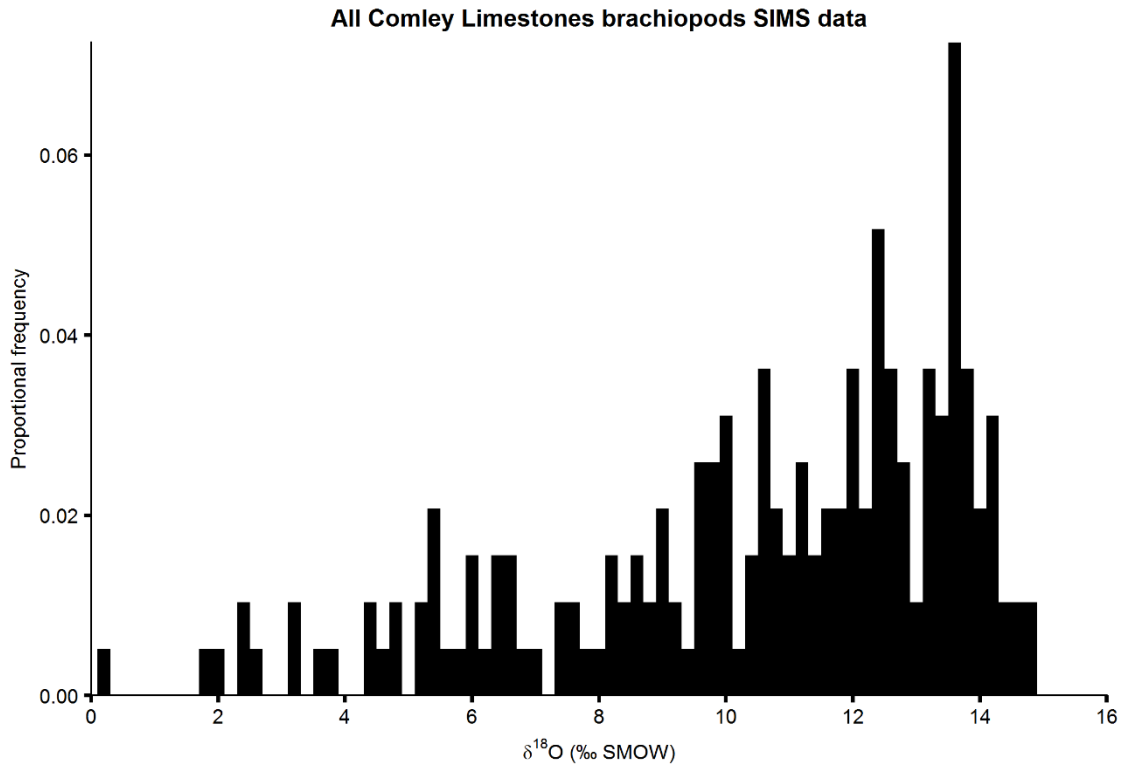


Figure 4-3. Histogram showing the distribution of SIMS measurements on Comley Limestones brachiopods.

SIMS analyses of pristine phosphatic microfossils from the Comley Limestones yielded $\delta^{18}\text{O}$ values of 1.88 ‰ to 14.78 ‰, with a mean value of 10.70 ‰ (Table 4-2; see Appendix D). SIMS isotope analyses of altered phosphatic microfossils from the Comley Limestones yielded $\delta^{18}\text{O}$ values of 2.36 ‰ to 14.74 ‰, with a mean value of 8.79 ‰. A Welch two sample t-test of the SIMS analyses of pristine SSFs against the SIMS analyses of altered SSFs found the population means to be significantly separated, with a p -value of 1.56×10^{-7} . Although the population means are significantly different, there is considerable overlap in the range of the two data sets, and this examined in more detail below.

Linguliformean brachiopods

In total, 189 SIMS measurements were made on 76 linguliformean brachiopod specimens from the Comley Limestones: 125 analyses on 52 pristine specimens and 64 analyses on 24 altered specimens. Analyses of pristine linguliformean brachiopods from the Comley Limestones yielded $\delta^{18}\text{O}$ values of 1.88 ‰ to 14.78 ‰, with a mean value of 11.11 ‰ (Table 4-2; Figure 4-3; see Appendix D), whereas altered brachiopods yielded $\delta^{18}\text{O}$ values of 3.12 ‰ to 14.74 ‰, with a mean value of 9.69 ‰. A Welch two sample t-test of the SIMS analyses of pristine SSFs against the SIMS analyses of altered

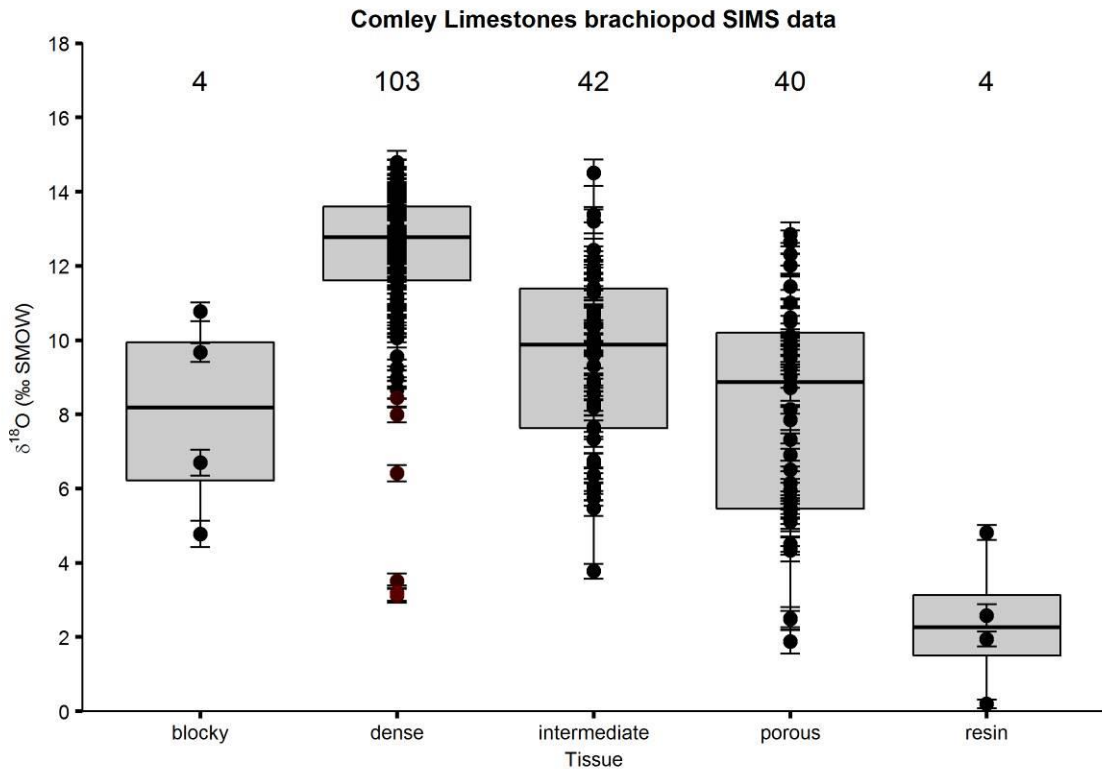


Figure 4-4. Boxplot of all Comley Limestones brachiopod SIMS measurements by tissue type.

SSFs found that the population means were significantly separated, with a p -value of 3.25×10^{-3} .

The substantial overlap between the two data sets is partly due to high tissue-specific intra-specimen variability that manifests as substantial isotopic differences between the brachiopod compact and porous laminae. Porous laminae are lighter and often more variable in their $\delta^{18}\text{O}$ composition than are brachiopod compact laminae (Figure 4-4). Measurements recorded as ‘intermediate’ were analysis spots that incorporated contributions from both types of laminae and are generally intermediate in isotopic composition (e.g. Figure 4-5), being lighter than compact laminae and heavier than porous laminae.

SIMS measurements of the compact laminae of all Comley Limestones brachiopods have a mean $\delta^{18}\text{O}$ value of 12.19 ‰, whereas porous laminae have a mean $\delta^{18}\text{O}$ value of 8.09 ‰. Pristine brachiopod compact laminae have a mean $\delta^{18}\text{O}$ value of 12.67 ‰, and porous laminae have a mean $\delta^{18}\text{O}$ value of 7.81 ‰. Altered brachiopod compact laminae have a mean $\delta^{18}\text{O}$ value of 10.94 ‰, and altered brachiopod porous laminae have a mean $\delta^{18}\text{O}$ value of 8.61 ‰. A Welch two sample t-test of the $\delta^{18}\text{O}$ values of pristine versus altered compact laminae found the population means to be significantly separated at the 95% confidence interval, with a p -value of 8.25×10^{-3} ,

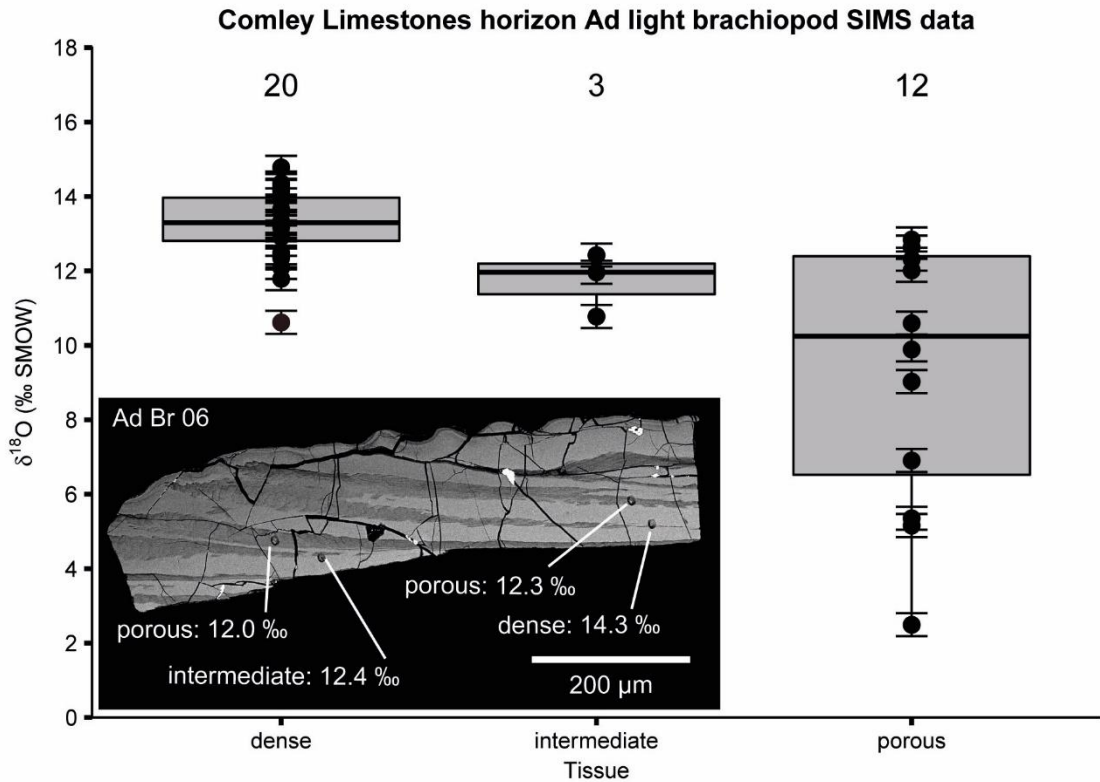


Figure 4-5. Comley Limestones Ad light-coloured brachiopods SIMS data. Inset: SEM image of specimen AdBr06 annotated with location of SIMS pits.

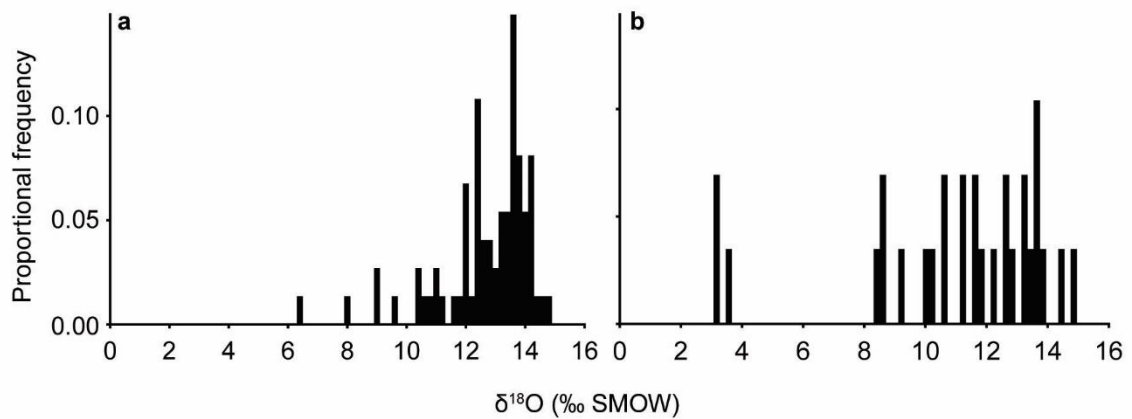


Figure 4-6. SIMS $\delta^{18}\text{O}$ data from the compact laminae of (a) pristine and (b) altered brachiopods from the Comley Limestones.

whilst the same test on the porous laminae of pristine and altered specimens revealed no significant difference between the population means at the 95 % confidence interval, with a p -value of 0.39.

The range of $\delta^{18}\text{O}$ values within the compact laminae of a single brachiopod specimen can exceed 2 ‰. This variability of measurements within compact laminae is more pronounced in altered specimens than pristine specimens (Figure 4-6), suggesting that variability increases with diagenetic alteration (cf. *Wheelely et al.* 2012). However,

this variability is also comparable to that found in analyses of modern brachiopod shells with coarser spatial resolution (Rodland *et al.* 2003), suggesting some of the variability, at least in pristine specimens, may be due to vital effects. Some of the intra-specimen variability found in modern brachiopods (Rodland *et al.* 2003) may also be partly due to tissue-specific $\delta^{18}\text{O}$ differences which is the largest cause of $\delta^{18}\text{O}$ variability in the Cambrian specimens examined here.

Rhombocorniculum

In total, 106 SIMS measurements were made on 38 *Rhombocorniculum* specimens from the Comley Limestones. Measurements on *Rhombocorniculum* specimens must be considered as analyses of the biogenic phosphatic wall of the sclerite (Tissue = wall), and analyses of the, sometimes phosphatic, abiogenic material that fills the central lumen (Tissue = core) of particular specimens (Table 4-2; see Appendix D).

The 48 measurements of the walls of 18 pristine *Rhombocorniculum* sclerites yielded $\delta^{18}\text{O}$ values of 3.34 ‰ to 14.54 ‰, with a mean value of 10.01 ‰. The 44 measurements on the walls of 20 altered *Rhombocorniculum* specimens yielded $\delta^{18}\text{O}$ values of 2.36 ‰ to 12.65 ‰, with a mean value of 7.58 ‰. The 14 measurements on the phosphatic infill of 8 *Rhombocorniculum* lumens yielded $\delta^{18}\text{O}$ values of 7.38 ‰ to 14.64 ‰, with a mean value of 11.46 ‰.

From measurements of the sclerite walls, the mean $\delta^{18}\text{O}$ value of pristine specimens is 2.43 ‰ heavier than the mean value from the altered specimens, consistent with the pattern observed in brachiopods and in the bulk analyses. However, the diagenetic phosphate of infilling the lumen of a few of the specimens is heavier than the wall measurements, by an average of 1.45 ‰. This may in part be due to differences in porosity, as the *Rhombocorniculum* sclerite wall is porous, comprising a stacked-straws, whilst the phosphatic infill of the central lumens has no observable porosity. However, this is unlikely to account for the entire difference between wall and lumen measurements, and there is likely to be a real underlying isotopic signal. This suggests that *Rhombocorniculum* sclerites may be more susceptible to isotopic alteration than was identified in the preservation protocol, but also that this alteration does not noticeably affect bulk $\delta^{18}\text{O}_{\text{phos}}$ values.

Torellella

A total of 27 measurements were made on 11 pristine *Torellella* specimens which yielded $\delta^{18}\text{O}$ values of 5.18 ‰ to 13.50 ‰, with a mean value of 9.68 ‰ (Table 4-2; see Appendix D). Although the *Torellella* tube walls are laminated, there were no

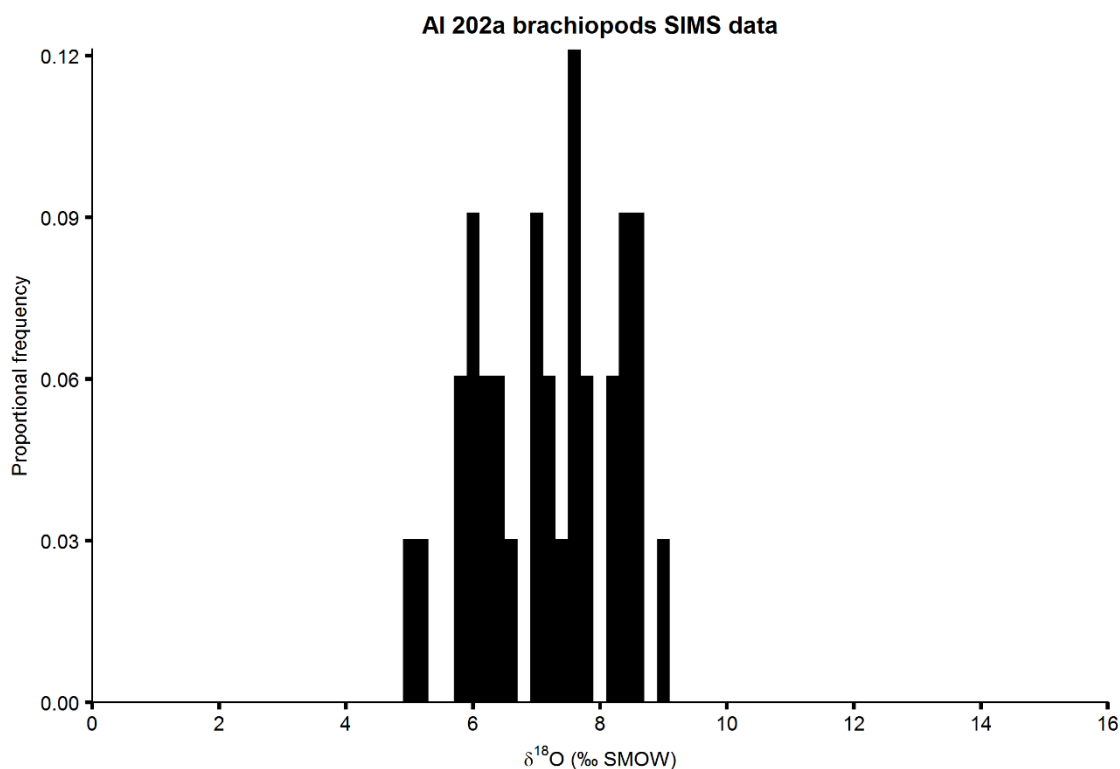


Figure 4-7. Histogram of SIMS analyses of linguliformean brachiopods from AI-202a.

identifiably different tissues. Although some areas appeared more porous than others, this is likely to be a polishing artefact.

The majority of analyses yielded much lighter $\delta^{18}\text{O}$ values than the bulk measurements of specimens from horizons Lb and Sa, and also lighter than pristine brachiopod compact laminae. Six specimens from the Comley Limestones horizon Lb were analysed and yielded $\delta^{18}\text{O}$ values of 9.59 ‰ to 13.50 ‰, with a mean value of 11.80 ‰. However, *Torellella* specimens from all other samples yielded $\delta^{18}\text{O}$ values much less than 10 ‰, comparable with brachiopod porous laminae. Whilst some of this may be attributable to matrix effects, there is likely to be a real underlying signal here.

SSFs from the High Atlas Mountains, Morocco

Thirty-one measurements were made on 14 specimens of linguliformean brachiopods from AI-202a (Table 4-2; see Appendix D). Following the protocol detailed in Chapter Three all of these specimens were found to be diagenetically altered. SIMS analyses of these altered brachiopod specimens yielded conspicuously light $\delta^{18}\text{O}$ values of 4.90 ‰ to 8.90 ‰, with a mean value of 7.18 ‰ (Table 4-2; Figure 4-7).

Most of the Moroccan specimens had a blocky appearance in cross section, lacking the laminated biological brachiopod microstructure of alternating compact and porous layers. This renders intra-specimen tissue-specific analysis impossible, but also

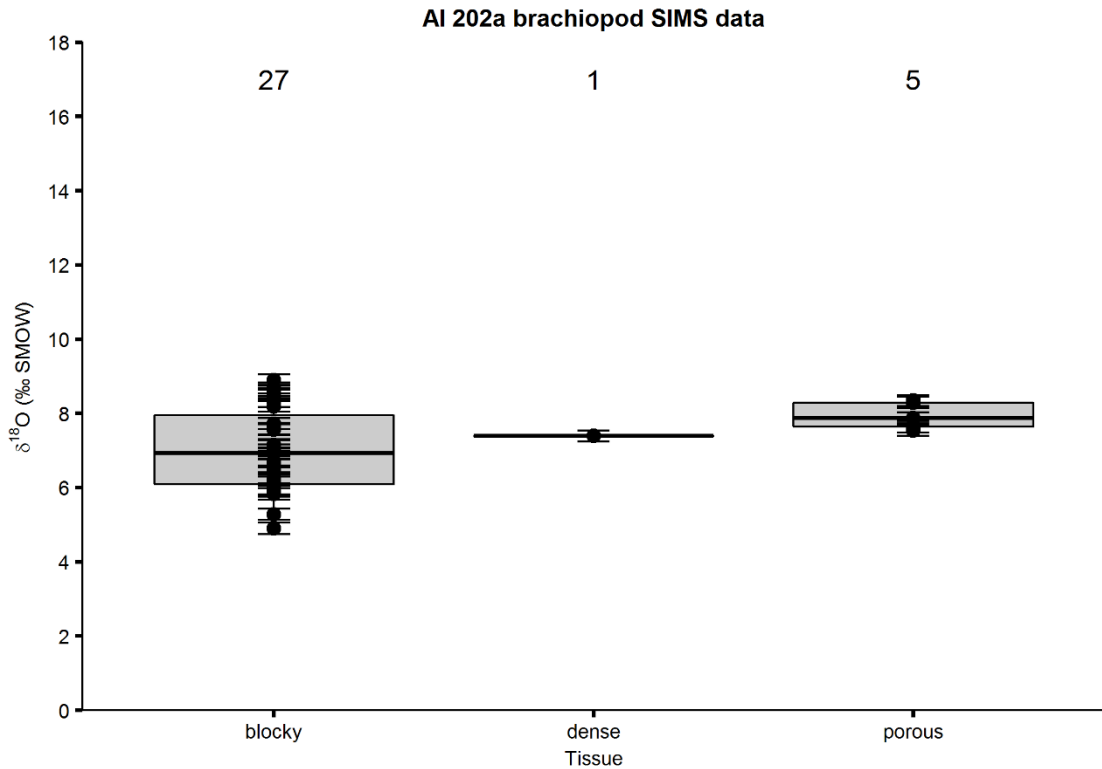


Figure 4-8. Boxplots of SIMS measurements on AI-202a brachiopods reveal that the shells are isotopically homogeneous.

suggests that there has been crude recrystallisation and potentially homogenisation of oxygen isotope values across each specimen. Twenty-seven analyses conducted on 12 specimens with blocky microstructure had a mean $\delta^{18}\text{O}$ value of 7.02 ‰, with a variance of 1.28 ‰.

However, biological laminae were resolvable in two specimens, and this allowed a small tissue-specific investigation of the Moroccan specimens. Five analyses of the porous laminae of two specimens yielded $\delta^{18}\text{O}$ values of 7.94 ‰ to 8.35 ‰, with a mean value of 7.94 ‰. A single analysis was possible on the compact laminae of one specimen, and this yielded a $\delta^{18}\text{O}$ value of 7.39 ‰.

The $\delta^{18}\text{O}$ values of both specimens that preserve porous and compact laminae is isotopically similar to the $\delta^{18}\text{O}$ values of the blocky specimens. Both tissues were within the range of values observed in the blocky analyses (Figure 4-8). This suggests that tissue-specific variability that is observed in specimens from the Comley Limestones is not wholly attributable to porosity differences or the growth of secondary, non-phosphate, minerals in the pore spaces.

Table 4-2. Summary of SIMS analyses conducted during this project.

Location	Horizon	Taxon	Preservation	Tissue*	Number of		$\delta^{18}\text{O}$			
					Specimens	Analyses	Mean	Variance	Minimum	Maximum
Comley	all	all	all	all	126	324	10.06	9.46	1.88	14.78
Comley	all	all	Altered	all	45	110	8.79	9.30	2.36	14.74
Comley	all	all	Pristine	all	81	214	10.70	8.35	1.88	14.78
Comley	all	Brachiopods	all	all	76	189	10.63	9.38	1.88	14.78
Comley	all	Brachiopods	all	dense	49	103	12.19	5.16	3.12	14.78
Comley	all	Brachiopods	all	porous	27	40	8.09	9.39	1.88	12.85
Comley	all	Brachiopods	Altered	all	24	64	9.69	9.78	3.12	14.74
Comley	all	Brachiopods	Altered	dense	12	29	10.94	10.07	3.12	14.74
Comley	all	Brachiopods	Altered	porous	10	14	8.61	5.71	4.33	11.44
Comley	all	Brachiopods	Pristine	all	52	125	11.11	8.57	1.88	14.78
Comley	all	Brachiopods	Pristine	dense	37	74	12.67	2.48	6.41	14.78
Comley	all	Brachiopods	Pristine	porous	17	26	7.81	11.45	1.88	12.85
Comley	all	<i>Hyolithellus</i>	Altered	all	1	2	6.69	12.30	4.21	9.17
Comley	all	<i>Rhombocorniculum</i>	all	all	38	106	9.19	8.88	2.36	14.64
Comley	all	<i>Rhombocorniculum</i>	all	core	8	14	11.46	7.37	7.38	14.64
Comley	all	<i>Rhombocorniculum</i>	all	wall	38	92	8.85	8.28	2.36	14.54
Comley	all	<i>Rhombocorniculum</i>	Altered	all (wall)	20	44	7.58	6.06	2.36	12.65
Comley	all	<i>Rhombocorniculum</i>	Pristine	all	18	62	10.33	7.82	3.34	14.64
Comley	all	<i>Rhombocorniculum</i>	Pristine	core	8	14	11.46	7.37	7.38	14.64
Comley	all	<i>Rhombocorniculum</i>	Pristine	wall	18	48	10.01	7.63	3.34	14.54

Comley	all	<i>Torellella</i>	Pristine	all	11	27	9.69	6.98	5.18	13.50
Comley	Aa	Brachiopods	Pristine	dense	2	2	13.94	0.24	13.59	14.29
Comley	Aa	Brachiopods	Pristine	intermediate	3	4	10.55	5.41	7.65	13.20
Comley	Aa	Brachiopods	Pristine	porous	3	4	5.96	16.42	1.88	11.44
Comley	Ad	Brachiopods	Pristine	dense	10	20	13.22	1.00	10.62	14.78
Comley	Ad	Brachiopods	Pristine	intermediate	3	3	11.73	0.73	10.78	12.43
Comley	Ad	Brachiopods	Pristine	porous	7	12	9.33	12.57	2.49	12.85
Comley	La2	Brachiopods	Altered	dense	1	1	10.27	NA	10.27	10.27
Comley	La2	Brachiopods	Altered	intermediate	4	7	6.22	3.24	3.77	9.77
Comley	La2	Brachiopods	Altered	porous	2	2	5.66	0.16	5.38	5.94
Comley	La2	Brachiopods	Pristine	dense	6	12	12.84	2.69	7.99	14.06
Comley	La2	Brachiopods	Pristine	intermediate	4	5	9.71	5.36	7.33	13.38
Comley	La2	Brachiopods	Pristine	porous	1	1	4.50	NA	4.50	4.50
Comley	La2	<i>Rhombocorniculum</i>	Altered	wall	3	4	8.00	6.76	4.10	9.42
Comley	La2	<i>Rhombocorniculum</i>	Pristine	core	1	3	10.63	0.22	10.18	11.12
Comley	La2	<i>Rhombocorniculum</i>	Pristine	wall	4	11	7.30	4.55	3.34	10.53
Comley	La2	<i>Torellella</i>	Pristine	dense	2	6	6.64	1.92	5.18	8.41
Comley	La2H	Brachiopods	Altered	dense	1	3	3.27	0.04	3.12	3.50
Comley	La2H	Brachiopods	Altered	porous	1	1	5.11	NA	5.11	5.11
Comley	La2H	Brachiopods	Pristine	dense	8	16	13.45	0.68	11.65	14.66
Comley	La2H	Brachiopods	Pristine	intermediate	2	2	8.71	7.68	6.75	10.67

Comley	La2H	<i>Rhombocorniculum</i>	Altered	wall	8	20	8.24	2.90	4.84	11.80
Comley	La2H	<i>Rhombocorniculum</i>	Pristine	core	1	3	7.82	0.15	7.38	8.09
Comley	La2H	<i>Rhombocorniculum</i>	Pristine	wall	1	5	10.47	0.14	9.89	10.92
Comley	La2H	<i>Torellella</i>	Pristine	dense	2	4	7.10	1.68	5.92	8.83
Comley	Lb	Brachiopods	Altered	dense	6	17	11.71	3.67	8.45	13.74
Comley	Lb	Brachiopods	Altered	intermediate	3	3	8.98	9.78	5.93	12.18
Comley	Lb	Brachiopods	Pristine	blocky	1	2	10.21	0.61	9.66	10.76
Comley	Lb	Brachiopods	Pristine	dense	9	21	11.47	3.48	6.41	13.87
Comley	Lb	Brachiopods	Pristine	intermediate	4	6	8.49	3.14	6.68	11.88
Comley	Lb	Brachiopods	Pristine	porous	3	5	5.49	3.36	2.49	7.32
Comley	Lb	<i>Rhombocorniculum</i>	Altered	wall	3	10	5.12	3.75	2.36	7.96
Comley	Lb	<i>Rhombocorniculum</i>	Pristine	core	5	7	12.92	4.70	8.07	14.30
Comley	Lb	<i>Rhombocorniculum</i>	Pristine	wall	8	21	10.06	7.27	5.64	13.61
Comley	Lb	<i>Torellella</i>	Pristine	dense	6	14	11.81	1.31	9.59	13.50
Comley	Lb	<i>Torellella</i>	Pristine	more porous	2	2	10.17	0.00	10.15	10.18
Comley	Sa	Brachiopods	Altered	blocky	1	2	5.74	1.86	4.77	6.70
Comley	Sa	Brachiopods	Altered	dense	4	8	12.28	3.13	10.05	14.74
Comley	Sa	Brachiopods	Altered	intermediate	5	9	11.17	2.52	9.31	14.51
Comley	Sa	Brachiopods	Altered	porous	7	11	9.47	3.63	4.33	11.44
Comley	Sa	Brachiopods	Pristine	dense	2	3	11.82	0.53	11.01	12.43
Comley	Sa	Brachiopods	Pristine	intermediate	3	3	10.86	0.85	9.97	11.81
Comley	Sa	Brachiopods	Pristine	porous	3	4	8.85	0.59	7.84	9.62

Comley	Sa	<i>Hyolithellus</i>	Altered	wall	1	2	6.69	12.30	4.21	9.17
Comley	Sa	<i>Rhombocorniculum</i>	Altered	wall	6	10	8.57	7.95	4.05	12.65
Comley	Sa	<i>Rhombocorniculum</i>	Pristine	core	1	1	14.64	NA	14.64	14.64
Comley	Sa	<i>Rhombocorniculum</i>	Pristine	wall	5	11	12.40	2.21	9.80	14.54
Comley	SaH	<i>Torellella</i>	Pristine	porous	1	1	7.68	NA	7.68	7.68
AI	202-a	Brachiopods	Altered	all	14	31	7.18	1.23	4.90	8.90
AI	202-a	Brachiopods	Altered	blocky	12	27	7.02	1.28	4.90	8.90
AI	202-a	Brachiopods	Altered	dense	1	1	7.39	NA	NA	NA
AI	202-a	Brachiopods	Altered	porous	2	5	7.94	0.14	7.54	8.35
STD	STD	Durango	STD	STD	6	292	8.67	0.08	7.42	9.34

*Tissues are defined as follows: blocky = absence of microstructure; dense = compact laminae of densely pack phosphate; intermediate = analysis spot includes both dense and porous laminae; porous = laminae with porosity and therefore lower density phosphate; resin = analysis spot was mostly or entirely in resin; STD = Durango standard analysis.

4.5. Discussion

The isotope data presented in this chapter show some consistent trends, briefly described above, but they deserve a fuller treatment. Importantly, there appear to be differences between specimens identified as well-preserved and specimens identified as altered (see Chapter Three). The ultimate goal from these isotope data is to provide estimates of Cambrian sea temperature (see Chapter Five), and it is therefore important to understand which data may be considered representative of palaeoenvironmental conditions and which may not.

4.5.1. Testing the efficacy of the preservation protocol

H1: Specimens identified as pristine will be isotopically heavier than specimens identified as diagenetically altered, for specimens from the same limestone sample.

In paired analyses of SSFs from the Comley Limestones, specimens identified *a priori* as pristine are isotopically heavier than their altered counterparts, with the mean pristine $\delta^{18}\text{O}_{\text{phos}}$ value 0.8 ‰ heavier than the altered $\delta^{18}\text{O}_{\text{phos}}$ value. In contrast, the means of potentially pristine and altered brachiopods from the Forteau Formation are not significantly separated (potentially pristine = 12.91 ‰; altered = 12.63 ‰). However, in each paired analysis of Forteau Formation specimens, the potentially pristine specimens are on average 0.4 ‰ heavier than altered specimens from the same horizon.

Furthermore, SIMS analyses found that potentially pristine specimens are also isotopically heavier than authigenic secondary phosphate. This is particularly apparent in analyses of specimens from sample DMQ which show a progression from the isotopically heaviest potentially pristine brachiopods (13.90 ‰), through lighter altered brachiopods (13.44 ‰) specimens, to the isotopically lightest phosphatised bivalve moulds (12.62 ‰).

The Comley and Forteau analyses should be contrasted with analyses of specimens from sample AI-202a, Morocco. The $\delta^{18}\text{O}$ values of the visually well-preserved and visibly altered samples from Ait Iyou (Morocco) are not significantly different to each other. This corroborates the more detailed observations following the preservation protocol (see §3.9.1) that all of these specimens have undergone some degree of alteration and recrystallisation. SIMS analyses of these samples demonstrate

that this is a pervasive isotopic alteration. These samples produce the lightest $\delta^{18}\text{O}$ values of any bulk samples analysed in this work.

The $\delta^{18}\text{O}$ value of a material is controlled by the $\delta^{18}\text{O}$ composition of the substance it formed from, and the temperature at which it formed. Therefore, diagenetic alteration of biominerals precipitated in equilibrium with seawater drives the mineral $\delta^{18}\text{O}$ to lighter values by facilitating isotopic exchange at elevated temperatures, and with fluids that are closer to the mantle $\delta^{18}\text{O}$ value of approximately 5.7 ‰ (Muehlenbachs & Clayton 1976). Alteration in contact with meteoric water is also likely to drive $\delta^{18}\text{O}$ to lighter values because of the comparatively lighter $\delta^{18}\text{O}$ composition of fresh water (Pearson 2012). Visually weathered limestone was removed prior to acetic acid maceration, so recent meteoric alteration is an unlikely cause of any isotopic differences in the samples analysed here. Therefore, the observed structural, chemical and isotopic alteration is more likely to have been caused by diagenesis affecting some of the specimens over the last > 500 million years.

In summary, bulk isotope analyses showed that specimens identified as pristine following the protocol detailed in Chapter Three are isotopically heavier than specimens from the same horizon which were identified as altered. Furthermore, both pristine and altered samples are typically heavier than samples of authigenic secondary phosphate. This reflects a diagenetic trend towards lighter values for more altered biogenic phosphate or phosphate with a later genetic origin. The isotope data therefore support the first hypothesis that pristine specimens are isotopically heavier than altered specimens and, further than that, pristine specimens are isotopically heavier than sedimentary or diagenetic phosphate.

4.5.2. *Tissue-specific variability*

H2: Within individual SSF specimens with both porous and compact laminae, and on average across all specimens in a sample, compact laminae are less susceptible to diagenetic alteration and will be isotopically heavier than porous laminae.

SIMS analyses of linguliformean brachiopod specimens from the Comley Limestones found consistent tissue-specific $\delta^{18}\text{O}$ variability (Figure 4-4), with compact laminae isotopically heavier, by at least 2 ‰, than porous laminae. SIMS $\delta^{18}\text{O}$ measurements of the compact laminae also have a much lower variance than measurements of the porous

laminae of these brachiopods. The $\delta^{18}\text{O}$ offset between compact and porous laminae is comparable with the offset observed between the hyaline and white matter tissues of conodont elements, where the higher porosity white matter is more susceptible to diagenetic alteration than compact laminae (Wheeley *et al.* 2012). This is also consistent with the observations presented in Chapter Three: that, in pristine brachiopod specimens, porous laminae show signs of elemental alteration, including incorporation of Fe and Mn, whilst compact laminae do not. The $\delta^{18}\text{O}$ data therefore support the interpretation that porous laminae are loci for diagenetic alteration and may act as conduits for diagenetic fluids.

However, this tissue-specific variation was also found in brachiopod specimens identified as altered, in which the compact laminae may also have undergone elemental alteration. Therefore, this tissue-specific variability may not reflect a true isotopic difference, but may instead be a technique-specific result arising from differences in texture, porosity, or chemical differences ('matrix effects') between the different tissues. These effects are not exclusive and can all influence the measured $\delta^{18}\text{O}$ composition of a mineral.

Porosity differences between the different laminae affect the amount of material that is analysed from each spot, which in turn affects the count rate of each oxygen isotope collected by the mass spectrometer. The greater the porosity difference the analysis spot and the Durango standard, the lower the accuracy of the measured $\delta^{18}\text{O}$ value. Porosity can also affect sample surface relief, due to the inherent surface irregularity within more porous materials and because porous materials are more difficult to polish smooth. The impact of surface relief on SIMS $\delta^{18}\text{O}$ measurements can be up to a few per mille (Kita *et al.* 2010), and therefore could cause the observed $\delta^{18}\text{O}$ variability.

Furthermore, measured $\delta^{18}\text{O}$ values can be influenced by the elemental composition of the analysed material, and such 'matrix effects' are well-documented in carbonate systems (e.g. Rollion-Bard & Marin-Carbonne 2011; Śliwiński *et al.* 2015). As shown in Chapter Three, the fossil material and the Durango standards are not perfectly matrix-matched, and the more porous laminae of fossil specimens were enriched in elements indicative of diagenetic alteration, notably Fe and Mn. These elements are likely to be present in clays, or as metal oxides which will have the dual effects of distorting the measured $\delta^{18}\text{O}$ value and adding a contaminating oxygen isotope source. Biogenic apatite can also include substantial quantities of Mg, with the

extant phosphatic brachiopod *Discina* having up to 6.7 wt% (Williams *et al.* 1997a). Trace quantities of Fe, Mn and Mg can all affect $\delta^{18}\text{O}$ measurements in the carbonate system (Śliwiński *et al.* 2015), and although no systematic study has been conducted on phosphatic materials, it could also be a problem here.

However, of the Moroccan brachiopod specimens, which are mostly recrystallised and display near-uniform $\delta^{18}\text{O}$ values, those specimens that do preserve biogenic microstructures do not display the same tissue-specific $\delta^{18}\text{O}$ variability seen in the Comley Limestones brachiopods. This suggests that the variability observed in the Comley Limestones specimens cannot be wholly explained by porosity or matrix effects, but is instead likely to include at least a component of tissue-specific $\delta^{18}\text{O}$ variability, either biogenic or diagenetic.

In summary, tissue-specific variability in linguliformean brachiopod $\delta^{18}\text{O}$ measurements is large, and whilst some of the signal may be due to SIMS technique-specific effects relating to porosity and chemical composition these cannot wholly account for the observed signal. The isotope data support the second hypothesis, that compact laminae are less susceptible to diagenetic alteration and therefore isotopically heavier than are porous laminae. Intra-specimen tissue-specific variability should be considered when examining inter-specimen variability. This means that comparisons between specimens should be made between analyses of the same tissues, which in linguliformean brachiopods is either the compact or porous laminae.

4.5.3. *Inter-specimen variability*

H3: In situ $\delta^{18}\text{O}$ analyses of specimens identified as pristine will have a lower variance than in situ $\delta^{18}\text{O}$ analyses of specimens identified as diagenetically altered, for specimens taken from the same horizon or limestone sample.

Because of the high degree of tissue-specific intra-specimen variability, inter-specimen comparisons are drawn between measurements made on the same tissues of each SSF. The variance of all $\delta^{18}\text{O}$ measurements on the compact laminae of pristine brachiopods ($n = 37$) from the Comley Limestones is 2.48 ‰, and for altered brachiopods ($n = 12$) is 10.07 ‰ (Table 4-2), supporting the third hypothesis. However, the variance of $\delta^{18}\text{O}$ measurements on the porous laminae of pristine brachiopods ($n = 17$) from the Comley Limestones is 11.45 ‰, compared to 5.71 ‰ for altered brachiopods ($n = 10$).

Preferential alteration of the porous laminae, discussed above, is likely to be the cause of this. Because alteration preferentially affects the porous laminae, pristine specimen porous laminae will have a combination of altered and well-preserved $\delta^{18}\text{O}$ values, whereas altered specimen porous laminae will all reflect diagenetic conditions.

The variance of measurements on the walls of pristine *Rhombocorniculum* sclerites ($n = 18$) from the Comley Limestones is 7.63 ‰, whereas the variance of measurement on altered specimens ($n = 20$) is 6.06 ‰ (Table 4-2). This does not support the third hypothesis of increasing variance with increasing alteration. In the case of *Rhombocorniculum*, interpretation is complicated by the porosity of the sclerite which will have a substantial direct effect on SIMS measurements. The porosity of the sclerite may also make diagenetic alteration more likely, either of the phosphate component of the apatite lattice, or of the structural and channel carbonate and hydroxyl ions which also contribute to SIMS measurements. Further investigation of the cation composition of *Rhombocorniculum* apatite is necessary for a full interpretation of these results. *Rhombocorniculum* $\delta^{18}\text{O}$ data should be considered with caution, pending further work.

In contrast to data from the Comley Limestones, the variance of $\delta^{18}\text{O}$ measurements on the Moroccan brachiopod specimens ($n = 14$) is remarkably low, at 1.17 ‰ (Table 4-2). Combined with the near-identical bulk isotope analyses of visually well-preserved and altered Moroccan brachiopods, the low variance suggests that the Moroccan strata have been pervasively diagenetically altered and are isotopically homogeneous. The uniformity of $\delta^{18}\text{O}$ values seen in these specimens indicates a high degree of alteration in contrast to the relatively minor offsets observed between pristine and altered specimens from the Comley Limestones.

The third hypothesis, that measurements of pristine specimens will have a lower variance than measurements of altered is supported by analyses of the compact laminae of linguliformean brachiopods from the Comley Limestones. However, analyses of *Rhombocorniculum* sclerites do not support this hypothesis, and nor do analyses of the porous laminae of linguliformean brachiopods. This may be because both *Rhombocorniculum* and brachiopod porous laminae are porous, and therefore more susceptible to diagenetic alteration and/or more pronounced matrix effects, than brachiopod compact laminae. Isotope measurements on *Rhombocorniculum* sclerites should therefore be viewed with caution and will not be used for palaeoenvironmental interpretations in this thesis. Interestingly, analyses of Moroccan brachiopods suggest

that variance decreases with extensive diagenetic alteration leading to homogenisation of isotope values. Therefore, whilst the hypothesis of increasing variance with increasing alteration can be accepted for measurements on little-altered brachiopod compact laminae, more nuanced hypotheses are needed to explain inter-specimen variability across the whole dataset.

4.5.4. Comparing analytical techniques: silver phosphate outperforms SIMS for ancient brachiopods

Because the majority of brachiopod shell phosphate mass is localised in the compact laminae (Williams *et al.* 2007; Schmahl *et al.* 2008), bulk $\delta^{18}\text{O}_{\text{phos}}$ values are likely to predominantly reflect the isotopic signal of the compact laminae. However, SIMS analyses of brachiopod compact laminae and bulk silver phosphate analyses do not yield identical results. Typically, the $\delta^{18}\text{O}_{\text{phos}}$ values of bulk analyses are 1 ‰ to 2 ‰ heavier than SIMS analyses of compact laminae, and much heavier than SIMS analyses of porous laminae (Figure 4-4). This may be due to difference in the matrix effects of the fossil and standard materials (e.g. Rollion-Bard & Marin-Carbonne 2011; Śliwiński *et al.* 2015), or it may be due to SIMS analyses incorporating a high proportion oxygen from non-phosphate sources, such as OH^- and CO_3^{2-} ions, into the $\delta^{18}\text{O}$ signal.

The variability observed within the compact laminae of pristine specimens, in excess of 2 ‰, is likely due to a combination of original vital effects (Rodland *et al.* 2003) and minor thermal alteration associated with burial diagenesis (Wheeley *et al.* 2012). However, the bulk silver phosphate $\delta^{18}\text{O}$ values of phosphatic microfossils that have been subjected to minor thermal alteration can still retain a palaeoenvironmentally informative signal (Joachimski *et al.* 2009). The aim of this work is to investigate the potential utility of phosphatic SSFs in interrogating early Cambrian environments. The discrepancy between silver phosphate and SIMS $\delta^{18}\text{O}$ values found in this study suggest that the SIMS analyses of these SSFs are subject to substantial porosity and matrix effects, as well as including $\delta^{18}\text{O}$ contributions from non-phosphate-bound oxygen such as hydroxyl and carbonate ions. Furthermore, all phosphate oxygen-temperature equations derived to date are based on silver phosphate measurements, incorporating only phosphate-bound oxygen (Longinelli & Nuti 1973; Kolodny *et al.* 1983; Lécuyer *et al.* 1996, 2013; Kim & O'Neil 1997; Pucéat *et al.* 2010; Chang & Blake 2015).

The most appropriate method for investigating ancient linguliformean brachiopod $\delta^{18}\text{O}$ values, therefore, is to use silver phosphate analyses for palaeoenvironmentally

informative data and *in situ* SIMS analyses to interrogate the isotopic preservation and internal variability of bulk samples. This approach ensures that the source of oxygen isotope data used for palaeoenvironmental interpretations is well constrained, i.e. that it comes from the phosphate-bound oxygen rather than from other sources. This also mitigates for the risk of conflicting matrix effects between standard and sample materials that is inherent in SIMS analyses from biasing palaeoenvironmental interpretations.

4.5.5. A palaeolatitudinal $\delta^{18}\text{O}$ gradient

H4: Pristine specimens sampled from different palaeolatitudes will be isotopically distinct from each other.

Most palaeocontinental reconstructions for Cambrian Series 2 Stage 4, approximately 515 Mya to 509 Mya, place the UK (Avalonia) at approximately 60 °S to 70 °S and western North America (Laurentia) at 15 °S to 30 °S (See Chapter Two and Chapter Six; Torsvik & Cocks 2009, 2013, 2016; Landing *et al.* 2013b). Bulk analyses of pristine SSFs from the Comley Limestones yielded $\delta^{18}\text{O}_{\text{phos}}$ values of 13.30 ‰ to 15.17 ‰, with a mean value of 14.43 ‰ (Table 4-1). Bulk, silver phosphate, analyses of potentially pristine SSFs from the Forteau Formation yielded $\delta^{18}\text{O}_{\text{phos}}$ values 11.84 ‰ to 13.90 ‰, with a mean value of 12.91 ‰. The mean $\delta^{18}\text{O}_{\text{phos}}$ values of pristine phosphatic SSFs from the low palaeolatitude Forteau Formation are 1.52 ‰ lighter than the mean $\delta^{18}\text{O}_{\text{phos}}$ values of pristine phosphatic SSFs from the higher palaeolatitude Comley Limestones.

Because of the inverse relationship between $\delta^{18}\text{O}$ values and temperature (see Chapter Five), lighter $\delta^{18}\text{O}$ values are expected from biominerals precipitated in warmer tropical settings compared to heavier $\delta^{18}\text{O}$ values from cooler high latitude settings. The higher latitude Avalonian SSFs are isotopically heavier than the Laurentian SSFs, which is consistent with the hypothesised palaeolatitudinal positions of each continent during the early Cambrian. This is more fully discussed in Chapter Five.

4.6. Conclusions

The preservation protocol devised in Chapter Three successfully distinguishes early Cambrian phosphatic fossils that are isotopically distinct. Isotopically pristine biogenic phosphate is preserved in phosphatic SSFs from the Comley Limestones, UK, and the

Forteau Formation, Canada, but not in SSFs from the Issafen Formation, Morocco. In bulk silver phosphate analyses, specimens identified *a priori* as pristine have heavier $\delta^{18}\text{O}_{\text{phos}}$ values than specimens identified *a priori* as altered. Furthermore, this appears to form a diagenetic trend towards the lighter isotope values of early diagenetic or authigenic sedimentary phosphate.

However, there is high within-sample variability caused by high variability within and between individual specimens. Intra-specimen variability is most severe as a tissue-specific effect whereby porous laminae are at least 2 ‰ lighter than compact laminae in pristine brachiopod specimens. This is likely to be due to a combination of porosity and matrix effects, and the inclusion of $\delta^{18}\text{O}$ contributions from non-phosphate-bound oxygen, as well as genuine differences in phosphate oxygen isotopic composition as porous laminae are more susceptible to diagenetic alteration than are compact laminae. Nevertheless, compact laminae comprise the majority of brachiopod shell phosphate, this does not have a substantial influence on bulk silver phosphate measurements.

Inter-specimen variability, accounting for tissue-specific variability, is greater in altered samples than in pristine samples, as has been documented in conodont element phosphate (Wheeley *et al.* 2012). Nevertheless, the variance of SIMS $\delta^{18}\text{O}$ measurements within all pristine samples from the Comley Limestones is still appreciable. Therefore, it is recommended that $\delta^{18}\text{O}_{\text{phos}}$ values from bulk silver phosphate analyses are used for drawing any palaeoenvironmental interpretations, with SIMS analyses being used to further interrogate isotopic preservation of samples. Bulk isotope analyses can absorb and mitigate for this increase in inter-specimen variability by recovering the average $\delta^{18}\text{O}_{\text{phos}}$ value of a large sample comprising tens to a few hundred individual specimens.

Furthermore, isotopic differences were observed between specimens from different palaeolatitudes. Therefore, phosphatic SSFs are a potentially valuable source of Cambrian $\delta^{18}\text{O}$ data, though fossil materials must be carefully screened for diagenetic alteration before isotope analyses are conducted, and phosphate crystallite preservation appears to be of critical importance. The palaeoclimatic implications of these early Cambrian biogenic phosphate $\delta^{18}\text{O}_{\text{phos}}$ values are discussed in detail in the following chapter.

Chapter Five: Early Cambrian sea surface temperatures

5.1. Chapter summary

In this chapter, the pristine $\delta^{18}\text{O}_{\text{phos}}$ data presented in Chapter Four are considered in the context of Palaeozoic $\delta^{18}\text{O}$ data in the literature. The secular trend in $\delta^{18}\text{O}$ values with age is considered, along with the implications this has for the evolution of the $\delta^{18}\text{O}$ value of sea water on geological timescales. Pristine $\delta^{18}\text{O}_{\text{phos}}$ data from the Comley Limestones (Avalonia) and the Forteau Formation (Laurentia) are used to estimate high and low latitude sea surface temperatures (SSTs) for early Cambrian oceans. Elements of this chapter, including the Comley Limestones data and a précis of the discussion on the isotopic composition of sea water, were recently published by Hearing *et al.* (2018).

5.2. Introduction

The Cambrian Period has historically been considered as a greenhouse climate interval, a conclusion drawn from geological data and indirect geochemical evidence such as the strontium isotope curve (Brasier 1992a; Peters & Gaines 2012; Boucot *et al.* 2013; Erwin & Valentine 2013). However, detailed and precise reconstructions of Cambrian climate have been hindered by the lack of quantitative palaeoenvironmental proxy data, in particular data for constraining sea temperatures. The stable oxygen isotope ratio ($\delta^{18}\text{O}$), perhaps the most commonly used geochemical palaeoclimate proxies, can now be applied to carefully selected and screened Cambrian phosphatic small shelly fossils (SSFs; see Chapter Three).

Analyses of pristine SSFs from the Comley Limestones, Avalonia, yielded a mean $\delta^{18}\text{O}_{\text{phos}}$ value of 14.4 ‰, and pristine SSF samples from the Forteau Formation, Laurentia, yielded a mean $\delta^{18}\text{O}_{\text{phos}}$ value of 12.9 ‰ (see Chapter Four). These $\delta^{18}\text{O}_{\text{phos}}$ measurements are comparable to $\delta^{18}\text{O}$ values from low latitude Early Ordovician conodont elements (Bassett *et al.* 2007; Trotter *et al.* 2008; Wheeley *et al.* 2012, 2018; Quinton *et al.* 2018), but interpretation of these values requires a nuanced discussion (see §5.4.1). The Cambrian $\delta^{18}\text{O}_{\text{phos}}$ measurements detailed in Chapter Four can be combined with a $\delta^{18}\text{O}_{\text{phos}}$ temperature equation in order to calculate estimates for early Cambrian sea surface temperatures (SSTs).

5.3. Phosphate oxygen temperature equations

There are several empirically derived phosphate oxygen isotope temperature equations, labelled equations 1 to 6 in Table 5-1, calculated from silver phosphate $\delta^{18}\text{O}_{\text{phos}}$

measurements on phosphate biomineralising marine invertebrates (Longinelli & Nuti 1973; Lécuyer *et al.* 1996), vertebrates (Kolodny *et al.* 1983; Pucéat *et al.* 2010), or both (Lécuyer *et al.* 2013), and from abiogenic synthetic phosphate (Chang & Blake 2015). Although there are differences between these equations, no systematic, taxonomic, variation is seen. Vital effects are accounted for in the empirical derivation of each equation, though plotting both vertebrate and invertebrate data together suggest that any vital effects are negligible in comparison to analytical uncertainty (Lécuyer *et al.* 1996, 2013). Phosphate in the shells of marine invertebrates and in the teeth of marine vertebrates is therefore likely to be precipitated in isotopic equilibrium with the surrounding sea water.

However, there have been problems with the application of equations 4 (Pucéat *et al.* 2010) and 6 (Chang & Blake 2015) to invertebrate fossil material (Bergmann *et al.* 2018), and neither equation is derived from data from invertebrate taxa. Equation 1 (Longinelli & Nuti 1973) does not have an uncertainty envelope associated with it, and equation 2 (Kolodny *et al.* 1983) is based purely on analyses of vertebrate material. Because equation 5 (Lécuyer *et al.* 2013) is an update on equation 3 (Lécuyer *et al.* 1996), equation 5 is considered to be the most appropriate for use in this study. For comparative purposes, and following discussion of the parameters, temperature estimates are shown from each of the equations.

Assuming they are well preserved, the $\delta^{18}\text{O}_{\text{phos}}$ values of phosphatic marine fossils are composite signals incorporating contributions from the oxygen isotopic composition of local sea water ($\delta^{18}\text{O}_{\text{sw}}$), and the temperature (T) of the sea water. Each $\delta^{18}\text{O}_{\text{phos}}$ temperature equation therefore has two unknowns: $\delta^{18}\text{O}_{\text{sw}}$ and T , with calculations of one requiring knowledge or assumption of the other (see §5.4).

Table 5-1. Published phosphate oxygen isotope temperature equations.

Eqn	Reference	Equation	Description
1	Longinelli & Nuti (1973)	$T(^{\circ}C) = 111 - 4.3(\delta^{18}O_{phos} - \delta^{18}O_{sw})$	The first published phosphate oxygen temperature equation; derived from the phosphatic shells of various invertebrates.
2	Kolodny <i>et al.</i> (1983)	$T(^{\circ}C) = 119.3(\pm 12.9) - 4.38(\pm 0.54)(\delta^{18}O_{phos} - \delta^{18}O_{sw})$	A revised phosphate oxygen temperature equation derived from fish and shark material.
3	Lécuyer <i>et al.</i> (1996)	$T(^{\circ}C) = 112.2(\pm 15.3) - 4.2(\pm 0.71)(\delta^{18}O_{phos} - \delta^{18}O_{sw})$	Derived from extant phosphatic brachiopods.
4	Pucéat <i>et al.</i> (2010)	$T(^{\circ}C) = 118.7(\pm 4.9) - 4.22(\pm 0.20)(\delta^{18}O_{phos} - [22.6 - \delta^{18}O_{NBS120c}] - \delta^{18}O_{sw})$	Derived from recent fish and shark material. Correction term to account for the value of NBS120c, currently 21.7 ‰ (Joachimski & Lambert 2015).
5	Lécuyer <i>et al.</i> (2013)	$T(^{\circ}C) = 117.4(\pm 9.5) - 4.50(\pm 0.43)(\delta^{18}O_{phos} - \delta^{18}O_{sw})$	A revised version of Lécuyer <i>et al.</i> (1996) combining extant brachiopod data with fish and shark data.
6	Chang & Blake (2015)	$T(^{\circ}C) = 273.15 + \frac{14430(\pm 380)}{1000 \ln \left(\frac{\delta^{18}O_{phos} + 1000}{\delta^{18}O_{sw} + 1000} \right) + 26.54(\pm 1.33)}$	Derived from synthetic apatite; originally in °K, rearranged here to for °C.

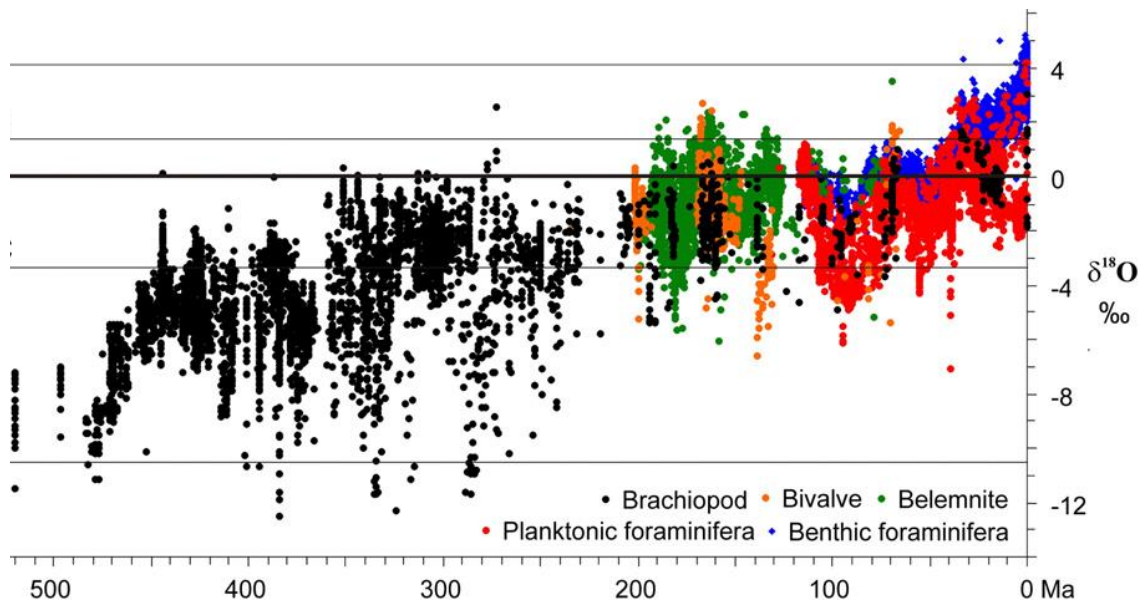


Figure 5-1. Carbonate biomineral $\delta^{18}\text{O}$ values become lighter back through the stratigraphic record. Modified from Veizer & Prokoph (2015), fig. 1.

5.4. The oxygen isotopic composition of Cambrian seas

The $\delta^{18}\text{O}$ composition of biominerals is strongly controlled by the $\delta^{18}\text{O}$ composition of the fluid from which it forms. The $\delta^{18}\text{O}$ composition of local sea water ($\delta^{18}\text{O}_{\text{sw}}$) is a function of the average global value in the oceans and the regional precipitation–evaporation (P/E) balance, which is the main cause of local variation around the global value (Pearson 2012). Freshwater sources, such as riverine input or ice melt-water from glaciers and ice sheets, can further modify local $\delta^{18}\text{O}_{\text{sw}}$.

5.4.1. Secular variation

There is a long-recognised trend of increasingly light (more negative) $\delta^{18}\text{O}$ values in the rock and fossil record with increasing age (Figure 5-1; Figure 5-2; e.g. Luz *et al.* 1984; Hudson & Anderson 1989; Veizer *et al.* 1999; Prokoph *et al.* 2008; Giles 2012; Grossman 2012b; Veizer & Prokoph 2015). Comparable secular trends have been documented in both whole-rock and biomineral $\delta^{18}\text{O}$ records throughout the Phanerozoic Eon. The most pronounced slope is found in the Palaeozoic record, and particularly the early Palaeozoic record where biomineral data are sparse. Cambrian biomineral $\delta^{18}\text{O}$ data are now beginning to fill this gap (Figure 5-2). The $\delta^{18}\text{O}$ secular trend requires consideration, as it may relate to the variation of $\delta^{18}\text{O}_{\text{sw}}$ values through time.

There are three commonly discussed explanations for the secular trend:

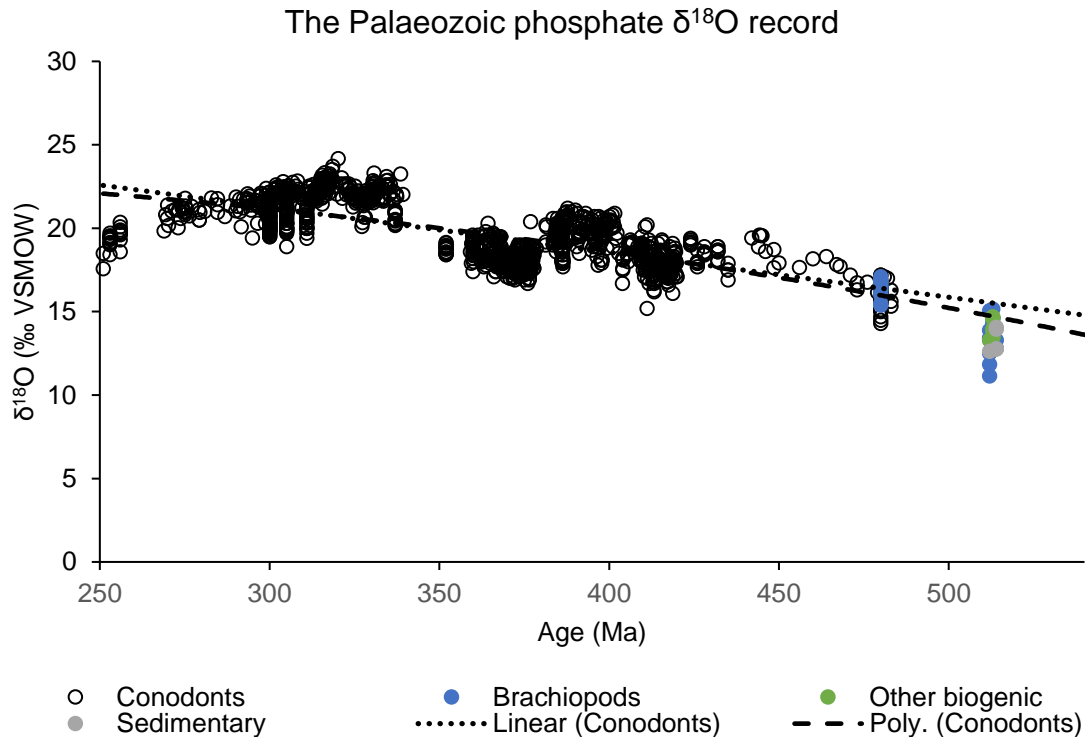


Figure 5-2. The Palaeozoic phosphate $\delta^{18}\text{O}$ record with superimposed linear and second order polynomial regression lines through the conodont dataset and projected back to the beginning of the Phanerozoic Eon. See Appendix E for details and references.

- a. the trend is due to progressive diagenetic alteration with increasing age (e.g. Degens & Epstein 1962; Killingley 1983);
- b. the trend is a real signal that reflects global cooling over the Phanerozoic Eon (e.g. Bassett *et al.* 2007; Trotter *et al.* 2008; Quinton *et al.* 2018); or
- c. the trend is a real signal that reflects an increasingly heavy (more positive) $\delta^{18}\text{O}$ composition of the global ocean over the Phanerozoic Eon (e.g. Veizer *et al.* 1999; Veizer & Prokoph 2015).

The null hypothesis, that the trend is due to increasing isotopic alteration with increasing age, is undermined by the co-occurrence of similar trends in the carbonate, phosphate and silica $\delta^{18}\text{O}$ records, and the recovery of similar magnitude signals from rocks of different localities and ages (Knauth & Epstein 1976; Luz *et al.* 1984; Hudson & Anderson 1989; Veizer *et al.* 1999; Grossman 2012b). The $\delta^{18}\text{O}$ values of the three mineral systems record similar second order isotopic excursions superimposed on the overall trend (e.g. Grossman 2012b). It is difficult to see how three common rock-forming oxygen species, carbonate, phosphate and silica, could have been systematically altered by similar degrees on a global scale without obliterating second-order signals that are also preserved in the $\delta^{18}\text{O}$ records from all three species on a

global scale. Furthermore, the low-Mg calcite fossils that originally revealed the secular trend in $\delta^{18}\text{O}$ data also record long- and short-period variability in the C, S, and Sr isotope systems, which is also unlikely if the fossils have been subjected to pervasive alteration (Veizer *et al.* 1999; Giles 2012). Although diagenesis is likely to account for some of the increased variability in geologically older data, it cannot account for the entire trend (Veizer *et al.* 1999; Grossman 2012a; Veizer & Prokoph 2015).

Long-term cooling of the Earth's ocean and atmosphere system has also been invoked to explain the secular trend in the $\delta^{18}\text{O}$ record (Knauth & Epstein 1976; Trotter *et al.* 2008). Global cooling of sufficient magnitude to account for the trend in the $\delta^{18}\text{O}$ record requires early Palaeozoic SSTs of more than 60 °C (Veizer & Prokoph 2015), exceeding the thermal tolerance of marine metazoans which is considered to be 45 °C to 47 °C from thermodynamic arguments (Pörtner 2001; Dilly *et al.* 2012), though appears to be below 44 °C for most modern marine metazoans (Hicks & McMahon 2002; Nguyen *et al.* 2011). Even most thermophilic eukaryotes have a thermal tolerance somewhat below 60 °C (Tansey & Brock 1972; Ravaux *et al.* 2013). Taking this approach implies biologically unfeasible temperatures dominated the oceans during the early Palaeozoic metazoan radiations.

There was indisputably an interval of declining temperatures between the end of the Cambrian Period and the Late Ordovician Hirnantian glaciation (Trotter *et al.* 2008; Vandenbroucke *et al.* 2010; Pohl *et al.* 2016). However, this cannot account for the continuation of the trend towards more recent heavier $\delta^{18}\text{O}$ values through the rest of the Palaeozoic, especially where second order, glacioeustatic, $\delta^{18}\text{O}$ signals are found superimposed on the long-term trend (Joachimski *et al.* 2006). Whilst a general lowering of global temperatures may account for some of the $\delta^{18}\text{O}$ trend, that alone cannot explain the entire Phanerozoic-scale trend.

This leaves the possibility that $\delta^{18}\text{O}_{\text{sw}}$ values have changed over time. Biogenic and whole-rock $\delta^{18}\text{O}$ data (Veizer *et al.* 1999; Veizer & Prokoph 2015) and $\delta^{18}\text{O}$ model data (Kasting *et al.* 2006; Jaffrés *et al.* 2007) suggest that the early Phanerozoic global average $\delta^{18}\text{O}_{\text{sw}}$ value was approximately -6‰ (Figure 5-3), increasing by an average of 0.01 ‰ per million years to the present day (ice-free) value of -1‰ . This is much more than the 1.4 ‰ shift attributable to the complete melting of glaciers and polar ice sheets (Lhomme *et al.* 2005). Oxygen isotope studies on Palaeozoic greenhouse intervals commonly assume a -1‰ value for $\delta^{18}\text{O}_{\text{sw}}$ (after Shackleton & Kennett 1975; e.g.

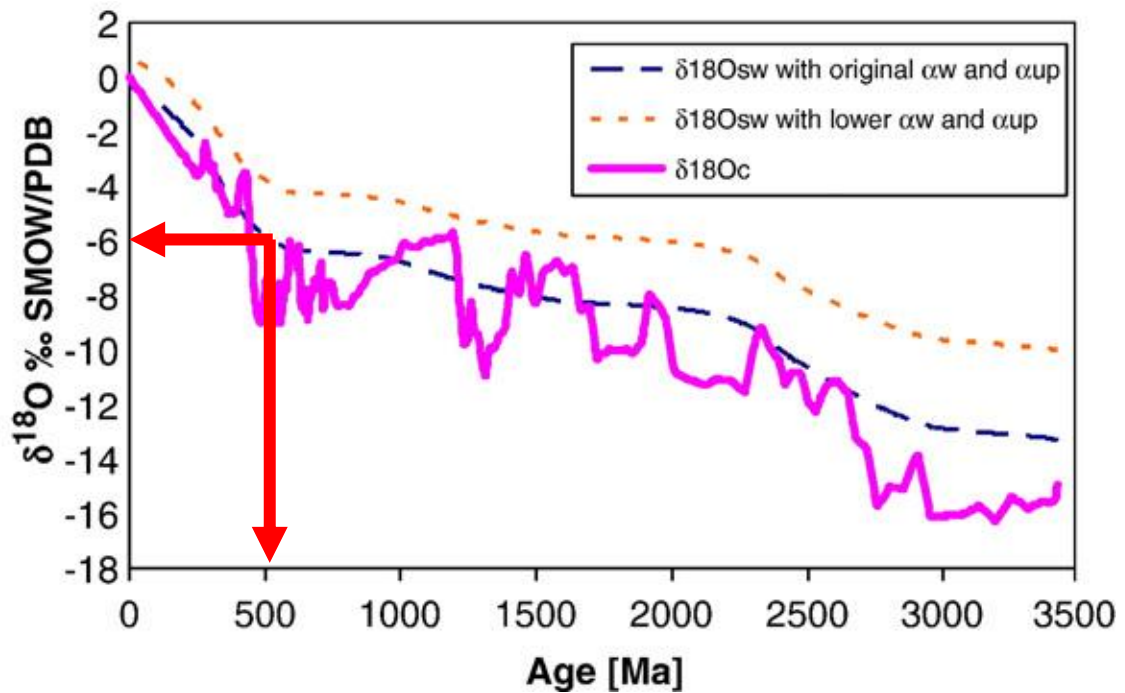


Figure 5-3. Modelling $\delta^{18}\text{O}_{\text{sw}}$ over Earth history predicts a value of approximately -6‰ for the early Phanerozoic. Adapted from Jaffrés *et al.* (2007), fig. 18.

Bassett *et al.* 2007; Trotter *et al.* 2008; Joachimski *et al.* 2009). Therefore, ice sheet fluctuations cannot account for the magnitude or consistency of the $\delta^{18}\text{O}$ trend.

On geological timescales, the first order control on global $\delta^{18}\text{O}_{\text{sw}}$ are the relative rates of hot hydrothermal alteration of oceanic crustal rocks and cold weathering of oceanic and continental crustal rocks (Muehlenbachs & Clayton 1976; Gregory & Taylor 1981). The balance of hot and cold alteration has been argued to maintain a constant $\delta^{18}\text{O}_{\text{sw}}$ value of $0 \pm 1\text{‰}$ over at least the Phanerozoic Eon (Muehlenbachs & Clayton 1976; Gregory & Taylor 1981; Gregory 1991; Muehlenbachs 1998). Cold alteration, i.e. weathering, of submarine basalts, $T < 250\text{ °C}$ to 350 °C , and increased terrestrial weathering, are sinks for ^{18}O and sources of ^{16}O in ocean water, and drive $\delta^{18}\text{O}_{\text{sw}}$ towards lighter values (Muehlenbachs 1998). Hot interactions of fluids and submarine basalt (hydrothermal alteration), $T > 250\text{ °C}$ to 350 °C , have the opposite effect, providing an ^{18}O source and ^{16}O sink driving $\delta^{18}\text{O}_{\text{sw}}$ towards heavier values (Muehlenbachs 1998).

The long-term balance of hot and cold submarine alteration is supported by analyses of oceanic crust from deep sea drilling or ophiolite outcrops. More recent support has also come from the developing field of carbonate clumped isotopes (Δ_{47} ; Came *et al.* 2007; Finnegan *et al.* 2011; Cummins *et al.* 2014; Bergmann *et al.* 2018; Henkes *et al.* 2018; Ryb & Eiler 2018). Initial concerns of inter-lab comparability

(Came *et al.* 2014) are beginning to be resolved and, although this remains under active debate, the technique is becoming more reliable (Henkes *et al.* 2018).

Nonetheless, deep time Δ_{47} temperature estimates are often very warm, with the process of determining the most reasonable temperature estimates often coming down to merely selecting the lowest values (Veizer & Prokoph 2015). These Δ_{47} temperature estimates commonly range into the biologically unfeasible, contradicting geological, palaeontological and climate model evidence (Vandenbroucke *et al.* 2009, 2010; Ghienne *et al.* 2014; Pohl *et al.* 2016), and often result in very heavy (positive) $\delta^{18}\text{O}_{\text{sw}}$ estimates that require exceptional and *ad hoc* explanations (Finnegan *et al.* 2011; Veizer & Prokoph 2015; Bergmann *et al.* 2018).

Similar *ad hoc* thresholds were used in recent work examining Palaeozoic dolomites for their Δ_{47} temperature and consequent $\delta^{18}\text{O}_{\text{sw}}$ estimates (Ryb & Eiler 2018). These analyses also experience the problem of unreasonably heavy (positive) $\delta^{18}\text{O}_{\text{sw}}$ estimates in both stratigraphically young and old samples (see also Veizer & Prokoph 2015). Furthermore, linear regression through the Palaeozoic dolomite water $\delta^{18}\text{O}$ estimates has a gradient of approximately 0.011 ‰ per million years, comparable to the $\delta^{18}\text{O}_{\text{sw}}$ gradient estimated from the carbonate $\delta^{18}\text{O}$ record (Veizer *et al.* 1999; Giles 2012; Veizer & Prokoph 2015) and modelled $\delta^{18}\text{O}$ data (Kasting *et al.* 2006; Jaffrés *et al.* 2007). The dolomite water $\delta^{18}\text{O}$ estimates are systematically heavier, by approximately 6.5 ‰ to 9.5 ‰, than the values estimated from the carbonate record. This result is expected of dolomite that formed in equilibrium with an isotopically heavy brine derived from normal sea water, as may be happening in parts of the Bahamas today (Murray & Swart 2017). Note that this also provides a mechanism for increasingly light dolomite water $\delta^{18}\text{O}$ estimates with age, as older dolomite-forming waters would have derived from isotopically lighter sea water.

Recent application of the clumped isotope thermometer to structural carbonate in the apatite of modern linguliformean brachiopods (Bergmann *et al.* 2018) yielded Δ_{47} temperature estimates exceeding 50 °C, far above the measured environmental annual mean temperatures, calling into question the reliability of this technique to recover palaeoenvironmental signals from some biominerals. Laboratory tests suggest that carbonate clumped isotope values may be robust to burial diagenesis on geological timescales at burial temperatures up to 100 °C (Dennis & Schrag 2010; Henkes *et al.* 2014). However, because Δ_{47} alteration is a lattice-level process, requiring only the re-organisation of adjacent carbonate C–O bonds, Δ_{47} values can be altered without any

other chemical or physical changes rendering such alteration effectively undetectable. In materials that have experienced some degree of bond reorganisation, Δ_{47} temperatures will reflect the closure temperature of lattice re-ordering, rather than the original formation temperature. The resistance of Δ_{47} values to diagenesis up to 100 °C is based on abiogenic carbonates and may not hold for biogenic carbonates in which lattice imperfections are more common and are likely to be stabilised during early burial by solid-state lattice annealing (Veizer & Prokoph 2015). Such stabilisation measurably affects Δ_{47} values (Passey & Henkes 2012). In contrast, $\delta^{18}\text{O}$ alteration requires oxygen isotope exchange across crystal boundaries. It is therefore postulated that the carbonate, phosphate and silica $\delta^{18}\text{O}$ systems are more robust recorders of ancient environmental conditions than the Δ_{47} system (Veizer *et al.* 1999; Bassett *et al.* 2007; Prokoph *et al.* 2008; Giles 2012; Veizer & Prokoph 2015).

Early Palaeozoic biomineral $\delta^{18}\text{O}$ data are sparse, and predominantly derive from analyses of conodont phosphate (Bassett *et al.* 2007; Trotter *et al.* 2008; Grossman 2012b; Wheelley *et al.* 2012, 2018). Published biogenic $\delta^{18}\text{O}$ data from the late Cambrian have previously suffered from a lack of scrutiny of the preservation of the material prior to isotopic analysis (Wadleigh & Veizer 1992; Elrick *et al.* 2011), or the materials were sampled from an environment that may have had a substantial freshwater influence (see §5.4.2; Bergmann *et al.* 2018). A lack of scrutiny of the preservation of material also precludes the use of some younger phosphatic brachiopod $\delta^{18}\text{O}$ analyses (Wenzel *et al.* 2000) in compilations of Palaeozoic data (Figure 5-2; see notes and references in Appendix E). However, the early Cambrian data presented in Chapter Four extend the reliable biogenic $\delta^{18}\text{O}$ record back to that time. The early Cambrian data presented in this thesis are consistent with the general trend of lighter $\delta^{18}\text{O}$ values with increasing age observed in conodont phosphate $\delta^{18}\text{O}$ data (Figure 5-2), and are in the range of values expected for a $\delta^{18}\text{O}/\text{age}$ gradient of approximately -0.01 ‰ per million years (Veizer *et al.* 1999; Kasting *et al.* 2006; Jaffrés *et al.* 2007; Prokoph *et al.* 2008; Giles 2012). Whilst these new early Cambrian $\delta^{18}\text{O}$ data are consistent with the Phanerozoic trend of $\delta^{18}\text{O}$, the data presented in Chapter Four are not used to infer early Cambrian $\delta^{18}\text{O}_{\text{sw}}$. Instead, the secular trend is inferred from $\delta^{18}\text{O}$ data and models published in the literature (Veizer *et al.* 1999; Kasting *et al.* 2006; Jaffrés *et al.* 2007; Prokoph *et al.* 2008; Giles 2012; Veizer & Prokoph 2015).

A secular trend in the isotopic composition of the global ocean accounts for both the range in values and consistency of the trend across different mineral systems.

Furthermore, acknowledging this as a secular trend in global ocean $\delta^{18}\text{O}_{\text{sw}}$ helps to reconcile sea surface temperature estimates from early Palaeozoic isotope data and climate models (Nardin *et al.* 2011). The secular trend in global ocean $\delta^{18}\text{O}_{\text{sw}}$ may have a magnitude of about 0.01 ‰ per million years, with early Cambrian oceans having an average $\delta^{18}\text{O}_{\text{sw}}$ value of -6 ‰ (Veizer *et al.* 1999; Jaffrés *et al.* 2007; Giles 2012; Veizer & Prokoph 2015). In summary, the most parsimonious interpretation of the available data is that there has been a secular trend of increasing $\delta^{18}\text{O}_{\text{sw}}$ over at least the Phanerozoic Eon, and an early Cambrian global ocean average $\delta^{18}\text{O}_{\text{sw}}$ value of -6 ‰ is used in the following calculations.

5.4.2. Local variation

As well as long-term secular variation, local variability in $\delta^{18}\text{O}_{\text{sw}}$ needs to be accounted for in isotopic temperature estimates. Local $\delta^{18}\text{O}_{\text{sw}}$ is a function of the overall global value in the oceans and the regional precipitation–evaporation (P/E) balance, which is the main cause of variations away from the global value (Pearson 2012). Freshwater sources, such as riverine input or ice melt from glaciers and ice sheets, can further modify local $\delta^{18}\text{O}_{\text{sw}}$. The $\delta^{18}\text{O}_{\text{sw}}$ range in the modern ocean is largely controlled by latitudinal variation of the P/E balance (Zachos *et al.* 1994). Typically, $\delta^{18}\text{O}_{\text{sw}}$ is heavier in low latitudes where evaporation dominates and lighter at high latitudes where precipitation is more important, due to the lightening $\delta^{18}\text{O}$ of atmospheric moisture as it migrates polewards. Interpolated water mass $\delta^{18}\text{O}_{\text{sw}}$ values for the surface ocean (≤ 50 m) range from -7.7 ‰ to $+2.5$ ‰ (Figure 5-4a), though individual measurements occupy a greater range of values (Schmidt *et al.* 1999; LeGrande & Schmidt 2006). Local $\delta^{18}\text{O}_{\text{sw}}$ variation therefore must be accounted for in palaeotemperature estimates.

The total range of modern $\delta^{18}\text{O}_{\text{sw}}$ is large (>10 ‰), though variability across most of the global ocean is more limited, typically 0 ± 1.5 ‰ (Figure 5-4; Schmidt *et al.* 1999; LeGrande & Schmidt 2006; Pearson 2012). Indeed, whilst there is a strong relationship between $\delta^{18}\text{O}_{\text{sw}}$ and latitude (e.g. Zachos *et al.* 1994), the most extreme $\delta^{18}\text{O}_{\text{sw}}$ anomalies are localised to restricted basins, such as the highly evaporative Mediterranean Sea, or the Arctic Ocean which has a large freshwater input from ice-melt and river run-off, or to areas with very large freshwater influence such as the Amazon river delta (Figure 5-4; Schmidt *et al.* 1999; LeGrande & Schmidt 2006; Pearson 2012). There are also zonal discrepancies between larger ocean basins, such as the 1 ‰ difference between the $\delta^{18}\text{O}_{\text{sw}}$ of the central Atlantic and Pacific oceans. A high

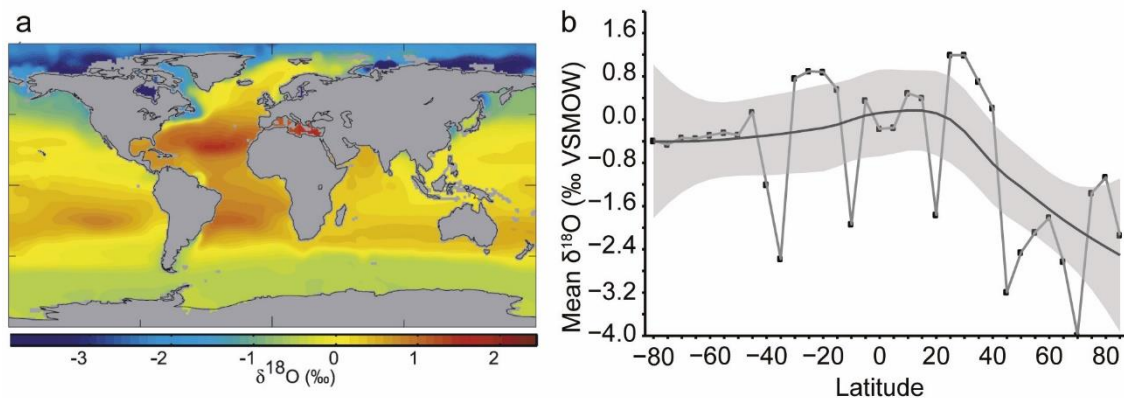


Figure 5-4. Variability of $\delta^{18}\text{O}_{\text{sw}}$ in the modern surface (top 50 m) ocean. (a) Gridded data set from LeGrande & Schmidt (2006). (b) Top 50 m $\delta^{18}\text{O}_{\text{sw}}$ data from Schmidt *et al.* (1999, accessed July 2018), plotted by 5 ° latitude bins: points = mean measured $\delta^{18}\text{O}_{\text{sw}}$; dark line = Loess model fitted through all data; grey band = 95 % confidence envelope of the Loess model.

precision palaeogeographic model, incorporating detailed estimates of bathymetry and the location and magnitude of major riverine inputs, in concert with an isotope-enabled GCM would be required to address these non-latitudinal drivers of $\delta^{18}\text{O}_{\text{sw}}$ variability. The $\delta^{18}\text{O}_{\text{sw}}$ –latitude relationship, on the other hand, provides a starting point from which to establish first order constraints on local $\delta^{18}\text{O}_{\text{sw}}$ variability.

There are currently no constraints on the latitudinal variability of Palaeozoic $\delta^{18}\text{O}_{\text{sw}}$. However, isotope-enabled climate models suggest that the $\delta^{18}\text{O}_{\text{sw}}$ distribution in early Cenozoic oceans, corrected for changes in global ice volume, was similar to that of modern oceans, with perhaps a slight increase in the magnitude of variability driven by an enhanced hydrological cycle (Tindall *et al.* 2010; Roberts *et al.* 2011). There is considerable asymmetry in the modern latitudinal distribution of $\delta^{18}\text{O}_{\text{sw}}$ in the Northern and Southern hemispheres (Figure 5-4; Schmidt *et al.* 1999). In contrast to present day continental configuration, early Cambrian continents were concentrated in the Southern Hemisphere (see Chapter Two; e.g. Torsvik & Cocks 2013, 2016). Because continental configuration exerts a primary control on ocean circulation, the modern Northern Hemisphere latitudinal $\delta^{18}\text{O}_{\text{sw}}$ gradient may be a better analogue for the latitudinal $\delta^{18}\text{O}_{\text{sw}}$ gradient in the early Cambrian Southern Hemisphere.

Cenozoic and Mesozoic oxygen isotope studies commonly apply a polynomial correction factor (Pearson 2012) derived from Southern Hemisphere $\delta^{18}\text{O}_{\text{sw}}$ data (Zachos *et al.* 1994):

$$\delta^{18}\text{O}_{\text{sw}} = 0.576 + 0.041L - 0.0017L^2 + 0.0000135L^3$$

where L = absolute latitude between 0° to 70°. For the Comley Limestones at approximately 65 °S, the Zachos *et al.* (1994) equation yields a $\delta^{18}\text{O}_{\text{sw}}$ correction factor

of -0.23 ‰. For the Forteau Formation at approximately 25 °S, the Zachos *et al.* (1994) equation yields a $\delta^{18}\text{O}_{\text{sw}}$ correction factor of $+0.75$ ‰. A Loess model fitted through $\delta^{18}\text{O}_{\text{sw}}$ data from depths < 50 m the Northern and Southern hemispheres of the modern ocean (Schmidt *et al.* 1999) at comparable absolute latitudes are approximately -1.1 ‰ and $+0.4$ ‰ (Figure 5-4b); discrepancies (c.f. Zachos *et al.* 1994) of 0.9 ‰ and 0.4 ‰, respectively. A third order polynomial regression through the modern data set of Schmidt *et al.* (1999):

$$\delta^{18}\text{O}_{\text{sw}} = -0.487 + 0.141L - 0.00556L^2 + 0.0000446L^3$$

yields $\delta^{18}\text{O}_{\text{sw}}$ estimates of -2.52 ‰ and $+0.28$ ‰; discrepancies (c.f. Zachos *et al.* 1994) of 2.29 ‰ and 0.47 ‰, respectively. Note that these $\delta^{18}\text{O}_{\text{sw}}$ estimates, in particular the high latitude values, are more extreme than the interpolated gridded water mass data set suggests for comparable latitudes (Schmidt *et al.* 1999; LeGrande & Schmidt 2006), and as such may be unrepresentative of the average picture. The large range in $\delta^{18}\text{O}_{\text{sw}}$ values at any given latitude and the discrepancies between different methods of estimating latitudinal $\delta^{18}\text{O}_{\text{sw}}$, combined with the uncertainty surrounding early Cambrian palaeocontinental configurations and its (unknown) impact on early ocean circulation, indicate an intermediate value for local $\delta^{18}\text{O}_{\text{sw}}$ variability may be most appropriate.

Both the Comley Limestones, Avalonia, and the Forteau Formation, Laurentia, are considered to have been deposited under normal marine conditions, with normal salinities, and well-connected to the global ocean, and are not thought to have been influenced by freshwater influxes (see Chapter Two). The most reasonable estimate for the latitudinal variability of $\delta^{18}\text{O}_{\text{sw}}$ for the Comley Limestones is approximately -0.5 ‰, and for the Forteau Formation about $+0.5$ ‰. These values are deviations from the early Cambrian global ocean average $\delta^{18}\text{O}_{\text{sw}}$ of -6 ‰. The following temperature estimates and discussion focus on calculations that assume a local $\delta^{18}\text{O}_{\text{sw}}$ value of -6.5 ‰ for the Comley Limestones SSFs and -5.5 ‰ for the Forteau Formation SSFs.

5.5. Early Cambrian sea surface temperature calculations

By making some reasonable assumptions for the isotopic composition of sea water it is possible to calculate SST values and so begin to quantify early Cambrian climates.

Using phosphate oxygen isotope temperature equation 1 (Lécuyer *et al.* 2013) with a $\delta^{18}\text{O}_{\text{sw}}$ value of -6.5 ‰ for the Comley Limestones, yields an SST estimate of 23 °C (T7; Table 5-2), with a range of 20 °C to 28 °C (Appendix B). Applying equation 1 to

the Forteau Formation data with a $\delta^{18}\text{O}_{\text{sw}}$ value of -5.5‰ yields a SST estimate of 35 °C (T5; Table 5-2), with a range of 30 °C to 39 °C (see Appendix B). This gives a tropical/sub-polar latitudinal temperature gradient of approximately 12 °C .

The estimated SSTs are strongly dependent on both the choice of equation and the $\delta^{18}\text{O}_{\text{sw}}$ value (Table 5-2). As discussed above, equation 5 (Lécuyer *et al.* 2013) is considered to be the most appropriate for this study (see §5.3). However, as with all of the equations, there is a large inherent uncertainty associated with the SST calculation. Temperatures calculated using equation 5 have an inherent uncertainty of 31 °C to 32 °C (Table 5-2), and so this approach requires an independent test (see Chapter Six). Such uncertainty is largely ignored in $\delta^{18}\text{O}$ Palaeozoic ocean temperature studies (Bassett *et al.* 2007; Trotter *et al.* 2008; Joachimski *et al.* 2009; Barham *et al.* 2012; Joachimski & Lambert 2015) and can only be resolved by improving the resolution of the phosphate oxygen temperature equations, which is beyond the scope of this work. In contrast, the SST error due to $\delta^{18}\text{O}_{\text{phos}}$ analytical uncertainty is negligible (Table 5-2).

Applying equation 5 with a $\delta^{18}\text{O}_{\text{sw}}$ value of -1‰ , as has typically been assumed in Palaeozoic isotopic temperature studies of greenhouse climate states (e.g. Trotter *et al.* 2008; Joachimski *et al.* 2009; Barham *et al.* 2012) leads to SST estimates, for both high and low latitudes, of 48 °C and 55 °C , respectively (Table 5-2). These high and low latitude SST estimates are biologically unfeasible, exceeding the theoretical and observed thermal tolerance of most metazoans (Pörtner 2001; Hicks & McMahon 2002; Nguyen *et al.* 2011; Dilly *et al.* 2012) in regions that are known to have been palaeobiologically diverse (Conway Morris 1989; Paterson *et al.* 2016; Hou *et al.* 2017).

However, SSTs calculated assuming $\delta^{18}\text{O}_{\text{sw}} = -1\text{‰}$ are comparable to those for the Early Ordovician derived from $\delta^{18}\text{O}$ analyses of well-preserved conodonts from northern Gondwana (Bassett *et al.* 2007) and Laurentia (Trotter *et al.* 2008). These Early Ordovician proxy-derived SST estimates are much higher than the SSTs predicted by early Palaeozoic GCM simulations, and it has been noted that much better agreement between early Palaeozoic data and model SST estimates can be achieved by accounting for a secular trend in $\delta^{18}\text{O}_{\text{sw}}$ (Nardin *et al.* 2011). De-trending $\delta^{18}\text{O}$ data to account for a secular trend in $\delta^{18}\text{O}_{\text{sw}}$, with or without a further P/E correction, is necessary in Palaeozoic palaeoclimate studies (Nardin *et al.* 2011).

One could infer a steeper secular trend, or more extreme latitudinal variation, of $\delta^{18}\text{O}_{\text{sw}}$, either of which would result in lower temperature estimates for high latitude

Avalonia. This cannot be directly addressed by the available $\delta^{18}\text{O}$ data, but can only be tackled using another, independent, approach (see Chapter Six). Following the above assumptions and considering the limitations of the phosphate oxygen isotope temperature equation, reasonable estimates of early Cambrian tropical and high latitude SSTs can be made. High latitude Avalonia was likely warm compared to similar modern latitudes, with an SST of approximately 23 °C, and low latitude Laurentia was likely similarly warm by comparison to a modern tropical settings, with an SST of approximately 35 °C (Table 5-2).

Table 5-2. Cambrian SST estimates from each of the six equations, using different $\delta^{18}\text{O}_{\text{sw}}$ values. The temperature estimates underlined and bold are considered to be the most suitable; see text for discussion. See also Appendix B.

#	Reference	SST estimates (°C)										
		Equation error ^{1,2}	Analytical error ¹	T1	T2	T3	T4	T5	T6	T7	T8	T9
		$\delta^{18}\text{O}_{\text{sw}} = -1 \text{ ‰}$	-1 ‰	-1 ‰	-2 ‰	-4 ‰	-5 ‰	-5.5 ‰	-6 ‰	-6.5 ‰	-7 ‰	-8 ‰
Comley Limestones												
1	Longinelli & Nuti 1973	NA	1.1	44.6	40.3	31.7	27.4	25.3	23.1	21.0	18.8	14.5
2	Kolodny et al. 1983	42.5	1.1	51.7	47.3	38.6	34.2	32.0	29.8	27.6	25.4	21.1
3	Lecuyer et al. 1996	52.5	1.1	47.4	43.2	34.8	30.6	28.5	26.4	24.3	22.2	18.0
4	Puceat et al. 2010	15.6	1.1	57.4	53.2	44.7	40.5	38.4	36.3	34.2	32.1	27.8
5	<u>Lecuyer et al. 2013</u>	32.3	1.2	48.0	43.5	34.5	30.0	27.7	25.5	<u>23.2</u>	21.0	16.5
6	Chang & Blake 2015	40.1	2.1	71.5	63.5	48.4	41.4	38.0	34.6	31.4	28.2	21.9
Forteau Formation												
1	Longinelli & Nuti 1973	NA	1.9	51.2	46.9	38.3	34.0	31.8	29.7	27.5	25.4	21.1
2	Kolodny et al. 1983	40.8	1.9	58.4	54.0	45.2	40.8	38.6	36.5	34.3	32.1	27.7
3	Lecuyer et al. 1996	50.4	1.8	53.8	49.6	41.2	37.0	34.9	32.8	30.7	28.6	24.4
4	Puceat et al. 2010	15.0	1.8	63.8	59.6	51.1	46.9	44.8	42.7	40.6	38.5	34.2
5	<u>Lecuyer et al. 2013</u>	31.0	2.0	54.8	50.3	41.3	36.8	<u>34.5</u>	32.3	30.0	27.8	23.3
6	Chang & Blake 2015	42.4	3.8	84.3	75.6	59.5	52.0	48.3	44.8	41.3	37.9	31.3

¹Equation and analytical temperature errors calculated assuming $\delta^{18}\text{O}_{\text{sw}} = -1 \text{ ‰}$. Assuming a lighter (more negative) value for $\delta^{18}\text{O}_{\text{sw}}$ reduces both equation and analytical error in temperature estimates.

²Equation error for each equation is the difference between T1 temperatures calculated using the maximum positive and maximum negative uncertainty (see Table 5-1) for each SST equation.

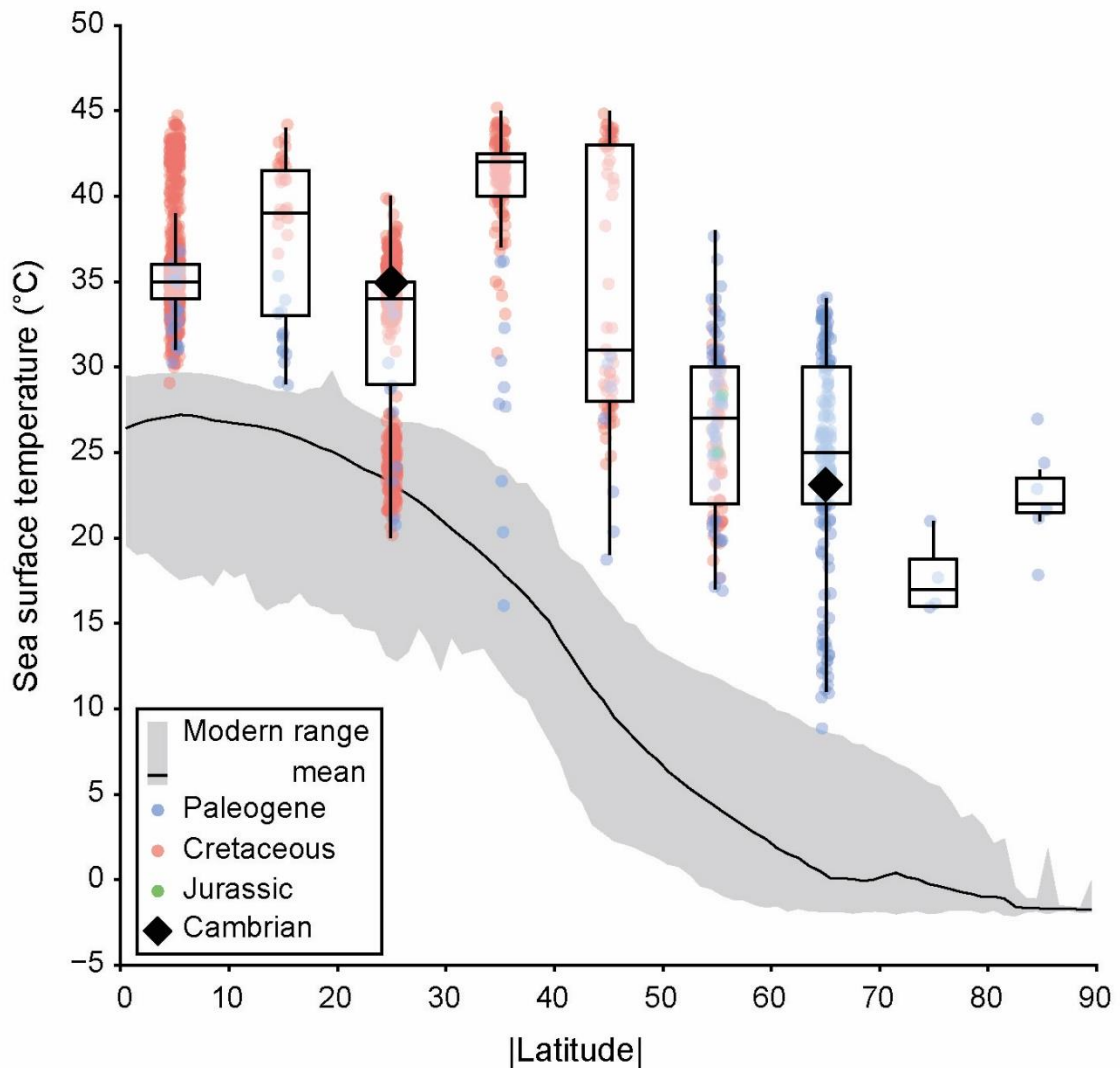


Figure 5-5. Cambrian isotopic SSTs alongside published SSTs from Mesozoic and early Cenozoic greenhouse climate intervals. Cambrian data (black diamonds) calculated from the $\delta^{18}\text{O}$ values of pristine SSF samples from the Comley Limestones (60 °S to 70 °S) and the Forteau Formation (20 °S to 30 °S); see text and Table 5-2 for details. Data are plotted in 10° bins of absolute paleolatitude to illustrate latitudinal temperature variation irrespective of paleocontinental configuration. Plotted points are summarized in box plots displaying the median and first and third quartiles, with whiskers extending up to 1.5 times the interquartile range. Cretaceous data = Cenomanian to Turonian; Paleogene data = Paleocene to Eocene. For references and literature data see Appendix F. Modern latitudinal mean (black line) and range (gray envelope) data from the 2013 World Ocean Atlas 1° resolution data set (Locarnini *et al.* 2013). Modified after Hearing *et al.* (2018), fig. 4.

5.6. Palaeoenvironmental implications

The Cambrian Period has long been considered a greenhouse interval in the history of Earth's climate (Brasier 1992a; Peng *et al.* 2012; Boucot *et al.* 2013; Erwin & Valentine 2013), but quantitative palaeotemperature data have proven elusive. However, the $\delta^{18}\text{O}$ SST estimates calculated above allow quantitative comparisons to be drawn with other, better constrained, climate regimes in Earth's past. The high latitude (*circa* 65 °S)

estimate of approximately 23 °C is considerable warmer than modern SSTs at similar latitudes, as is the low latitude (*circa* 25 °S) estimate of approximately 35 °C (Figure 5-5). However, these SST estimates are within the range of more recent and better understood greenhouse intervals in Earth's past, such as the late Mesozoic (Littler *et al.* 2011; Jenkyns *et al.* 2012; Ando *et al.* 2015; O'Brien *et al.* 2017; Robinson *et al.* 2017) and early Cenozoic (Bijl *et al.* 2009; Sluijs *et al.* 2009; Douglas *et al.* 2014; Frieling *et al.* 2017, 2018; Suan *et al.* 2017; Evans *et al.* 2018). The $\delta^{18}\text{O}$ SST estimates presented here suggest that the early Cambrian was not an interval of extreme warmth, as has been hypothesised (Trotter *et al.* 2008), but was instead consistent with younger Phanerozoic greenhouse climates (Figure 5-5).

Greenhouse climate states are characterized by shallow latitudinal temperature gradients (Ho & Laepple 2016; Suan *et al.* 2017). Geological data support a moderate latitudinal temperature gradient in the early Cambrian Period (Boucot *et al.* 2013; see also Chapter Six), although loose age constraints on many of these geological data, often in excess of 10 Ma, have hindered construction of a detailed global picture. However, other geochemical data also support the inference of an early Cambrian greenhouse climate. The Cambrian Epoch 2/Miaolingian transition is also associated with a 900 Myr acme in the strontium isotope curve, corresponding to a peak in continental weathering rates at approximately 500 Ma (Peters & Gaines 2012). A strong greenhouse climate would likely have facilitated enhanced continental weathering, probably including an expanded tropical weathering belt. However, such global inferences require a global data set that cannot yet be achieved with the level of sampling of reliable Cambrian biomineral $\delta^{18}\text{O}$ data.

5.7. Conclusions

Early Cambrian phosphatic SSFs can preserve useful geochemical proxy data of ancient oceanography. However, these fossils need to be carefully screened to avoid diagenetically altered samples. The screening protocol detailed earlier in this thesis allows reasonable estimates of early Cambrian SSTs to be made. However, due to the nature of the phosphate oxygen isotope temperature equations, the SST estimates are based on key assumptions of ancient sea water.

The $\delta^{18}\text{O}$ presented in this thesis support a first order secular trend in the evolution of $\delta^{18}\text{O}_{\text{sw}}$ over the Phanerozoic Eon. Data published in the literature suggest that the global average $\delta^{18}\text{O}_{\text{sw}}$ has become heavier over time, and in the early Cambrian

was approximately -6 ‰ . One of the key assumptions about ancient sea water is that this trend must be accounted for in deep time palaeotemperature calculations. The other key assumption is that latitudinal variability in $\delta^{18}\text{O}_{\text{sw}}$ due to the balance of global precipitation and evaporation has been broadly consistent over time. Although this assumption is reasonable and consistent with the data presented here, there are currently no independent data or model constraints on Palaeozoic $\delta^{18}\text{O}_{\text{sw}}$ latitudinal variability.

By far the largest uncertainty in these temperature estimates comes directly from the phosphate oxygen temperature equation itself. The most suitable temperature equation for invertebrate phosphate biominerals has an inherent uncertainty in excess of 30 °C . Addressing uncertainty in palaeotemperature equations should be a major focus for future investigations.

Notwithstanding the uncertainty, the most parsimonious interpretation of the biomineral $\delta^{18}\text{O}$ data suggests that the early Cambrian was a typical greenhouse interval in the evolution of Earth's climate. High latitude (65 °S) SSTs are estimated to have been approximately 23 °C , and tropical (25 °S) SSTs approximately 35 °C . The early Cambrian was therefore not an interval of extreme warmth, but rather was within the bounds of younger, better understood, greenhouse intervals in Earth's climate history. In order to have confidence in the reasoned assumptions made in this chapter, and the estimated SSTs that result from them, an independent test is required. That test follows in Chapter Six.

Chapter Six: Modelling early Cambrian climates

6.1. Chapter summary

The final data chapter of this thesis presents the results of general circulation model (GCM) simulations and subsequent comparison of model results with isotopic and geological data. GCM simulations are initiated to test a range of plausible orbital and greenhouse gas conditions against four different early Cambrian palaeocontinental configurations. The GCM results are calibrated against the isotopic temperature estimates presented in Chapter Five. The GCM simulations are scored against a database of climatically sensitive lithologies in order to evaluate model (dis)agreement with the geological data used up until now to constrain Cambrian climates.

6.2. Introduction

6.2.1. *The Cambrian greenhouse world?*

Atmospheric greenhouse gas (GHG) concentrations in the early Cambrian Period are thought to have been high, with $p\text{CO}_2$ in excess of 15 times preindustrial atmospheric levels (PAL = 280 ppm), resulting in low latitudinal temperature gradients and thermally stratified oceans (e.g. Boucot *et al.* 2013; Erwin & Valentine 2013; Royer *et al.* 2014; Rasmussen *et al.* 2016; Stolper & Keller 2018). This thesis has presented quantitative evidence constraining early Cambrian climates using the phosphate oxygen isotope palaeothermometer (see Chapter Five). Isotopic data suggest that global seas were warm, and that the early Cambrian was comparable to late Mesozoic and early Cenozoic greenhouse worlds. However, this inference of global climate state derives from spatially isolated data points during a well constrained interval in time (see Chapter Two). As such, the inference of an early Cambrian greenhouse may only represent specific time intervals. It may not represent the general case for early Cambrian climates, and it is difficult to infer a picture of global climate from spatially isolated data. Therefore, other techniques and proxy data should be sought, with the aim of better constraining Earth's physical climate at the beginning of the Phanerozoic Eon.

Most geological evidence supports interpretation of the Cambrian Period as a greenhouse interval in Earth's climate history (Boucot *et al.* 2013). In particular, there are geographically widespread early and middle Cambrian evaporite deposits, extensive carbonate platforms and metazoan reef complexes, and potentially high latitude bauxite and laterite deposits (Geyer & Landing 2006; Warren 2010; Boucot *et al.* 2013; Kerner

& Debrenne 2013). However, there are also reports of early Cambrian age low altitude glaciogenic deposits that could be indicative of an icehouse climate. These include putatively glaciogenic diamictite textures and shoreline freeze-thaw structures (Lindström 1972; Landing & MacGabhann 2010; Runkel *et al.* 2010), as well as geochemical evidence for cooler intervals during the Cambrian (Saltzman *et al.* 2000, 2004; Cherns *et al.* 2013).

Taken at face value, the available data appear to require contradictory inferences of the state of the Cambrian climate system. Unfortunately, the spatial coverage and temporal correlation of much of this palaeoclimate proxy data, including the isotopic data presented in Chapter Five, is not yet sufficient to resolve Cambrian climate variability over long timeframes or over wide geographical areas. However, a different approach, using general circulation models (GCM) to simulate Cambrian climates, may allow examination of temporal and geographical climate patterns on greater spatial scales, but at lower spatial resolution, than is afforded by the available isotope data.

6.2.2. *Aims, objectives and rationale*

Early Cambrian palaeomagnetic, palaeontological and lithological data are often contradictory, and may perhaps only be reconciled due to their loose age constraints. This has led to marked differences in palaeocontinental reconstructions (Figure 6-1). Whilst these reconstructions broadly agree on the number and composition of the major palaeocontinents, the global configuration of those continents can be very different. Three of the continental configurations (Figure 6-1a, c, d) are essentially “antarcotocentric” in construction (Landing *et al.* 2013b, p. 1022), i.e. they feature a large continent (Gondwana) spanning the full range of southern palaeolatitudes, with present-day North Africa or South America residing over the South Pole. The other configuration (Figure 6-1b) is distinctly zonal, with a continental distribution generally similar to the other configurations except for Gondwana, which is rotated clockwise by $\sim 270^\circ$ so that North Africa and South America lie in equatorial and northern mid-latitudes, respectively. These different continental configurations have substantial implications for interpreting palaeobiogeographic patterns of the Cambrian metazoan radiation, as well as for interpreting early Cambrian regional climate and oceanography.

Modelling (Cambrian) climate conditions under different palaeocontinental configurations and palaeogeographies will allow for the comparison of predicted and observed climate conditions, the latter based on geological evidence. Climatically

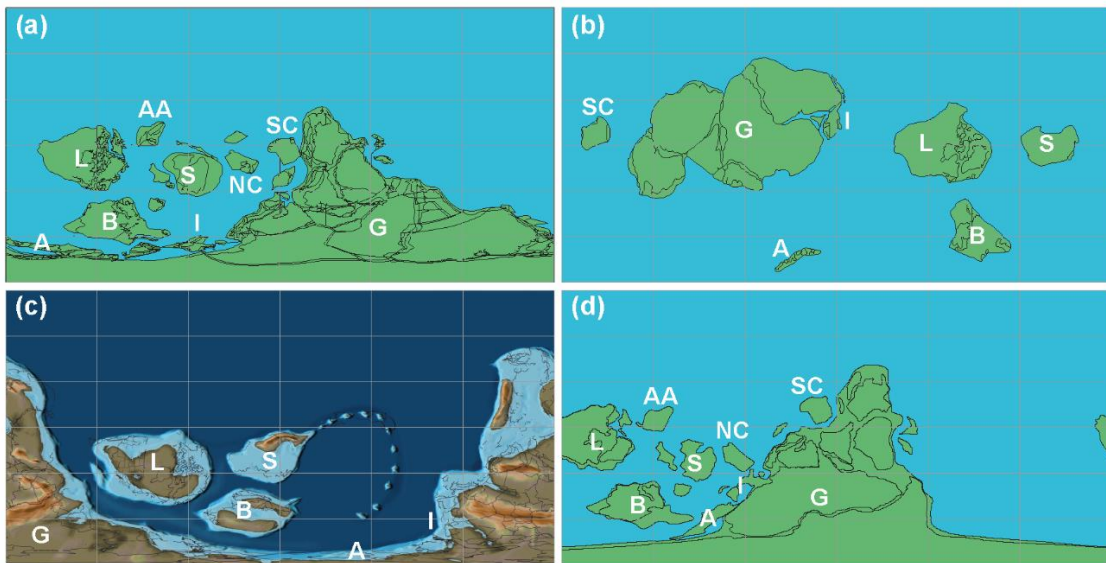


Figure 6-1. Four contrasting views of the early Cambrian world in equirectangular projection. (a) The 510 Ma palaeocontinental configuration produced using the BugPlates software (Torsvik & Cocks 2009, see also 2013, see also 2016). (b) The Ediacaran/Cambrian transition palaeocontinental configuration of (Landing *et al.* 2013b, fig. 1). (c) The early Cambrian PALAEOMAP reconstruction (see also GPlates). (d) The Cambrian reconstruction presented by (Álvaro *et al.* 2013, fig. 19.1). Abbreviations: A = Avalonia; AA = Arctic Alaska; B = Baltica; G = Gondwana; I = Iberia; L = Laurentia; NC = North China; S = Siberia; SC = South China.

sensitive lithologies have been used in geological studies since the nineteenth century to reconstruct palaeoenvironmental conditions (Agassiz 1838), and in the context of the Cambrian include evaporite and oolitic limestone deposits.

Aims

- a. To establish a (semi-)quantitative global picture of early Cambrian climates.
- b. To place physical constraints on early Cambrian palaeogeography.
- c. To place physical constraints on early Cambrian oceanography, particularly regarding deep ocean circulation (e.g. Edwards *et al.* 2017; Stolper & Keller 2018).

Objectives

- i. Produce GCM simulations of the early Cambrian for a range of boundary conditions, including different palaeocontinental reconstructions.
- ii. Evaluate the climatic and oceanographic properties simulated under different boundary conditions.
- iii. Calibrate the GCM simulations using available isotopic temperature data (see Chapter Five).
- iv. Evaluate the calibrated GCM simulations against a global database of early Cambrian climatically sensitive lithologies.

- v. Identify regional (dis)agreement between climate predictions from climatically sensitive lithological data and climate simulations.

6.3. Methods in modelling early Cambrian climate

6.3.1. The Fast Ocean Atmosphere Model (FOAM)

The Fast Ocean Atmosphere Model (FOAM) version 1.5 (Jacob 1997; Jacob *et al.* 2001; see also https://wiki.mcs.anl.gov/FOAM/index.php/Users_Guide), is a three dimensional coupled ocean-atmosphere general circulation model (GCM) that is widely applied to deep time palaeoclimate questions (Poulsen & Jacob 2004; Donnadieu *et al.* 2009; Nardin *et al.* 2011; Pohl *et al.* 2016). FOAM comprises two connected modules: one for the atmosphere and one for the oceans. The atmospheric module is an upgraded parallelized version of the National Center for Atmospheric Research (NCAR) Community Climate Model 2 (CCM2) which includes radiative and hydrologic physics from CCM3 version 3.2. The atmospheric module was run with R15 spectral resolution (4.5° x 7.5°) and 18 vertical levels. The ocean module is Ocean Model version 3 (OM3) with 1.4° x 2.8° longitude-latitude resolution and 24 vertical levels including the uppermost 0 m to 10 m and 10 m to 50 m surface ocean levels. There are no flux corrections in the coupled model.

FOAM reproduces most of the major aspects of modern climate (Jacob 1997; Notaro *et al.* 2005) including tropical climate variability dominated by the El Niño Southern Oscillation (ENSO) in ENSO rather than La Niña mode (Liu *et al.* 2000), tropical Atlantic variability (Liu & Wu 2000), and monsoons (Jacob 1997; Harrison *et al.* 2003). FOAM has a slight bias to modelling cooler Northern and warmer Southern hemisphere SSTs (Figure 6-2), with the warmer Southern Hemisphere temperatures thought to be explained by high diffusion coefficients in the ocean model (Jacob 1997). Overall, FOAM is comparable to GCMs of similar age and complexity (Jacob 1997; Notaro *et al.* 2005).

The FOAM simulations were integrated for 2,000 years to reach deep-ocean equilibrium; the short turnaround time allows for millennial-scale integrations. There was no apparent drift in the upper ocean during the final 100 years of the simulations and negligible change in deep ocean temperature (< 0.01 °C at –3700 m). The climatology files used in these analyses were built from the last 50 years of the model runs. Dr Alexandre Pohl (CEREGE, France) ran the FOAM simulations after I produced the base maps and specified the boundary conditions.

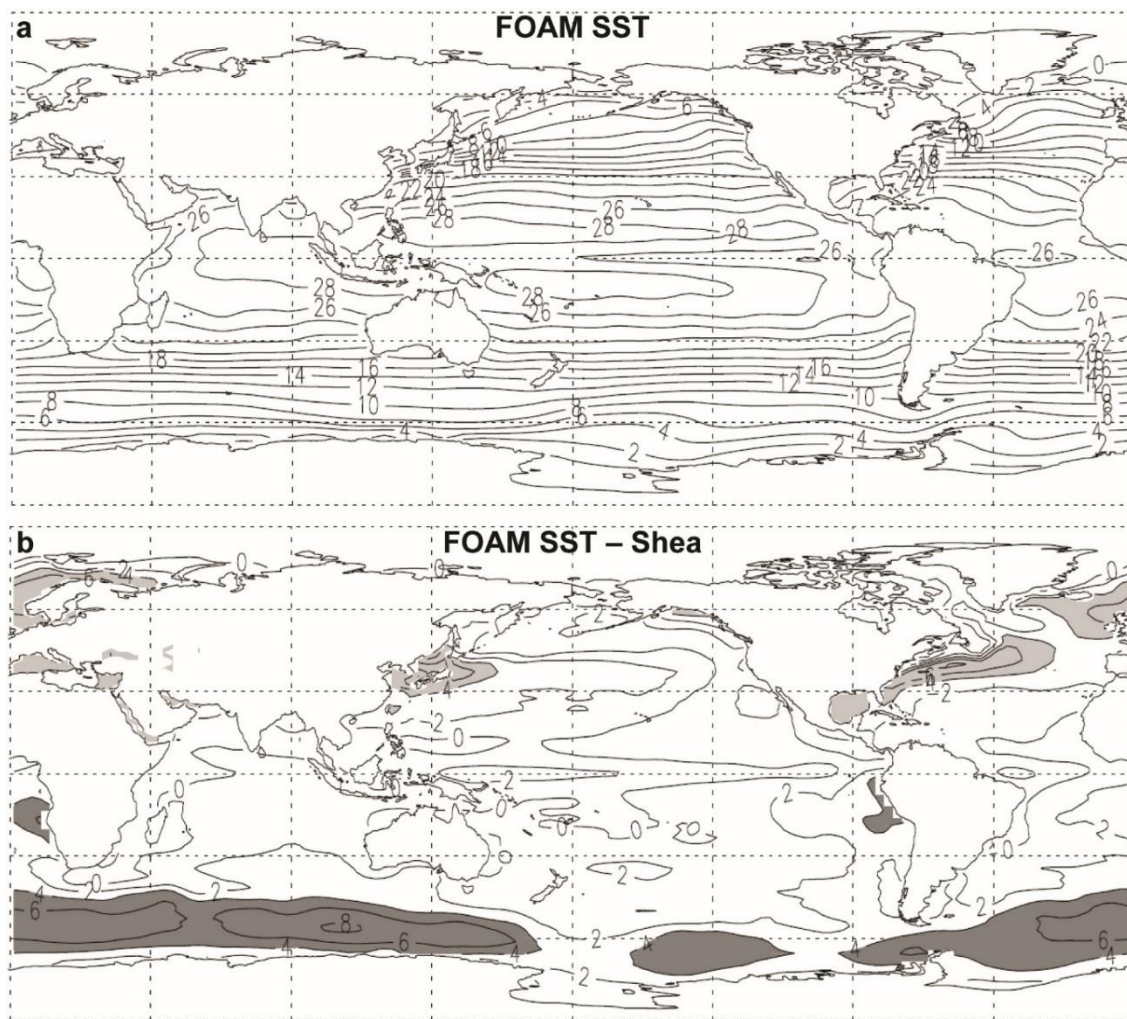


Figure 6-2. Comparison of FOAM-modelled SST and present day measured conditions. (a) FOAM-modelled SST. (b) FOAM-modelled SST minus Shea *et al.* (1990) SST measurements. Light shading = discrepancy < -4 °C. Dark shading = discrepancy $> +4$ °C. Modified from Jacob (1997), fig. 14.

6.3.2. Model boundary conditions

A suite of boundary conditions are required to run FOAM. These include: the intensity of solar luminosity, Earth's orbital parameters, the greenhouse gas (GHG) composition of the atmosphere, initial temperature fields for the ocean and atmosphere, the nature (albedo) of any land surface, and a topographic base map. All simulations were initialised with a warm ice-free ocean of homogeneous salinity (35 ‰). Due to the absence of vascular land plants in the Cambrian, the land surface was defined as a rocky desert with an albedo of 0.24, which was modified by snow and ice if present. Solar luminosity (L) was decreased by 4.3 % compared to its present value of $1,368 \text{ Wm}^{-2}$ following equation (6.1) (Gough 1981):

where t_0 = the Main Sequence lifetime of the Sun (~ 4.7 Ga; Gough 1981), and t = time interval of interest (0.52 Ga for these simulations). At $t = 0.52$ Ga, $L_t = 1310 \text{ Wm}^{-2}$.

FOAM has the option of specifying the levels of several atmospheric gases, including carbon dioxide and methane. The oldest $p\text{CO}_2$ proxy data are Early Devonian palaeosols and stomatal density (not stomatal index) calculations (Driese *et al.* 2000; Roth-Nebelsick & Konrad 2003; Royer 2014), notwithstanding putatively unaltered Neoproterozoic boron isotope data (Kasemann *et al.* 2010). Therefore, Earth systems box models are the best method available for constraining the composition of the early Phanerozoic atmosphere, and thus the GHG boundary conditions for FOAM (Figure 6-3). The GEOCARBSULF model of Berner (2006, 2008, 2009), updated by Royer *et al.* (2014), predicts $p\text{CO}_2$ values of ~1,200 ppm to ~12,000 ppm, with a likely range of 6,000 ppm to 10,200 ppm, or 21 to 36 times preindustrial atmospheric levels (PAL = 280 ppm). For comparison, the related COPSE model predicts $p\text{CO}_2$ values of ~8 to ~18 PAL (Lenton *et al.* 2018) and the GEOCLIM model predicts $p\text{CO}_2$ values > 25 PAL (Godd ris *et al.* 2014). Recent modelling work using global subduction zone length estimates suggests that CO_2 production from mid-ocean ridges and island arcs greatly increased during the terminal Neoproterozoic (Van Der Meer *et al.* 2014; Mills *et al.* 2017), supporting high $p\text{CO}_2$ levels during the early Phanerozoic.

Estimating the early Cambrian greenhouse effect solely from modelled $p\text{CO}_2$ is likely to underestimate the total GHG forcing because it does not account for other GHGs. The other potentially important GHG is atmospheric methane (CH_4), the greenhouse effect of which is more than an order of magnitude greater than that of CO_2 (Rodhe 1990). The few studies that have looked at atmospheric methane in Earth's history suggest that $p\text{CH}_4$ was similar to or slightly lower than PAL of 350 ppbv during the Cambrian Period (Bartdorff *et al.* 2008). Indeed, $p\text{CH}_4$ is considered to have remained low following the collapse of the methane-rich early atmosphere, due to the Great Oxidation Event at approximately 2400 Ma (Lyons *et al.* 2014). This low methane atmosphere is thought to have persisted until the development of extensive continental wetlands, which are prolific methane sources, in the Carboniferous and Permian periods (Bartdorff *et al.* 2008). However, there is very little available data to constrain these models. The most parsimonious approach, therefore, was to maintain all atmospheric gas levels, other than $p\text{CO}_2$, at their preindustrial values. The $p\text{CO}_2$

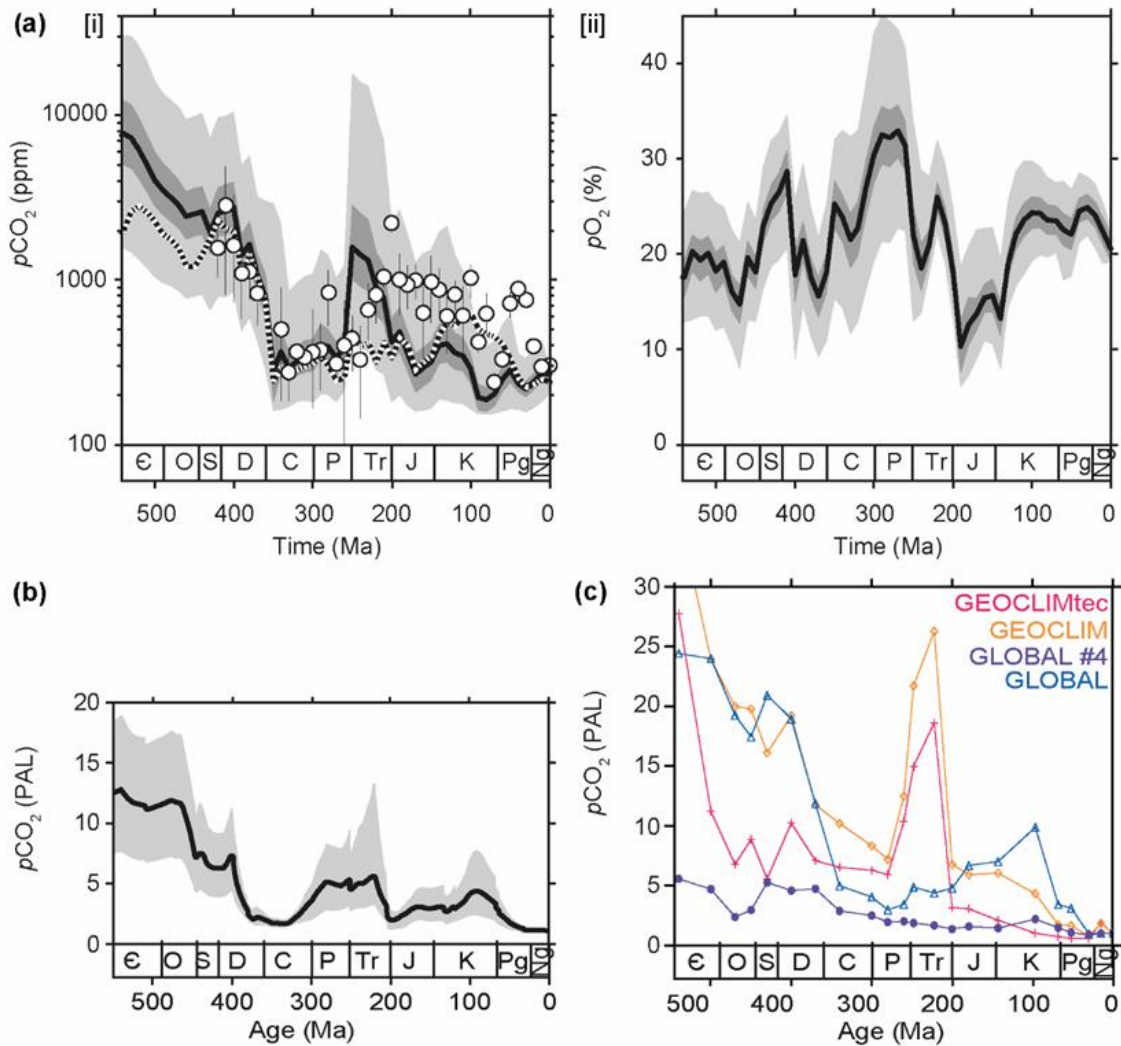


Figure 6-3. Modelled pCO₂ over the Phanerozoic Eon. (a) Atmospheric pCO₂ [i] and pO₂ [ii] GEOCARBSULF model predictions, modified after (Royer et al. 2014, fig. 2). [i] Open circles represent pCO₂ geological proxy data. (b) Atmospheric pCO₂ COPSE model predictions, (Lenton et al. 2018, fig. 13). Grey envelope represents the range of tested hypotheses in (Lenton et al. 2018). Plot scaled to match (c). (c) Atmospheric pCO₂ GEOCLIM model predictions, modified after (Goddéris et al. 2014). GLOBAL = simplified GEOCARB model with zero-dimensional climate; GLOBAL #4 = as GLOBAL, but with forcing only from the changing solar constant and palaeogeography; GEOCLIM = full GEOCLIM simulation with three-dimensional climate; GECLIMtec = as GEOCLIM, but with forcing only from the changing solar constant and palaeogeography.

boundary condition could therefore be regarded as a pCO₂-equivalent greenhouse forcing and is likely to be an underestimate of the total GHG radiative effect. Standard practice in climate modelling is to test the sensitivity of simulations to the doubling of atmospheric pCO₂, because the radiative forcing from doubling pCO₂ is effectively independent of background pCO₂ levels (Myhre *et al.* 2017). In keeping with this, and to span the range of modelled Cambrian pCO₂ (Figure 6-3), GCM simulations were run with pCO₂ values of 16 PAL, 32 PAL and 64 PAL.

Table 6-1. Orbital parameters for the FOAM climate simulations.

Description	Obliquity	Eccentricity	Longitude of perihelion
PD: Present day	23.4463	0.016724	77.9610
WN: Warm north	24.5	0.07	90 (perihelion June)
WS: Warm south	24.5	0.07	270 (perihelion December)
OL: Obliquity minimum	22.0	0.0	90
OH: Obliquity maximum	24.5	0.0	90

The overlap of the secular resonance the inner (rocky) planets of the solar system introduces a chaotic component to Earth’s orbit that precludes precise calculation of orbital conditions beyond a few tens of millions of years (Laskar *et al.* 2004). There are, therefore, no model simulations of Earth’s orbital parameters during the Cambrian Period. To circumvent this, a plausible range of orbital parameters were tested (Table 6-1). These included present day (PD) orbital conditions, conditions likely to cause warm northern (WN) and southern hemispheres (WS), and conditions that account for the minimum (OL) and maximum (OH) obliquity variability. In order to evaluate the relative impacts of changing $p\text{CO}_2$ and orbital parameters, initial simulations were run assuming PD conditions at 16 PAL, 32 PAL and 64 PAL $p\text{CO}_2$. Following initial simulations under PD orbital parameters, simulations were run using all orbital parameters under a constant $p\text{CO}_2$ of 32 PAL. This allowed evaluation of the relative roles of orbital and greenhouse forcing on the GCM simulations, without excessive model run times.

6.3.3. Palaeotopographic and palaeobathymetric maps

Four contrasting continental configurations for the early Cambrian were used to produce base maps for the climate simulations (Figure 6-4): (A) BugPlates 510 Ma (Torsvik & Cocks 2009), (B) the reconstruction in Landing *et al.* (2013a, b), (C) PALEOMAP (GPlates) reconstruction (Scotese 2016), and (D) a modified BugPlates reconstruction based on trilobite palaeobiogeography (Álvaro *et al.* 2013). These were chosen because they represent continental reconstructions that may be considered end-members of the

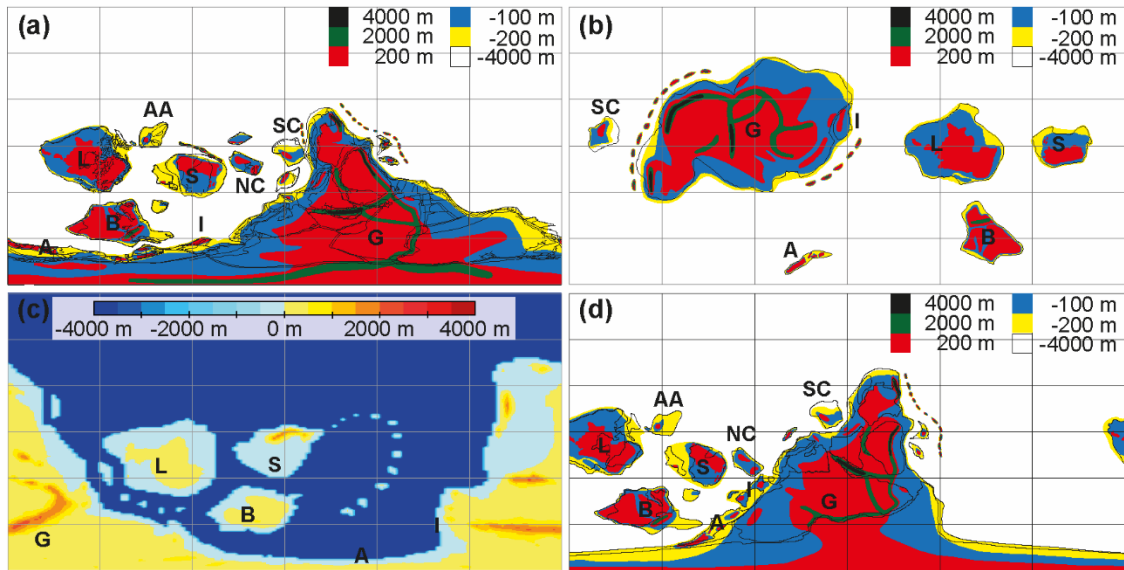


Figure 6-4. Topographic and bathymetric base maps used in the climate model simulations. (a) Map A based on the 510 Ma palaeocontinental configuration of the BugPlates software (Torsvik & Cocks 2009; see also 2013, 2016). (b) Map B based on the Ediacaran/Cambrian transition palaeocontinental configuration of Landing *et al.* (2013b, fig. 1). (c) Map C based on the early Cambrian PALAEOMAP configuration (Scotese 2016). (d) Map D based on the Cambrian continental configuration presented by Álvaro *et al.* (2013, fig. 19.1). Abbreviations: A = Avalonia; AA = Arctic Alaska; B = Baltica; G = Gondwana; I = Iberia; L = Laurentia; NC = North China; S = Siberia; SC = South China. High-resolution maps and discussion of their construction is available in Appendix G.

spectrum of early Cambrian continental reconstructions. Of the major palaeocontinents, the palaeolatitudinal positions of Laurentia, Siberia and Baltica are fairly stable across models, whereas the position of Gondwana is highly variable (Figure 6-1).

The palaeocontinental configuration of Map A is the 510 Ma reconstruction from BugPlates (Torsvik & Cocks 2009), primarily based on palaeomagnetic and brachiopod palaeobiogeographic data. BugPlates and related continental configurations have been widely used over the last decade by palaeontologists examining palaeobiogeographic patterns (e.g. Harper & Servais 2013). This is one of the many variants of an antarctocentric early Cambrian world-view in which a large portion of West Gondwana, in this case North Africa, lies over the South Pole (Figure 6-1a). In Map A, Avalonia is in a peri-Gondwanan position adjacent to North Africa at 65 °S to 70 °S, and northwest Newfoundland is situated at approximately 30 °S (Figure 6-1a).

The palaeocontinental configuration of Map B is the “terminal Ediacaran – Early Cambrian transition” reconstruction of Landing *et al.* (2013a, b), following Landing & Westrop (2004). This reconstruction presents a provocative alternative to the otherwise consensus “antarctocentric” Gondwana models (Landing *et al.* 2013b). Landing *et al.* (2013b) are critical of the reliability of early Cambrian palaeomagnetic data on which

many of the antarctocentric palaeocontinental configurations are based, and which often come with large temporal uncertainties. Landing *et al.* (2013b) are also critical of the common usage of Cambrian Stage 3/4, rather than earlier, taxa to infer early Cambrian palaeogeography. Map B, is primarily based on lithostratigraphic correlations, in particular making use of the carbonate-rich successions in West Gondwana. The rooting of this palaeocontinental configuration in sedimentological data introduces an element of circularity into analyses comparing model and geological data. However, it has never been tested whether this configuration does out-perform configurations rooted in palaeomagnetic and/or palaeobiogeographic data when comparing palaeoclimate model outputs and palaeoclimate data.

It should also be noted that, without explanation, the palaeocontinent of North China does not appear on this continental configuration, despite the presence of a thick succession of Cambrian rocks there (e.g. Chough *et al.* 2010; Yun *et al.* 2016). In other configurations, North China is regarded as residing at low (equatorial to tropical) latitudes during the early Cambrian (e.g. Torsvik & Cocks 2009, 2013, 2016; Álvaro *et al.* 2013; Yang *et al.* 2015a; Scotese 2016). In Map B, Avalonia is isolated at 70 °S to 85 °S, and northwest Newfoundland is situated at approximately 25 °S (Figure 6-1b).

The palaeocontinental configuration of Map C is the 510 Ma reconstruction from GPlates (Scotese 2016), a partial successor to BugPlates that is now becoming more widely used in the Palaeozoic palaeontological community. This map was kindly provided by Dr Christopher Scotese with topographic and bathymetric data already appended. It is broadly similar to Map A, but Gondwana is rotated slightly anti-clockwise, placing Avalonia, rather than North Africa, directly over the South Pole. In Map C, Avalonia is in a peri-Gondwanan position adjacent to North Africa at 80 °S to 90 °S, and northwest Newfoundland is situated at approximately 40 °S (Figure 6-1c).

The palaeocontinental configuration of Map D follows the work of (Álvaro *et al.* 2013), and is based on trilobite palaeobiogeographic patterns. Map D is substantially similar to a contemporaneously produced reconstruction based on archaeocyathan palaeobiogeographic distributions (Kerner & Debrenne 2013), though these were independently formulated continental configurations. Map D is another antarctocentric reconstruction, in which Gondwana is rotated clockwise with respect to Map A so that South America resides over the South Pole, and North Africa is in the mid- to high-latitudes. In Map D, Avalonia is in a peri-Gondwanan position adjacent to North Africa at 55 °S to 65 °S, and northwest Newfoundland is situated at approximately 30 °S

Table 6-2. Altitude categories for palaeogeographic reconstructions following Pohl *et al.* (2014).

Category	Altitude (m)	Examples of evidence used
Active orogeny	4000	High pressure metamorphism dated to 515 Ma \pm 20 Ma
Old (inactive) orogeny	2000	High pressure metamorphism dated to 535 Ma to 600 Ma
Continental plain	200	Terrestrial, not active or old orogeny
Shallow shelf	-100	Shallow water limestones, wave-formed fabrics
Deep shelf	-200	Turbidites, (hemi-)pelagic mudstones
Abyssal ocean	-4000	Offshore of deep shelf

(Figure 6-1d). Together, these four continental configurations capture much of the range of palaeocontinental configurations used by palaeontologists studying the ecological and biogeographical patterns of the Cambrian explosion, though many more are available (e.g. Meert 2014; Yang *et al.* 2015a).

Because FOAM uses three-dimensional atmosphere and ocean modules, topography and bathymetry need to be specified in addition to the continental configurations detailed above. With the exception of Map C, for which the data were provided by Dr Christopher Scotese, palaeotopography and palaeobathymetry was reconstructed using published geological data. Six broad altitude/bathymetry categories were used, following the method previously adopted by Pohl *et al.* (2014), amongst others (Table 6-2). The geological data used to reconstruct palaeotopography and palaeobathymetry are detailed in Appendix G.

Active orogenic belts were defined as being 4000 m above sea level. Active mountain building was inferred to be linear along continental or craton boundaries where amphibolite, eclogite, granulite or blue schist metamorphism of age 515 \pm 20 Ma has been reported. Blue schist metamorphism along ocean-facing continental margins is interpreted as subduction-related (Andean-type) orogenesis. The main active orogenic belts comprised the Terra Australis orogen, that stretches along modern east Australia and approximately follows the line of the Transantarctic mountains, and parts of the Pan-African orogen, although activity on large parts of the Pan-African orogen had ceased by the early Cambrian (Cawood 2005). The Terra Australis orogen incorporates the Antarctic Ross/Delamerian orogen which was active from ~515 Ma to 490 Ma, with a possible early phase of activity evident from the beginning of the Cambrian Period.

The Baltic Timanide orogen is also interpreted as an active orogeny here, based on the early Cambrian development of a foreland basin and terminal Ediacaran late-orogenic subduction beneath NE Baltica, dated to ~550 Ma to 620 Ma, in addition to mafic rocks with ocean island basalt-type chemistry (Pease *et al.* 2004). Some authors (e.g. Nielsen & Schovsbo 2011) find support for an actively subsiding foreland basin on Baltica during the Cambrian, which suggests active orogenesis may have occurred throughout the Period. In addition, there are reports of transitional greenschist-blueschist facies metamorphism ($T = 350\text{ }^{\circ}\text{C}$ to $400\text{ }^{\circ}\text{C}$; $p = 7\text{ kbar}$ to 8 kbar) in the Kvar Kush Anticline, west of the Northern Urals, dated to ~535 Ma, indicating early Cambrian subduction activity (Beckholmen & Glodny 2004). The probability is that much of the evidence for the Timanide orogen has been lost to erosion during the Cambrian marine transgression (Nielsen & Schovsbo 2011), or to subsequent Uralian and Caledonian orogenic activity (Beckholmen & Glodny 2004). Active orogenic belts were also given an envelope of the old orogeny altitude class to account for the drop-off in altitude towards the continental plain.

Old or inactive orogenic belts were defined as being 2000 m above sea level. Similar to active orogenic belts, old orogenic activity was inferred to be linear along continental or craton boundaries where amphibolite, eclogite, granulite or blue schist metamorphism has been reported between 600 Ma to 535 Ma. The largest inactive orogenic belt is the Pan-African orogen, the collision of which is largely thought to have finished during the terminal Neoproterozoic (e.g. Yoshida *et al.* 2003; Cawood 2005; Torsvik & Cocks 2013), with a few exceptions as outlined above. Island arc chains were assumed to reach the altitude of old inactive orogenic belts.

Continental plains were defined as being 200 m above sea level. Continental plains are used to define all terrestrial areas that are not active or old orogenies. In addition to terrestrial sedimentary deposits, evidence for continental plains frequently derives from an absence of sedimentation adjacent to shallow marine environments (i.e. inferred subaerial exposure) not associated with active or ancient metamorphic activity.

Shallow marine-shelf areas were defined as being 100 m below sea level. Geological evidence is primarily characterised as marine deposition within storm wave-base, typically expressed as shallow water carbonate and clastic rocks with wave-generated sedimentary structures. Stromatolites are also taken as evidence for shallow marine deposition, given their typical composition of photosynthesising cyanobacterial

mats. Deposits with structures such as slump folds or turbidite-like mass flow structures are interpreted as being deposited in deeper water settings.

Marine deep shelf areas were defined as 200 m below sea level. Sedimentological evidence is primarily characterised as marine deposition below storm wave-base, typically expressed as turbidites and fine-grained rocks, including flysch and (hemi-) pelagic mudstones. In the absence of any better constraints, the distal margins of the ‘deep marine–shelf’ category was defined along or adjacent to the boundaries of continental blocks (Figure 6-1).

Abyssal ocean plains were defined as 4000 m below sea level. Because abyssal ocean rocks are usually lost to subduction on timescales of 10^6 years, excepting the rare cases of obduction, areas of abyssal ocean are inferred as lying offshore of deep shelf settings. It should be noted that abyssal ocean plains are modelled as flat-bottomed, following previous Palaeozoic climate modelling studies (Pohl *et al.* 2014, 2017), and therefore there is no deep sea topography. This is important because ocean ridges and trenches interact with deep ocean circulation, and can block or divert currents, as well as encourage vertical mixing through upwelling. The location, length and depth of early Palaeozoic mid-ocean ridge systems can only be inferred from modelling plate dynamics within a palaeocontinental framework. Given that palaeocontinental configurations are being tested here, the influence of sea floor topography on ocean circulation is left here as a question for further work.

6.4. Early Cambrian climate model results

The results of all GCM simulations for the four palaeocontinental configurations are summarised by their zonal SST (Figure 6-6) and precipitation (Figure 6-5) patterns. The dominant control on global temperatures for each of the four palaeocontinental configurations is the specified greenhouse gas (GHG) forcing; changes to the orbital parameters produce only minor effects on global temperatures (Figure 6-6). All GCM simulations produce equatorial annual average SSTs within the tolerance range of modern metazoans ($T < 41$ °C for subtidal ectothermal animals; Nguyen *et al.* 2011). The equatorial saddle in the zonal SST gradient around the equator is likely the result of Ekman pumping driving upwelling in the upper levels of the ocean.

The mean annual surface air temperatures (MAATs; Figure 6-7) predicted by each simulation are higher than the modern value of approximately 14 °C (NASA 2010). Similarly to SSTs, MAATs also respond more strongly to changing $p\text{CO}_2$ level

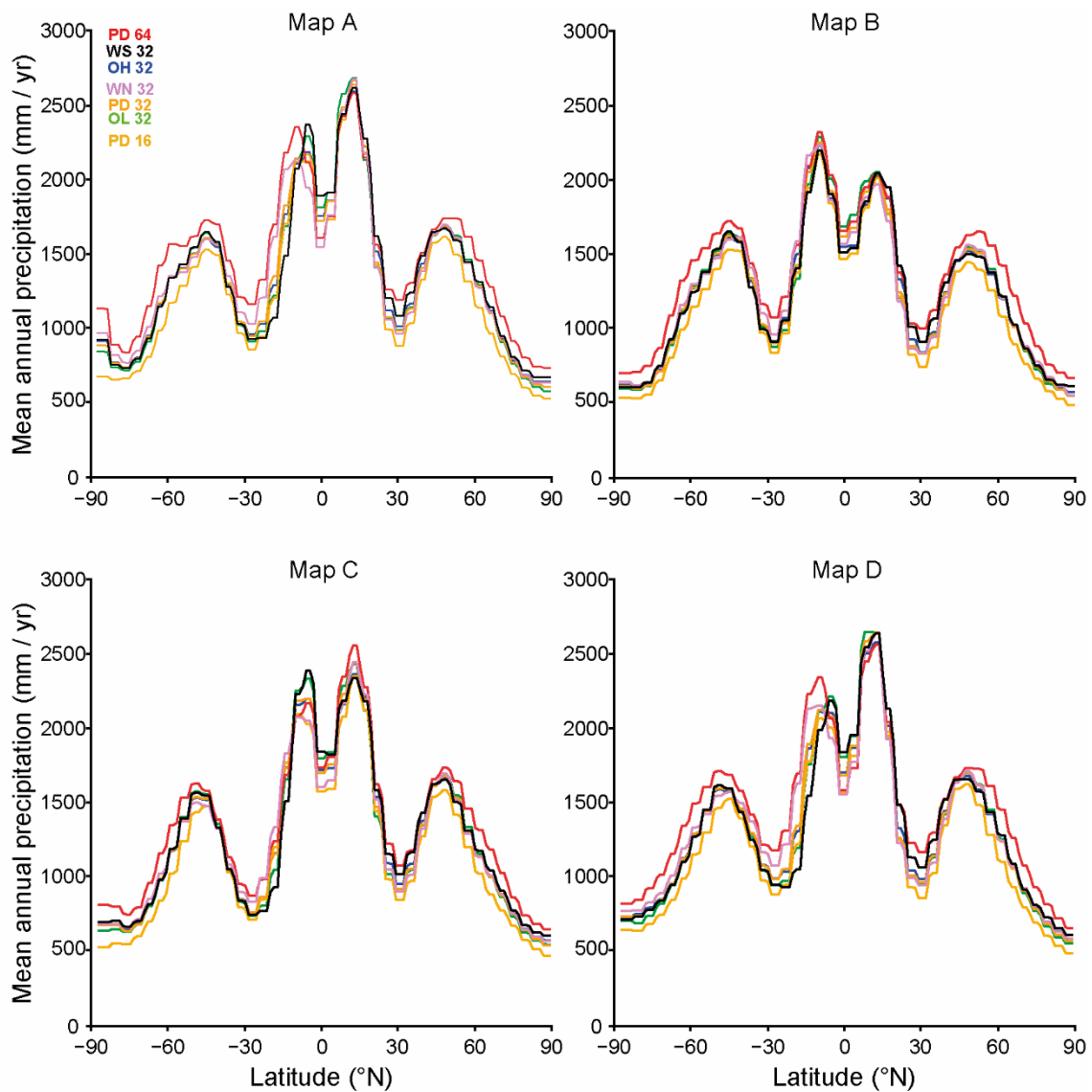


Figure 6-5. Zonal annual precipitation under different model conditions. Legend alphanumeric: letters indicate orbital configuration (see Table 6-1); numbers indicate $p\text{CO}_2$ conditions (PAL).

and basemap selection than to changing orbital parameters (Figure 6-7). Basemap selection exerts a consistent control on MAAT for different $p\text{CO}_2$ levels (Figure 6-7). This results in a systematic offset with Map C yielding consistently lower MAAT predictions compared to the other palaeogeographies. This basemap control on MAAT does not affect the climate sensitivity, temperature response to a doubling of radiative forcing (e.g. Rohling *et al.* 2012), over the range of $p\text{CO}_2$ values examined in this study. This suggests that climate sensitivity modelled here for the Cambrian greenhouse is not dependent on the palaeogeographic state, though the absolute MAAT values are.

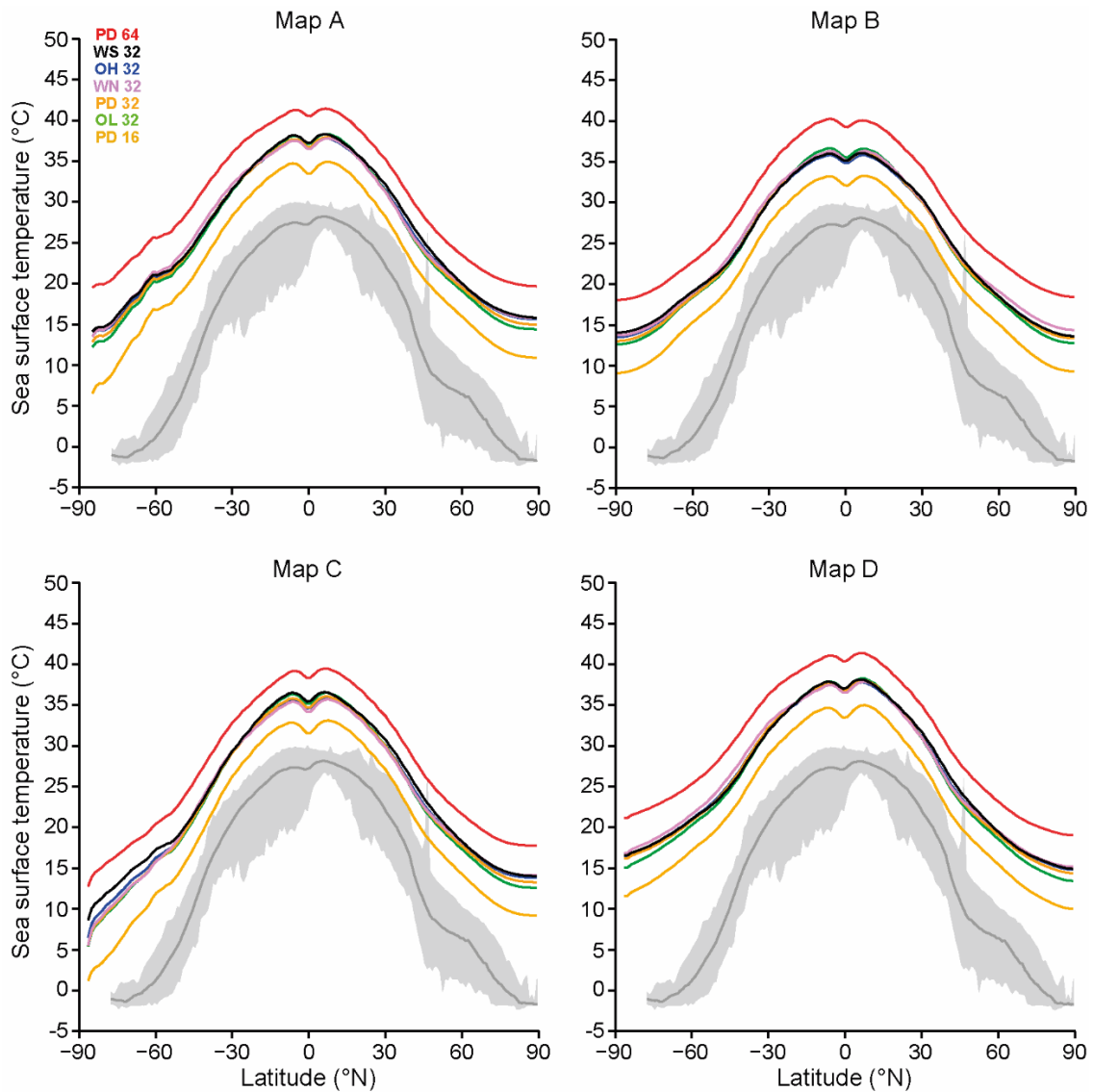


Figure 6-6. Zonal average sea surface temperatures (SSTs) under different model conditions (coloured lines) plotted with the modern SST zonal average (grey line) and zonal range (grey envelope). Legend alphanumeric: letters indicate orbital configuration (see Table 6-1); numbers indicate pCO₂ conditions (PAL). Modern data from the World Ocean Atlas (Locarnini et al. 2013).

Global precipitation shows much less variability with changing GHG forcing or orbital parameters. Changing orbital parameters produces no systematic effect on the zonal precipitation gradient (Figure 6-5). At mid- to high latitudes, mean annual precipitation (MAP) increases slightly with increasing GHG forcing, and this is also seen in the total MAP (Figure 6-8). Similarly to MAAT, GHG forcing and base map are more important in determining MAP than changing orbital parameters (Figure 6-8). At lower palaeolatitudes, this systematic change diminishes to become indistinguishable about the equator, and under Map C it is negligible even at mid-latitudes. The symmetrical troughs in zonal average precipitation at approximately 30 °N and 30 °S, seen in all

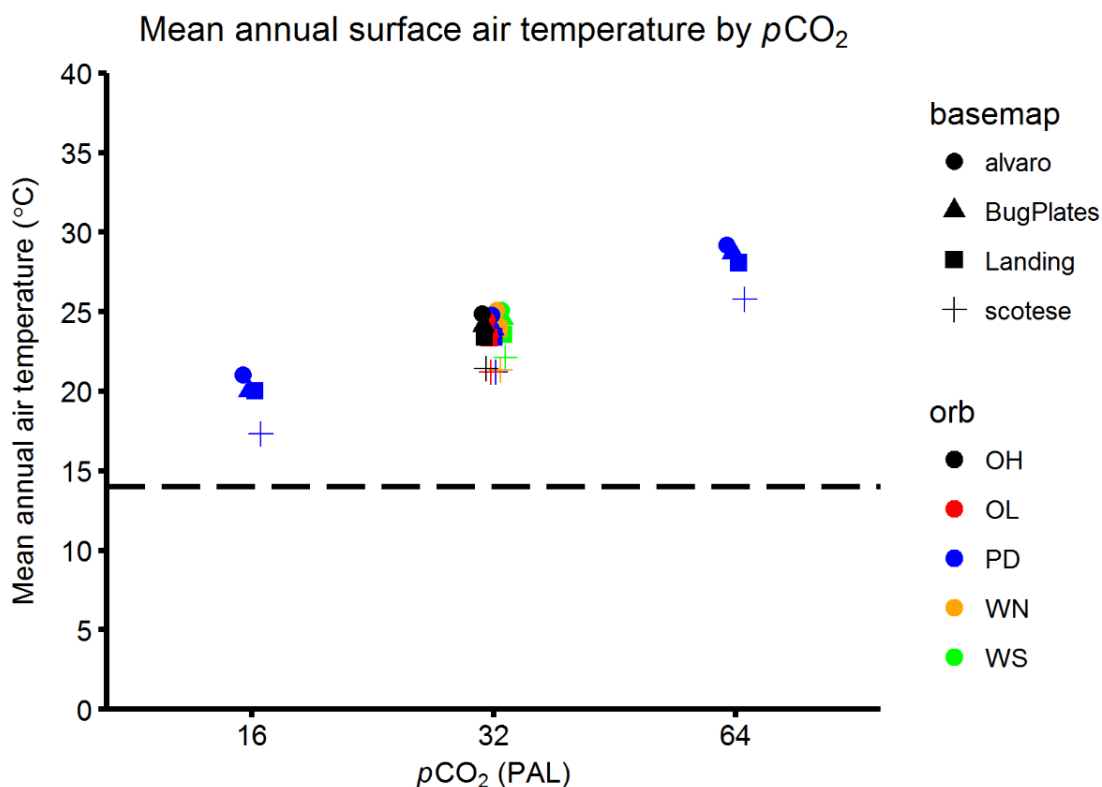


Figure 6-7. Cross plot of modelled mean annual surface air temperature (MAAT) against pCO₂ for each palaeocontinental (basemap) and orbital (orb) configuration. Dashed line = modern MAAT (NASA 2010). Orb: OH = high obliquity; OL = low obliquity; PD = present day; WN = warm Northern Hemisphere; WS = warm Southern Hemisphere; see Table 6-1.

climate simulations, likely correspond to the descending limbs of the Hadley Cell causing regions of high pressure and dry air. This is reinforced by the twin peaks in precipitation at tropical latitudes either side of the equator, and again at mid-latitudes. The ocean module parameter CONVEC2 is a proxy for deep ocean convection in the ocean module of FOAM (Figure 6-9). Deep ocean convection simulated for each of the palaeocontinental configurations is sluggish. Very few regions have the capacity in vertical mixing to drive a strong thermohaline circulation in the deep ocean. Overall, a (southern) polar continent seems to be required to induce any vertical mixing in the global ocean. Warm deep oceans were simulated for all configurations, with bottom water temperatures ($z = -3700$ m) in excess of 10 °C in all GCM simulations (Figure 6-10).

6.4.1. Map A

The zonal SST gradient in low to mid-latitudes (up to 60 ° either side of the equator) is essentially symmetrical. Further north (> 60 °N) the SST gradient flattens, with meridional ocean heat transport apparently becoming more efficient (Figure 6-6a). SSTs at high southern latitudes continue to decrease towards the South Pole and the margins

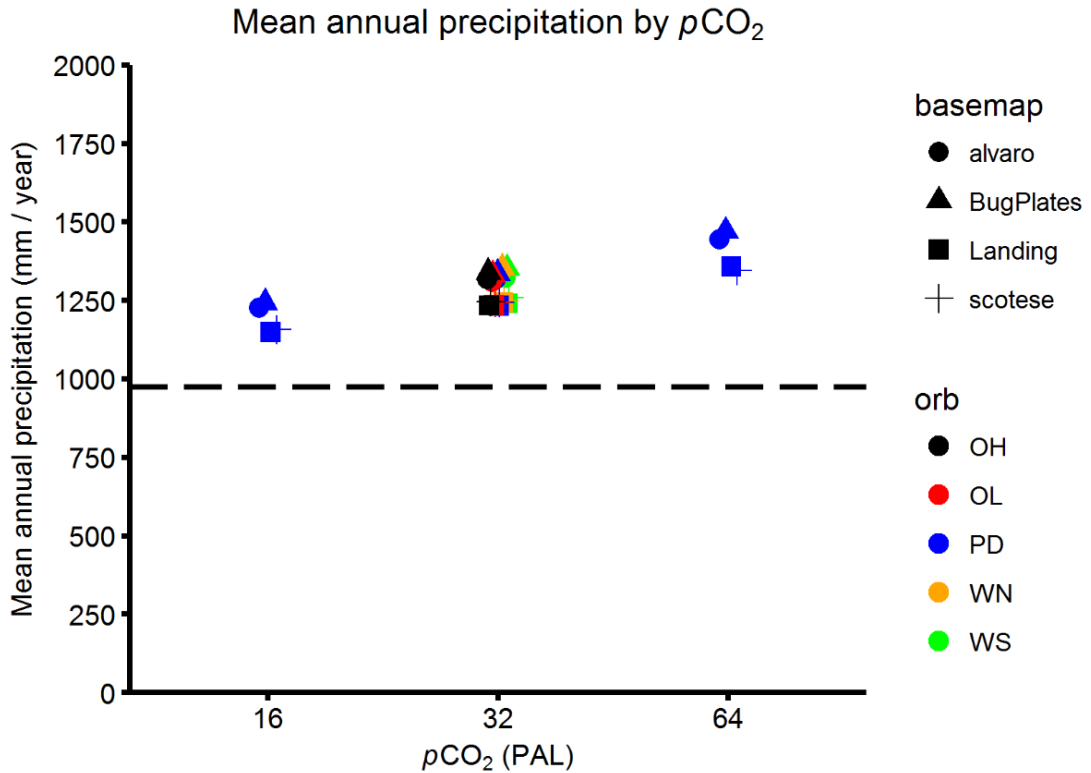


Figure 6-8. Cross plot of mean annual precipitation (MAP) against pCO₂ for each palaeocontinental (basemap) and orbital (orb) configuration. Dashed line = present day MAP. Orb: OH = high obliquity; OL = low obliquity; PD = present day; WN = warm Northern Hemisphere; WS = warm Southern Hemisphere; see Table 6-1.

of Gondwana. Freezing SSTs (< -1.8 °C for seawater) are only simulated during austral winter and spring (July to November) for the lowest pCO₂ run (16 PAL) along the margins of Gondwana at high southern latitudes. Cooler SSTs at high southern latitudes may be related to basin geometries producing poor ocean circulation and preventing warm deep ocean waters from interacting with the shallow waters of marginal, partially restricted, ocean basins. Simulations with higher pCO₂ levels (32 PAL and 64 PAL) do not produce freezing, or even negative, SSTs.

6.4.2. Map B

The zonal SST gradients produced by simulations using Map B are essentially symmetrical about the equator across all latitudes. They are comparable to the Northern Hemisphere gradients produced by simulations using Map A, including the high latitude flattening of the zonal SST gradient (Figure 6-6b). This results in warmer SSTs at high southern latitudes as well, precluding ice-forming conditions from developing under any of the simulations. The absence of a high latitude cold water site has implications for deep ocean circulation; notably that there is no source of (cold saline) deep water to

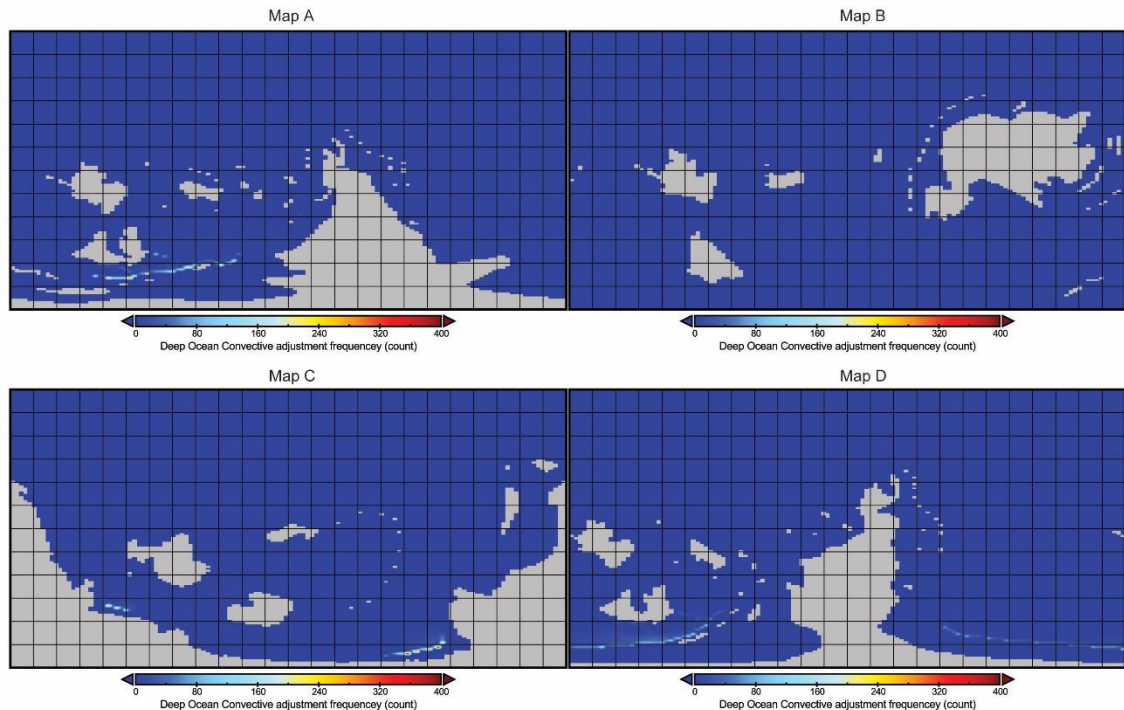


Figure 6-9. Deep ocean circulation simulated by the CONVEC2 parameter in FOAM for each of the basemaps at PD 32 conditions for month 9, when the CONVEC2 value was greatest.

drive a meridional thermohaline circulation system. Mean annual precipitation (MAP) in Map B simulations is lower than that observed under Map A simulations.

6.4.3. Map C

The zonal SST gradient in low to mid-latitudes (up to 60° either side of the equator) is essentially symmetrical. Further north ($> 60^\circ\text{N}$) the SST gradient flattens, with meridional ocean heat transport apparently becoming more efficient (Figure 6-6c). SSTs at high southern latitudes continue to decrease towards the South Pole and the margins of Gondwana. Freezing SSTs are only simulated during austral winter and spring (July to November) for the low $p\text{CO}_2$ run (16 PAL) along the margins of Gondwana at high southern latitudes. The cooler SSTs of high southern, compared to northern, latitudes may reflect increased vertical mixing induced by high latitude continents (see Figure 6-9) or reduced zonal mixing caused by lower latitude continents impeding the polewards migration of heat. Simulations with higher $p\text{CO}_2$ levels (32 PAL and 64 PAL) do not produce freezing, or even negative, SSTs.

6.4.4. Map D

The zonal SST gradient is essentially symmetrical across the equator, with a much smaller divergence from symmetry at high southern palaeolatitudes than simulations using the other antarctocentric configurations (maps A, C; Figure 6-6d). As such, SSTs

at high southern palaeolatitudes are comparatively warm, with a zonal average $> 10\text{ }^{\circ}\text{C}$ even for the lowest GHG forcing. There is no persistent region of deep-water formation, and hence the modelled ocean is thermally stratified (Figure 6-10).

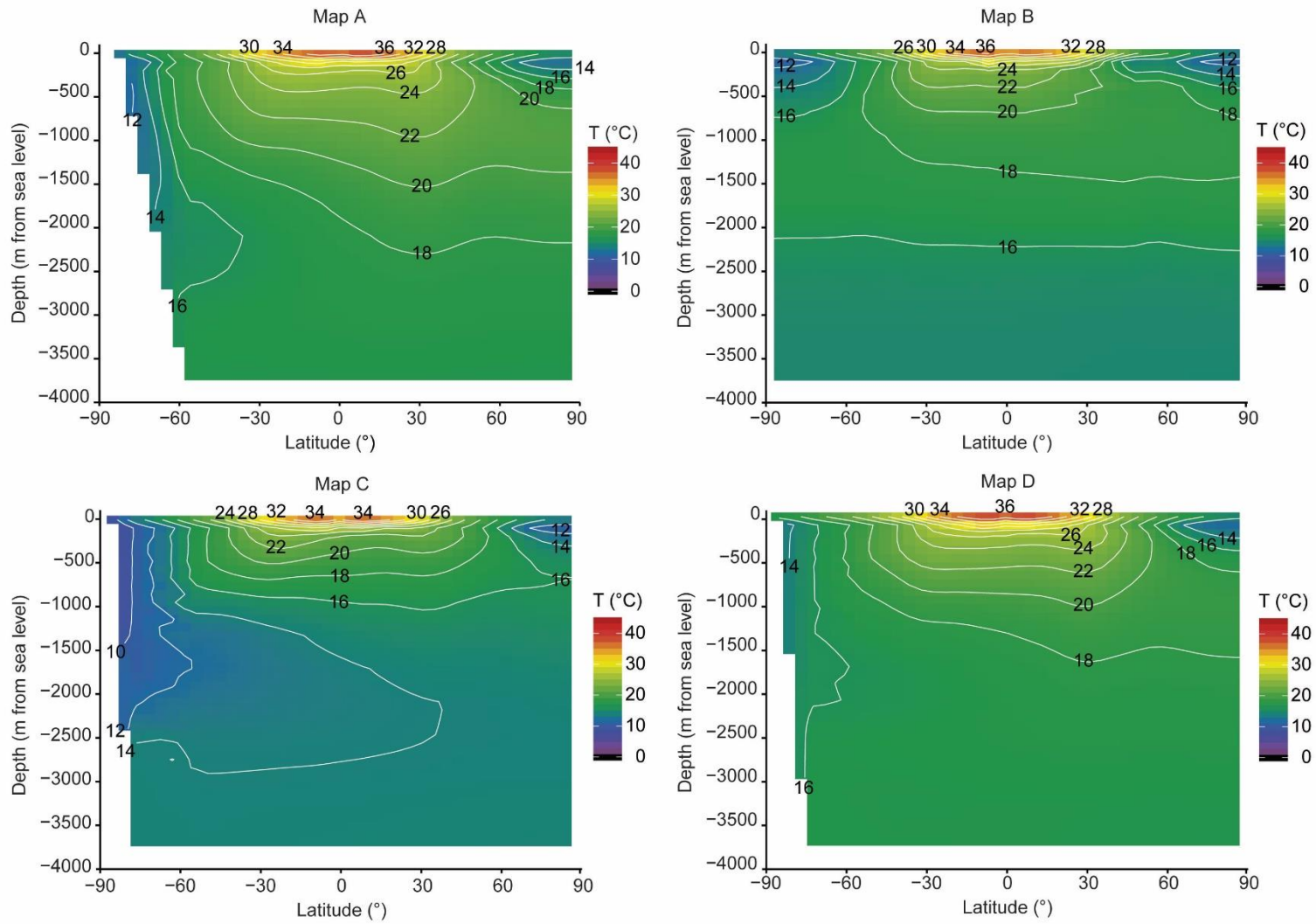


Figure 6-10. Temperature depth profiles through the modelled oceans of each map under PD 32 conditions.

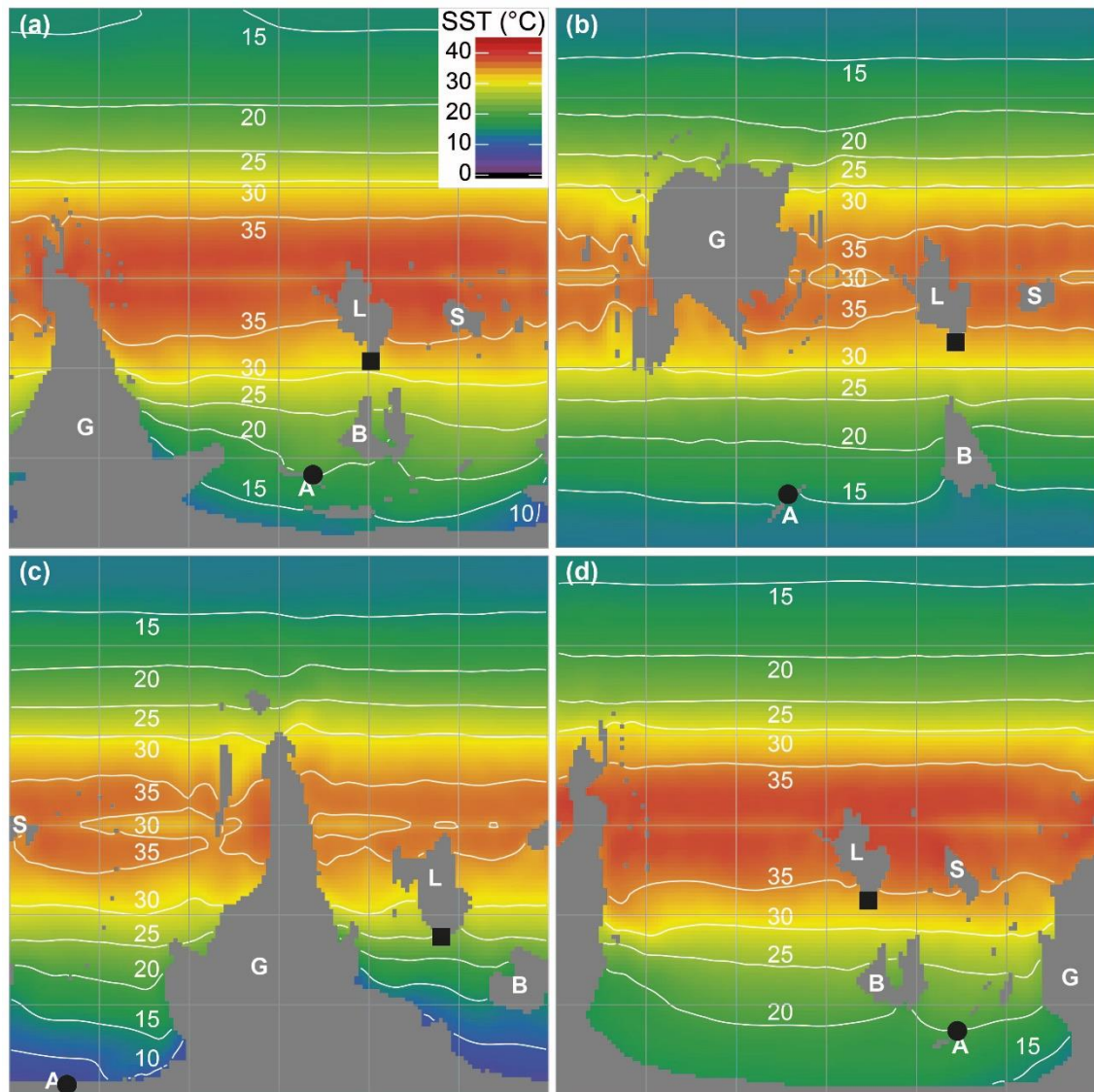


Figure 6-11. Isotopic temperature/model calibration points. Isotopic temperatures overlaid on climate model SSTs for PD 32 conditions. (a) Map A; (b) Map B; (c) Map C; (d) Map D. Circle = Avalonia calibration point. Square = Laurentia calibration. See Table 6-3

6.4.5. Model calibration

In order to calibrate the GCM simulations, the results of each simulation are compared to the isotopic SST estimates derived in Chapter Five. The results of the FOAM simulations for each map (A to D) are presented here and are compared to the phosphate oxygen isotope data from the Comley Limestones, Avalonia, and the Forteau Formation, Laurentia (Table 6-3). These two sites consistently represent high and low southern latitude settings respectively (Figure 6-11), despite the substantial differences in palaeocontinental configurations between the different maps. Isotopic SSTs are estimated from $\delta^{18}\text{O}$ values of fossils determined to comprise pristine biogenic phosphate (see Chapter Three) using a recent phosphate oxygen temperature equation

(Lécuyer *et al.* 2013) and assuming a global average seawater $\delta^{18}\text{O}$ value of -6.0‰ with additional latitudinal variation (Zachos *et al.* 1994; Schmidt *et al.* 1999; LeGrande & Schmidt 2006; Tindall *et al.* 2010; Roberts *et al.* 2011).

All mid- and high- $p\text{CO}_2$ Map A simulations predict Avalonian SSTs close to the estimated isotopic value of 23 °C , and Laurentian SSTs close to the estimated isotopic value of 35 °C (Table 6-3). The low- $p\text{CO}_2$ (16 PAL) simulation predicts Avalonian SSTs 5 °C to 10 °C below isotopic estimates, and Laurentian SSTs a few degrees below the isotopic value. For both low and high latitude sites, high- $p\text{CO}_2$ (64 PAL) simulations predict SSTs at the higher end of the range of values supported by the isotopic data. All Map A simulations, except A PD 16, find agreement or very near agreement with the isotopic data.

Only the high- $p\text{CO}_2$ Map B simulation predicts both the Avalonian and Laurentian SSTs close to the estimated isotopic values of 23 °C and 35 °C (Table 6-3). Whilst there is close correspondence between the low palaeolatitude Laurentian model and isotopic SSTs in Map B simulations, both the low- and mid- $p\text{CO}_2$ simulations predict SSTs between 3 to 12 °C below the isotopic estimates for Avalonia. Simulation B PD 64 fits well with the isotopic data, and B WN 32 and B WS 32 are close to agreement. However, this palaeocontinental configuration was produced for the Ediacaran/Cambrian transition, with Avalonia moving steadily north through the Cambrian Period (Landing & Westrop 2004; Landing *et al.* 2013b). Because the isotopic temperatures are Cambrian Epoch 2 in age, it is possible under this configuration that the northwards movement of Avalonia had carried it into warmer waters than these model simulations suggest.

All Map C simulations predict Avalonian SSTs substantially below the isotopic estimates of 18 °C to 26 °C , even accounting for the higher palaeolatitude of Avalonia in this continental configuration (Table 6-3). Simulation C PD 64 is the closest, but even under these elevated $p\text{CO}_2$ conditions polar SSTs are still $> 6\text{ °C}$ below the isotopic estimates, and Laurentian SSTs are a few degrees below the isotopic value. The isotopic data do not support the continental configuration of Map C.

The Map D mid- $p\text{CO}_2$ simulations are all consistent with the Avalonian and Laurentian isotopic SSTs (Table 6-3). The low- $p\text{CO}_2$ (16 PAL) simulation predicts Avalonian SSTs only 3 °C below the isotopic value, and Laurentian SSTs at the lower end of the isotopic data. The high- $p\text{CO}_2$ (64 PAL) simulations predict SSTs slightly above the values indicated by the isotopic data.

Isotopic data therefore support the following GCM simulations: A OH 32, A OL 32, A PD 32, A PD 64, A WN 32, A WS 32; B PD 64; D OH 32, D OL 32, D PD 32, D PD 64, D WN 32, D WS 32. No Map C simulations were supported by the isotope data as the modelled SSTs are consistently too cold, and all but one of the Map B simulations were incompatible with the range of isotopic temperatures calculated for Avalonia (Table 6-3).

Table 6-3. Model calibration using Avalonian isotopic sea temperatures.

Map	Boundary conditions ¹	Comley Limestones, Avalonia				Forteau Formation, southern Laurentia			
		Latitude (°S)	Model SST (°C) ²	$\delta^{18}\text{O}_{\text{sw}}$ (‰) ³	Isotopic SST (°C) ⁴	Latitude (°S)	Model SST (°C) ²	$\delta^{18}\text{O}_{\text{sw}}$ (‰) ³	Isotopic SST (°C) ⁴
A	OH 32	65 to 70	20	-6.5	20 to 28	27 to 29	31	-5.5	30 to 36
	OL 32	65 to 70	19	-6.5	20 to 28	27 to 29	31	-5.5	30 to 36
	PD 16	65 to 70	15	-6.5	20 to 28	27 to 29	28	-5.5	30 to 36
	PD 32	65 to 70	20	-6.5	20 to 28	27 to 29	31	-5.5	30 to 36
	PD 64	65 to 70	25	-6.5	20 to 28	27 to 29	36	-5.5	30 to 36
	WN 32	65 to 70	20	-6.5	20 to 28	27 to 29	33	-5.5	30 to 36
	WS 32	65 to 70	20	-6.5	20 to 28	27 to 29	32	-5.5	30 to 36
B	OH 32	70 to 80	16	-6.5	20 to 28	25 to 27	33	-5.5	30 to 36
	OL 32	70 to 80	15	-6.5	20 to 28	25 to 27	34	-5.5	30 to 36
	PD 16	70 to 80	13	-6.5	20 to 28	25 to 27	29	-5.5	30 to 36
	PD 32	70 to 80	16	-6.5	20 to 28	25 to 27	33	-5.5	30 to 36
	PD 64	70 to 80	21	-6.5	20 to 28	25 to 27	36	-5.5	30 to 36
	WN 32	70 to 80	17	-6.5	20 to 28	25 to 27	34	-5.5	30 to 36
	WS 32	70 to 80	17	-6.5	20 to 28	25 to 27	34	-5.5	30 to 36
C	OH 32	85 to 90	8	-7.0	18 to 26	25 to 27	24	-5.5	30 to 36
	OL 32	85 to 90	8	-7.0	18 to 26	25 to 27	24	-5.5	30 to 36
	PD 16	85 to 90	1	-7.0	18 to 26	25 to 27	21	-5.5	30 to 36
	PD 32	85 to 90	8	-7.0	18 to 26	25 to 27	24	-5.5	30 to 36
	PD 64	85 to 90	12	-7.0	18 to 26	25 to 27	28	-5.5	30 to 36
	WN 32	85 to 90	7	-7.0	18 to 26	25 to 27	25	-5.5	30 to 36

	WS 32	85 to 90	9	-7.0	18 to 26	25 to 27	24	-5.5	30 to 36
D	OH 32	55 to 60	23	-6.5	20 to 28	25	34	-5.5	30 to 36
	OL 32	55 to 60	21	-6.5	20 to 28	25	34	-5.5	30 to 36
	PD 16	55 to 60	17	-6.5	20 to 28	25	30	-5.5	30 to 36
	PD 32	55 to 60	26	-6.5	20 to 28	25	34	-5.5	30 to 36
	PD 64	55 to 60	27	-6.5	20 to 28	25	37	-5.5	30 to 36
	WN 32	55 to 60	24	-6.5	20 to 28	25	34	-5.5	30 to 36
	WS 32	55 to 60	22	-6.5	20 to 28	25	33	-5.5	30 to 36

¹AA = orbital parameters (see Table 6-1); ## = pCO₂ PAL (see Figure 6-3).

²Modelled mean annual sea surface temperature.

³Assuming Cambrian $\delta^{18}\text{O}_{\text{smow}} = -6.0$ ‰.

⁴Calculated using the phosphate oxygen temperature equation of Lécuyer *et al.* (2013). The range of values reflects the range of the measured $\delta^{18}\text{O}_{\text{phos}}$ data.

6.5. Methods in early Cambrian data–model comparison

The second part of this chapter examines a method for evaluating the agreement between geological and GCM-derived palaeoclimate proxy data. Although geochemical proxy data can provide high precision calibration points for GCM simulations (see §6.4.5), they only provide snap-shots of climatic conditions in space and time. The aim of this chapter is to investigate the broader global picture of Cambrian environments, and it would be useful to assess the agreement of each model with data that have a greater palaeogeographic distribution. Geological data have been used for nearly two centuries to make inferences about past climate (e.g. Agassiz 1838, 1840; Lyell 1840), and a large compendia of Phanerozoic-age climatically sensitive lithologies has recently been compiled (Boucot *et al.* 2013). Climatically sensitive lithologies are rock types that form under characteristic conditions and include such rock types as coal, evaporite and tillite deposits (e.g. Boucot *et al.* 2013; Cao *et al.* 2018). A detailed analysis of Devonian to Holocene climatically sensitive lithologies suggests that these deposits are restricted to particular latitudes, broadly zonal climate patterns (Cao *et al.* 2018).

Climatically sensitive lithologies respond to climate parameters such as temperature, humidity, and the precipitation–evaporation balance; i.e. these rocks are deposited or not deposited depending on the local climate regime. This is necessarily an overly simplified statement – for instance, platform carbonate deposition is also dependent on the rate of clastic supply. However, the environmental tolerance of climatically sensitive lithologies can be thought of as boundary conditions on the local climate.

The environmental conditions that climatically sensitive lithologies respond to, like temperature, precipitation, and evaporation, are also outputs of GCM simulations. It should, therefore, be possible to compare the lithologies deposited in any given location with GCM simulation outputs for that location. This approach has been applied to deep-time palaeoclimate problems; in particular to investigations of the distribution of Mesozoic bauxite, calcrete, coal, evaporite, and laterite deposits (e.g. Price *et al.* 1995, 1997b; Sellwood *et al.* 2000), and prevailing wind directions over the supercontinent Pangaea as evidenced by aeolian sandstones (Parrish & Peterson 1988). This approach has also been used to produce predictive models for the formation of climatically sensitive facies including modern-day bauxite deposition (Price *et al.* 1997a), and Mesozoic and Cenozoic upwelling regions from the distribution of organic-rich rocks

(Scotese & Summerhayes 1986). More recently this method has been used to compare the depositional settings of Cretaceous and Ordovician black shales with the Earth system model predictions of ocean anoxia (Monteiro *et al.* 2012; Pohl *et al.* 2017). This is a powerful approach for evaluating our understanding of global and regional palaeoclimate patterns, especially where more precise palaeoclimate proxy data are lacking, such as the Cambrian Period. .

6.5.1. Climate classification

Temperature and the precipitation–evaporation balance are the two most important parameters in determining the overall climate state of a region. These two parameters have the double advantages of being *relatively* readily preserved in the rock record and being primary outputs from GCM simulations. Temperature and the P/E balance are also the basis for most climate classification schemes, several of which have been developed. Climate classification schemes have been utilised by workers investigating the distribution of particular climatically sensitive lithologies (e.g. evaporites; Warren 2010), but have not been used systematically before. The major benefits of utilising a climate classification are that it:

- (a) applies a systematic approach to evaluating the climate state of a region;
- (b) creates variable levels of precision that can be adapted to the precision of available proxies; and
- (c) combines two of the key climate parameters important for determining surface geological processes into a single climate value, namely temperature and precipitation/evaporation.

This last is perhaps the most important, because it facilitates point-wise comparison of climatically sensitive geological data and the output of climate models.

The Köppen-Geiger classification is probably the most widely used such scheme, and is a generic climate classification scheme developed during the late 19th and early 20th centuries with the aim of relating global climate to vegetation patterns (Köppen 1884, 2011; Rubel & Kottek 2011). The Köppen-Geiger climate classes are based on monthly and annual temperatures and the P/E balance (Table 6-4; (Peel *et al.* 2007). In this chapter, an updated and simplified version of the scheme is employed that uses two out of the three levels of information.

The Köppen-Geiger scheme has five main climate categories (A to E) which are defined by temperature thresholds. The climate categories A to D can be subdivided on

Table 6-4. Thresholds of Köppen-Geiger climate classification scheme used here. After Peel *et al.* (2007).

Main climate	Secondary climate	Description	Criteria*
A	f	Tropical fully humid	$T_{\text{cold}} \geq 18$ $P_{\text{dry}} \geq 60$
	m	monsoonal	$P_{\text{dry}} < 60$ & $P_{\text{dry}} \geq 100 - (\text{MAP}/25)$
	w	savannah	$P_{\text{dry}} < 60$ & $P_{\text{dry}} < 100 - (\text{MAP}/25)$
B		Arid	$\text{MAP} < 10 \times P_{\text{thresh}}$
	W	desert	$\text{MAP} < 5 \times P_{\text{thresh}}$
	S	steppe	$\text{MAP} \geq 5 \times P_{\text{thresh}}$
C		Temperate	$T_{\text{hot}} > 10$ & $0 < T_{\text{cold}} < 18$
	s	dry summer	$P_{\text{sdry}} < 40$ & $P_{\text{sdry}} < P_{\text{wwet}} / 3$
	w	dry winter	$P_{\text{wdry}} < P_{\text{swet}} / 10$
	f	no dry season	Not Cs or Cw
D		Cold	$T_{\text{hot}} > 10$ & $T_{\text{cold}} \leq 0$
	s	dry summer	$P_{\text{sdry}} < 40$ & $P_{\text{sdry}} < P_{\text{wwet}} / 3$
	w	dry winter	$P_{\text{wdry}} < P_{\text{swet}} / 10$
	f	no dry season	Not Ds or Dw
E		Polar	$T_{\text{hot}} < 10$
	T	tundra	$T_{\text{cold}} > 0$
	F	frost	$T_{\text{cold}} \leq 0$

*Dimensions: P = mm/month; T = °C.

MAP = mean annual precipitation; MAT = mean annual temperature.

P_{dry} = precipitation of driest month; P_{sdry} = precipitation of driest summer month.

P_{wet} = precipitation of wettest month; P_{swet} = precipitation of wettest summer month; P_{wwet} = precipitation of wettest winter month.

T_{cold} = temperature of the coldest month; T_{hot} = temperature of hottest month.

If 70 % MAP in winter, $P_{\text{thresh}} = 2 \times \text{MAT}$; if 70 % MAP in summer, $P_{\text{thresh}} = (2 \times \text{MAT}) + 28$; else, $P_{\text{thresh}} = (2 \times \text{MAT}) + 14$. P_{thresh} is therefore temperature-dependent.

Summer/Winter are defined as the warmer/cooler six-month period ONDJFM (austral summer) or AMJJAS (boreal summer).

the basis of precipitation, considering the wettest and driest months of the year. The polar climate class (E) is simply divided on grounds of temperature. A third refinement can also be employed which describes the distribution of temperatures throughout the year (e.g. hot/cold summer). Such seasonality in temperature is beyond the resolution of available Cambrian proxy data, and to use this third layer of the classification scheme would constitute an unjustifiable level of precision. The first two levels of the Köppen-Geiger climate classification scheme, which account for annual temperature and precipitation/evaporation conditions, are therefore used here (Table 6-4).

6.5.2. Lithological data

Climatically sensitive lithologies

Many of the commonly used climatically sensitive lithologies are not available for use in constraining climates of Cambrian age. For instance, coal, one of the most iconic climatically sensitive lithologies, does not become a significant part of the rock record until the Late Devonian (Boucot *et al.* 2013). However, there are still a wide range of useful deposits available for this sort of analysis (Table 6-5). An additional uncertainty, and one that is likely insurmountable and unquantifiable, is that we are dealing with a non-uniformitarian ocean whose chemistry was substantially different from the modern global ocean. Therefore, any experiments or calculations based on modern ocean chemistry may not fully hold for the Cambrian ocean. Because the majority of lithologies used here are abiogenic we can have some confidence that well-characterised physical and chemical processes, like the carbonate phases precipitated from sea water, still hold. Each lithology was weighted according to the degree of certainty in its environmental conditions of formation (Table 6-5). The weighting value is between 0 and 1, where 1 indicates that we are near certain of its conditions of formation. This is, by necessity, a qualitative assessment, and the rationale for the weighting of each lithology is detailed below.

Marine evaporites are precipitated under arid conditions, but not necessarily associated with high temperatures (Warren 2010). It is, however, hard to explain regionally widespread marine evaporites by local aridity, for example in rain shadows. The P/E balance, rather than temperature, is the main controlling factor on the deposition of evaporites (Ziegler *et al.* 2003), and the position of the modern warm arid belts is determined by the position of the atmospheric Hadley cells. It may be possible to infer Hadley cell fluctuation from the location of ancient evaporitic belts. The Ediacaran/Cambrian transition, and the early Cambrian Period in particular, was a time of enormous evaporite, predominantly halite, deposition (Warren 2010). The mostly halite composition of Cambrian evaporite deposits provides support for the lower sulphate concentrations of the early Phanerozoic oceans suggested by sulphur isotope data (Algeo *et al.* 2015). However, some of this may be driven by regional differences, perhaps due to latitude or restricted ocean basins, as Siberia and central Australia both host mega-sulphate deposits of Cambrian age (Warren 2010).

Calcretes are typically deposited in semi-arid to arid continental settings with a fluctuating water table that persists on millennial timescales (Arakel 1991). Where

evaporation exceeds precipitation in soils, groundwater becomes supersaturated in calcium carbonate which precipitates in voids in the drying soil. Calcrete refers to the calcium carbonate end-member of mineralisation in soils produced by evaporation. Gypcrete and silcrete are the other important, but less common, types which form from waters supersaturated in sulphate and silica respectively. Whilst the type of mineralisation is typically controlled by the soil substrate (Arakel 1991), climate determines the extent and morphology of the precipitated duricrust. In the absence of plant roots penetrating and respiring in the soil, the main method of varying local soil $p\text{CO}_2$ (Wanke & Wanke 2007), evaporation is the main driver of calcrete formation. The precipitation of silcretes is predominantly pH and temperature dependent (with silcretes precipitating at lower temperatures (Wanke & Wanke 2007)). In summary, whilst often found in warm environments, which can help enhance evaporation, duricrust deposits are evidence of persistent semi-arid or arid conditions.

Lateritic products including bauxites, kaolinite, laterites and oolitic ironstones, specifically those comprising berthierine and chamosite, are the products of intensive continental weathering, in hot and humid conditions, analogous to modern monsoonal climates. Laterites typically form in regions where mean annual temperatures are in excess of 22 °C, and where precipitation consistently exceeds evaporation (Porrenga 1967; Nicolas & Bildgen 1979; Tardy *et al.* 1990; Tabor & Poulsen 2008; Boucot *et al.* 2013). Laterites have low preservation potential, as they are susceptible to metamorphic and meteoric weathering alteration, as well as being soft and therefore poorly resistant to physical erosion. However, putative early Cambrian laterites have been reported from North Africa (Avigad *et al.* 2005) and Siberia (Sukharina 1977), and alteration products of lateritic minerals including kaolinite have been reported from early and middle Cambrian *Konservat-Lagerstätten* on East Gondwana and Laurentia (Anderson *et al.* 2018).

Oolitic limestones are deposited in high energy shallow tropical seas supersaturated with calcium carbonate. Microbial and oolitic limestones dominated the deposition of carbonate platforms during the Cambrian Period (Kiessling *et al.* 2003). The majority of early Cambrian carbonate platforms were deposited as carbonate ramps rather than shelves (Burchette & Wright 1992; Kiessling *et al.* 2003). Despite the archaeocyathan extinction event around the early-middle Cambrian transition, most early Cambrian carbonate platforms persisted into the middle Cambrian, presumably along with the requisite environmental conditions (Kiessling *et al.* 2003). Oolitic

limestones form in a wider range of climates and latitudes than evaporites (Ziegler *et al.* 2003; Cao *et al.* 2018). However, combining information from the two records can be used to examine both temperature and humidity changes across latitudes.

Of the many *glaciogenic sediments*, only tillites, freeze-thaw structures and diamictites (which are not necessarily glaciogenic) have been reported from rocks of possibly early Cambrian age. These reports (e.g. Chumakov 2007) were largely dismissed by Boucot *et al.* (2013) on the basis of imprecise dating and comparison with more widespread and better constrained lithological indicators that support warmer climate regimes (c.f. Avigad *et al.* 2005). The absence of precise dating mechanisms makes all Neoproterozoic and lower Cambrian deposits difficult to assess, but Boucot *et al.* (2013) considered these glaciogenic deposits to relate to earlier (cooler) Neoproterozoic and perhaps earliest Cambrian climates.

Finally, *archaeocyathan reefs* are included in these analyses. Archaeocyathans were the first prolific metazoan reef architects, building major carbonate structures in conjunction with calcifying bacteria (Kerner & Debrenne 2013); but see also Wood (2011) and Mehra & Maloof (2018) for discussion of the possible reef-forming activities of *Cloudina*). Archaeocyathans are considered to be an extinct clade of sponges, and the ecological precursors to cnidarian corals which became the dominant reef-building organisms from the Ordovician Period (Lee & Riding 2018). Archaeocyathan reefs are considered to be stenothermal, stenohaline and stenobathyal constructions, mostly limited to intertropical climatic conditions with a normal range of salinities (Kerner & Debrenne 2013). The temperature setting of archaeocyathan reefs is not particularly well constrained, as water depth uncertainty might hide some of the temperature tolerance (Gandin & Debrenne 2010), and this is reflected in the lower confidence ascribed to the archaeocyathan reefs category (Table 6-5). In settings with increased salinity, where evaporate deposits are found, archaeocyathan reefs comprise a low diversity fauna with simple morphology and are only found in the lime muds between evaporitic deposits (Kerner & Debrenne 2013). In particular, the scarcity of archaeocyathans in early Cambrian rocks of South China (Steiner *et al.* 2004), combined with the widespread evaporite deposition on this palaeocontinent supports the idea that these were stenohaline organisms, and their absence from high latitude Avalonia suggests a stenothermal ecology.

Table 6-5. Formation conditions of climatically sensitive lithologies.

Lithology	Category	Weight	Formation conditions	References
Archaeocyathan reefs	Archaeocyathans (A)	0.50	Tropical/subtropical marine conditions with normal salinity	Kerner & Debrenne (2013); Lee & Riding (2018)
Calcretes	Calcrete (C)	1.00	Persistent semi-arid to arid continental conditions on millennial timescales, with fluctuating groundwater level and evaporation rate exceeding precipitation rate.	(Arakel (1991); Tabor & Poulsen (2008)
Halite	Evaporite (E)	1.00	Arid conditions, often with a (partially) isolated marine basin and dry air brought by the descending limb of the Hadley cell. MAP < approximately 400 mm, and evaporation rate exceeding precipitation in every month of the year.	Warren (2010)
Gypsum	Evaporite (E)	1.00	Arid conditions; MAP < approximately 400 mm, and evaporation exceeding precipitation in every month of the year.	Warren (2010)
Evaporite pseudomorphs (after gypsum or halite)	Evaporite (E)	0.50	Arid conditions; subsequent dissolution; MAP < ~400 mm; evaporation exceeding precipitation in every month of the year; down-weighted due to indirect evidence, i.e. inference of evaporite deposit that has been lost to alteration.	Patzkowsky <i>et al.</i> (1991); Warren (2010)
Length-slow chalcedony	Evaporite (E)	1.00	Arid conditions; semi-arid alkaline soils; forms in association with sulphate and halite evaporites.	Folk & Pittman (1971)
Tillite	Glaciogenic (G)	1.00	Cold (freezing) conditions with significant ice present.	Eyles (1993)
Striated dropstones	Glaciogenic (G)	1.00	Cold (freezing) conditions nearby.	Eyles (1993); Boucot <i>et al.</i> (2013)

Bauxite	Lateritic product (L)	1.00	Intense continental weathering under high humidity and temperature; precipitation exceeding evaporation for 9 to 11 months of the year; MAT > 25 °C and MAP > 1800 mm	Tardy <i>et al.</i> (1990); Tabor & Poulsen (2008)
Kaolinite	Lateritic product (L)	1.00	Intense continental weathering; high humidity and temperature	Boucot <i>et al.</i> (2013)
Laterite	Lateritic product (L)	1.00	Intense continental weathering under high humidity and temperature; precipitation exceeding evaporation for 11 months of the year; MAT > 25 °C	Nicolas & Bildgen (1979); Tabor & Poulsen (2008); Boucot <i>et al.</i> (2013)
Oolitic ironstone (berthierine, chamosite)	Lateritic product (L)	0.75	Intense continental weathering under high humidity and temperature; energetic shallow marine environment	Porrenga (1967); Boucot <i>et al.</i> (2013)
Oolitic limestone	Oolitic limestone (O)	1.00	Normal salinity (sub)tropical energetic shallow marine conditions; starved of clastic sediment input; high primary productivity	Nichols (2012, p. 226)

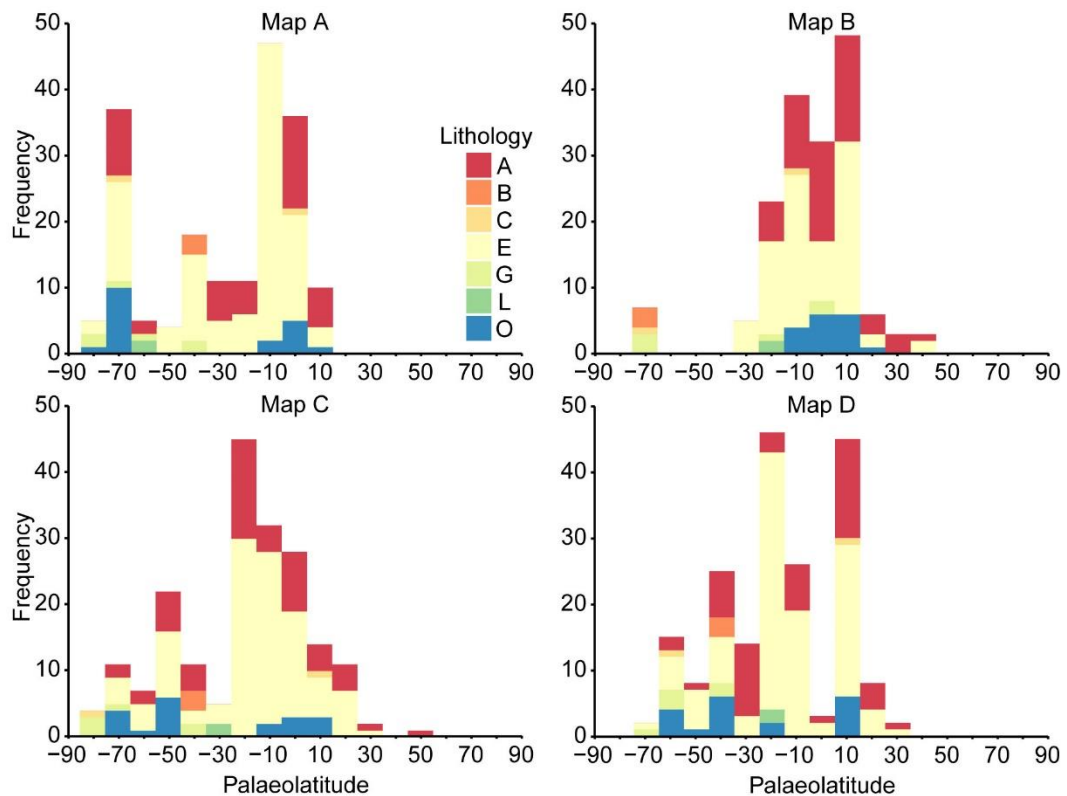


Figure 6-12. Palaeolatitudinal distribution of climatically sensitive lithologies under each palaeocontinental configuration. (a) Map A; (b) Map B; (c) Map C; (d) Map D. Lithology IDs: A = archaeocyathan reefs; C = calcrete; E = evaporite; G = glaciogenic; L = lateritic product; O = oolitic limestone. See Table 6-5.

Literature data

The compilation of an early Cambrian database of climatically sensitive lithologies (Appendix I) was inspired by the work of Boucot *et al.* (2013) who attempted such a compilation covering the whole Phanerozoic. Although the compilation of Boucot *et al.* (2013) provides a good starting point, the Cambrian dataset is not comprehensive, and in particular the age constraints on the lithologies required refining before use in the following analyses. Additional literature searches were completed using Google Scholar, searching for early and early/middle Cambrian occurrences of calcrete, evaporite, glaciogenic, kaolinite and other lateritic products including oolitic ironstones, and oolitic limestone. Information was also collected about stromatolites, but this was not used in the final analysis because of the uncertainty about the relative roles of climatic versus ecological factors on their distribution.

A search of the Palaeobiology Database (PBDB) revealed over 4,000 archaeocyathan occurrences. However, to avoid introducing a large collector bias into the dataset, particularly given the relative lack of understanding of the environmental constraints on archaeocyathan distributions, these data were not used. Archaeocyathan

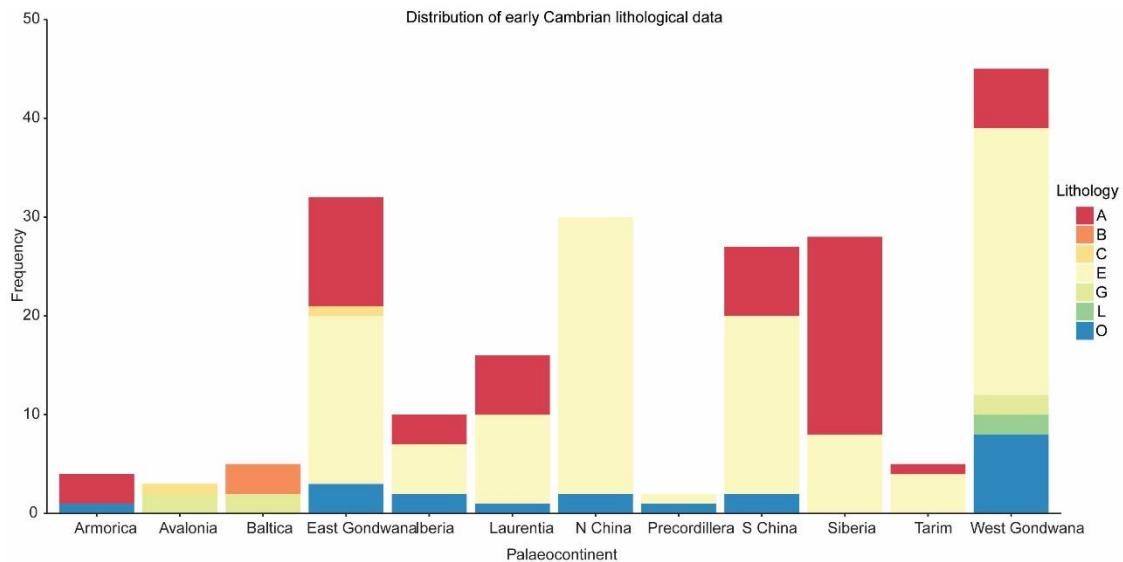


Figure 6-13. Frequency distribution of climatically sensitive lithologies in the database by palaeocontinent. Lithology IDs follow Table 6-5.

data used in the following analyses were taken from commonly used compendia of these fossils (Zhuravlev 1986; McKerrow *et al.* 1992; Kerner & Debrenne 2013).

Whilst comprehensive, this literature search was not exhaustive. The precise location (longitude, latitude) of many of the available data is not known (i.e. not published), so unless it was possible to estimate their modern-day position, for instance if they are plotted on a map, these data were excluded from analyses. There are loose age constraints, > 10 Myr, on many of the lithological data. However, it was relatively straightforward to assign an “Early” Cambrian age, corresponding to the current Terreneuvian Series or Series 2, or a “Middle” Cambrian age, corresponding to the Miaolingian Series. Analyses were conducted on lithological data with both “Early” Cambrian age or within a particular numerical age range.

Data collection was sufficient to incorporate information from polar to equatorial latitudes, and from all of the major Palaeozoic continents (Figure 6-12; Figure 6-13). However, few lithological data were available from modern South America or central Africa. Europe is relatively well-represented in these analyses, as is North America. Both the North and South China regions have very high degrees of data coverage, owing to the availability of a systematic review of Cambrian-age economically important salt-bearing formations (Wang *et al.* 2013).

6.5.3. Calculating data–model agreement

Scoring data–model agreement

The model and lithological data sets had to be converted into a common language in order to calculate agreement between them. The Köppen-Geiger climate classification scheme was used in this study (Table 6-4). Just as the GCM simulation outputs are translated into maps of Köppen-Geiger climate classes (Figure 6-14), the lithological data are also translated into the climate classes under which they could form (Table 6-5 and Table 6-6). The scoring system of Monteiro *et al.* (2012) was used to calculate an agreement score (φ):

$$\varphi = \frac{1}{2} \left(\frac{\sum_{i=1:n} A_i W_i}{\sum_{i=1:n} W_i} + 1 \right)$$

for n observations of weight W and agreement A . Where model cell and lithology datum are in agreement, $A = 1$, and where model cell and datum are in disagreement, $A = -1$. Where a lithological indicator is only formed under certain well-constrained climatic conditions, $W = 1$. However, where a lithological indicator may form under a wider range of conditions, or where there remains substantial uncertainty about the environmental tolerance of an indicator, $0 < W < 1$, with lower weight (closer to 0) being applied to those indicators with greater uncertainty (Table 6-5). For example, archaeocyathans are thought to have been stenothermal, stenohaline and stenobathyal organisms (Kerner & Debrenne 2013), but their range of environmental tolerance is not so well constrained as, for example, evaporites which only form under arid conditions.

Possible sampling biases

Working with collection-based data sets invariably introduces an element of sampling bias. To understand the possible impacts of sampling biases within the lithological dataset, the frequency distribution of the present day and ancient geographic positions of the lithologies are plotted (Figure 6-12; Figure 6-13). It is evident that some regions, and some palaeocontinents, are underrepresented with respect to others in the dataset, and this will result in some degree of sampling bias. Much of this bias is due to variable degrees of rock preservation, outcrop area, and exploration and data collection.

However, because these data are the result of physical and chemical (climatic) processes, the observed geographic presence/absence pattern is not simply bias in post-depositional processes but in fact carries a climatic signal. Therefore, whilst several sampling strategies, principally using rarefaction techniques, were considered for this study, all analyses were conducted using the full available lithological dataset (after

accounting for temporal constraints as outlined below). Rarefaction-based, data reduction, techniques were ruled out on the grounds that it is difficult to reasonably justify a standard area over which to rarefy data. Furthermore, there is the very likely risk that rarefaction would also remove a substantial amount of climatic signal, not just bias-induced noise.

Sampling strategy

Because the traditional “Early/Middle” Cambrian boundary is considered to be approximately equivalent to the current Series 2/Miaolingian boundary at ~509 Ma (Peng *et al.* 2012), analyses were run on:

- a. all lithologies identified as “Early” Cambrian in age ($n = 207$), and
- b. all lithologies with an estimated depositional age between 520 Ma to 510 Ma ($n = 142$).

The fine-scale correlation of this boundary across global deposits remains problematic, not least because of the absence until very recently of a ratified boundary section and marker, but there is good general recognition of traditional “Early/Middle” Cambrian boundary sections around the world. This should allow sufficient temporal resolution to interrogate broad, global, patterns in ancient climate by excluding lithologies identified as (a) “Middle Cambrian” or younger, or (b) younger than 509 Ma in age from data/model agreement analyses, and therefore outside of the temporal range of isotopic temperature estimates presented earlier (see Chapter Five).

Lithological data were not reduced or rarefied in any way other than constraining by time interval of interest prior to analysis. This does result in some model cells containing many more lithological data points than others. Dealing with sampling biases in the stratigraphic record is a challenging field all of its own (Alroy 2010; Dunne 2018; Dunne *et al.* 2018), and exploring this field is likely to be a profitable avenue for future work in geological data/model comparisons.

6.6. Results of early Cambrian data–model comparisons

6.6.1. Early Cambrian modelled Köppen-Geiger classification

Applying the Köppen-Geiger climate classification scheme to the climate model data reveals a consistent equatorial monsoon belt between 5° to 15° latitude either side of the equator (Figure 6-14; Figure 6-15). The distribution of climate zones is essentially zonal, progressing from equatorial (Köppen-Geiger: A) to temperate (Köppen-Geiger: C) climates in the mid to high latitudes and, where there are high latitude continents,

continental/cold climates (Köppen-Geiger: D). Where arid conditions (Köppen-Geiger: B) prevail, they do so at $\sim 30^\circ$ either side of the equator, and presumably mark the descending limbs of the atmospheric Hadley Cells. As $p\text{CO}_2$ increases from 16 to 32 to 64 PAL, the equatorial belts expand, pushing temperate climate zones to higher latitudes, and any continental/cold climate zones are substantially reduced in area and pushed back into the continental interiors (Figure 6-14; Figure 6-15). Regional climates similar to modern polar regions (Köppen-Geiger: EF, polar frost, and ET, polar tundra) are not predicted in any of the simulations.

The climate zones simulated under Map A, and all of the antarctocentric base maps (A, C, D), show distinctly different Northern and Southern hemisphere climate patterns (Figure 6-15), as anticipated by the zonal SST patterns (Figure 6-6). The distribution of climate zones in the Northern Hemisphere is purely zonal: there are no continental barriers to ocean and atmosphere circulation. The coolest climates (Köppen-Geiger: D) are found in West Gondwana (North Africa and South America), but only under lower $p\text{CO}_2$ simulations as the climate of this region becomes warm temperate under higher $p\text{CO}_2$ conditions.

The climate zones simulated under Map B are almost purely zonal in distribution. At $p\text{CO}_2$ levels of up to 32 PAL, equatorial climates dominate well into the mid-latitudes (up to $\sim 45^\circ$ either side of the equator) and expanding out to $\pm 60^\circ$ latitude when $p\text{CO}_2$ levels reach 64 PAL. Even at the lower end of $p\text{CO}_2$ values (16 PAL), the high latitudes are dominated by warm temperate climates. There is little change to the distribution of arid regions under different simulations with Map B, except that they expand slightly as $p\text{CO}_2$ increases. Arid regions simulated under Map B are notably more expansive than those modelled under the antarctocentric basemaps.

The climate zones simulated under Map C are comparable to those of Map A, but with an increased frequency of cold (D) climate states at high southern latitudes (Figure 6-15). The low latitude arid zones are also expanded with respect to Map A, as expected from the predicted MAP values, and maps B and C are consistently lower than A and D. Simulated climates in central Gondwana are uniformly cool to cold, under all tested boundary conditions. Arid and semi-arid regimes dominate lower latitudes, including on tropical Gondwana. Monsoonal climate regimes are of lesser frequency with Map C, suggesting that perhaps the hydrological cycle was somewhat less vigorous.

The climate zones simulated under Map D are typical of the antarctocentric models (Figure 6-14), but are generally slightly warmer, as characterised by the broader

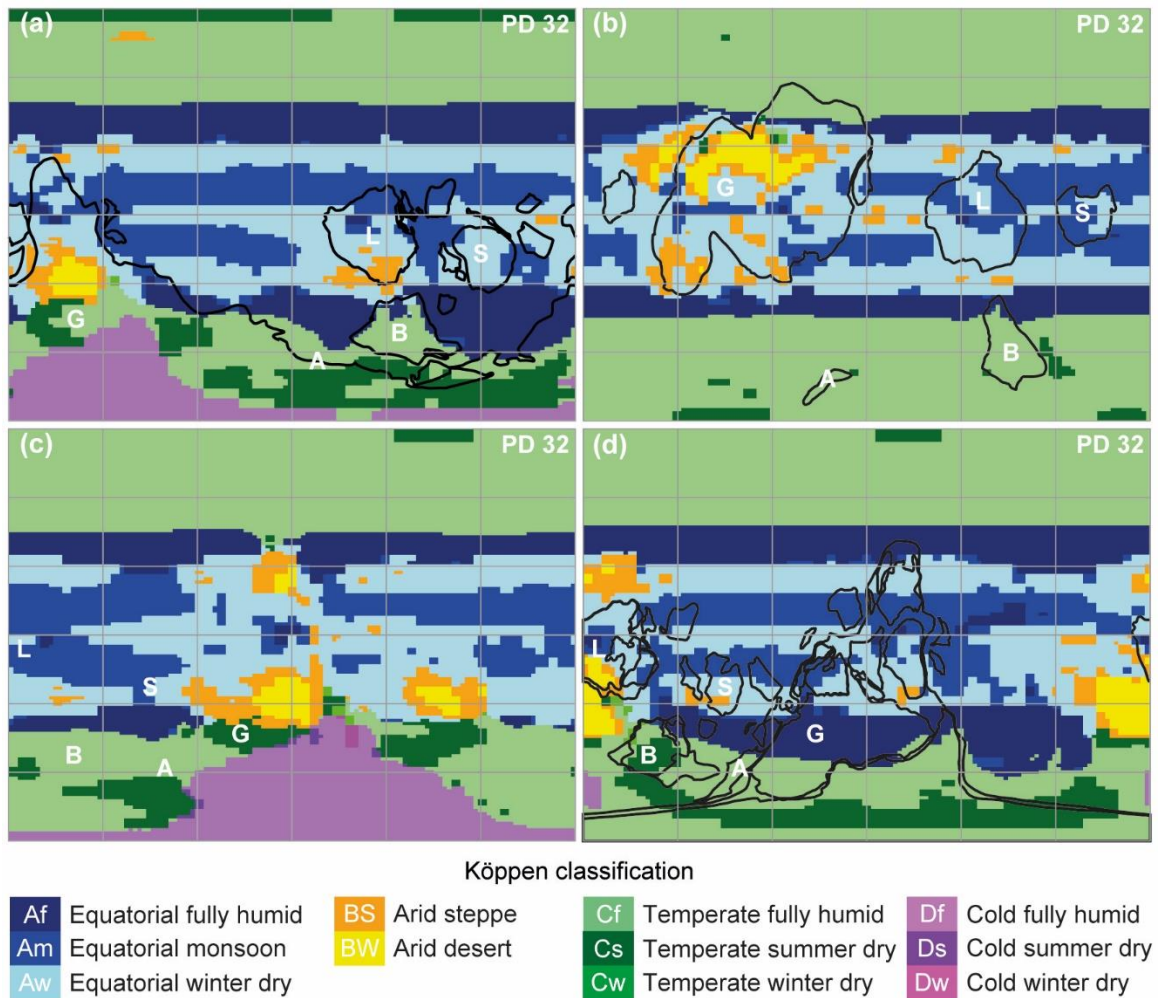


Figure 6-14. PD 32 Köppen Geiger classification maps for each palaeocontinental configuration. (a) Map A; (b) Map B; (c) Map C; (d) Map D. See Table 6-4 for climate classes.

expanse of fully humid equatorial (Köppen-Geiger: Af) conditions (Figure 6-15). This is further supported by Map D simulations producing the warmest global MAATs (Figure 6-7). Arid conditions are restricted to the lower $\sim 35^\circ$ latitude. The majority of Gondwana resided under a humid or monsoonal climate regime, with some regions with seasonally dry climates, and very minor regions of arid regimes under some simulations.

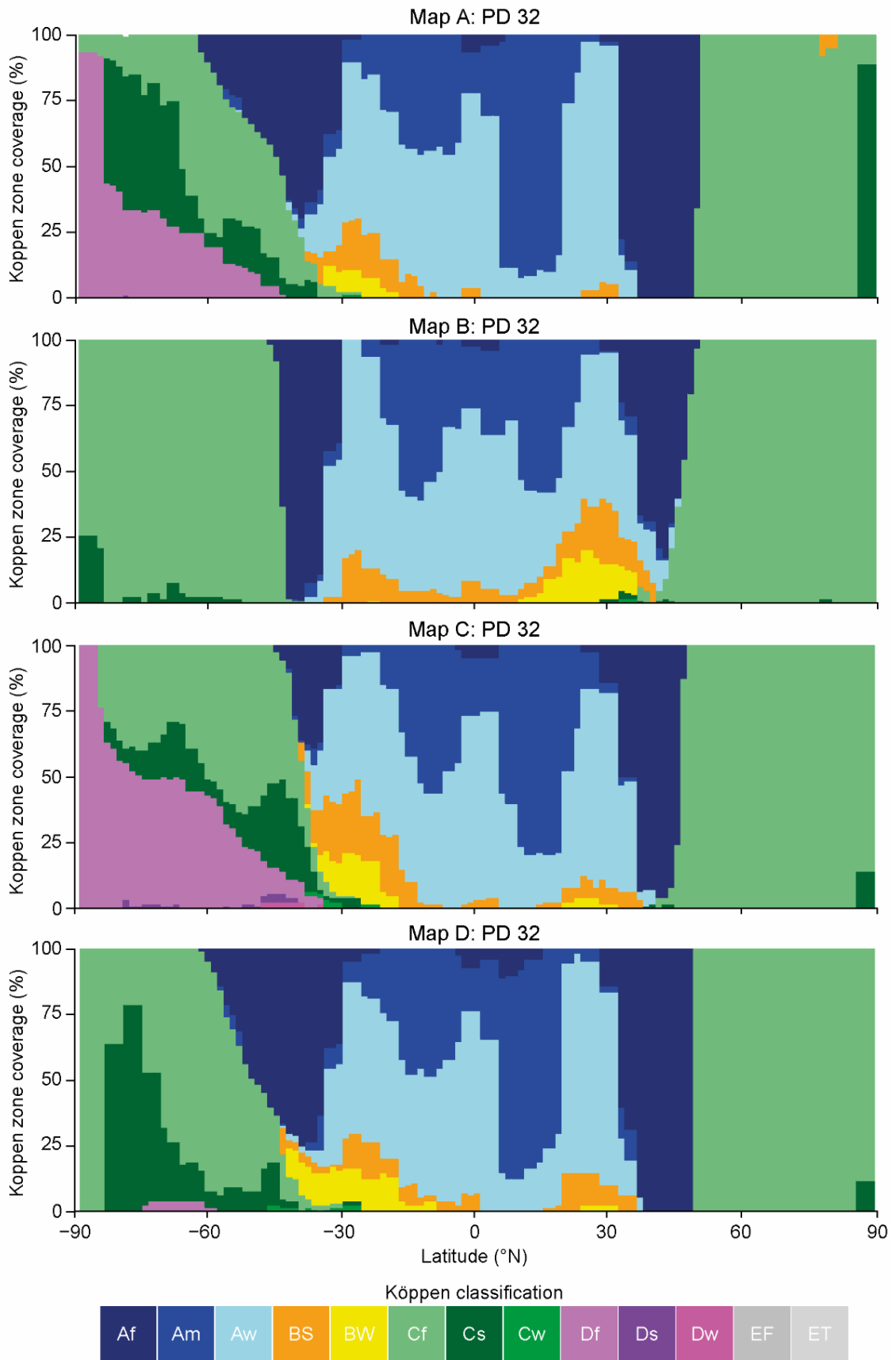


Figure 6-15. Frequency distribution of Köppen-Geiger climate classes for each basemap from PD 32 simulations. (a) Map A; (b) Map B; (c) Map C; (d) Map D. See Table 6-4 for climate classes.

Table 6-6. Scoring agreement of lithological occurrences and Köppen-Geiger climate zones

Lithology	ID	Köppen-Geiger climate zone													
		(A) Equatorial			(B) Arid		(C) Warm temperate			(D) Continental/Cold			(E) Polar		
		f	m	w	S	W	f	s	w	f	s	w	EF	ET	
Archaeocyathans	A	X	X	X			X	X	X						
Calcretes	C			X	X	X		X	X		X	X			
Evaporites	E				X	X									
Glaciogenic	G									X	X	X	X	X	
Lateritic products	L	X	X												
Oolitic limestone	O	X	X	X											

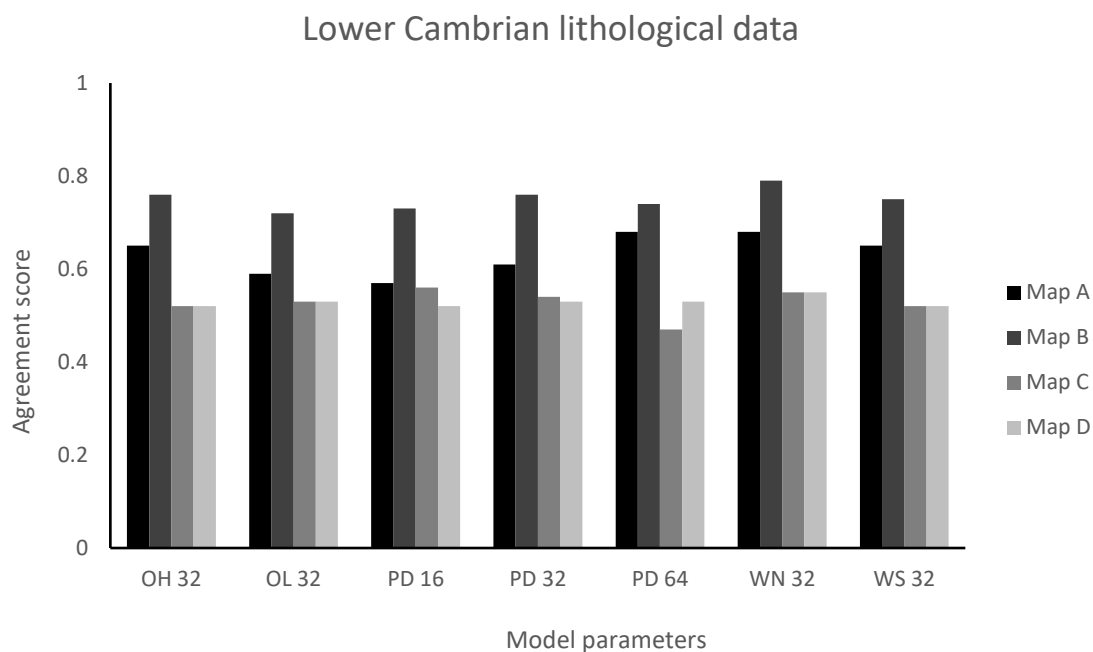


Figure 6-16. Data/model agreement scores calculated for all deposits dated as "Lower Cambrian" in age. See Table 6-7 for scores.

Table 6-7. Data/model agreement scores calculated for all "Lower Cambrian" deposits, calculated following Table 6-5, Table 6-6, and equation (6.1). Perfect agreement = 1; perfect disagreement = 0. Entries in italics are not supported by isotopic SSTs calculated in Chapter Five (see Table 6-3), and entries in bold are supported.

Boundary conditions	Map A	Map B	Map C	Map D
OH 32	0.65	<i>0.76</i>	<i>0.52</i>	0.52
OL 32	0.59	<i>0.72</i>	<i>0.53</i>	0.53
PD 16	<i>0.57</i>	<i>0.73</i>	<i>0.56</i>	<i>0.52</i>
PD 32	0.61	<i>0.76</i>	<i>0.54</i>	0.53
PD 64	0.68	0.74	<i>0.47</i>	0.53
WN 32	0.68	<i>0.79</i>	<i>0.55</i>	0.55
WS 32	0.65	<i>0.75</i>	<i>0.52</i>	0.52

6.6.2. Data/model comparison

The agreement between lithological proxy data and modelled climate zones, calculated according to Table 6-6 and equation 6.1, is shown in Table 6-7 and Table 6-8, and summarised in Figure 6-16 and Figure 6-17.

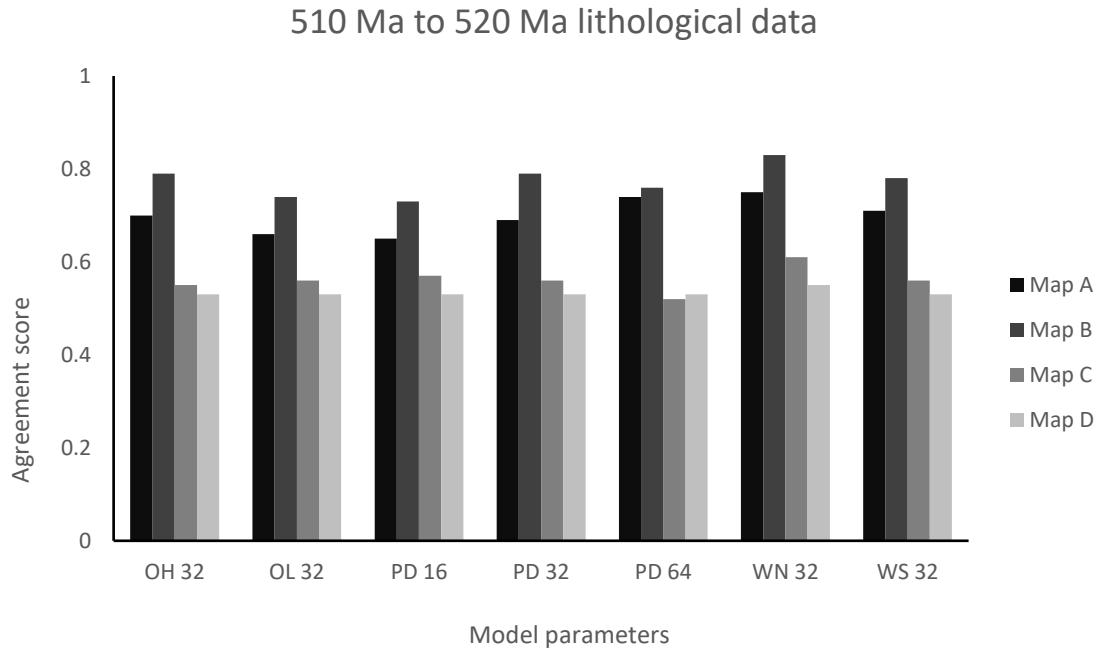


Figure 6-17. Data/model agreement scores calculated for all deposits dated between 510 Ma to 520 Ma. See Table 6-8 for scores.

Table 6-8. Data/model agreement scores calculated for all deposits with depositional ages between 510 Ma to 520 Ma, calculated following Table 6-5, Table 6-6, and equation (6.1). Perfect agreement = 1; perfect disagreement = 0. Entries in italics are not supported by isotopic SSTs calculated in Chapter Five (see Table 6-3), and entries in bold are supported.

Boundary conditions	Map A	Map B	Map C	Map D
OH 32	0.70	<i>0.79</i>	<i>0.55</i>	0.53
OL 32	0.66	<i>0.74</i>	<i>0.56</i>	0.53
PD 16	<i>0.65</i>	<i>0.73</i>	<i>0.57</i>	<i>0.53</i>
PD 32	0.69	<i>0.79</i>	<i>0.56</i>	0.53
PD 64	0.74	0.76	<i>0.52</i>	0.53
WN 32	0.75	<i>0.83</i>	<i>0.61</i>	0.55
WS 32	0.71	<i>0.78</i>	<i>0.56</i>	0.53

Overall, agreement between models and climatically sensitive lithological data was typically less than 80 %. The highest data-model agreement was found for simulations run using Map B. Consistently, maps C and D produced the lowest agreement scores. The WN (warm north) orbital conditions generate the highest agreement scores for each map using the 510 Ma to 520 Ma data, and nearly all of the

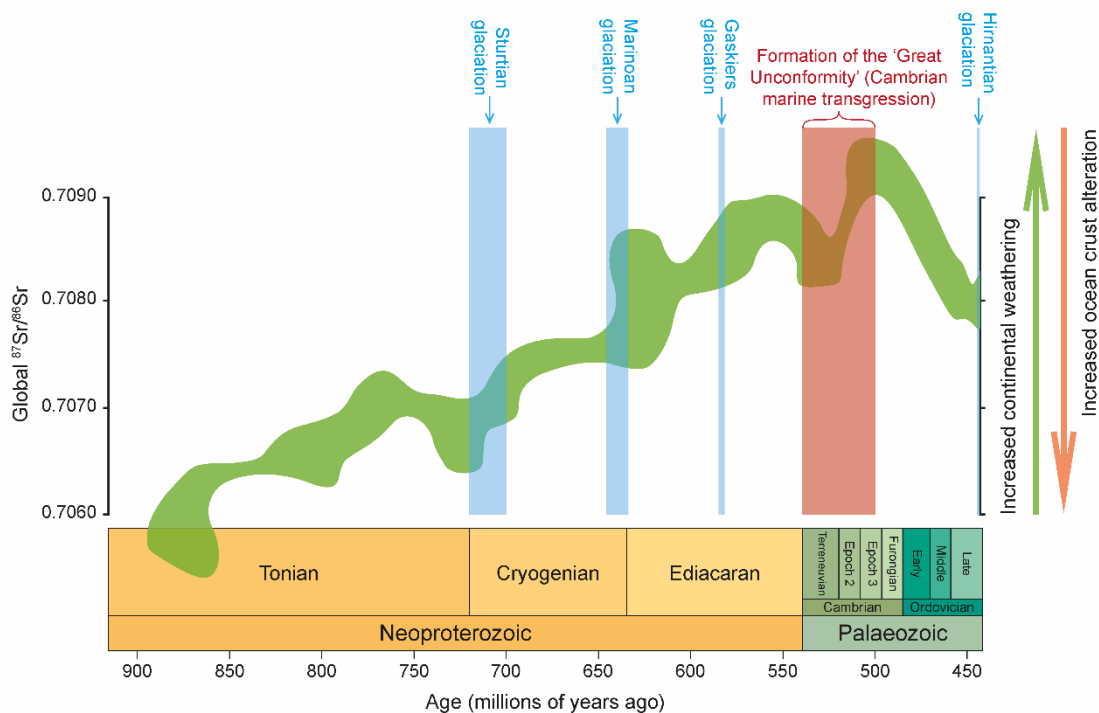


Figure 6-18. The strontium isotope curve for the Neoproterozoic Phanerozoic transition. The Sr isotope ratio increases steadily to an acme at ~500 Ma and has been linked to the early Cambrian marine transgression. Adapted after Hearing (2017) and Peters & Gaines (2012).

highest scores using the “Early Cambrian” data. The low $p\text{CO}_2$ simulations (16 PAL) also generate low agreement scores, though there is little difference between the middle and high $p\text{CO}_2$ simulations.

6.7. Discussion

6.7.1. Models, geological data and isotopic temperatures

All of the continental configurations under all of the tested boundary conditions simulate a greenhouse climate state with no established low altitude ice on land or sea. Broadly, this corroborates inferences from isotopic temperature estimates presented in Chapter Five, and the majority of climatically sensitive lithological data, which imply a greenhouse climate with low latitudinal temperature gradient in the early Cambrian. The GCM simulations also produce SST estimates (Figure 6-6; Figure 6-11) within the environmental tolerance limits of modern metazoans (Pörtner 2001; Hicks & McMahon 2002; Nguyen *et al.* 2011; Dilly *et al.* 2012), suggesting that the range of modelled Cambrian $p\text{CO}_2$ values (Figure 6-3) is biologically feasible.

Precipitation patterns suggest that there was enhanced activity of the hydrological cycle during the early Cambrian, with precipitation rates consistently exceeding modern values (Figure 6-8). This is supported by rare but palaeogeographically widespread

laterite deposits, which require hot humid conditions to form, and form today in regions with intense continental weathering. Intense continental weathering is also supported by the strontium isotope curve (Peters & Gaines 2012), which climbs steadily through the early to mid-Cambrian and peaks at ~500 Ma (Figure 6-18). High rates of continental weathering have been linked to the high and rising sea level of the Cambrian marine transgression (Peters & Gaines 2012). The GCM simulations presented here suggest that a more active hydrological cycle, involving elevated precipitation rates, could also be involved.

Perhaps unsurprisingly, the highest lithological data/model agreement scores are for Map B, which was constructed largely on the basis of lithological correlations and the expected geographical distribution of evaporites and carbonate platforms (Landing *et al.* 2013b). However, all simulations, except the highest $p\text{CO}_2$ (64 PAL) run, with Map B underestimate Avalonian SSTs by 3 to 7 °C with respect to the isotopic values, though there is general agreement between model and isotopic SSTs for Laurentia (Table 6-3). A partial explanation may be that the continental configuration was drawn for the “terminal Ediacaran – Early Cambrian” whereas the isotopic data are of later early Cambrian age, by which time Avalonia would have migrated further north, under this model (Landing *et al.* 2013b). However, this configuration is used to illustrate events throughout the early Cambrian (Landing *et al.* 2013a).

6.7.2. Irreconcilable differences?

Despite the general picture of a greenhouse climate supported by the isotopic, lithological, and model data sets, there are some notable inconsistencies. Geographically widespread evaporite deposition during the early Cambrian is difficult to explain in concert with geographically widespread laterite deposition, without invoking changes in seawater chemistry. It is possible that the wide palaeogeographic distribution of evaporites is a function of a non-uniformitarian Earth system, rather than a function of climate variability as we see it today. In other words: the climatic conditions needed to form evaporites with modern water chemistry may be different to those needed under conditions of Cambrian sea water chemistry. Sea water sulphate concentration estimates for the Cambrian carry large uncertainties, but were likely an order of magnitude lower than today (Canfield & Farquhar 2009).

The antarctocentric early Cambrian continental configurations (maps A, C, D) undoubtedly form a more parsimonious continuum with post-Cambrian

palaeogeographies constructed on the basis of palaeomagnetic data with better age constraints and biogeographic interpretations from more cosmopolitan taxa (e.g. Torsvik & Cocks 2013, 2016) than does Map B (Landing *et al.* 2013a, b). However, these configurations raise the problem of explaining evaporite and oolitic limestone deposition on modern North Africa (Avigad *et al.* 2005; Geyer & Landing 2006) and South America (Gaucher *et al.* 2003, 2007; Sprechmann *et al.* 2004), along with archaeocyathan reef development, at or near the Cambrian South Pole. The climate models presented here do not support the SSTs needed to form oolitic limestone deposits, or allow the development of extensive carbonate ramp systems, at high southern latitudes. Furthermore, the isotopic temperature data for Avalonia do not support Map C in placing Avalonia over the South Pole in Cambrian Stage 4. There are, therefore, fundamental mismatches between the early Cambrian palaeogeographic paradigm (Landing *et al.* 2013a; Torsvik & Cocks 2013) and both quantitative and qualitative palaeoclimate data. South American and North African deposits cannot be reconciled with the position of this sector of West Gondwana residing at or near the South Pole during the early Cambrian.

However, the available palaeomagnetic data do not support the drastic re-configuring of the major Palaeozoic continents required to move from a Map B-type world in Cambrian Stage 4 to the better palaeomagnetically constrained Early Ordovician palaeogeographies (Pollock *et al.* 2009; Torsvik & Cocks 2013, 2016). A fresh approach needs to be taken if the positions of the early Phanerozoic continents are to be correctly determined.

6.7.3. Deep ocean circulation perspectives on oxygen and phosphate

The absence of (high latitude) regions of cold water likely precludes a strong thermohaline circulation from developing. The deep ocean modelled with each continental configuration is therefore thermally stratified, with temperatures comparable to those estimated for Eocene greenhouse conditions (John *et al.* 2013). Indeed, deep ocean circulation is modelled in FOAM as the CONVEC2 parameter. Deep ocean circulation is consistently low across all GCM simulations (Figure 6-9). Ocean temperature depth profiles in the open ocean show a warm deep ocean with little vertical mixing. The only clear indication of deep-water formation is found in simulations using Map C, where a tongue of cooler water (still > 10 °C) projects north towards the equator from near the southern polar Gondwana margin.

Modelling of the oxygen and phosphorous cycles suggests that increasing the depth and intensity of bioturbation of previously stratified sediments (i.e. the state before the Cambrian explosion) decreases global ocean oxygenation, when weathering rates are high (Boyle *et al.* 2014). Although ocean oxygen levels decrease, this occurs without inducing widespread anoxia, but does cause a concomitant decrease in global phosphate availability (Boyle *et al.* 2014). Globally low levels of ocean oxygenation around the early to middle Cambrian (Epoch 2/Miaolingian transition) are supported by multiple redox-sensitive proxies, both geochemical and palaeobiological (Zhuravlev & Wood 1996; Boyle *et al.* 2014; Faggetter *et al.* 2017). Furthermore, recent analysis of ophiolite basalt over the last 3500 Ma suggests that deep ocean oxygen levels remained very low until at least the post-Cambrian Palaeozoic (Stolper & Keller 2018). This follows analyses of cerium over the Proterozoic/Phanerozoic transition which suggest an oxygenation pulse in the terminal Neoproterozoic, followed by a return to low oxygen conditions for the early Palaeozoic (Wallace *et al.* 2017). Just as the hypothesis of ocean deoxygenation finds support in Cambrian palaeoenvironmental data, so too does the concomitant decrease in the availability of phosphate in the oceans. Phosphorite deposits, widespread throughout the late Neoproterozoic, dwindle through the Cambrian Period (Cook 1992). This could in part be due to a transition from a less to a more stratified ocean with reduced upwelling (as modelled here). This global decline in phosphate deposition has been correlated with the closure of the phosphatisation taphonomic window, and so the apparent reduction in SSF diversity (Porter 2004).

6.7.4. Early Cambrian glaciation on Avalonia?

None of the boundary conditions tested simulate ice-forming conditions on or around Avalonia or Baltica (Figure 6-14); in particular, these simulations do not support early Cambrian low altitude glaciation on Avalonia or Baltica (cf. Lindström 1972; Landing & MacGabhann 2010). A southern polar continent is required to induce cold climates at high latitudes (Figure 6-14). Indeed, only under Map C does a region of cold water develop around Avalonia, when Avalonia is situated almost directly over the South Pole. This is likely to be a function of the high $p\text{CO}_2$ values expected during the Cambrian (Figure 6-3), and the greater heat capacity of water (oceans) compared to land. This modelling work is in general agreement with isotopic temperatures (Chapter Five) which support interpretations of warm high latitude sea surface temperatures. The

evidence for Avalonian glaciation comprises two occurrences of putative dropstone diamictites in the lower Terreneuvian Chapel Island Formation, eastern Newfoundland, and the Booley Bay Formation, southeast Ireland (Landing & MacGabhann 2010). However, although it was interpreted as glaciogenic, the Chapel Island diamictite comprising outsized clasts suspended in a massive muddy matrix, is also consistent with deposition from a debris flow (Landing & MacGabhann 2010). The Booley Bay Formation lacks reliable age constraints, and although it was considered early to middle Cambrian by Landing & MacGabhann (2010), it may well be of late Neoproterozoic age. In summary, glaciation on Avalonia during at least Cambrian Series 2, if not the whole of the early Cambrian, is not supported by sedimentological, geochemical, or climate modelling evidence.

6.7.5. Early Cambrian climate and biodiversity

The later part of the Cambrian explosion was not biologically stable. Three of the most significant carbon isotopic excursions of the Cambrian Period occur during Cambrian Age 4 (Zhu *et al.* 2006; Peng *et al.* 2012), and are all correlated to extinction or radiation events found in the fossil record. The first (MICE), positive, excursion has been correlated with peak archaeocyathid sponge diversity on the Siberian Platform (Brasier *et al.* 1994b; Zhu *et al.* 2006), whilst the second (AECE) and third (ROECE) excursions, both negative, are correlated with archaeocyathid and trilobite extinction events, respectively (Zhu *et al.* 2006; Ishikawa *et al.* 2014; Chang *et al.* 2017; Faggetter *et al.* 2017).

The drivers of these extinction events remain uncertain, though the terminal Age 4 trilobite extinction has been causally linked to activity of the Kalkarindji Large Igneous Province (LIP) in northern Gondwana (Jourdan *et al.* 2014; Faggetter *et al.* 2017). However, extinction rates are typically higher when global temperatures are higher (Mayhew *et al.* 2012). The early Cambrian was an interval of low (Boyle *et al.* 2014; Stolper & Keller 2018) and fluctuating (Faggetter *et al.* 2017; Hammarlund *et al.* 2017; Guilbaud *et al.* 2018; Wang *et al.* 2018; Wei *et al.* 2018) ocean oxygen levels which, combined with prolonged warm temperatures, would have contributed to the environmental stress faced by these early animals.

Archaeocyathids are thought to have been stenohaline and stenothermal organisms, preferring water with low turbidity (Kerner & Debrenne 2013). A warm greenhouse climate with a low latitudinal temperature gradient would have helped to

facilitate the diversification of archaeocyathids and their expansion into high southern latitudes, including North Africa (Kerner & Debrenne 2013). Falling levels of ocean phosphate (Boyle *et al.* 2014) – the main limiting nutrient in the oceans – under a Cambrian greenhouse climate would have negatively impacted primary productivity and hence had a knock-on negative effect on filter-feeding organisms.

The ‘reef gap’, from the beginning of the Miaolingian Epoch to the Early Ordovician, saw the replacement of relatively diverse reef systems, with archaeocyathan sponges, radiocyaths and coralomorphs, with low diversity assemblages of calcimicrobes and lithistid sponges capable of tolerating low oxygen environments (Lee & Riding 2018). This was coincident with declining ocean oxygen levels (e.g. Boyle *et al.* 2014), which may tentatively be linked to warm and stagnant oceans. However, the climatic conditions that form the backdrop to early Cambrian biological boom and bust may have played a role in preserving the biotic record of this interval.

6.7.6. Biodiversity, Konservat-Lagerstätten and Cambrian climates

The Cambrian System is characterised by assemblages of exceptionally preserved fossils that record early animal evolution and the Cambrian metazoan radiation. Most of the currently known Cambrian macrofossil *Konservat-Lagerstätten* that illuminate the Cambrian explosion were deposited at low to mid-palaeolatitudes (Muscente *et al.* 2017) – on Laurentia (Conway Morris *et al.* 1987; Conway Morris 1989; Peel & Ineson 2011), Gondwana (Paterson *et al.* 2016), and South China (Hou *et al.* 2017). These were likely within an expanded greenhouse tropical belt, with enhanced continental weathering rates and in the warmest regions of the ocean during an interval of global deoxygenation (Boyle *et al.* 2014). Enhanced continental weathering rates are supported by the Cambrian Epoch 2/Miaolingian acme in the Sr isotope curve (Peters & Gaines 2012). The high temperature and humidity of a strong greenhouse climate would have facilitated enhanced continental chemical weathering, including an expanded tropical climate belt (Figure 6-14; Figure 6-15).

Climate simulations under the antarctocentric maps (A, C, D) suggest that the equatorial monsoon belt (Köppen-Geiger: Am) and humid tropical climates (Köppen-Geiger: Af) would have covered the Rocky Mountains, Canada (Laurentia), northern Greenland, Denmark (Laurentia), South China, and southern Australia, famed for the Burgess Shale, Sirius Passet, Chengjiang, and Emu Bay Shales, respectively (Figure 6-19). Current research in the fields of experimental taphonomy (e.g. McMahon *et al.*

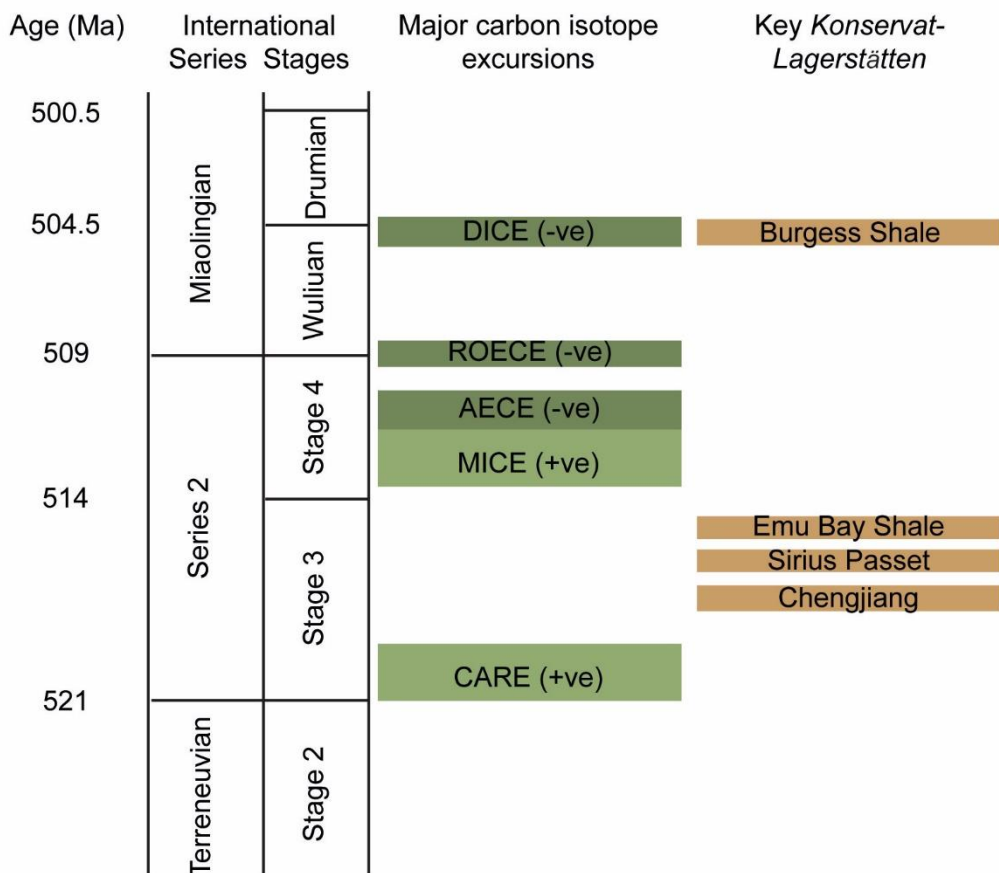
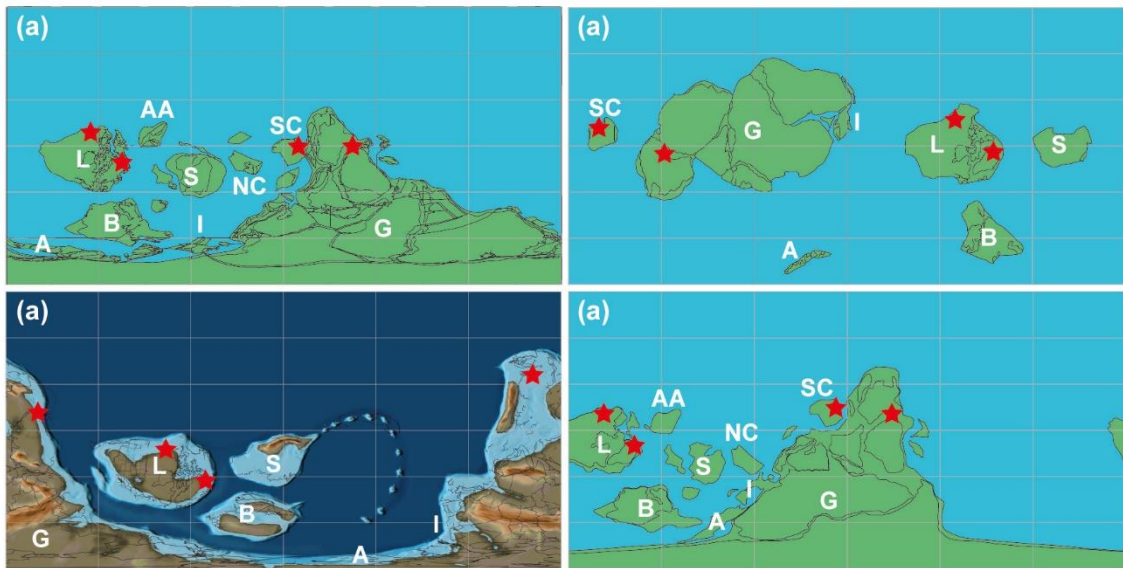


Figure 6-19. Stratigraphic context of the major Cambrian Konservat-Lagerstätten, and their palaeogeographic distributions on the four basemaps tested here. Adapted after Peng *et al.* (2012).

2016) and sedimentary petrology (Anderson *et al.* 2018) support an association between certain clay minerals and the exceptional preservation of non-biomineralising anatomy. The clay minerals most closely associated with exceptional preservation including kaolinite and its alteration products berthierine/chamosite (McMahon *et al.* 2016;

Anderson *et al.* 2018) which are common tropical weathering products, produced today by intense continental weathering in regions with equatorial monsoon climates. It is important to note that the mineral space of BST preservation shown by Anderson *et al.* (2018) is a subset of the mineral space of ‘ordinary’ skeletal preservation. Therefore, these clay minerals cannot be the only factor controlling the distribution of early Cambrian exceptional preservation, and other factors such as low oxygen availability and rapid burial may also play a role (Anderson *et al.* 2018).

6.8. Conclusions

This chapter aimed to:

- (a) establish a (semi-)quantitative global view of early Cambrian climates;
- (b) put physical climatic constraints on early Cambrian palaeogeography; and
- (c) place physical climatic constraints on early Cambrian oceanography.

Firstly, GCMs initiated with boundary conditions spanning a plausible range of values for the early Cambrian simulated SST estimates that are within the habitable range of modern metazoans. These modelled SSTs are in good general agreement with isotopic SST estimates from early Cambrian high and low latitude phosphatic microfossils (Chapter Five). Both sets of data also concur with the generally held view, established from lithological data, that the Cambrian Period was a greenhouse interval in Earth’s climate history. Isotopic SST estimates can be used to calibrate GCM simulations to build a quantitative picture of early Cambrian climates.

Secondly, isotopically calibrated GCM simulations can be combined with a database of qualitative data on climatically sensitive lithologies to evaluate climatic patterns under different palaeocontinental configurations. Although early Cambrian palaeogeography remains poorly constrained, GCM simulations combined with the distribution of climatically sensitive lithological data can contribute to the debate around refining palaeocontinental configurations. Further work is needed to fully account for the observed early Cambrian sedimentological data as none of the GCM simulations find particularly strong agreement. The ‘antarctocentric’ palaeocontinental configurations especially perform poorly, suggesting that either (a) they are not supported by the geological data, (b) better constraints are needed on the climates under which these lithologies form, or (c) a higher resolution GCM is needed for this type of analysis.

Thirdly, all of the GCM simulations explored here predict a warm deep ocean, with water temperatures in excess of 10 °C at the sea floor (−4000 m). This may be solely a function of the physics of the model, or reflect a real and inevitable result of a greenhouse climate, the GCMs result in warm deep ocean temperatures with limited deep-water formation and little deep ocean circulation. Interestingly, these simulations support the notion of a thermally stratified deep ocean at the beginning of the Phanerozoic Eon supported by recent work suggesting that deep ocean oxygenation did not occur until later in the Palaeozoic (Stolper & Keller 2018).

If the data/model comparison technique works, Map B must be considered the most plausible of the examined continental configurations for the early Cambrian. However, the method requires further testing before such a drastic revision of decades of research around early Cambrian continental configurations should be considered. Inconsistencies remain between early Cambrian climate model outputs, geological and isotopic data. Even under the greenhouse conditions suggested by isotopic and GCM temperature estimates, evaporite, oosparite and archaeocyathan reef formation at the South Pole is implausible, but so is Avalonian glaciation. Although discrepancies remain between the different available data sets, the three independent lines of evidence are in broad agreement that the early Cambrian was a typical greenhouse interval in Earth's climate history.

Chapter Seven: Conclusions

7.1. Thesis aims

The primary aim of this study was to place first-order quantitative constraints on early Cambrian marine environments. Working towards this aim required finding and assessing the preservation of novel sources of Cambrian palaeoclimate data. Following establishment of a protocol to assess the preservation of phosphatic ‘small shelly fossils’ (SSFs), oxygen isotope data were measured and translated into estimates of early Cambrian sea surface temperatures (SSTs). A different approach to the problem, using general circulation model (GCM) simulations, was also explored, and the results of the two independent investigations were then combined in an effort to establish a quantitative global picture of the early Cambrian climate.

7.2. Assessing phosphate oxygen isotopic preservation in deep time

Carefully selected phosphate-biomineralising SSFs were examined to establish their physical and chemical preservation. Specimens that were visually distinct under optical microscopy were assembled into candidate ‘pristine’ and ‘altered’ samples for isotopic analysis. Representative specimens taken from these visually distinct samples were found to have consistent ultrastructural and chemical differences. High resolution imaging of phosphate crystallite ultrastructure was the most consistent method for distinguishing between optically distinct specimens.

The optically distinct specimens were also shown to be consistently isotopically distinct. The preservation protocol outlined in Chapter Three therefore successfully distinguishes between isotopically distinct early Cambrian phosphatic SSFs. Specimens determined *a priori* as pristine were consistently isotopically heavier than specimens considered identified as diagenetically altered. Both pristine and altered SSFs were also generally isotopically heavier than authigenic or diagenetic phosphate from the same localities. This lightening diagenetic trend is comparable to that observed in phosphatic conodonts (e.g. Epstein *et al.* 1977; Rejebian *et al.* 1987; Joachimski *et al.* 2009).

Interestingly, *in situ* $\delta^{18}\text{O}$ analyses revealed high tissue-specific intra-specimen isotopic variability. This corroborated qualitative chemical analyses that revealed increased abundance of elements characteristic of diagenetic alteration in the porous laminae of linguliformean brachiopods relative to the compact laminae. This suggests that densely phosphatic microfossils, or fossils with densely phosphatic laminae, are

most likely to preserve palaeoenvironmental $\delta^{18}\text{O}$ signatures. Isotopically pristine early Cambrian phosphatic microfossils can be identified and selectively analysed to yield palaeoenvironmentally informative $\delta^{18}\text{O}$ data.

7.3. The Cambrian $\delta^{18}\text{O}$ record and temperature estimates

The early Cambrian $\delta^{18}\text{O}$ values of pristine phosphatic SSFs are comparable to values obtained from Early Ordovician conodont and brachiopod biominerals (e.g. Bassett *et al.* 2007; Trotter *et al.* 2008; Veizer & Prokoph 2015; Quinton *et al.* 2018). Early Palaeozoic oxygen isotope data display a secular trend that is most readily explained by a progressively isotopically heavier global ocean, from an early Phanerozoic value of approximately -6‰ to the recent ice-free value of approximately -1‰ (Veizer *et al.* 1999; Shields *et al.* 2003; Kasting *et al.* 2006; Jaffrés *et al.* 2007; Prokoph *et al.* 2008; Giles 2012; Veizer & Prokoph 2015). This contrasts with results from the developing carbonate clumped isotope field (Came *et al.* 2007; Finnegan *et al.* 2011; Bergmann *et al.* 2018; Henkes *et al.* 2018; Ryb & Eiler 2018), with which a reconciliation would be useful.

By accounting for the secular trend in $\delta^{18}\text{O}_{\text{sw}}$, early Cambrian microfossil $\delta^{18}\text{O}_{\text{phos}}$ values can be used to quantitatively constrain Cambrian climates. In particular, SSF $\delta^{18}\text{O}$ data yield SST estimates of approximately 23 °C and 35 °C at high and low palaeolatitudes, respectively. These values are within the thermal tolerance limits of modern metazoans (e.g. Pörtner 2001; Hicks & McMahon 2002; Nguyen *et al.* 2011), and are comparable to high and low latitude SST estimates for younger, better understood, greenhouse climates of the late Mesozoic (Littler *et al.* 2011; Jenkyns *et al.* 2012; Ando *et al.* 2015; O'Brien *et al.* 2017; Robinson *et al.* 2017) and early Cenozoic (Bijl *et al.* 2009; Sluijs *et al.* 2009; Douglas *et al.* 2014; Frieling *et al.* 2017, 2018; Suan *et al.* 2017; Evans *et al.* 2018).

7.4. The early Cambrian marine environment

Isotopic SST estimates place first-order quantitative constraints on the early Cambrian marine environment and suggest that the Cambrian climate was comparable to other Phanerozoic greenhouse intervals. This interpretation is supported by GCM simulations initiated using a range of boundary conditions plausible for the early Cambrian. Both the GCM and isotopic temperature estimates corroborate the general picture built up from qualitative and semi-quantitative geological data that the Cambrian was generally

a greenhouse world (Boucot *et al.* 2013) with high continental chemical weathering rates (Peters & Gaines 2012).

The GCM simulations further predict a thermally stratified ocean, with limited vertical movement of water masses and a warm deep ocean. This corroborates evidence indicating deep ocean dysoxia (Zhuravlev & Wood 1996; Boyle *et al.* 2014; Faggetter *et al.* 2017) until at least the early Palaeozoic (Stolper & Keller 2018). However, this is unlikely to reflect the state of the ocean throughout the whole Cambrian Period, as there is an emerging picture of an interval of low (Boyle *et al.* 2014; Stolper & Keller 2018) but fluctuating (Faggetter *et al.* 2017; Hammarlund *et al.* 2017; Guilbaud *et al.* 2018; Wang *et al.* 2018; Wei *et al.* 2018) ocean oxygenation, perhaps including the development of oxygen minimum zones in the Cambrian (Hammarlund *et al.* 2017; Guilbaud *et al.* 2018). Increasing the stratigraphic range and resolution of the Cambrian $\delta^{18}\text{O}$ record should be a priority for future work.

Although the Cambrian world appears to have been within the bounds of modern greenhouse climate states, this was undoubtedly a stressful environment for the emerging mobile metazoan biota. High ocean temperatures, concomitant poor ocean circulation and low oxygen conditions would have contributed to ecosystem instability during the early Cambrian, witnessed by the episodic metazoan extinctions and negative carbon isotope excursions throughout the early and middle Cambrian. It was against this backdrop that early metazoan ecosystems evolved.

7.5. Future work

This study is a proof-of-concept for expanding the biogenic phosphate oxygen isotope record back into the early Cambrian Period. As such, one of the more pressing tasks is to improve both the palaeogeographic and stratigraphic coverage of the data set. Both of these are needed in order to confidently assess palaeobiological against quantitative palaeoclimatic patterns. Whilst such work can now incorporate $\delta^{18}\text{O}$ data, other quantitative and semi-quantitative proxies for palaeoenvironmental factors should also be examined at high stratigraphic resolution.

This study has highlighted, however, a more fundamental area for future work: better constraining the phosphate oxygen isotope temperature equation. It is of prime importance that the inherent uncertainty of the current phosphate temperature equations is thoroughly addressed in order to better constrain temperature estimates throughout the Palaeozoic.

Combining lithological data and palaeoclimate models is a promising avenue for future work. Lithological indicators of palaeoclimate provide a more widespread, though cruder, measure of ancient environmental conditions than quantitative proxy data will ever achieve. In concert with climate models, such data can reveal regional climate patterns and even help to constrain palaeogeographic interpretations. Future work in this area is likely to include making refinements for sampling biases, and the range and climatic inferences of lithological indicators that are used. In particular, this method could be useful in examining older environments for which continental configurations are less well constrained and for which quantitative palaeoenvironmental data is unavailable.

Bibliography

- Agassiz, L. 1838. On the Erratic Blocks of the Jura. *The Edinburgh New Philosophical Journal*, **24**, 176–179.
- Agassiz, L. 1840. *Études Sur Les Glaciers*. Neuchâtel, Gent & Gassman.
- Algeo, T.J., Luo, G.M., Song, H.Y., Lyons, T.W. & Canfield, D.E. 2015. Reconstruction of secular variation in seawater sulfate concentrations. *Biogeosciences*, **12**, 2131–2151, <https://doi.org/10.5194/bg-12-2131-2015>.
- Alroy, J. 2010. Fair Sampling of Taxonomic Richness and Unbiased Estimation of Origination and Extinction Rates. *The Paleontological Society Papers*, **16**, 55–80, <https://doi.org/10.1017/S1089332600001819>.
- Álvaro, J.J. & Clausen, S. 2007. Botoman (Lower Cambrian) turbid- and clear-water reefs and associated environments from the High Atlas, Morocco. *Geological Society, London, Special Publications*, **275**, 51–70, <https://doi.org/10.1144/GSL.SP.2007.275.01.04>.
- Álvaro, J.J., Ahlberg, P., et al. 2013. Chapter 19 Global Cambrian trilobite palaeobiogeography assessed using parsimony analysis of endemism. *Geological Society, London, Memoirs*, **38**, 273–296, <https://doi.org/10.1144/M38.19>.
- Álvaro, J.J., Benziane, F., Thomas, R., Walsh, G.J. & Abdelaziz, Y. 2014. Neoproterozoic–Cambrian stratigraphic framework of the Anti-Atlas and Ouzellagh promontory (High Atlas), Morocco. *Journal of African Earth Sciences*, **98**, 19–33, <https://doi.org/10.1016/j.jafrearsci.2014.04.026>.
- Anderson, R.P., Tosca, N.J., Gaines, R.R., Koch, N.M. & Briggs, D.E.G. 2018. A mineralogical signature for Burgess Shale–type fossilization. *Geology*, **46**, 347–350, <https://doi.org/10.1130/G39941.1>.
- Ando, A., Huber, B.T., MacLeod, K.G. & Watkins, D.K. 2015. Early Cenomanian ‘hot greenhouse’ revealed by oxygen isotope record of exceptionally well-preserved foraminifera from Tanzania. *Paleoceanography*, **30**, 1556–1572, <https://doi.org/10.1002/2015PA002854>.
- Arakel, A.V. 1991. Evolution of Quaternary duricrusts in Karinga Creek drainage system, Central Australian groundwater discharge zone. *Australian Journal of Earth Sciences*, **38**, 333–347, <https://doi.org/10.1080/08120099108727976>.
- Armstrong, H.A., Pearson, D.G. & Griselin, M. 2001. Thermal effects on rare earth element and strontium isotope chemistry in single conodont elements. *Geochimica et Cosmochimica Acta*, **65**, 435–441, [https://doi.org/10.1016/S0016-7037\(00\)00548-2](https://doi.org/10.1016/S0016-7037(00)00548-2).
- Avigad, D., Sandler, A., Kolodner, K., Stern, R.J., McWilliams, M., Miller, N. & Beyth, M. 2005. Mass-production of Cambro–Ordovician quartz-rich sandstone as a consequence of chemical weathering of Pan-African terranes: Environmental implications. *Earth and Planetary Science Letters*, **240**, 818–826, <https://doi.org/10.1016/j.epsl.2005.09.021>.

- Babcock, L.E., Peng, S., Zhu, M., Xiao, S. & Ahlberg, P. 2014. Proposed reassessment of the Cambrian GSSP. *Journal of African Earth Sciences*, **98**, 3–10, <https://doi.org/10.1016/j.jafrearsci.2014.06.023>.
- Balthasar, U. 2009. The brachiopod *Eoobolus* from the Early Cambrian Mural Formation (Canadian Rocky Mountains). *Paläontologische Zeitschrift*, **83**, 407–418, <https://doi.org/10.1007/s12542-009-0026-4>.
- Barham, M., Murray, J., Joachimski, M.M. & Williams, D.M. 2012. The onset of the Permo-Carboniferous glaciation: reconciling global stratigraphic evidence with biogenic apatite $\delta^{18}\text{O}$ records in the late Viséan. *Journal of the Geological Society*, **169**, 119–122, <https://doi.org/10.1144/0016-76492011-102>.
- Bartdorff, O., Wallmann, K., Latif, M. & Semenov, V. 2008. Phanerozoic evolution of atmospheric methane. *Global Biogeochemical Cycles*, **22**, GB1008, <https://doi.org/10.1029/2007GB002985>.
- Bassett, D., Macleod, K.G., Miller, J.F. & Ethington, R.L. 2007. Oxygen Isotopic Composition of Biogenic Phosphate and the Temperature of Early Ordovician Seawater. *PALAIOS*, **22**, 98–103, <https://doi.org/10.2110/palo.2005.p05-089r>.
- Beckholmen, M. & Glodny, J. 2004. Timanian blueschist-facies metamorphism in the Kvar Kush metamorphic basement, Northern Urals, Russia. *Geological Society, London, Memoirs*, **30**, 125–134, <https://doi.org/10.1144/GSL.MEM.2004.030.01.11>.
- Beecher, C.E. 1891. Development of the Brachiopoda, Part I. Introduction. *American Journal of Science*, **41**, 343–357.
- Bell, W.C. 1944. Early Upper Cambrian brachiopods. In: *Early Upper Cambrian Faunas of Central Montana*. Geological Society of America special paper, **54**, 144–153.
- Bengtson, S. 1992. Proterozoic and Earliest Cambrian Skeletal Metazoans. In: Schopf, J. W. & Klein, C. (eds) *The Proterozoic Biosphere: A Multidisciplinary Study*. Cambridge, UK, Cambridge University Press, 1017–1033.
- Bengtson, S. 2004. Early skeletal fossils. In: Lipps, J. H. & Waggoner, B. M. (eds) *Neoproterozoic-Cambrian Biological Revolutions*. The Paleontological Society, The Paleontological Society Papers, **10**, 67–77.
- Bengtson, S., Conway Morris, S., Cooper, B.J., Jell, P.A. & Runnegar, B. 1990. *Early Cambrian Fossils from South Australia*. Brisbane, Association of Australasian Palaeontologists, Association of Australasian Palaeontologists, Memoir, **9**.
- Bennett, C.E., Williams, M., et al. 2018. Oxygen isotope analysis of the eyes of pelagic trilobites: Testing the application of sea temperature proxies for the Ordovician. *Gondwana Research*, **57**, 157–169, <https://doi.org/10.1016/j.gr.2018.01.006>.
- Bergmann, K.D., Finnegan, S., Creel, R., Eiler, J.M., Hughes, N.C., Popov, L.E. & Fischer, W.W. 2018. A paired apatite and calcite clumped isotope thermometry approach to estimating Cambro-Ordovician seawater temperatures and isotopic composition. *Geochimica et Cosmochimica Acta*, **224**, 18–41, <https://doi.org/10.1016/j.gca.2017.11.015>.

- Berner, R.A. 2006. Inclusion of the Weathering of Volcanic Rocks in the GEOCARBSULF Model. *American Journal of Science*, **306**, 295–302, <https://doi.org/10.2475/05.2006.01>.
- Berner, R.A. 2008. Addendum to “Inclusion of the Weathering of Volcanic Rocks in the GEOCARBSULF Model” (R. A. Berner, 2006, V. 306, p. 295–302). *American Journal of Science*, **308**, 100–103, <https://doi.org/10.2475/01.2008.04>.
- Berner, R.A. 2009. Phanerozoic atmospheric oxygen: New results using the GEOCARBSULF model. *American Journal of Science*, **309**, 603–606, <https://doi.org/10.2475/07.2009.03>.
- Bijl, P.K., Schouten, S., Sluijs, A., Reichert, G.-J., Zachos, J.C. & Brinkhuis, H. 2009. Early Palaeogene temperature evolution of the southwest Pacific Ocean. *Nature*, **461**, 776–779, <https://doi.org/10.1038/nature08399>.
- Billings, E. 1861. Note on a new genus of Palaeozoic Brachiopoda. *Canadian Journal of Industry, Science and Art*, **6**, 148.
- Blake, R.E., O’Neil, J.R. & Garcia, G.A. 1997. Oxygen isotope systematics of biologically mediated reactions of phosphate: I. Microbial degradation of organophosphorus compounds. *Geochimica et Cosmochimica Acta*, **61**, 4411–4422, [https://doi.org/10.1016/S0016-7037\(97\)00272-X](https://doi.org/10.1016/S0016-7037(97)00272-X).
- Blake, R.E., Chang, S.J. & Lepland, A. 2010. Phosphate oxygen isotopic evidence for a temperate and biologically active Archaean ocean. *Nature*, **464**, 1029–1032, <https://doi.org/10.1038/nature08952>.
- Bottjer, D.J. 2012. The cambrian substrate revolution and early evolution of the phyla. *Journal of Earth Science*, **21**, 21–24, <https://doi.org/10.1007/s12583-010-0160-7>.
- Bottjer, D.J., Hagadorn, J.W. & Dornbos, S.Q. 2000. The Cambrian Substrate Revolution. *GSA Today*, **10**, 1–7.
- Boucot, A.J., Xu, C., Scotese, C.R. & Morley, R.J. 2013. *Phanerozoic Paleoclimate: An Atlas of Lithologic Indicators of Climate*, 1st ed. SEPM (Society for Sedimentary Geology), SEPM Concepts in Sedimentology and Paleontology, **11**.
- Boyle, R.A., Dahl, T.W., et al. 2014. Stabilization of the coupled oxygen and phosphorus cycles by the evolution of bioturbation. *Nature Geoscience*, **7**, 671–676, <https://doi.org/10.1038/ngeo2213>.
- Boyle, R.A., Dahl, T.W., Bjerrum, C.J. & Canfield, D.E. 2018. Bioturbation and directionality in Earth’s carbon isotope record across the Neoproterozoic–Cambrian transition. *Geobiology*, **16**, 252–278, <https://doi.org/10.1111/gbi.12277>.
- Brand, U., Logan, A. & Bitner, M.A. 2011. What is the ideal proxy of Palaeozoic seawater chemistry? *Memoirs of the Association of Australasian Palaeontologists*, **41**, 9–24.
- Brasier, M.D. 1986. The succession of small shelly fossils (especially conoidal microfossils) from English Precambrian-Cambrian boundary beds. *Geological Magazine*, **123**, 237–256.
- Brasier, M.D. 1989. Sections in England and their correlation. In: Cowie, J. W. & Brasier, M. D. (eds) *The Precambrian—Cambrian Boundary*. Oxford, Clarendon Press, 82–104.

- Brasier, M.D. 1990. Phosphogenic events and skeletal preservation across the Precambrian-Cambrian boundary interval. *Geological Society, London, Special Publications*, **52**, 289–303, <https://doi.org/10.1144/GSL.SP.1990.052.01.21>.
- Brasier, M.D. 1992a. Global ocean—atmosphere change across the Precambrian—Cambrian transition. *Geological Magazine*, **129**, 161–168, <https://doi.org/10.1017/S0016756800008256>.
- Brasier, M.D. 1992b. Paleoceanography and Changes in the Biological Cycling of Phosphorus across the Precambrian—Cambrian Boundary. *In: Lipps, J. H. & Signor, P. W. (eds) Origin and Early Evolution of the Metazoa*. Springer US, Topics in Geobiology, **10**, 483–523., https://doi.org/10.1007/978-1-4899-2427-8_15.
- Brasier, M.D. & Callow, R.H. 2007. Changes in the patterns of phosphatic preservation across the Proterozoic-Cambrian transition. *Memoirs of the Association of Australasian Palaeontologists*, 377.
- Brasier, M.D., Cowie, J. & Taylor, M. 1994a. Decision on the Precambrian-Cambrian boundary stratotype. *Episodes*, **17**, 3–8.
- Brasier, M.D., Corfield, R.M., Derry, L.A., Rozanov, A.Y. & Zhuravlev, A.Y. 1994b. Multiple $\delta^{13}\text{C}$ excursions spanning the Cambrian explosion to the Botomian crisis in Siberia. *Geology*, **22**, 455–458, [https://doi.org/10.1130/0091-7613\(1994\)022<0455:MCESTC>2.3.CO;2](https://doi.org/10.1130/0091-7613(1994)022<0455:MCESTC>2.3.CO;2).
- Brenchley, P.J., Rushton, A.W.A., Howells, M. & Cave, R. 2006. Cambrian and Ordovician: the early Palaeozoic tectonostratigraphic evolution of the Welsh Basin, Midland and Monian Terranes of Eastern Avalonia. *In: Brenchley, P. J. & Rawson, P. F. (eds) The Geology of England and Wales*. London, The Geological Society, London, 25–74.
- Brooks, K. 2012. Sirius Passet, Greenland and the Cambrian Explosion. *Geology Today*, **28**, 144–146.
- Buggisch, W., Joachimski, M.M., Sevastopulo, G. & Morrow, J.R. 2008. Mississippian $\delta^{13}\text{C}_{\text{carb}}$ and conodont apatite $\delta^{18}\text{O}$ records — Their relation to the Late Palaeozoic Glaciation. *Palaeogeography, Palaeoclimatology, Palaeoecology*, **268**, 273–292, <https://doi.org/10.1016/j.palaeo.2008.03.043>.
- Burchette, T.P. & Wright, V.P. 1992. Carbonate ramp depositional systems. *Sedimentary Geology*, **79**, 3–57, [https://doi.org/10.1016/0037-0738\(92\)90003-A](https://doi.org/10.1016/0037-0738(92)90003-A).
- Butterfield, N.J. 2009. Oxygen, animals and oceanic ventilation: an alternative view. *Geobiology*, **7**, 1–7, <https://doi.org/10.1111/j.1472-4669.2009.00188.x>.
- Came, R.E., Eiler, J.M., Veizer, J., Azmy, K., Brand, U. & Weidman, C.R. 2007. Coupling of surface temperatures and atmospheric CO_2 concentrations during the Palaeozoic era. *Nature*, **449**, 198–201, <https://doi.org/10.1038/nature06085>.
- Came, R.E., Brand, U. & Affek, H.P. 2014. Clumped isotope signatures in modern brachiopod carbonate. *Chemical Geology*, **377**, 20–30, <https://doi.org/10.1016/j.chemgeo.2014.04.004>.

- Canfield, D.E. & Farquhar, J. 2009. Animal evolution, bioturbation, and the sulfate concentration of the oceans. *Proceedings of the National Academy of Sciences*, **106**, 8123–8127, <https://doi.org/10.1073/pnas.0902037106>.
- Cao, W., Williams, S., Flament, N., Zahirovic, S., Scotese, C. & Müller, R.D. 2018. Palaeolatitudinal distribution of lithologic indicators of climate in a palaeogeographic framework. *Geological Magazine*, 1–24, <https://doi.org/10.1017/S0016756818000110>.
- Caron, J.-B., Smith, M.R. & Harvey, T.H.P. 2013. Beyond the Burgess Shale: Cambrian microfossils track the rise and fall of hallucigeniid lobopodians. *Proceedings of the Royal Society B: Biological Sciences*, **280**, 20131613–20131613, <https://doi.org/10.1098/rspb.2013.1613>.
- Cawood, P.A. 2005. Terra Australis Orogen: Rodinia breakup and development of the Pacific and Iapetus margins of Gondwana during the Neoproterozoic and Paleozoic. *Earth-Science Reviews*, **69**, 249–279, <https://doi.org/10.1016/j.earscirev.2004.09.001>.
- Chang, C., Hu, W., Wang, X., Yu, H., Yang, A., Cao, J. & Yao, S. 2017. Carbon isotope stratigraphy of the lower to middle Cambrian on the eastern Yangtze Platform, South China. *Palaeogeography, Palaeoclimatology, Palaeoecology*, **479**, 90–101, <https://doi.org/10.1016/j.palaeo.2017.04.019>.
- Chang, S.J. & Blake, R.E. 2015. Precise calibration of equilibrium oxygen isotope fractionations between dissolved phosphate and water from 3 to 37°C. *Geochimica et Cosmochimica Acta*, **150**, 314–329, <https://doi.org/10.1016/j.gca.2014.10.030>.
- Chen, J., Algeo, T.J., Zhao, L., Chen, Z.-Q., Cao, L., Zhang, L. & Li, Y. 2015. Diagenetic uptake of rare earth elements by bioapatite, with an example from Lower Triassic conodonts of South China. *Earth-Science Reviews*, **149**, 181–202, <https://doi.org/10.1016/j.earscirev.2015.01.013>.
- Chenery, C., Müldner, G., Evans, J., Eckardt, H. & Lewis, M. 2010. Strontium and stable isotope evidence for diet and mobility in Roman Gloucester, UK. *Journal of Archaeological Science*, **37**, 150–163, <https://doi.org/10.1016/j.jas.2009.09.025>.
- Cherns, L., Wheelley, J.R., Popov, L.E., Pour, M.G., Owens, R.M. & Hemsley, A.R. 2013. Long-period orbital climate forcing in the early Palaeozoic? *Journal of the Geological Society*, **170**, 707–710.
- Chough, S.K., Lee, H.S., et al. 2010. Cambrian stratigraphy of the North China Platform: revisiting principal sections in Shandong Province, China. *Geosciences Journal*, **14**, 235–268, <https://doi.org/10.1007/s12303-010-0029-x>.
- Chumakov, N.M. 2007. Climates and climate zonality of the Vendian: geological evidence. *Geological Society, London, Special Publications*, **286**, 15–26, <https://doi.org/10.1144/SP286.2>.
- Clarke, A. 2017. *Principles of Thermal Ecology: Temperature, Energy and Life*. Oxford, United Kingdom, Oxford University Press.

- Cobbold, E.S. 1910. On some small Trilobites from the Cambrian Rocks of Comley, Shropshire. *Quarterly Journal of the Geological Society*, **66**, 19–51, <https://doi.org/10.1144/GSL.JGS.1910.066.01-04.04>.
- Cobbold, E.S. 1911. Trilobites from the Paradoxides Beds of Comley Shropshire. *Quarterly Journal of the Geological Society*, **67**, 282–299, <https://doi.org/10.1144/GSL.JGS.1911.067.01-04.12>.
- Cobbold, E.S. 1913. The Trilobite Fauna of the Comley Breccia-Bed (Shropshire). *Quarterly Journal of the Geological Society*, **69**, 27–44, <https://doi.org/10.1144/GSL.JGS.1913.069.01-04.04>.
- Cobbold, E.S. 1921. The Cambrian horizons of Comely (Shropshire) and their Brachiopoda, Pteropoda, Gasteropoda, etc. *Quarterly Journal of the Geological Society*, **86**, 325–386.
- Cobbold, E.S. 1925. Unconformities in south Shropshire. *Proceedings of the Geologists' Association*, **36**, 364–375.
- Cobbold, E.S. 1927. The Stratigraphy and Geological Structure of the Cambrian Area of Comley, Shropshire. *Quarterly Journal of the Geological Society*, **83**, 551–573, <https://doi.org/10.1144/GSL.JGS.1927.083.01-05.22>.
- Cobbold, E.S. 1931. Additional Fossils from the Cambrian Rocks of Comley, Shropshire. *Quarterly Journal of the Geological Society*, **87**, 459–512, <https://doi.org/10.1144/GSL.JGS.1931.087.01-04.17>.
- Cobbold, E.S. 1936. The Conchostraca of the Cambrian Area of Comley, Shropshire, with a note on a New Variety of *Atops reticulatus* Walcott. *Quarterly Journal of the Geological Society*, **92**, 221-NP, <https://doi.org/10.1144/GSL.JGS.1936.092.01-04.12>.
- Cobbold, E.S. & Pocock, R.W. 1934. The Cambrian area of Rushton (Shropshire). *Philosophical Transactions of the Royal Society of London. Series B*, **223**, 306–409.
- Cocks, L.R.M. 2008. A revised review of British Lower Palaeozoic brachiopods. *Monograph of the Palaeontographical Society*, **161**, 1–276.
- Cohen, P.A., Schopf, J.W., Butterfield, N.J., Kudryavtsev, A.B. & Macdonald, F.A. 2011. Phosphate biomineralization in mid-Neoproterozoic protists. *Geology*, **39**, 539–542, <https://doi.org/10.1130/G31833.1>.
- Cohen, P.A., Strauss, J.V., Rooney, A.D., Sharma, M. & Tosca, N. 2017. Controlled hydroxyapatite biomineralization in an ~810 million-year-old unicellular eukaryote. *Science Advances*, **3**, e1700095, <https://doi.org/10.1126/sciadv.1700095>.
- Conway Morris, S. 1989. Burgess Shale Faunas and the Cambrian Explosion. *Science*, **246**, 339–346.
- Conway Morris, S., Peel, J.S., Higgins, A.K., Soper, N.J. & Davis, N.C. 1987. A Burgess shale-like fauna from the Lower Cambrian of North Greenland. *Nature*, **326**, 181–183, <https://doi.org/10.1038/326181a0>.
- Cook, P.J. 1992. Phosphogenesis around the Proterozoic-Phanerozoic transition. *Journal of the Geological Society*, **149**, 615–620, <https://doi.org/10.1144/gsjgs.149.4.0615>.

- Cooper, R.A., Sadler, P.M., Hammer, O. & Gradstein, F.M. 2012. Chapter 20 - The Ordovician Period. *In: Gradstein, F. M., Schmitz, J. G. O. D. & Ogg, G. M. (eds) The Geologic Time Scale*. Boston, Elsevier, 489–523.
- Creveling, J.R., Knoll, A.H. & Johnston, D.T. 2014. Taphonomy of Cambrian Phosphatic Small Shelly Fossils. *PALAIOS*, **29**, 295–308, <https://doi.org/10.2110/palo.2014.002>.
- Cummins, R.C., Finnegan, S., Fike, D.A., Eiler, J.M. & Fischer, W.W. 2014. Carbonate clumped isotope constraints on Silurian ocean temperature and seawater $\delta^{18}\text{O}$. *Geochimica et Cosmochimica Acta*, **140**, 241–258, <https://doi.org/10.1016/j.gca.2014.05.024>.
- Cusack, M. & Williams, A. 1996. Chemico-Structural Degradation of Carboniferous Lingulid Shells. *Philosophical Transactions of the Royal Society of London B: Biological Sciences*, **351**, 33–49, <https://doi.org/10.1098/rstb.1996.0003>.
- Cusack, M., Williams, A. & Buckman, J.O. 1999. Chemico-structural evolution of linguloid brachiopod shells. *Palaeontology*, **42**, 799–840, <https://doi.org/10.1111/1475-4983.00098>.
- Degens, E.T. & Epstein, S. 1962. Relationship between O18/O16 ratios in coexisting carbonates, cherts and diatomites. *American Association of Petroleum Geologists Bulletin*, **46**, 534–542.
- Dennis, K.J. & Schrag, D.P. 2010. Clumped isotope thermometry of carbonatites as an indicator of diagenetic alteration. *Geochimica et Cosmochimica Acta*, **74**, 4110–4122, <https://doi.org/10.1016/j.gca.2010.04.005>.
- Destombes, J., Hollard, H. & Willefert, S. 1985. Lower Palaeozoic rocks of Morocco. *In: Holland, C. H. (ed.) Lower Palaeozoic of North-Western and West Central Africa*. London, John Wiley & Sons Ltd, 91–336.
- Dilly, G.F., Young, C.R., Lane, W.S., Pangilinan, J. & Girguis, P.R. 2012. Exploring the limit of metazoan thermal tolerance via comparative proteomics: thermally induced changes in protein abundance by two hydrothermal vent polychaetes. *Proceedings of the Royal Society B: Biological Sciences*, **279**, 3347–3356, <https://doi.org/10.1098/rspb.2012.0098>.
- Donnadieu, Y., Godd ris, Y. & Bouttes, N. 2009. Exploring the climatic impact of the continental vegetation on the Mesozoic atmospheric CO₂ and climate history. *Clim. Past*, **5**, 85–96, <https://doi.org/10.5194/cp-5-85-2009>.
- Douglas, P.M.J., Affek, H.P., et al. 2014. Pronounced zonal heterogeneity in Eocene southern high-latitude sea surface temperatures. *Proceedings of the National Academy of Sciences*, **111**, 6582–6587, <https://doi.org/10.1073/pnas.1321441111>.
- Driese, S.G., Mora, C.I. & Elick, J.M. 2000. The Paleosol Record of Increasing Plant Diversity and Depth of Rooting and Changes in Atmospheric pCO₂ in the Siluro-Devonian. *The Paleontological Society Papers*, **6**, 47–62, <https://doi.org/10.1017/S108933260000070X>.
- Dunne, E.M. 2018. Patterns in Palaeontology: How do we measure biodiversity in the past? *PALAEONTOLOGY[online]*, **8**, 1–9.

- Dunne, E.M., Close, R.A., Button, D.J., Brocklehurst, N., Cashmore, D.D., Lloyd, G.T. & Butler, R.J. 2018. Diversity change during the rise of tetrapods and the impact of the 'Carboniferous rainforest collapse'. *Proc. R. Soc. B*, **285**, 20172730, <https://doi.org/10.1098/rspb.2017.2730>.
- Edwards, C.T., Saltzman, M.R., Royer, D.L. & Fike, D.A. 2017. Oxygenation as a driver of the Great Ordovician Biodiversification Event. *Nature Geoscience*, **10**, 925–929, <https://doi.org/10.1038/s41561-017-0006-3>.
- Elliott, J.C. 2002. Calcium Phosphate Biominerals. *Reviews in Mineralogy and Geochemistry*, **48**, 427–453, <https://doi.org/10.2138/rmg.2002.48.11>.
- Elrick, M., Rieboldt, S., Saltzman, M. & McKay, R.M. 2011. Oxygen-isotope trends and seawater temperature changes across the Late Cambrian Steptoean positive carbon-isotope excursion (SPICE event). *Geology*, **39**, 987–990, <https://doi.org/10.1130/G32109.1>.
- Engwell, S. & Hall, M. 2008. EIMF: Epoxy Resins. *EIMF, The University of Edinburgh* <https://www.ed.ac.uk/geosciences/facilities/ionprobe/technical/epoxyresin>.
- Epstein, A.G., Epstein, J.B. & Harris, L.D. 1977. Conodont colour alteration – an index to organic metamorphism. *Geological Survey America Professional Paper*, **995**, 1–27.
- Erwin, D.H. 2009. Climate as a Driver of Evolutionary Change. *Current Biology*, **19**, R575–R583, <https://doi.org/10.1016/j.cub.2009.05.047>.
- Erwin, D.H. 2015. Early metazoan life: divergence, environment and ecology. *Phil. Trans. R. Soc. B*, **370**, 20150036, <https://doi.org/10.1098/rstb.2015.0036>.
- Erwin, D.H. & Valentine, J.W. 2013. *The Cambrian Explosion: The Reconstruction of Animal Biodiversity*, 1st ed. Greenwood Village, CO, Roberts & Co.
- Erwin, D.H., Laflamme, M., Tweedt, S.M., Sperling, E.A., Pisani, D. & Peterson, K.J. 2011. The Cambrian Conundrum: Early Divergence and Later Ecological Success in the Early History of Animals. *Science*, **334**, 1091–1097, <https://doi.org/10.1126/science.1206375>.
- Evans, D., Sagoo, N., et al. 2018. Eocene greenhouse climate revealed by coupled clumped isotope-Mg/Ca thermometry. *Proceedings of the National Academy of Sciences*, 201714744, <https://doi.org/10.1073/pnas.1714744115>.
- Eyles, N. 1993. Earth's glacial record and its tectonic setting. *Earth-Science Reviews*, **35**, 1–248, [https://doi.org/10.1016/0012-8252\(93\)90002-O](https://doi.org/10.1016/0012-8252(93)90002-O).
- Faggetter, L.E., Wignall, P.B., Pruss, S.B., Newton, R.J., Sun, Y. & Crowley, S.F. 2017. Trilobite extinctions, facies changes and the ROECE carbon isotope excursion at the Cambrian Series 2–3 boundary, Great Basin, western USA. *Palaeogeography, Palaeoclimatology, Palaeoecology*, **478**, 53–66, <https://doi.org/10.1016/j.palaeo.2017.04.009>.
- Ferretti, A., Malferrari, D., Medici, L. & Savioli, M. 2017. Diagenesis does not invent anything new: Precise replication of conodont structures by secondary apatite. *Scientific Reports*, **7**, 1624, <https://doi.org/10.1038/s41598-017-01694-4>.

- Finnegan, S., Bergmann, K., et al. 2011. The Magnitude and Duration of Late Ordovician–Early Silurian Glaciation. *Science*, **331**, 903–906, <https://doi.org/10.1126/science.1200803>.
- Fisher, D.W. 1962. Other small conoidal shells. In: Moore, R. C. (ed.) *Treatise on Invertebrate Paleontology: (W) Miscellanea*. Geological Society of America and University of Kansas Press, W98–W143.
- Folk, R.L. & Pittman, J.S. 1971. Length-slow chalcedony; a new testament for vanished evaporites. *Journal of Sedimentary Research*, **41**, 1045–1058, <https://doi.org/10.1306/74D723F1-2B21-11D7-8648000102C1865D>.
- Freeman, J.J., Wopenka, B., Silva, M.J. & Pasteris, J.D. 2001. Raman spectroscopic detection of changes in bioapatite in mouse femora as a function of age and in vitro fluoride treatment. *Calcified Tissue International*, **68**, 156–162.
- Frieling, J., Gebhardt, H., et al. 2017. Extreme warmth and heat-stressed plankton in the tropics during the Paleocene-Eocene Thermal Maximum. *Science Advances*, **3**, e1600891, <https://doi.org/10.1126/sciadv.1600891>.
- Frieling, J., Reichart, G.-J., Middelburg, J.J., Röhl, U., Westerhold, T., Bohaty, S.M. & Sluijs, A. 2018. Tropical Atlantic climate and ecosystem regime shifts during the Paleocene–Eocene Thermal Maximum. *Clim. Past*, **14**, 39–55, <https://doi.org/10.5194/cp-14-39-2018>.
- Gandin, A. & Debrenne, F. 2010. Distribution of the archaeocyath-calcimicrobial bioconstructions on the Early Cambrian shelves. *Palaeoworld*, **19**, 222–241, <https://doi.org/10.1016/j.palwor.2010.09.010>.
- Gatrall, M., Jenkyns, H.C. & Parsons, C. 1972. Limonitic concretions from the European Jurassic, with particular reference to the ‘snuff-boxes’ of southern England. *Sedimentology*, **18**, 79–103.
- Gaucher, C., Boggiani, P.C., Sprechmann, P., Sial, A.N. & Fairchild, T. 2003. Integrated correlation of the Vendian to Cambrian Arroyo del Soldado and Corumba’ Groups (Uruguay and Brazil): palaeogeographic, palaeoclimatic and palaeobiologic implications. *Precambrian Research*, **120**, 241–278.
- Gaucher, C., Sial, A.N., Ferreira, V.P., Pimentel, M.M., Chiglino, L. & Sprechmann, P. 2007. Chemostratigraphy of the Cerro Victoria Formation (Lower Cambrian, Uruguay): Evidence for progressive climate stabilization across the Precambrian–Cambrian boundary. *Chemical Geology*, **237**, 28–46, <https://doi.org/10.1016/j.chemgeo.2006.06.014>.
- Geyer, G. 1989. Late Precambrian to early Middle Cambrian lithostratigraphy of southern Morocco. *Beringeria*, **1**, 115–143.
- Geyer, G. 1990a. Proposal of formal lithostratigraphical units for the Terminal Proterozoic to early Middle Cambrian of southern Morocco. *Newsletters on Stratigraphy*, 87–109, <https://doi.org/10.1127/nos/22/1990/87>.
- Geyer, G. 1990b. Revised Lower to lower Middle Cambrian biostratigraphy of Morocco. *Newsletters on Stratigraphy*, **22**, 53–70, <https://doi.org/10.1127/nos/22/1990/53>.

- Geyer, G. & Landing, E. 1995. The Cambrian of the Moroccan Atlas regions. *In: Geyer, G. & Landing, E. (eds) Morocco '95—The Lower–Middle Cambrian Standard of Western Gondwana*. Beringeria Special Issue, **2**, 7–46.
- Geyer, G. & Landing, E. 2004. A unified Lower – Middle Cambrian chronostratigraphy for West Gondwana. *Acta Geologica Polonica*, **54**, 179–218.
- Geyer, G. & Landing, E. 2006. Latest Ediacaran and Cambrian of the Moroccan Atlas regions. *In: Geyer, G. & Landing, E. (eds) Morocco 2006. Ediacaran–Cambrian Depositional Environments and Stratigraphy of the Western Atlas Regions. Explanatory Description and Field Excursion Guide*. Beringeria Special Issue, **6**, 9–75.
- Geyer, G. & Vincent, T. 2015. The Paradoxides puzzle resolved: the appearance of the oldest paradoxidines and its bearing on the Cambrian Series 3 lower boundary. *Paläontologische Zeitschrift*, **89**, 335–398, <https://doi.org/10.1007/s12542-014-0225-5>.
- Ghienne, J.-F., Desrochers, A., et al. 2014. A Cenozoic-style scenario for the end-Ordovician glaciation. *Nature Communications*, **5**, 4485, <https://doi.org/10.1038/ncomms5485>.
- Giles, P.S. 2012. Low-latitude Ordovician to Triassic brachiopod habitat temperatures (BHTs) determined from $\delta^{18}\text{O}$ [brachiopod calcite]: A cold hard look at ice-house tropical oceans. *Palaeogeography, Palaeoclimatology, Palaeoecology*, **317–318**, 134–152, <https://doi.org/10.1016/j.palaeo.2012.01.002>.
- Glenn, C.R., Follmi, K.B., et al. 1994. Phosphorus and phosphorites: Sedimentology and environments of formation. *Eclogae Geologicae Helveticae*, **87**, 747–788.
- Goddéris, Y., Donnadiéu, Y., Lefebvre, V., Le Hir, G. & Nardin, E. 2012. Tectonic control of continental weathering, atmospheric CO₂, and climate over Phanerozoic times. *Comptes Rendus Geoscience*, **344**, 652–662, <https://doi.org/10.1016/j.crte.2012.08.009>.
- Goddéris, Y., Donnadiéu, Y., Le Hir, G., Lefebvre, V. & Nardin, E. 2014. The role of palaeogeography in the Phanerozoic history of atmospheric CO₂ and climate. *Earth-Science Reviews*, **128**, 122–138, <https://doi.org/10.1016/j.earscirev.2013.11.004>.
- Goldoff, B., Webster, J.D. & Harlov, D.E. 2012. Characterization of fluor-chlorapatites by electron probe microanalysis with a focus on time-dependent intensity variation of halogens. *American Mineralogist*, **97**, 1103–1115, <https://doi.org/10.2138/am.2012.3812>.
- Gough, D.O. 1981. Solar interior structure and luminosity variations. *Solar Physics*, **74**, 21–34, <https://doi.org/10.1007/BF00151270>.
- Grandjean-Lécuyer, P., Feist, R. & Albarède, F. 1993. Rare earth elements in old biogenic apatites. *Geochimica et Cosmochimica Acta*, **57**, 2507–2514, [https://doi.org/10.1016/0016-7037\(93\)90413-Q](https://doi.org/10.1016/0016-7037(93)90413-Q).
- Gregory, R.T. 1991. Oxygen isotope history of seawater revisited: timescales for boundary event changes in oxygen isotope composition of seawater. *In: Taylor, H. P., O'Neil, J. R. & Kaplan, I. R. (eds) Stable Isotope Geochemistry: A Tribute to Samuel Epstein*. Geochemical Society Special Publication, 65–76.

- Gregory, R.T. & Taylor, H.P. 1981. An oxygen isotope profile in a section of Cretaceous oceanic crust, Samail Ophiolite, Oman: Evidence for $\delta^{18}\text{O}$ buffering of the oceans by deep (>5 km) seawater-hydrothermal circulation at mid-ocean ridges. *Journal of Geophysical Research: Solid Earth*, **86**, 2737–2755, <https://doi.org/10.1029/JB086iB04p02737>.
- Grossman, E.L. 2012a. Applying Oxygen Isotope Paleothermometry in Deep Time. *The Paleontological Society Papers*, **18**, 39–68, <https://doi.org/10.1017/S1089332600002540>.
- Grossman, E.L. 2012b. Oxygen Isotope Stratigraphy. In: *The Geologic Time Scale*. Elsevier, 181–206.
- Guilbaud, R., Slater, B.J., Poulton, S.W., Harvey, T.H.P., Brocks, J.J., Nettersheim, B.J. & Butterfield, N.J. 2018. Oxygen minimum zones in the early Cambrian ocean. *Geochemical Perspectives Letters*, 33–38, <https://doi.org/10.7185/geochemlet.1806>.
- Halverson, G.P., Hurtgen, M.T., Porter, S.M. & Collins, A.S. 2009. Chapter 10 Neoproterozoic-Cambrian Biogeochemical Evolution. In: Gaucher, C., Sial, A. N., Frimmel, H. E. & Halverson, G. P. (eds) *Developments in Precambrian Geology*. Elsevier, Neoproterozoic-Cambrian Tectonics, Global Change And Evolution: A Focus On South Western Gondwana, 351–365., [https://doi.org/10.1016/S0166-2635\(09\)01625-9](https://doi.org/10.1016/S0166-2635(09)01625-9).
- Hammarlund, E.U., Gaines, R.R., Prokopenko, M.G., Qi, C., Hou, X.-G. & Canfield, D.E. 2017. Early Cambrian oxygen minimum zone-like conditions at Chengjiang. *Earth and Planetary Science Letters*, **475**, 160–168, <https://doi.org/10.1016/j.epsl.2017.06.054>.
- Harper, D.A.T. & Brasier, M.D. 2005. *Microfossils*, Second. Oxford, Blackwell Publishing Ltd.
- Harper, D.A.T. & Servais, T. (eds). 2013. *Early Palaeozoic Biogeography and Palaeogeography*. Geological Society, London, Geological Society, London, Memoir.
- Harrison, S.P., Kutzbach, J.E., et al. 2003. Mid-Holocene climates of the Americas: a dynamical response to changed seasonality. *Climate Dynamics*, **20**, 663–688, <https://doi.org/10.1007/s00382-002-0300-6>.
- Harvey, T.H.P., Williams, M., et al. 2011. A refined chronology for the Cambrian succession of southern Britain. *Journal of the Geological Society*, **168**, 705–716, <https://doi.org/10.1144/0016-76492010-031>.
- Hearing, T.W., Harvey, T.H.P., et al. 2018. An early Cambrian greenhouse climate. *Science Advances*, **4**, eaar5690, <https://doi.org/10.1126/sciadv.aar5690>.
- Henkes, G.A., Passey, B.H., Grossman, E.L., Shenton, B.J., Pérez-Huerta, A. & Yancey, T.E. 2014. Temperature limits for preservation of primary calcite clumped isotope paleotemperatures. *Geochimica et Cosmochimica Acta*, **139**, 362–382, <https://doi.org/10.1016/j.gca.2014.04.040>.
- Henkes, G.A., Passey, B.H., Grossman, E.L., Shenton, B.J., Yancey, T.E. & Pérez-Huerta, A. 2018. Temperature evolution and the oxygen isotope composition of Phanerozoic oceans from carbonate clumped isotope thermometry. *Earth and Planetary Science Letters*, **490**, 40–50, <https://doi.org/10.1016/j.epsl.2018.02.001>.

- Hicks, D. & McMahon, R. 2002. Temperature acclimation of upper and lower thermal limits and freeze resistance in the nonindigenous brown mussel, *Perna perna* (L.), from the Gulf of Mexico. *Marine Biology*, **140**, 1167–1179, <https://doi.org/10.1007/s00227-002-0787-8>.
- Hinnov, L.A. & Hilgen, F.J. 2012. Chapter 4 - Cyclostratigraphy and Astrochronology. In: Gradstein, F. M., Ogg, J. G., Schmitz, M. D. & Ogg, G. M. (eds) *The Geologic Time Scale*. Boston, Elsevier, 63–83., <https://doi.org/10.1016/B978-0-444-59425-9.00004-4>.
- Hinz, I. 1987. The Lower Cambrian microfauna of Comley and Rushton, Shropshire/England. *Palaeontographica Abt. A*, **198**, 41–100.
- Ho, S.L. & Laepple, T. 2016. Flat meridional temperature gradient in the early Eocene in the subsurface rather than surface ocean. *Nature Geoscience*, **9**, 606–610, <https://doi.org/10.1038/ngeo2763>.
- Holm, G. 1893. Sveriges kambrisk-siluriska Hyolithidae och Conularidae. *Sveriges Geologiska Undersökning, Afhandlingar och Uppsatser C*, **112**, 1–172.
- Holmer, L.E. 2001. Phylogeny and classification: Linguliformea and Craniiformea. In: Carlson, S. J. & Sandy, M. R. (eds) *Brachiopods Ancient and Modern: A Tribute to G. Arthur Cooper*. Pittsburgh, The Paleontological Society, 11–26.
- Hornberger, G.M. 1995. New manuscript guidelines for the reporting of stable hydrogen, carbon, and oxygen isotope ratio data. *Water Resources Research*, **31**, 2895–2895, <https://doi.org/10.1029/95WR02430>.
- Hou, X., Siveter, D.J., et al. 2017. *The Cambrian Fossils of Chengjiang, China: The Flowering of Early Animal Life*, 2nd ed. John Wiley & Sons, Ltd, <https://doi.org/10.1002/9781118896372.ch8>.
- Hudson, J.D. & Anderson, T.F. 1989. Ocean temperatures and isotopic compositions through time. *Earth and Environmental Science Transactions of The Royal Society of Edinburgh*, **80**, 183–192, <https://doi.org/10.1017/S0263593300028625>.
- Hughes, J.M. & Rakovan, J. 2002. The Crystal Structure of Apatite, Ca₅(PO₄)₃(F,OH,Cl). *Reviews in Mineralogy and Geochemistry*, **48**, 1–12, <https://doi.org/10.2138/rmg.2002.48.1>.
- Iba, Y., Sano, S., Mutterlose, J. & Kondo, Y. 2012. Belemnites originated in the Triassic—A new look at an old group. *Geology*, **40**, 911–914, <https://doi.org/10.1130/G33402.1>.
- Ishikawa, T., Ueno, Y., et al. 2014. The $\delta^{13}\text{C}$ excursions spanning the Cambrian explosion to the Canglangpuian mass extinction in the Three Gorges area, South China. *Gondwana Research*, **25**, 1045–1056, <https://doi.org/10.1016/j.gr.2013.03.010>.
- Jacob, R., Schafer, C., Foster, I., Tobis, M. & Anderson, J. 2001. Computational Design and Performance of the Fast Ocean Atmosphere Model, Version One. In: Alexandrov, V. N., Dongarra, J. J., Juliano, B. A., Renner, R. S. & Tan, C. J. K. (eds) *Computational Science — ICCS 2001*. Springer Berlin Heidelberg, Lecture Notes in Computer Science, 175–184.
- Jacob, R.L. 1997. *Low Frequency Variability in a Simulated Atmosphere-Ocean System*.

- Jaffrés, J.B.D., Shields, G.A. & Wallmann, K. 2007. The oxygen isotope evolution of seawater: A critical review of a long-standing controversy and an improved geological water cycle model for the past 3.4 billion years. *Earth-Science Reviews*, **83**, 83–122, <https://doi.org/10.1016/j.earscirev.2007.04.002>.
- James, N.P., Stevens, R.K., Barnes, C.R. & Knight, I. 1989. Evolution of a Lower Palaeozoic continental margin carbonate platform, northern Canadian Appalachians. *In*: Crevello, T., Sarg, J. Rick, Read, J. F. & Wilson, J. L. (eds) *Controls on Carbonate Platforms and Basin Development*. SEPM (Society for Sedimentary Geology), Society of Economic Palaeontologists and Mineralogists, Special Publication, **44**, 123–146., <https://doi.org/10.2110/pec.89.44.0123>.
- Jenkyns, H.C. & Senior, J.R. 1991. Geological evidence for intra-Jurassic faulting in the Wessex Basin and its margins. *Journal of the Geological Society*, **148**, 245–260, <https://doi.org/10.1144/gsjgs.148.2.0245>.
- Jenkyns, H.C., Schouten-Huibers, L., Schouten, S. & Sinninghe Damsté, J.S. 2012. Warm Middle Jurassic–Early Cretaceous high-latitude sea-surface temperatures from the Southern Ocean. *Clim. Past*, **8**, 215–226, <https://doi.org/10.5194/cp-8-215-2012>.
- Jensen, S. 2003. The Proterozoic and earliest Cambrian trace fossil record; patterns, problems and perspectives. *Integrative and Comparative Biology*, **43**, 219–228.
- Jensen, S., Droser, M.L. & Gehling, J.G. 2005. Trace fossil preservation and the early evolution of animals. *Palaeogeography, Palaeoclimatology, Palaeoecology*, **220**, 19–29, <https://doi.org/10.1016/j.palaeo.2003.09.035>.
- Jeppsson, L., Anehus, R. & Fredholm, D. 1999. The optimal acetate buffered acetic acid technique for extracting phosphatic fossils. *Journal of Paleontology*, **73**, 964–972.
- Joachimski, M.M. & Buggisch, W. 2002. Conodont apatite $\delta^{18}\text{O}$ signatures indicate climatic cooling as a trigger of the Late Devonian mass extinction. *Geology*, **30**, 711–714, [https://doi.org/10.1130/0091-7613\(2002\)030<0711:CAOSIC>2.0.CO;2](https://doi.org/10.1130/0091-7613(2002)030<0711:CAOSIC>2.0.CO;2).
- Joachimski, M.M. & Lambert, L.L. 2015. Salinity contrast in the US Midcontinent Sea during Pennsylvanian glacio-eustatic highstands: Evidence from conodont apatite $\delta^{18}\text{O}$. *Palaeogeography, Palaeoclimatology, Palaeoecology*, **433**, 71–80, <https://doi.org/10.1016/j.palaeo.2015.05.014>.
- Joachimski, M.M., Geldern, R. van, Breisig, S., Buggisch, W. & Day, J. 2004. Oxygen isotope evolution of biogenic calcite and apatite during the Middle and Late Devonian. *International Journal of Earth Sciences*, **93**, 542–553, <https://doi.org/10.1007/s00531-004-0405-8>.
- Joachimski, M.M., von Bitter, P.H. & Buggisch, W. 2006. Constraints on Pennsylvanian glacioeustatic sea-level changes using oxygen isotopes of conodont apatite. *Geology*, **34**, 277, <https://doi.org/10.1130/G22198.1>.
- Joachimski, M.M., Breisig, S., et al. 2009. Devonian climate and reef evolution: Insights from oxygen isotopes in apatite. *Earth and Planetary Science Letters*, **284**, 599–609, <https://doi.org/10.1016/j.epsl.2009.05.028>.

- John, E.H., Pearson, P.N., Coxall, H.K., Birch, H., Wade, B.S. & Foster, G.L. 2013. Warm ocean processes and carbon cycling in the Eocene. *Phil. Trans. R. Soc. A*, **371**, 20130099, <https://doi.org/10.1098/rsta.2013.0099>.
- Jourdan, F., Hodges, K., et al. 2014. High-precision dating of the Kalkarindji large igneous province, Australia, and synchrony with the Early–Middle Cambrian (Stage 4–5) extinction. *Geology*, **42**, 543–546, <https://doi.org/10.1130/G35434.1>.
- Kasemann, S.A., Prave, A.R., Fallick, A.E., Hawkesworth, C.J. & Hoffmann, K.-H. 2010. Neoproterozoic ice ages, boron isotopes, and ocean acidification: Implications for a snowball Earth. *Geology*, **38**, 775–778, <https://doi.org/10.1130/G30851.1>.
- Kasting, J.F., Howard, M.T., Wallmann, K., Veizer, J., Shields, G. & Jaffrés, J. 2006. Paleoclimates, ocean depth, and the oxygen isotopic composition of seawater. *Earth and Planetary Science Letters*, **252**, 82–93, <https://doi.org/10.1016/j.epsl.2006.09.029>.
- Kerner, A. & Debrenne, F. 2013. Chapter 6 The role of Archaeocyatha in Cambrian biostratigraphy and biogeography. *Geological Society, London, Memoirs*, **38**, 59–66, <https://doi.org/10.1144/M38.6>.
- Kiessling, W., Flügel, E. & Golonka, J. 2003. Patterns of Phanerozoic carbonate platform sedimentation. *Lethaia*, **36**, 195–225, <https://doi.org/10.1080/00241160310004648>.
- Killingley, J.S. 1983. Effects of diagenetic recrystallization on $^{18}\text{O}/^{16}\text{O}$ values of deep-sea sediments. *Nature*, **301**, 594–597, <https://doi.org/10.1038/301594a0>.
- Kim, S.-T. & O’Neil, J.R. 1997. Equilibrium and nonequilibrium oxygen isotope effects in synthetic carbonates. *Geochimica et Cosmochimica Acta*, **61**, 3461–3475, [https://doi.org/10.1016/S0016-7037\(97\)00169-5](https://doi.org/10.1016/S0016-7037(97)00169-5).
- Kita, N.T., Huberty, J.M., Kozdon, R., Beard, B.L. & Valley, J.W. 2010. High-precision SIMS oxygen, sulfur and iron stable isotope analyses of geological materials: accuracy, surface topography and crystal orientation. *Surface and Interface Analysis*, **43**, 427–431, <https://doi.org/10.1002/sia.3424>.
- Knauth, L.P. & Epstein, S. 1976. Hydrogen and oxygen isotope ratios in nodular and bedded cherts. *Geochimica et Cosmochimica Acta*, **40**, 1095–1108, [https://doi.org/10.1016/0016-7037\(76\)90051-X](https://doi.org/10.1016/0016-7037(76)90051-X).
- Knight, I. 2013. *The Forteau Formation, Labrador Group, in Gros Morne National Park: A Preliminary Reassessment of Its Stratigraphy and Lithofacies*. Geological Survey Report **13–1**, Current Research. Newfoundland and Labrador Department of Mines and Energy.
- Knight, I., Boyce, W.D., Skovsted, C. & Balthasar, U. 2017. *The Lower Cambrian Forteau Formation, Southern Labrador and Great Northern Peninsula, Western Newfoundland: Lithostratigraphy, Trilobites, and Depositional Setting*. Occasional Papers **2017–01**, Government of Newfoundland and Labrador, Department of Natural Resources, Geological Survey, St. John’s.
- Kohn, M.J. & Cerling, T.E. 2002. Stable Isotope Compositions of Biological Apatite. *Reviews in Mineralogy and Geochemistry*, **48**, 455–488, <https://doi.org/10.2138/rmg.2002.48.12>.

- Kohn, M.J., Schoeninger, M.J. & Barker, W.W. 1999. Altered states: effects of diagenesis on fossil tooth chemistry. *Geochimica et Cosmochimica Acta*, **63**, 2737–2747, [https://doi.org/10.1016/S0016-7037\(99\)00208-2](https://doi.org/10.1016/S0016-7037(99)00208-2).
- Kolodny, Y., Luz, B. & Navon, O. 1983. Oxygen isotope variations in phosphate of biogenic apatites, I. Fish bone apatite - rechecking the rules of the game. *Earth and Planetary Science Letters*, 398–404, [https://doi.org/10.1016/0012-821X\(83\)90100-0](https://doi.org/10.1016/0012-821X(83)90100-0).
- Köppen, W. 1884. The thermal zones of the Earth according to the duration of hot, moderate and cold periods and to the impact of heat on the organic world. *Meteorologische Zeitschrift*, **1**, 215–226.
- Köppen, W. 2011. The thermal zones of the Earth according to the duration of hot, moderate and cold periods and to the impact of heat on the organic world. *Meteorologische Zeitschrift*, **20**, 351–360, <https://doi.org/10.1127/0941-2948/2011/105>.
- Kouchinsky, A., Bengtson, S., Runnegar, B., Skovsted, C., Steiner, M. & Vendrasso, M. 2012. Chronology of early Cambrian biomineralization. *Geological Magazine*, **149**, 221–251, <https://doi.org/10.1017/S0016756811000720>.
- Kouchinsky, A., Bengtson, S., Clausen, S. & Vendrasso, Michael. 2015. An early Cambrian fauna of skeletal fossils from the Emyaksin Formation, northern Siberia. *Acta Palaeontologica Polonica*, **60**, 421–512, <https://doi.org/10.4202/app.2012.0004>.
- Landing, E. 1988. Lower Cambrian of Eastern Massachusetts: Stratigraphy and Small Shelly Fossils. *Journal of Paleontology*, **62**, 661–695.
- Landing, E. 1994. Precambrian-Cambrian boundary global stratotype ratified and a new perspective of Cambrian time. *Geology*, **22**, 179–182, [https://doi.org/10.1130/0091-7613\(1994\)022<0179:PCBGSR>2.3.CO;2](https://doi.org/10.1130/0091-7613(1994)022<0179:PCBGSR>2.3.CO;2).
- Landing, E. 1995. Upper Placentian—Branchian series of mainland Nova Scotia (middle-upper Lower Cambrian): Faunas, paleoenvironments, and stratigraphic revision. *Journal of Paleontology*, **69**, 475–495, <https://doi.org/10.1017/S0022336000034879>.
- Landing, E. 1996. Avalon: Insular continent by the latest Precambrian. *In: Special Paper 304: Avalonian and Related Peri-Gondwanan Terranes of the Circum-North Atlantic*. Geological Society of America, 29–63., <https://doi.org/10.1130/0-8137-2304-3.29>.
- Landing, E. & MacGabhann, B.A. 2010. First evidence for Cambrian glaciation provided by sections in Avalonian New Brunswick and Ireland: Additional data for Avalon–Gondwana separation by the earliest Palaeozoic. *Palaeogeography, Palaeoclimatology, Palaeoecology*, **285**, 174–185, <https://doi.org/10.1016/j.palaeo.2009.11.009>.
- Landing, E. & Westrop, S.R. 2004. Environmental patterns in the origin and diversification loci of Early Cambrian skeletalized Metazoa: Evidence from the Avalon microcontinent. *The Paleontological Society Papers*, **10**, 93–106, <https://doi.org/10.1017/S1089332600002369>.
- Landing, E., Bowring, S.A., Davidek, K.L., Westrop, S.R., Geyer, G. & Heldmaier, W. 1998. Duration of the Early Cambrian: U–Pb ages of volcanic ashes from Avalon and Gondwana. *Canadian Journal of Earth Sciences*, **35**, 329–338.

- Landing, E., Geyer, G. & Heldmaier, W. 2006. Distinguishing eustatic and epeirogenic controls on Lower–Middle Cambrian boundary successions in West Gondwana (Morocco and Iberia). *Sedimentology*, **53**, 899–918, <https://doi.org/10.1111/j.1365-3091.2006.00780.x>.
- Landing, E., Geyer, G. & Brasier, M.D. 2013a. Cambrian Evolutionary Radiation: context, correlation, and chronostratigraphy—overcoming deficiencies of the first appearance datum (FAD) concept. *Earth-Science Reviews*, **123**, 133–172, <https://doi.org/10.1016/j.earscirev.2013.03.008>.
- Landing, E., Westrop, S.R. & Bowring, S.A. 2013b. Reconstructing the Avalonia palaeocontinent in the Cambrian: A 519 Ma caliche in South Wales and transcontinental middle Terreneuvian sandstones. *Geological Magazine*, **150**, 1022–1046, <https://doi.org/10.1017/S0016756813000228>.
- Lang, L., Kirsimäe, K. & Vahur, S. 2015. Diagenetic fate of bioapatite in linguliform brachiopods: multiple apatite phases in shells of Cambrian lingulate brachiopod *Ungula ingraca* (Eichwald). *Lethaia*, n/a-n/a, <https://doi.org/10.1111/let.12127>.
- Laskar, J., Robutel, P., Joutel, F., Gastineau, M., Correia, A.C.M. & Levrard, B. 2004. A long-term numerical solution for the insolation quantities of the Earth. *Astronomy & Astrophysics*, **428**, 261–285, <https://doi.org/10.1051/0004-6361:20041335>.
- Lécuyer, C., Grandjean, P. & Emig, C.C. 1996. Determination of oxygen isotope fractionation between water and phosphate from living lingulids: potential application to palaeoenvironmental studies. *Palaeogeography, Palaeoclimatology, Palaeoecology*, **126**, 101–108, [https://doi.org/10.1016/S0031-0182\(96\)00073-9](https://doi.org/10.1016/S0031-0182(96)00073-9).
- Lécuyer, C., Amiot, R., Touzeau, A. & Trotter, J. 2013. Calibration of the phosphate $\delta^{18}\text{O}$ thermometer with carbonate–water oxygen isotope fractionation equations. *Chemical Geology*, **347**, 217–226, <https://doi.org/10.1016/j.chemgeo.2013.03.008>.
- Lee, J.-H. & Riding, R. 2018. Marine oxygenation, lithistid sponges, and the early history of Paleozoic skeletal reefs. *Earth-Science Reviews*, **181**, 98–121, <https://doi.org/10.1016/j.earscirev.2018.04.003>.
- Legeros, R.Z., Trautz, O.R., Legeros, J.P., Klein, E. & Shirra, W.P. 1967. Apatite Crystallites: Effects of Carbonate on Morphology. *Science*, **155**, 1409–1411, <https://doi.org/10.1126/science.155.3768.1409>.
- LeGeros, R.Z., Pan, C.-M., Suga, S. & Watabe, N. 1985. Crystallo-chemical properties of apatite in atremate brachiopod shells. *Calcified Tissue International*, **37**, 98–100, <https://doi.org/10.1007/BF02557687>.
- LeGrande, A.N. & Schmidt, G.A. 2006. Global gridded data set of the oxygen isotopic composition in seawater. *Geophysical Research Letters*, **33**, L12604, <https://doi.org/10.1029/2006GL026011>.
- Lenton, T.M., Boyle, R.A., Poulton, S.W., Shields-Zhou, G.A. & Butterfield, N.J. 2014. Co-evolution of eukaryotes and ocean oxygenation in the Neoproterozoic era. *Nature Geoscience*, **7**, 257–265, <https://doi.org/10.1038/ngeo2108>.

- Lenton, T.M., Daines, S.J. & Mills, B.J.W. 2018. COPSE reloaded: An improved model of biogeochemical cycling over Phanerozoic time. *Earth-Science Reviews*, **178**, 1–28, <https://doi.org/10.1016/j.earscirev.2017.12.004>.
- Lhomme, N., Clarke, G.K.C. & Ritz, C. 2005. Global budget of water isotopes inferred from polar ice sheets. *Geophysical Research Letters*, **32**, <https://doi.org/10.1029/2005GL023774>.
- Li, G. & Holmer, L.E. 2004. Early Cambrian lingulate brachiopods from the Shaanxi Province, China. *GFF*, **126**, 193–211, <https://doi.org/10.1080/11035890401262193>.
- Li, G., Zhu, M. & Steiner, M. 2003. Microstructure and functional morphology of the Early Cambrian problematical fossil *Rhombocorniculum*. *Progress in Natural Science*, **13**, 831–835, <https://doi.org/10.1080/10020070312331344510>.
- Lindström, M. 1972. Cold Age Sediment in Lower Cambrian of South Sweden. *Geologica et Paleontologica*, **6**, 9–23.
- Linnarsson, J.G.O. 1871. Om några försteningar från Sveriges och Norges "Primordialzon". *Öfversikt af Kongliga Vetenskaps-Akademiens Förhandlingar*, **6**, 789–796.
- Littler, K., Robinson, S.A., Bown, P.R., Nederbragt, A.J. & Pancost, R.D. 2011. High sea-surface temperatures during the Early Cretaceous Epoch. *Nature Geoscience*, **4**, 169–172, <https://doi.org/10.1038/ngeo1081>.
- Liu, Z. & Wu, L. 2000. Tropical Atlantic variability in a coupled GCM. *Atmospheric Science Letters*, **1**, 26–36, <https://doi.org/10.1006/asle.2000.0003>.
- Liu, Z., Kutzbach, J. & Wu, L. 2000. Modeling climate shift of El Nino variability in the Holocene. *Geophysical Research Letters*, **27**, 2265–2268, <https://doi.org/10.1029/2000GL011452>.
- Longinelli, A. & Nuti, S. 1973. Revised phosphate-water isotopic temperature scale. *Earth and Planetary Science Letters*, **19**, 373–376, [https://doi.org/10.1016/0012-821X\(73\)90088-5](https://doi.org/10.1016/0012-821X(73)90088-5).
- Lowenstam, H.A. 1981. Minerals formed by organisms. *Science*, **211**, 1126–1131.
- Lowenstam, H.A. & Weiner, S. 1989. *On Biomineralization*. Oxford University Press.
- Luz, B., Kolodny, Y. & Kovach, J. 1984. Oxygen isotope variations in phosphate of biogenic apatites, III. Conodonts. *Earth and Planetary Science Letters*, **69**, 255–262, [https://doi.org/10.1016/0012-821X\(84\)90185-7](https://doi.org/10.1016/0012-821X(84)90185-7).
- Lyell, C. 1840. *Principles of Geology*. London, John Murray.
- Lyons, T.W., Reinhard, C.T. & Planavsky, N.J. 2014. The rise of oxygen in Earth's early ocean and atmosphere. *Nature*, **506**, 307–315, <https://doi.org/10.1038/nature13068>.
- Maloof, A.C., Schrag, D.P., Crowley, J.L. & Bowring, S.A. 2005. An expanded record of Early Cambrian carbon cycling from the Anti-Atlas Margin, Morocco. *Canadian Journal of Earth Sciences*, **42**, 2195–2216, <https://doi.org/10.1139/e05-062>.

- Maloof, A.C., Ramezani, J., Bowring, S.A., Fike, D.A., Porter, S.M. & Mazouad, M. 2010a. Constraints on early Cambrian carbon cycling from the duration of the Nemakit-Daldynian–Tommotian boundary $\delta^{13}\text{C}$ shift, Morocco. *Geology*, **38**, 623–626, <https://doi.org/10.1130/G30726.1>.
- Maloof, A.C., Porter, S.M., et al. 2010b. The earliest Cambrian record of animals and ocean geochemical change. *Geological Society of America Bulletin*, **122**, 1731–1774, <https://doi.org/10.1130/B30346.1>.
- Marshall, C.R. 2006. Explaining the Cambrian “explosion” of animals. *Annu. Rev. Earth Planet. Sci.*, **34**, 355–384.
- Martin, E.L.O., Pittet, B., et al. 2016. The Lower Ordovician Fezouata Konservat-Lagerstätte from Morocco: Age, environment and evolutionary perspectives. *Gondwana Research*, **34**, 274–283, <https://doi.org/10.1016/j.gr.2015.03.009>.
- Matthew, G.F. 1902. Notes on Cambrian Faunas. *Transactions of the Royal Society of Canada, Series 2, Section 4*, **8**, 93–112.
- Mayhew, P.J., Bell, M.A., Benton, T.G. & McGowan, A.J. 2012. Biodiversity tracks temperature over time. *Proceedings of the National Academy of Sciences*, **109**, 15141–15145, <https://doi.org/10.1073/pnas.1200844109>.
- Mazumdar, A. & Strauss, H. 2006. Sulfur and strontium isotopic compositions of carbonate and evaporite rocks from the late Neoproterozoic–early Cambrian Bilara Group (Nagaur-Ganganagar Basin, India): Constraints on intrabasinal correlation and global sulfur cycle. *Precambrian Research*, **149**, 217–230, <https://doi.org/10.1016/j.precamres.2006.06.008>.
- McIlroy, D., Green, O.R. & Brasier, M.D. 2001. Palaeobiology and evolution of the earliest agglutinated Foraminifera: Platysolenites, Spirosolenites and related forms. *Lethaia*, **34**, 13–29, <https://doi.org/10.1080/002411601300068170>.
- McKenzie, N.R., Horton, B.K., Loomis, S.E., Stockli, D.F., Planavsky, N.J. & Lee, C.-T.A. 2016. Continental arc volcanism as the principal driver of icehouse–greenhouse variability. *Science*, **352**, 444–447, <https://doi.org/10.1126/science.aad5787>.
- McKerrow, W.S., Scotese, C.R. & Brasier, M.D. 1992. Early Cambrian continental reconstructions. *Journal of the Geological Society*, **149**, 599–606, <https://doi.org/10.1144/gsjgs.149.4.0599>.
- McMahon, S., Anderson, R.P., Saupe, E.E. & Briggs, D.E.G. 2016. Experimental evidence that clay inhibits bacterial decomposers: Implications for preservation of organic fossils. *Geology*, **44**, 867–870, <https://doi.org/10.1130/G38454.1>.
- Meert, J.G. 2014. Ediacaran–Early Ordovician paleomagnetism of Baltica: A review. *Gondwana Research*, **25**, 159–169, <https://doi.org/10.1016/j.gr.2013.02.003>.
- Mehra, A. & Maloof, A. 2018. Multiscale approach reveals that Cloudina aggregates are detritus and not in situ reef constructions. *Proceedings of the National Academy of Sciences*, 201719911, <https://doi.org/10.1073/pnas.1719911115>.

- Mii, H., Grossman, E.L. & Yancey, T.E. 1999. Carboniferous isotope stratigraphies of North America: Implications for Carboniferous paleoceanography and Mississippian glaciation. *GSA Bulletin*, **111**, 960–973, [https://doi.org/10.1130/0016-7606\(1999\)111<0960:CISONA>2.3.CO;2](https://doi.org/10.1130/0016-7606(1999)111<0960:CISONA>2.3.CO;2).
- Mills, B.J.W., Scotese, C.R., Walding, N.G., Shields, G.A. & Lenton, T.M. 2017. Elevated CO₂ degassing rates prevented the return of Snowball Earth during the Phanerozoic. *Nature Communications*, **8**, 1110, <https://doi.org/10.1038/s41467-017-01456-w>.
- Mills, D.B., Ward, L.M., Jones, C., Sweeten, B., Forth, M., Treusch, A.H. & Canfield, D.E. 2014. Oxygen requirements of the earliest animals. *Proceedings of the National Academy of Sciences*, **111**, 4168–4172, <https://doi.org/10.1073/pnas.1400547111>.
- Missarževskij, V.V. 1977. Conodonts (?) and phosphatic problematica from the Cambrian of Mongolia and Siberia [in Russian]. In: Tatarinov, L. P. (ed.) *Bespozvonočnye paleozoâ Mongolii*. 10–19.
- Missarževskij, V.V. & Mambetov, A.M. 1981. Stratigraphy and fauna of the Cambrian and Precambrian boundary beds of the Lesser Karatau Range [in Russian]. *Trudy Geologičeskogo Instituta AN SSSR*, **326**, 1–92.
- Montanez, I.P. & Osleger, D.A. 1993. Parasequence Stacking Patterns, Third-Order Accommodation Events, and Sequence Stratigraphy of Middle to Upper Cambrian Platform Carbonates, Bonanza King Formation, Southern Great Basin: Chapter 12. **168**, 305–326.
- Monteiro, F.M., Pancost, R.D., Ridgwell, A. & Donnadieu, Y. 2012. Nutrients as the dominant control on the spread of anoxia and euxinia across the Cenomanian-Turonian oceanic anoxic event (OAE2): Model-data comparison. *Paleoceanography*, **27**, PA4209, <https://doi.org/10.1029/2012PA002351>.
- Muehlenbachs, K. 1998. The oxygen isotopic composition of the oceans, sediments and the seafloor. *Chemical Geology*, **145**, 263–273, [https://doi.org/10.1016/S0009-2541\(97\)00147-2](https://doi.org/10.1016/S0009-2541(97)00147-2).
- Muehlenbachs, K. & Clayton, R.N. 1976. Oxygen isotope composition of the oceanic crust and its bearing on seawater. *Journal of Geophysical Research*, **81**, 4365–4369, <https://doi.org/10.1029/JB081i023p04365>.
- Murray, S.T. & Swart, P.K. 2017. Evaluating formation fluid models and calibrations using clumped isotope paleothermometry on Bahamian dolomites. *Geochimica et Cosmochimica Acta*, **206**, 73–93, <https://doi.org/10.1016/j.gca.2017.02.021>.
- Muscente, A.D., Schiffbauer, J.D., et al. 2017. Exceptionally preserved fossil assemblages through geologic time and space. *Gondwana Research*, **48**, 164–188, <https://doi.org/10.1016/j.gr.2017.04.020>.
- Myhre, G., Myhre, C.L., Forster, P.M. & Shine, K.P. 2017. Halfway to doubling of CO₂ radiative forcing. *Nature Geoscience*, **10**, 710–711, <https://doi.org/10.1038/ngeo3036>.
- Nardin, E., Godd ris, Y., Donnadieu, Y., Hir, G.L., Blakey, R.C., Puc at, E. & Aretz, M. 2011. Modeling the early Paleozoic long-term climatic trend. *Geological Society of America Bulletin*, B30364.1, <https://doi.org/10.1130/B30364.1>.

- NASA. 2010. World of Change: Global Temperatures <https://earthobservatory.nasa.gov/WorldOfChange/decadaltemp.php>.
- Nathan, Y. 1984. The Mineralogy and Geochemistry of Phosphorites. *In: Nriagu, J. O. & Moore, P. B. (eds) Phosphate Minerals*. Springer-Verlag, 275–291.
- Neary, M.T., Reid, D.G., Mason, M.J., Frišćić, T., Duer, M.J. & Cusack, M. 2011. Contrasts between organic participation in apatite biomineralization in brachiopod shell and vertebrate bone identified by nuclear magnetic resonance spectroscopy. *Journal of The Royal Society Interface*, **8**, 282–288, <https://doi.org/10.1098/rsif.2010.0238>.
- Nguyen, K.D.T., Morley, S.A., Lai, C.-H., Clark, M.S., Tan, K.S., Bates, A.E. & Peck, L.S. 2011. Upper Temperature Limits of Tropical Marine Ectotherms: Global Warming Implications. *PLOS ONE*, **6**, e29340, <https://doi.org/10.1371/journal.pone.0029340>.
- Nichols, G. 2012. *Sedimentology and Stratigraphy*, Second Edition. John Wiley & Sons.
- Nicolas, J. & Bildgen, P. 1979. Relations between the location of the karst bauxites in the northern hemisphere, the global tectonics and the climatic variations during geological time. *Palaeogeography, Palaeoclimatology, Palaeoecology*, **28**, 205–239, [https://doi.org/10.1016/0031-0182\(79\)90120-2](https://doi.org/10.1016/0031-0182(79)90120-2).
- Nielsen, A.T. & Schovsbo, N.H. 2011. The Lower Cambrian of Scandinavia: Depositional environment, sequence stratigraphy and palaeogeography. *Earth-Science Reviews*, **107**, 207–310, <https://doi.org/10.1016/j.earscirev.2010.12.004>.
- Notaro, M., Liu, Z., Gallimore, R., Vavrus, S.J., Kutzbach, J.E., Prentice, I.C. & Jacob, R.L. 2005. Simulated and Observed Preindustrial to Modern Vegetation and Climate Changes. *Journal of Climate*, **18**, 3650–3671, <https://doi.org/10.1175/JCLI3501.1>.
- O'Brien, C.L., Robinson, S.A., et al. 2017. Cretaceous sea-surface temperature evolution: Constraints from TEX86 and planktonic foraminiferal oxygen isotopes. *Earth-Science Reviews*, **172**, 224–247, <https://doi.org/10.1016/j.earscirev.2017.07.012>.
- Oji, T., Dornbos, S.Q., et al. 2018. Penetrative trace fossils from the late Ediacaran of Mongolia: early onset of the agronomic revolution. *Royal Society Open Science*, **5**, 172250, <https://doi.org/10.1098/rsos.172250>.
- O'Neil, J.R., Roe, L.J., Reinhard, E. & Blake, R.E. 1994. A rapid and precise method of oxygen isotope analysis of biogenic phosphate. *Israel Journal of Earth Science*, **43**, 203–212.
- Ortega-Hernández, J., Azizi, A., Hearing, T.W., Harvey, T.H.P., Edgecombe, G.D., Hafid, A. & Hariri, K.E. 2017. A xandarellid artiopodan from Morocco – a middle Cambrian link between soft-bodied euarthropod communities in North Africa and South China. *Scientific Reports*, **7**, srep42616, <https://doi.org/10.1038/srep42616>.
- Osleger, D.A. 1995. Depositional Sequences on Upper Cambrian Carbonate Platforms: Variable Sedimentologic Responses to Allogenic Forcing. *In: Sequence Stratigraphy and Depositional Response to Eustatic, Tectonic and Climatic Forcing*. Springer, Dordrecht, Coastal Systems and Continental Margins, 247–276., https://doi.org/10.1007/978-94-015-8583-5_9.

- Özdikmen, H. 2009. Nomenclatural changes for twenty trilobites genera. *Munis Entomology & Zoology*, **4**, 155–171.
- Parkinson, D., Curry, G.B., Cusack, M. & Fallick, A.E. 2005. Shell structure, patterns and trends of oxygen and carbon stable isotopes in modern brachiopod shells. *Chemical Geology*, **219**, 193–235, <https://doi.org/10.1016/j.chemgeo.2005.02.002>.
- Parrish, J.T. & Peterson, F. 1988. Wind directions predicted from global circulation models and wind directions determined from eolian sandstones of the western United States—A comparison. *Sedimentary Geology*, **56**, 261–282, [https://doi.org/10.1016/0037-0738\(88\)90056-5](https://doi.org/10.1016/0037-0738(88)90056-5).
- Passey, B.H. & Henkes, G.A. 2012. Carbonate clumped isotope bond reordering and geospeedometry. *Earth and Planetary Science Letters*, **351–352**, 223–236, <https://doi.org/10.1016/j.epsl.2012.07.021>.
- Paterson, J.R., García-Bellido, D.C., Jago, J.B., Gehling, J.G., Lee, M.S.Y. & Edgecombe, G.D. 2016. The Emu Bay Shale Konservat-Lagerstätte: a view of Cambrian life from East Gondwana. *Journal of the Geological Society*, **173**, 1–11, <https://doi.org/10.1144/jgs2015-083>.
- Patzkowsky, M.E., Smith, L.H., Markwick, P.J., Engberts, C.J. & Gyllenhaal, E.D. 1991. Application of the Fujita-Ziegler paleoclimate model: Early Permian and Late Cretaceous examples. *Palaeogeography, Palaeoclimatology, Palaeoecology*, **86**, 67–85, [https://doi.org/10.1016/0031-0182\(91\)90006-D](https://doi.org/10.1016/0031-0182(91)90006-D).
- Pearson, P.N. 2012. Oxygen isotopes in foraminifera: overview and historical review. In: *Reconstructing Earth's Deep Time Climate—The State of the Art in 2012, Paleontological Society Short Course, November 3, 2012*. The Paleontological Society, The Paleontological Society Papers, 1–38.
- Pease, V., Dovzhikova, E., Beliakova, L. & Gee, D.G. 2004. Late Neoproterozoic granitoid magmatism in the basement to the Pechora Basin, NW Russia: geochemical constraints indicate westward subduction beneath NE Baltica. *Geological Society, London, Memoirs*, **30**, 75–85, <https://doi.org/10.1144/GSL.MEM.2004.030.01.08>.
- Peel, J.S. & Ineson, J.R. 2011. The extent of the Sirius Passet Lagerstätte (early Cambrian) of North Greenland. *Bulletin of Geosciences*, **86**, 535–543, <https://doi.org/10.3140/bull.geosci.1269>.
- Peel, M.C., Finlayson, B.L. & McMahon, T.A. 2007. Updated world map of the Köppen-Geiger climate classification. *Hydrol. Earth Syst. Sci.*, **11**, 1633–1644, <https://doi.org/10.5194/hess-11-1633-2007>.
- Peng, S., Babcock, L.E. & Cooper, R.A. 2012. The Cambrian Period. In: Gradstein, F. M., Ogg, J. G., Schmitz, M. D. & Ogg, G. M. (eds) *The Geologic Time Scale*. Elsevier, 437–488.
- Peters, S.E. 2007. The problem with the Paleozoic. *Paleobiology*, **33**, 165–181, <https://doi.org/10.1666/06067.1>.
- Peters, S.E. & Gaines, R.R. 2012. Formation of the 'Great Unconformity' as a trigger for the Cambrian explosion. *Nature*, **484**, 363–366, <https://doi.org/10.1038/nature10969>.

- Peterson, K.J., McPeck, M.A. & Evans, D.A.D. 2005. Tempo and mode of early animal evolution: inferences from rocks, Hox, and molecular clocks. *Paleobiology*, **31**, 36–55, [https://doi.org/10.1666/0094-8373\(2005\)031\[0036:TAMOEAE\]2.0.CO;2](https://doi.org/10.1666/0094-8373(2005)031[0036:TAMOEAE]2.0.CO;2).
- Pohl, A., Donnadieu, Y., Le Hir, G., Buoncristiani, J.-F. & Vennin, E. 2014. Effect of the Ordovician paleogeography on the (in)stability of the climate. *Clim. Past*, **10**, 2053–2066, <https://doi.org/10.5194/cp-10-2053-2014>.
- Pohl, A., Donnadieu, Y., Le Hir, G., Ladant, J.-B., Dumas, C., Alvarez-Solas, J. & Vandenbroucke, T.R.A. 2016. Glacial onset predated Late Ordovician climate cooling. *Paleoceanography*, **31**, 2016PA002928, <https://doi.org/10.1002/2016PA002928>.
- Pohl, A., Donnadieu, Y., Le Hir, G. & Ferreira, D. 2017. The climatic significance of Late Ordovician-early Silurian black shales. *Paleoceanography*, **32**, 2016PA003064, <https://doi.org/10.1002/2016PA003064>.
- Pollock, J.C., Hibbard, J.P. & Sylvester, P.J. 2009. Early Ordovician rifting of Avalonia and birth of the Rheic Ocean: U-Pb detrital zircon constraints from Newfoundland. *Journal of the Geological Society*, **166**, 501–515, <https://doi.org/10.1144/0016-76492008-088>.
- Porrenga, D.H. 1967. Glauconite and chamosite as depth indicators in the marine environment. *Marine Geology*, **5**, 495–501, [https://doi.org/10.1016/0025-3227\(67\)90056-4](https://doi.org/10.1016/0025-3227(67)90056-4).
- Porter, S.M. 2004. Closing the Phosphatization Window: Testing for the Influence of Taphonomic Megabias on the Pattern of Small Shelly Fossil Decline. *PALAIOS*, **19**, 178–183, [https://doi.org/10.1669/0883-1351\(2004\)019<0178:CTPWTF>2.0.CO;2](https://doi.org/10.1669/0883-1351(2004)019<0178:CTPWTF>2.0.CO;2).
- Pörtner, H.O. 2001. Climate change and temperature-dependent biogeography: oxygen limitation of thermal tolerance in animals. *Die Naturwissenschaften*, **88**, 137–146.
- Poulsen, C.J. & Jacob, R.L. 2004. Factors that inhibit snowball Earth simulation. *Paleoceanography*, **19**, PA4021, <https://doi.org/10.1029/2004PA001056>.
- Price, G.D., Sellwood, B.W. & Valdes, P.J. 1995. Sedimentological evaluation of general circulation model simulations for the “greenhouse” Earth: Cretaceous and Jurassic case studies. *Sedimentary Geology*, **100**, 159–180, [https://doi.org/10.1016/0037-0738\(95\)00106-9](https://doi.org/10.1016/0037-0738(95)00106-9).
- Price, G.D., Valdes, P.J. & Sellwood, B.W. 1997a. Prediction of modern bauxite occurrence: implications for climate reconstruction. *Palaeogeography, Palaeoclimatology, Palaeoecology*, **131**, 1–13, [https://doi.org/10.1016/S0031-0182\(96\)00145-9](https://doi.org/10.1016/S0031-0182(96)00145-9).
- Price, G.D., Valdes, P.J. & Sellwood, B.W. 1997b. Quantitative palaeoclimate GCM validation: Late Jurassic and mid-Cretaceous case studies. *Journal of the Geological Society*, **154**, 769–772, <https://doi.org/10.1144/gsjgs.154.5.0769>.
- Prokoph, A., Shields, G.A. & Veizer, J. 2008. Compilation and time-series analysis of a marine carbonate $\delta^{18}\text{O}$, $\delta^{13}\text{C}$, $87\text{Sr}/86\text{Sr}$ and $\delta^{34}\text{S}$ database through Earth history. *Earth-Science Reviews*, **87**, 113–133, <https://doi.org/10.1016/j.earscirev.2007.12.003>.

- Pucéat, E., Joachimski, M.M., et al. 2010. Revised phosphate–water fractionation equation reassessing paleotemperatures derived from biogenic apatite. *Earth and Planetary Science Letters*, **298**, 135–142, <https://doi.org/10.1016/j.epsl.2010.07.034>.
- Puura, I. & Nemliher, J. 2001. Apatite varieties in Recent and fossil linguloid brachiopod shells. In: Brunton, C. H. C., Cocks, L. R. M. & Long, S. L. (eds) *Brachiopods Past and Present*. The Systematics Association, The Systematics Association Special Volume Series, **63**, 6–16.
- Quinton, P.C., Leslie, S.A., Herrmann, A.D. & MacLeod, K.G. 2016. Effects of extraction protocols on the oxygen isotope composition of conodont elements. *Chemical Geology*, **431**, 36–43, <https://doi.org/10.1016/j.chemgeo.2016.03.023>.
- Quinton, P.C., Speir, L., Miller, J., Ethington, R. & Macleod, K.G. 2018. EXTREME HEAT IN THE EARLY ORDOVICIAN. *PALAIOS*, **33**, 353–360, <https://doi.org/10.2110/palo.2018.031>.
- Rasmussen, C.M.Ø., Ullmann, C.V., et al. 2016. Onset of main Phanerozoic marine radiation sparked by emerging Mid Ordovician icehouse. *Scientific Reports*, **6**, 18884, <https://doi.org/10.1038/srep18884>.
- Ravaux, J., Hamel, G., et al. 2013. Thermal Limit for Metazoan Life in Question: In Vivo Heat Tolerance of the Pompeii Worm. *PLOS ONE*, **8**, e64074, <https://doi.org/10.1371/journal.pone.0064074>.
- Rees, A.J., Thomas, A.T., Lewis, M., Hughes, H.E. & Turner, P. 2014. Sequence stratigraphy, tectonostratigraphy and basin analysis. *Geological Society, London, Memoirs*, **42**, 101–134, <https://doi.org/10.1144/M42.3>.
- Rejebian, V.A., Harris, A.G. & Huebner, J.S. 1987. Conodont color and textural alteration: An index to regional metamorphism, contact metamorphism, and hydrothermal alteration. *GSA Bulletin*, **99**, 471–479, [https://doi.org/10.1130/0016-7606\(1987\)99<471:CCATAA>2.0.CO;2](https://doi.org/10.1130/0016-7606(1987)99<471:CCATAA>2.0.CO;2).
- Roberts, C.D., LeGrande, A.N. & Tripathi, A.K. 2011. Sensitivity of seawater oxygen isotopes to climatic and tectonic boundary conditions in an early Paleogene simulation with GISS ModelE-R. *Paleoceanography*, **26**, PA4203, <https://doi.org/10.1029/2010PA002025>.
- Robinson, S.A., Ruhl, M., et al. 2017. Early Jurassic North Atlantic sea-surface temperatures from TEX86 palaeothermometry. *Sedimentology*, **64**, 215–230, <https://doi.org/10.1111/sed.12321>.
- Rodhe, H. 1990. A Comparison of the Contribution of Various Gases to the Greenhouse Effect. *Science*, **248**, 1217–1219, <https://doi.org/10.1126/science.248.4960.1217>.
- Rodland, D., L., Kowalewski, M., Dettman, D.L., Flessa, K.W., Atudorei, V. & Sharp, Z.D. 2003. High-resolution analysis of $\delta^{18}\text{O}$ in the biogenic phosphate of modern and fossil lingulid brachiopods. *The Journal of Geology*, **111**, 441–453.
- Rohling, E.J., Sluijs, A., et al. 2012. Making sense of palaeoclimate sensitivity. *Nature*, **491**, 683–691, <https://doi.org/10.1038/nature11574>.

- Rollion-Bard, C. & Marin-Carbonne, J. 2011. Determination of SIMS matrix effects on oxygen isotopic compositions in carbonates. *Journal of Analytical Atomic Spectrometry*, **26**, 1285–1289, <https://doi.org/10.1039/COJA00213E>.
- Roth-Nebelsick, A. & Konrad, W. 2003. Assimilation and transpiration capabilities of rhyniophytic plants from the Lower Devonian and their implications for paleoatmospheric CO₂ concentration. *Palaeogeography, Palaeoclimatology, Palaeoecology*, **202**, 153–178, [https://doi.org/10.1016/S0031-0182\(03\)00634-5](https://doi.org/10.1016/S0031-0182(03)00634-5).
- Royer, D.L. 2014. 6.11 - Atmospheric CO₂ and O₂ During the Phanerozoic: Tools, Patterns, and Impacts. In: Holland, H. D. & Turekian, K. K. (eds) *Treatise on Geochemistry (Second Edition)*. Oxford, Elsevier, 251–267., <https://doi.org/10.1016/B978-0-08-095975-7.01311-5>.
- Royer, D.L., Donnadieu, Y., Park, J., Kowalczyk, J. & Godd eris, Y. 2014. Error analysis of CO₂ and O₂ estimates from the long-term geochemical model GEOCARBSULF. *American Journal of Science*, **314**, 1259–1283, <https://doi.org/10.2475/09.2014.01>.
- Rubel, F. & Kottek, M. 2011. Comments on: *Meteorologische Zeitschrift*, 361–365, <https://doi.org/10.1127/0941-2948/2011/0285>.
- Runkel, A.C., Mackey, T.J., Cowan, C.A. & Fox, D.L. 2010. Tropical shoreline ice in the late Cambrian: Implications for Earth’s climate between the Cambrian Explosion and the Great Ordovician Biodiversification Event. *GSA Today*, 4–10, <https://doi.org/10.1130/GSATG84A.1>.
- Rushton, A.W.A. 1974. The Cambrian of Wales and England. In: Holland, C. H. (ed.) *Cambrian of the British Isles, Norden and Spitzbergen*. London, John Wiley & Sons Ltd, 43–122.
- Rushton, A.W.A. 1999. Chapter 5: Cambrian rocks of England. In: Rushton, Adrian W. A., Owen, A. W., Owens, R. M. & Prigmore, J. K. (eds) *British Cambrian to Ordovician Stratigraphy*. Peterborough, Joint Nature Conservation Committee, Joint Nature Conservation Committee, 70–87.
- Rushton, A.W.A. 2011. Midland Microcraton. In: Rushton, A. W. A., Br uck, P. M., Molyneux, S. G., Williams, M. & Woodcock, N. H. (eds) *A Revised Correlation of the Cambrian Rocks on the British Isles*. The Geological Society of London, 28–34., <https://doi.org/10.1144/SR25.8>.
- Rushton, A.W.A., Br uck, P.M., Molyneux, S.G., Williams, M. & Woodcock, N.H. 2011. *A Revised Correlation of the Cambrian Rocks in the British Isles*. Geological Society, London, Special Report, **25**.
- Ryb, U. & Eiler, J.M. 2018. Oxygen isotope composition of the Phanerozoic ocean and a possible solution to the dolomite problem. *Proceedings of the National Academy of Sciences*, 201719681, <https://doi.org/10.1073/pnas.1719681115>.
- Saltzman, M.R. & Thomas, E. 2012. Chapter 11 - Carbon Isotope Stratigraphy. In: *The Geologic Time Scale*. Boston, Elsevier, 207–232.
- Saltzman, M.R., Ripperdan, R.L., et al. 2000. A global carbon isotope excursion (SPICE) during the Late Cambrian: relation to trilobite extinctions, organic-matter burial and sea level.

Palaeogeography, Palaeoclimatology, Palaeoecology, **162**, 211–223,
[https://doi.org/10.1016/S0031-0182\(00\)00128-0](https://doi.org/10.1016/S0031-0182(00)00128-0).

- Saltzman, M.R., Cowan, C.A., Runkel, A.C., Runnegar, B., Stewart, M.C. & Palmer, A.R. 2004. The Late Cambrian Spice ($\delta^{13}\text{C}$) Event and the Sauk II-Sauk III Regression: New Evidence from Laurentian Basins in Utah, Iowa, and Newfoundland. *Journal of Sedimentary Research*, **74**, 366–377, <https://doi.org/10.1306/120203740366>.
- Schmahl, W.W., Griesshaber, E., et al. 2008. Hierarchical fibre composite structure and micromechanical properties of phosphatic and calcitic brachiopod shell biomaterials – an overview. *Mineralogical Magazine*, **72**, 541–562, <https://doi.org/10.1180/minmag.2008.072.2.541>.
- Schmidt, G.A., Bigg, G.R. & Rohling, E.J. 1999. Global Seawater Oxygen-18 Database - v1.21.
- Scholle, P.A. & Ulmer-Scholle, D.S. 2003. *A Colour Guide to the Petrography of Carbonate Rocks: Grains, Textures, Porosity, Diagenesis*. The American Association of Petroleum Geologists, American Association of Petroleum Geologists Memoir, **77**.
- Scotese, C.R. 2016. *PALEOMAP PaleoAtlas for GPlates and the PaleoData Plotter Program, PALEOMAP Project*.
- Scotese, C.R. & Summerhayes, C.P. 1986. Computer model of paleoclimate predicts coastal upwelling. *Geobyte*, **1**, 28–42.
- Seilacher, A., Buatois, L.A. & Gabriela Mángano, M. 2005. Trace fossils in the Ediacaran–Cambrian transition: Behavioral diversification, ecological turnover and environmental shift. *Palaeogeography, Palaeoclimatology, Palaeoecology*, **227**, 323–356, <https://doi.org/10.1016/j.palaeo.2005.06.003>.
- Sellwood, B.W., Valdes, P.J. & Price, G.D. 2000. Geological evaluation of multiple general circulation model simulations of Late Jurassic palaeoclimate. *Palaeogeography, Palaeoclimatology, Palaeoecology*, **156**, 147–160, [https://doi.org/10.1016/S0031-0182\(99\)00138-8](https://doi.org/10.1016/S0031-0182(99)00138-8).
- Servais, T., Danelian, T., Harper, D.A.T. & Munnecke, A. 2014. Possible oceanic circulation patterns, surface water currents and upwelling zones in the Early Palaeozoic. *GFF*, **136**, 229–233, <https://doi.org/10.1080/11035897.2013.876659>.
- Shackleton, N.J. & Kennett, N.J. 1975. Paleotemperature history of the Cenozoic and the initiation of Antarctic glaciation: oxygen and carbon isotope analyses in DSDP sites 277, 279, and 281. *Initial Report of the Deep Sea Drilling Project, Leg 29*, 743–755, <https://doi.org/doi:10.2973/dsdp.proc.29.117.1975>.
- Sharp, Z.D. & Cerling, T.E. 1996. A laser GC-IRMS technique for in situ stable isotope analyses of carbonates and phosphates. *Geochimica et Cosmochimica Acta*, **60**, 2909–2916, [https://doi.org/10.1016/0016-7037\(96\)00128-7](https://doi.org/10.1016/0016-7037(96)00128-7).
- Sharp, Z.D., Atudorei, V. & Furrer, H. 2000. The effect of diagenesis on oxygen isotope ratios of biogenic phosphates. *American Journal of Science*, **300**, 222–237, <https://doi.org/10.2475/ajs.300.3.222>.

- Shemesh, A., Kolodny, Y. & Luz, B. 1983. Oxygen isotope variations in phosphate of biogenic apatites, II. Phosphorite rocks. *Earth and Planetary Science Letters*, **64**, 405–416, [https://doi.org/10.1016/0012-821X\(83\)90101-2](https://doi.org/10.1016/0012-821X(83)90101-2).
- Shields, G., Kimura, H., Yang, J. & Gammon, P. 2004. Sulphur isotopic evolution of Neoproterozoic-Cambrian seawater: new francolite-bound sulphate $\delta^{34}\text{S}$ data and a critical appraisal of the existing record. *Chemical Geology*, **204**, 163–182, <https://doi.org/10.1016/j.chemgeo.2003.12.001>.
- Shields, G.A. 2017. Earth system transition during the Tonian–Cambrian interval of biological innovation: nutrients, climate, oxygen and the marine organic carbon capacitor. *Geological Society, London, Special Publications*, **448**, 161–177, <https://doi.org/10.1144/SP448.17>.
- Shields, G.A. 2018. Carbon and carbon isotope mass balance in the Neoproterozoic Earth system. *Emerging Topics in Life Sciences*, ETL20170170, <https://doi.org/10.1042/ETLS20170170>.
- Shields, G.A., Carden, G.A.F., Veizer, J., Meidla, T., Rong, J.-Y. & Li, R.-Y. 2003. Sr, C, and O isotope geochemistry of Ordovician brachiopods: a major isotopic event around the Middle-Late Ordovician transition. *Geochimica et Cosmochimica Acta*, **67**, 2005–2025, [https://doi.org/10.1016/S0016-7037\(02\)01116-X](https://doi.org/10.1016/S0016-7037(02)01116-X).
- Siveter, D.J., Williams, M. & Waloszek, D. 2001. A phosphatocopid crustacean with appendages from the Lower Cambrian. *Science*, **293**, 474–479.
- Siveter, D.J., Waloszek, D. & Williams, M. 2003. An Early Cambrian phosphatocopid crustacean with three-dimensionally preserved soft parts from Shropshire, England. *Special Papers in Palaeontology*, **70**, 9–30.
- Skovsted, C.B. & Peel, J.S. 2001. The problematic fossil *Mongolitubulus* from the Lower Cambrian of Greenland. *Bulletin of the Geological Society of Denmark*, **48**, 135–147.
- Skovsted, C.B. & Peel, J.S. 2007. Small shelly fossils from the argillaceous facies of the Lower Cambrian Forteau Formation of western Newfoundland. *Acta Palaeontologica Polonica*, **52**, 729–748.
- Skovsted, C.B. & Peel, J.S. 2011. *Hyolithellus* in Life Position from the Lower Cambrian of North Greenland. *Journal of Paleontology*, **85**, 37–47, <https://doi.org/10.1666/10-065.1>.
- Skovsted, C.B., Knight, I., Balthasar, U. & Boyce, W.D. 2017. Depth related brachiopod faunas from the lower Cambrian Forteau Formation of southern Labrador and western Newfoundland, Canada. *Palaeontologia Electronica*, **20**, 1–52, <https://doi.org/https://doi.org/10.26879/775>.
- Śliwiński, M.G., Kitajima, K., Kozdon, R., Spicuzza, M.J., Fournelle, J.H., Denny, A. & Valley, J.W. 2015. Secondary Ion Mass Spectrometry Bias on Isotope Ratios in Dolomite–Ankerite, Part I: $\delta^{18}\text{O}$ Matrix Effects. *Geostandards and Geoanalytical Research*, **40**, 157–172, <https://doi.org/10.1111/j.1751-908X.2015.00364.x>.
- Sluijs, A., Schouten, S., et al. 2009. Warm and wet conditions in the Arctic region during Eocene Thermal Maximum 2. *Nature Geoscience*, **2**, 777–780, <https://doi.org/10.1038/ngeo668>.

- Smith, M.P. & Harper, D.A.T. 2013. Causes of the Cambrian Explosion. *Science*, **341**, 1355–1356, <https://doi.org/10.1126/science.1239450>.
- Smith, M.P., Sansom, I.J. & Cochrane, K.D. 2002. The Cambrian origin of vertebrates. *In*: Ahlberg, P. E. (ed.) *Major Events in Early Vertebrate Evolution*. Systematics Association, Systematics Association special volume, **61**, 67–84.
- Sperling, E.A., Robinson, J.M., Pisani, D. & Peterson, K.J. 2010. Where's the glass? Biomarkers, molecular clocks, and microRNAs suggest a 200-Myr missing Precambrian fossil record of siliceous sponge spicules: Sponge biomarkers, molecular clocks and microRNAs. *Geobiology*, **8**, 24–36, <https://doi.org/10.1111/j.1472-4669.2009.00225.x>.
- Sperling, E.A., Frieder, C.A., Raman, A.V., Girguis, P.R., Levin, L.A. & Knoll, A.H. 2013. Oxygen, ecology, and the Cambrian radiation of animals. *Proceedings of the National Academy of Sciences*, **110**, 13446–13451, <https://doi.org/10.1073/pnas.1312778110>.
- Sprechmann, P., Gaucher, C., Blanco, G. & Montaña, J. 2004. Stromatolitic and Trace Fossils Community of the Cerro Victoria Formation, Arroyo del Soldado Group (Lowermost Cambrian, Uruguay). *Gondwana Research*, **7**, 753–766, [https://doi.org/10.1016/S1342-937X\(05\)71061-3](https://doi.org/10.1016/S1342-937X(05)71061-3).
- Steiner, M., Li, G., Qian, Y. & Zhu, M. 2004. Lower Cambrian Small Shelly Fossils of northern Sichuan and southern Shaanxi (China), and their biostratigraphic importance. *Geobios*, **37**, 259–275, <https://doi.org/10.1016/j.geobios.2003.08.001>.
- Steiner, M., Hu, S., Liu, J. & Keupp, H. 2012. A new species of *Hallucigenia* from the Cambrian Stage 4 Wulongqing Formation of Yunnan (South China) and the structure of sclerites in lobopodians. *Bulletin of Geosciences*, **87**, 107–124.
- Stevens, K., Mutterlose, J. & Schweigert, G. 2014. Belemnite ecology and the environment of the Nusplingen Plattenkalk (Late Jurassic, southern Germany): evidence from stable isotope data. *Lethaia*, **47**, 512–523, <https://doi.org/10.1111/let.12076>.
- Stolper, D.A. & Keller, C.B. 2018. A record of deep-ocean dissolved O₂ from the oxidation state of iron in submarine basalts. *Nature*, <https://doi.org/10.1038/nature25009>.
- Stormer, J.C. & Pierson, M.L. 1993. Variation of F and Cl X-ray intensity due to anisotropic diffusion in apatite during electron microprobe analysis: an addendum. *American Mineralogist Supplemental Data*.
- Stormer, J.C., Pierson, M.L. & Tacker, R.C. 1993. Variation of F and Cl X-ray intensity due to anisotropic diffusion in apatite during electron microprobe analysis. *American Mineralogist*, **78**, 641–648.
- Strauss, H., Banerjee, D.M. & Kumar, V. 2001. The sulfur isotopic composition of Neoproterozoic to early Cambrian seawater — evidence from the cyclic Hanseran evaporites, NW India. *Chemical Geology*, **175**, 17–28, [https://doi.org/10.1016/S0009-2541\(00\)00361-2](https://doi.org/10.1016/S0009-2541(00)00361-2).
- Suan, G., Popescu, S.-M., et al. 2017. Subtropical climate conditions and mangrove growth in Arctic Siberia during the early Eocene. *Geology*, G38547.1, <https://doi.org/10.1130/G38547.1>.

- Sukharina, A.N. 1977. Lower Cambrian bauxite occurrences in the mountain complexes of Western Siberia. *International Geology Review*, **19**, 186–194, <https://doi.org/10.1080/00206817709471011>.
- Sundberg, F.A., Geyer, G., Kruse, P.D., McCollum, L.B., Pegel, T.V., Zylinska, A. & Zhuravlev, A.Y. 2016. International correlation of the Cambrian series 2-3, stages 4-5 boundary interval. *Australasian Palaeontological Memoirs*, 83.
- Tabor, N.J. & Poulsen, C.J. 2008. Palaeoclimate across the Late Pennsylvanian–Early Permian tropical palaeolatitudes: A review of climate indicators, their distribution, and relation to palaeophysiographic climate factors. *Palaeogeography, Palaeoclimatology, Palaeoecology*, **268**, 293–310, <https://doi.org/10.1016/j.palaeo.2008.03.052>.
- Tansey, M.R. & Brock, T.D. 1972. The Upper Temperature Limit for Eukaryotic Organisms. *Proceedings of the National Academy of Sciences*, **69**, 2426–2428, <https://doi.org/10.1073/pnas.69.9.2426>.
- Tardy, Y., Kobilsek, B., Roquin, C. & Paquet, H. 1990. Influence of periatlantic climates and paleoclimates on the distribution and mineralogical composition of bauxites and ferricretes. *Chemical Geology*, **84**, 179–182, [https://doi.org/10.1016/0009-2541\(90\)90205-L](https://doi.org/10.1016/0009-2541(90)90205-L).
- Thomas, D.B., McGoverin, C.M., Fordyce, R.E., Frew, R.D. & Gordon, K.C. 2011. Raman spectroscopy of fossil bioapatite - A proxy for diagenetic alteration of the oxygen isotope composition. *Palaeogeography, Palaeoclimatology, Palaeoecology*, **310**, 62–70, <https://doi.org/10.1016/j.palaeo.2011.06.016>.
- Tindall, J., Flecker, R., Valdes, P., Schmidt, D.N., Markwick, P. & Harris, J. 2010. Modelling the oxygen isotope distribution of ancient seawater using a coupled ocean–atmosphere GCM: Implications for reconstructing early Eocene climate. *Earth and Planetary Science Letters*, **292**, 265–273, <https://doi.org/10.1016/j.epsl.2009.12.049>.
- Torsvik, T.H. & Cocks, L.R.M. 2009. *BugPlates: Linking Biogeography and Palaeogeography*. Centre for Geodynamics, Trondheim, Norway.
- Torsvik, T.H. & Cocks, L.R.M. 2013. Chapter 2 New global palaeogeographical reconstructions for the Early Palaeozoic and their generation. *Geological Society, London, Memoirs*, **38**, 5–24, <https://doi.org/10.1144/M38.2>.
- Torsvik, T.H. & Cocks, L.R.M. 2016. *Earth History and Palaeogeography*. Cambridge, UK, Cambridge University Press.
- Trotter, J.A. & Eggins, S.M. 2006. Chemical systematics of conodont apatite determined by laser ablation ICPMS. *Chemical Geology*, **233**, 196–216, <https://doi.org/10.1016/j.chemgeo.2006.03.004>.
- Trotter, J.A., Williams, I.S., Barnes, C.R., Lecuyer, C. & Nicoll, R.S. 2008. Did Cooling Oceans Trigger Ordovician Biodiversification? Evidence from Conodont Thermometry. *Science*, **321**, 550–554, <https://doi.org/10.1126/science.1155814>.
- Trueman, C.N. & Tuross, N. 2002. Trace Elements in Recent and Fossil Bone Apatite. *Reviews in Mineralogy and Geochemistry*, **48**, 489–521, <https://doi.org/10.2138/rmg.2002.48.13>.

- Urey, H.C. 1947. The thermodynamic properties of isotopic substances. *Journal of the Chemical Society (Resumed)*, 562–581, <https://doi.org/10.1039/JR9470000562>.
- Urey, H.C., Lowenstam, H.A., Epstein, S. & McKINNEY, C.R. 1951. Measurement of Paleotemperatures and Temperatures of the Upper Cretaceous of England, Denmark, and the Southeastern United States. *Geological Society of America Bulletin*, **62**, 399–416, [https://doi.org/10.1130/0016-7606\(1951\)62\[399:MOPATO\]2.0.CO;2](https://doi.org/10.1130/0016-7606(1951)62[399:MOPATO]2.0.CO;2).
- Ushatinskaya, G.T., Zhuravlev, A.Y. & Riding, R. 2001. Brachiopods. In: *The Ecology of the Cambrian Radiation*. Critical moments in palaeobiology and earth history series, 350–369.
- Van Der Meer, D.G., Zeebe, R.E., Hinsbergen, D.J.J. van, Sluijs, A., Spakman, W. & Torsvik, T.H. 2014. Plate tectonic controls on atmospheric CO₂ levels since the Triassic. *Proceedings of the National Academy of Sciences*, **111**, 4380–4385, <https://doi.org/10.1073/pnas.1315657111>.
- Vandenbroucke, T.R.A., Armstrong, H.A., Williams, M., Zalasiewicz, J.A. & Sabbe, K. 2009. Ground-truthing Late Ordovician climate models using the paleobiogeography of graptolites. *Paleoceanography*, **24**, <https://doi.org/10.1029/2008PA001720>.
- Vandenbroucke, T.R.A., Armstrong, H.A., et al. 2010. Polar front shift and atmospheric CO₂ during the glacial maximum of the Early Paleozoic Icehouse. *Proceedings of the National Academy of Sciences*, **107**, 14983–14986, <https://doi.org/10.1073/pnas.1003220107>.
- Veizer, J. & Prokoph, A. 2015. Temperatures and oxygen isotopic composition of Phanerozoic oceans. *Earth-Science Reviews*, **146**, 92–104, <https://doi.org/10.1016/j.earscirev.2015.03.008>.
- Veizer, J., Ala, D., et al. 1999. ⁸⁷Sr/⁸⁶Sr, $\delta^{13}\text{C}$ and $\delta^{18}\text{O}$ evolution of Phanerozoic seawater. *Chemical Geology*, **161**, 59–88, [https://doi.org/10.1016/S0009-2541\(99\)00081-9](https://doi.org/10.1016/S0009-2541(99)00081-9).
- Vennemann, T.W., Fricke, H.C., Blake, R.E., O’Neil, J.R. & Colman, A. 2002. Oxygen isotope analysis of phosphates: a comparison of techniques for analysis of Ag₃PO₄. *Chemical Geology*, **185**, 321–336, [https://doi.org/10.1016/S0009-2541\(01\)00413-2](https://doi.org/10.1016/S0009-2541(01)00413-2).
- Vinn, O. 2006. Possible cnidarian affinities of *Torellella* (Hyalithelminthes, Upper Cambrian, Estonia). *Palaontologische Zeitschrift*, **80**, 384–389.
- Wadleigh, M.A. & Veizer, J. 1992. ¹⁸O/¹⁶O and ¹³C/¹²C in lower Paleozoic articulate brachiopods: Implications for the isotopic composition of seawater. *Geochimica et Cosmochimica Acta*, **56**, 431–443, [https://doi.org/10.1016/0016-7037\(92\)90143-7](https://doi.org/10.1016/0016-7037(92)90143-7).
- Walcott, C.D. 1886. Second contribution to the studies on the Cambrian faunas of North America. *Bulletin of the United States Geological Survey*, **30**, 1–369.
- Walcott, C.D. 1902. Cambrian Brachiopoda: Acrotreta, Linnarssonina, Obolus: With descriptions of new species. *Proceedings of the United States National Museum*, **25**, 577–612.
- Walcott, C.D. 1910. *Olenellus* and other genera of the Mesonacidae. Cambrian Geology and Paleontology I, Number 6. *Smithsonian Miscellaneous Collections*, **53**, 231–422.

- Walker, L.J., Wilkinson, B.H. & Ivany, L.C. 2002. Continental Drift and Phanerozoic Carbonate Accumulation in Shallow-Shelf and Deep-Marine Settings. *The Journal of Geology*, **110**, 75–87, <https://doi.org/10.1086/324318>.
- Wallace, M.W., Hood, A. vS., Shuster, A., Greig, A., Planavsky, N.J. & Reed, C.P. 2017. Oxygenation history of the Neoproterozoic to early Phanerozoic and the rise of land plants. *Earth and Planetary Science Letters*, **466**, 12–19, <https://doi.org/10.1016/j.epsl.2017.02.046>.
- Walliser, O.H. 1958. *Rhombocorniculum comleyense* n. gen., n. sp. *Paläontologische Zeitschrift*, **32**, 176–180.
- Wang, D., Ling, H.-F., et al. 2018. Coupling of ocean redox and animal evolution during the Ediacaran-Cambrian transition. *Nature Communications*, **9**, 2575, <https://doi.org/10.1038/s41467-018-04980-5>.
- Wang, S., Zheng, M., Liu, X., Niu, X., Chen, W. & Su, K. 2013. Distribution of Cambrian salt-bearing basins in China and its significance for halite and potash finding. *Journal of Earth Science*, **24**, 212–233, <https://doi.org/10.1007/s12583-013-0319-0>.
- Wanke, H. & Wanke, A. 2007. Lithostratigraphy of the Kalahari Group in northeastern Namibia. *Journal of African Earth Sciences*, **48**, 314–328, <https://doi.org/doi:10.1016/j.jafrearsci.2007.05.002>.
- Warren, J.K. 2010. Evaporites through time: Tectonic, climatic and eustatic controls in marine and nonmarine deposits. *Earth-Science Reviews*, **98**, 217–268, <https://doi.org/10.1016/j.earscirev.2009.11.004>.
- Watabe, N. & Pan, C.-M. 1984. Phosphatic Shell Formation in Atremate Brachiopods. *American Zoologist*, **24**, 977–985.
- Wei, G.-Y., Planavsky, N.J., Tarhan, L.G., Chen, X., Wei, W., Li, D. & Ling, H.-F. 2018. Marine redox fluctuation as a potential trigger for the Cambrian explosion. *Geology*, **46**, 587–590, <https://doi.org/10.1130/G40150.1>.
- Wenzel, B., Lécuyer, C. & Joachimski, M.M. 2000. Comparing oxygen isotope records of silurian calcite and phosphate— $\delta^{18}\text{O}$ compositions of brachiopods and conodonts. *Geochimica et Cosmochimica Acta*, **64**, 1859–1872, [https://doi.org/10.1016/S0016-7037\(00\)00337-9](https://doi.org/10.1016/S0016-7037(00)00337-9).
- Westrop, S.R. & Landing, E. 2000. Lower cambrian (branchian) trilobites and biostratigraphy of the hanford brook formation, southern new brunswick. *Journal of Paleontology*, **74**, 858–878, [https://doi.org/10.1666/0022-3360\(2000\)074<0858:LCBTAB>2.0.CO;2](https://doi.org/10.1666/0022-3360(2000)074<0858:LCBTAB>2.0.CO;2).
- Wheelely, J.R., Smith, M.P. & Boomer, I. 2012. Oxygen isotope variability in conodonts: implications for reconstructing Palaeozoic palaeoclimates and palaeoceanography. *Journal of the Geological Society*, **169**, 239–250.
- Wheelely, J.R., Jardine, P.E., Raine, R.J., Boomer, I. & Smith, M.P. 2018. Paleoecologic and paleoceanographic interpretation of $\delta^{18}\text{O}$ variability in Lower Ordovician conodont species. *Geology*, **46**, 467–470, <https://doi.org/10.1130/G40145.1>.

- Williams, A. & Cusack, M. 1999. Evolution of a rhythmic lamination in the organophosphatic shells of brachiopods. *Journal of Structural Biology*, **126**, 227–240.
- Williams, A., Mackay, S. & Cusack, M. 1992. Structure of the Organo-Phosphatic Shell of the Brachiopod *Discina*. *Philosophical Transactions of the Royal Society of London B: Biological Sciences*, **337**, 83–104, <https://doi.org/10.1098/rstb.1992.0086>.
- Williams, A., Cusack, M. & Mackay, S. 1994. Collagenous chitinophosphatic shell of the brachiopod *Lingula*. *Philosophical Transactions: Biological Sciences*, **346**, 223–266.
- Williams, A., James, M.A., et al. 1997a. *Part H, Brachiopoda (Revised), Vol. 1*. Kaesler, R. L. (ed.). Kansas, USA, Paleontological Institute, Treatise on Invertebrate Paleontology.
- Williams, A., Brunton, C.H.C., et al. 1997b. *Part H, Brachiopoda (Revised) Volume 2: Linguliformea, Craniiformea, and Rhynchonelliformea (Part)*. Kaesler, R. L. (ed.). Kansas, USA, Paleontological Institute, Treatise on Invertebrate Paleontology.
- Williams, A., Brunton, C.H.C., et al. 2007. *Part H, Brachiopoda (Revised), Vol. 6: Supplement*. Selden, P. A. (ed.). Kansas, USA, Paleontological Institute, Treatise on Invertebrate Paleontology.
- Williams, M., Rushton, A.W.A., Cook, A.F., Zalasiewicz, J., Martin, A.P., Condon, D.J. & Winrow, P. 2013. Dating the Cambrian Purley Shale Formation, Midland Microcraton, England. *Geological Magazine*, **150**, 937–944, <https://doi.org/10.1017/S0016756813000010>.
- Williams, M., Vandenbroucke, T.R.A., Perrier, V., Siveter, D.J. & Servais, T. 2015. A link in the chain of the Cambrian zooplankton: bradoriid arthropods invade the water column. *Geological Magazine*, **152**, 923–934, <https://doi.org/10.1017/S0016756815000059>.
- Winrow, P. 2015. *A Review of Cambrian Lingulate Brachiopods of England and Wales*. PhD Thesis (unpub.), Imperial College, University of London.
- Wood, R., Bowyer, F., Penny, A. & Poulton, S.W. 2018. Did anoxia terminate Ediacaran benthic communities? Evidence from early diagenesis. *Precambrian Research*, **313**, 134–147, <https://doi.org/10.1016/j.precamres.2018.05.011>.
- Wood, R.A. 2011. Paleoecology of the earliest skeletal metazoan communities: Implications for early biomineralization. *Earth-Science Reviews*, **106**, 184–190, <https://doi.org/10.1016/j.earscirev.2011.01.011>.
- Wopenka, B. & Pasteris, J.D. 2005. A mineralogical perspective on the apatite in bone. *Materials Science and Engineering: C*, **25**, 131–143, <https://doi.org/10.1016/j.msec.2005.01.008>.
- Yang, B., Steiner, M. & Keupp, H. 2015a. Early Cambrian palaeobiogeography of the Zhenba–Fangxian Block (South China): Independent terrane or part of the Yangtze Platform? *Gondwana Research*, **28**, 1543–1565, <https://doi.org/10.1016/j.gr.2014.09.020>.
- Yang, J., Ortega-Hernández, J., Gerber, S., Butterfield, N.J., Hou, J., Lan, T. & Zhang, X. 2015b. A superarmored lobopodian from the Cambrian of China and early disparity in the evolution of Onychophora. *Proceedings of the National Academy of Sciences*, **112**, 8678–8683, <https://doi.org/10.1073/pnas.1505596112>.

- Yoshida, M., Windley, B.F. & Dasgupta, S. (eds). 2003. *Proterozoic East Gondwana: Supercontinent Assembly and Breakup*. London, Geological Society, London, Geological Society, London, Special Publications, **206**.
- Yun, H., Zhang, X., Li, L., Zhang, M. & Liu, W. 2016. Skeletal fossils and microfacies analysis of the lowermost Cambrian in the southwestern margin of the North China Platform. *Journal of Asian Earth Sciences*, **129**, 54–66, <https://doi.org/10.1016/j.jseaes.2016.07.029>.
- Zachos, J., Pagani, M., Sloan, L., Thomas, E. & Billups, K. 2001. Trends, Rhythms, and Aberrations in Global Climate 65 Ma to Present. *Science*, **292**, 686–693, <https://doi.org/10.1126/science.1059412>.
- Zachos, J.C., Stott, L.D. & Lohmann, K.C. 1994. Evolution of Early Cenozoic marine temperatures. *Paleoceanography*, **9**, 353–387, <https://doi.org/10.1029/93PA03266>.
- Zazzo, A., Lécuyer, C. & Mariotti, A. 2004. Experimentally-controlled carbon and oxygen isotope exchange between bioapatites and water under inorganic and microbially-mediated conditions. *Geochimica et Cosmochimica Acta*, **68**, 1–12, [https://doi.org/10.1016/S0016-7037\(03\)00278-3](https://doi.org/10.1016/S0016-7037(03)00278-3).
- Zhu, M., Strauss, H. & Shields, G.A. 2007. From snowball earth to the Cambrian bioradiation: Calibration of Ediacaran–Cambrian earth history in South China. *Palaeogeography, Palaeoclimatology, Palaeoecology*, **254**, 1–6, <https://doi.org/10.1016/j.palaeo.2007.03.026>.
- Zhu, M.-Y., Babcock, L.E. & Peng, S.-C. 2006. Advances in Cambrian stratigraphy and paleontology: Integrating correlation techniques, paleobiology, taphonomy and paleoenvironmental reconstruction. *Palaeoworld*, **15**, 217–222, <https://doi.org/10.1016/j.palwor.2006.10.016>.
- Zhuravlev, A.Y. 1986. Evolution of archaeocyaths and palaeobiogeography of the Early Cambrian. *Geological Magazine*, **123**, 377–385, <https://doi.org/10.1017/S0016756800033471>.
- Zhuravlev, A.Y. & Wood, R.A. 1996. Anoxia as the cause of the mid-Early Cambrian (Botomian) extinction event. *Geology*, **24**, 311–314, [https://doi.org/10.1130/0091-7613\(1996\)024<0311:AATCOT>2.3.CO;2](https://doi.org/10.1130/0091-7613(1996)024<0311:AATCOT>2.3.CO;2).
- Ziegler, A., Eshel, G., Rees, P.M., Rothfus, T., Rowley, D. & Sunderlin, D. 2003. Tracing the tropics across land and sea: Permian to present. *Lethaia*, **36**, 227–254, <https://doi.org/10.1080/00241160310004657>.
- Zougrou, I.M., Katsikini, M., Brzhezinskaya, M., Pinakidou, F., Papadopoulou, L., Tsoukala, E. & Paloura, E.C. 2016. Ca L2,3-edge XANES and Sr K-edge EXAFS study of hydroxyapatite and fossil bone apatite. *The Science of Nature*, **103**, 60, <https://doi.org/10.1007/s00114-016-1383-y>.

Appendices

Appendix A

EPMA data *[electronic]*

Appendix A comprises the full electron probe microanalysis (EPMA) data set used in this thesis. Along with the Excel spreadsheet, PCA and element oxide plots are also included. Appendix A is available as a digital appendix.

Appendix B

Bulk silver phosphate $\delta^{18}\text{O}$ data and temperature calculations *[electronic]*

Appendix B comprises an Excel spreadsheet containing bulk $\delta^{18}\text{O}_{\text{phos}}$ data collected during this project and the temperature calculations performed on these data. Appendix B is available as a digital appendix.

Appendix C

Processing raw secondary ion mass spectrometry (SIMS) $\delta^{18}\text{O}$ data

Introduction

SIMS isotope data were collected at the Edinburgh Ion Microprobe Facility (EIMF) over three sessions in November 2016, February 2017 and July 2017. What should have been a single session, comprising five days of analyses, became three sessions due to multiple technical challenges, including a campus-wide power cut at EIMF. The final session was completed by Dr John Craven (EIMF) in July 2017, working on block ES027 following directions provided by the author. All other analyses were performed by the author.

Raw SIMS isotope ratio data need to be transformed into isotopic composition ($\delta^{18}\text{O}$) values, and need to be monitored and corrected for instrument drift over the course of each measurement session. Instrument drift corrections are routinely performed by applying a linear regressions across all analyses of the standard material collected during one session (e.g. Wheeley et al. 2012). The rate of analytical drift can change throughout a session, and therefore more than one linear regression may be needed to correct for drift in each session. However, it is best to use the lowest possible number of linear regressions to correct for analytical drift in a single session.

The data in Appendix D, and the data plotted here, include all analyses conducted in the three SIMS sessions. This includes material that is not otherwise used in this thesis. However, all data collected during an analytical run are needed to calculate instrument drift, and hence they are included here. The standard material used in these analyses are fragments of a Durango apatite crystal. The $\delta^{18}\text{O}$ value of this crystal was characterised as 8.70 ‰ (VSMOW) by the NERC Isotope Geoscience Facility (NIGF) before this study.

Data processing

Calculating $\delta^{18}\text{O}$

SIMS measurements were made using the CAMECA IMS-1270 ion microprobe which does not output $\delta^{18}\text{O}$ values directly, but rather reports the ratio of ^{18}O to ^{16}O collected simultaneously on dual Faraday cups (L'2 and H'2). The $\delta^{18}\text{O}$ value was calculated according to equation (A-C1):

$$\delta^{18}\text{O} (\text{‰ VSMOW}) = \left(\left(\frac{{}^{18}\text{O}/{}^{16}\text{O}_i}{{}^{18}\text{O}/{}^{16}\text{O}_{\text{avg}}} \right) * (8.70 + 1000) \right) - 1000 \quad (\text{A-C1})$$

where ${}^{18}\text{O}/{}^{16}\text{O}_i$ is the measured isotope ratio for that point, ${}^{18}\text{O}/{}^{16}\text{O}_{\text{avg}}$ is the session average isotope, and 8.70 ‰ is the expected $\delta^{18}\text{O}$ value for the Durango fragment.

Correcting instrument drift

Linear regressions were used to correct for instrument drift. Linear regression analyses were performed in Microsoft Excel on the original data files produced by each SIMS analysis (see) and checked with the `lm()` function in R. Copies of all raw data files were kept. The linear regressions calculated for each run are summarised in Table A-C1. During runs 1, 3, 6, 7, and 8, instrument drift was at a consistent rate throughout. During runs 2, 4, 5, and 9, the rate of instrument drift was variable. The fewest possible linear regressions were applied to each run.

Data and figures

In total, 292 analyses were made on six fragments of Durango apatite from a crystal with a $\delta^{18}\text{O}_{\text{phos}}$ value of 8.70 ‰. The regression-corrected SIMS $\delta^{18}\text{O}$ analyses had a mean value of 8.67 ‰ and a standard deviation of 0.28 ‰. 267 analyses on five fragments were used in runs with SSF specimens from the Comley Limestones. The regression-corrected SIMS $\delta^{18}\text{O}$ analyses on the Durango fragments used in runs with Comley Limestones SSFs had a mean value of 8.66 ‰ and a standard deviation of 0.29 ‰. One fragment was embedded in block ES023 which were surrounded solely by specimens from Ait Iyou, Morocco. 25 analyses were conducted on the Durango embedded in ES023, and these measurements had a regression-corrected mean value of 8.70 ‰ and a standard deviation of 0.15 ‰.

Table A-C1. Summary of Durango standard SIMS analyses. The values in bused to calculate the final data set. See full data set in Appendix D.

Run	Block	Data	Linear regression			$\delta^{18}\text{O}$		
			r^2	Gradient	Intercept	Mean	SD	SEM
1	ES023	Raw	NA	NA	NA	8.70	0.44	0.09
1	ES023	RTOT: 1-55	0.89	4.39E-08	2.02E-03	8.70	0.15	0.03
1	ES023	R1: 1-24	0.46	3.31E-08	2.02E-03	8.70	0.15	0.04
1	ES023	R2: 20-55	0.81	4.99E-08	2.02E-03	8.70	0.16	0.04
2	ES019	Raw	NA	NA	NA	8.66	0.45	0.06
2	ES019	RTOT: 1-124	0.12	-8.00E-09	2.03E-03	8.69	0.42	0.05
2	ES019	R1: 11-124	0.42	-1.57E-08	2.03E-03	8.69	0.33	0.04
2	ES019	R2: 11-56	0.08	-9.10E-09	2.03E-03	8.70	0.25	0.05
2	ES019	R3: 50-67	0.53	-1.05E-07	2.04E-03	8.70	0.30	0.08
2	ES019	R4: 63-124	0.05	6.30E-09	2.03E-03	8.68	0.26	0.05
3	ES019	Raw	NA	NA	Na	8.70	0.69	0.15
3	ES019	RTOT: 1-42	0.88	9.15E-08	2.03E-03	8.70	0.24	0.05
3	ES019	R1: 1-26	0.81	9.12E-08	2.03E-03	8.70	0.21	0.05
3	ES019	R2: 22-42	0.61	9.38E-08	2.03E-03	8.70	0.28	0.08
4	ES018	Raw	NA	NA	Na	8.70	0.81	0.13
4	ES018	RTOT: 1-104	0.36	2.92E-08	2.03E-03	8.70	0.65	0.11
4	ES018	R1: 1-26	0.98	1.75E-07	2.03E-03	8.70	0.07	0.03
4	ES018	R2: 22-104	0.19	9.00E-09	2.04E-03	8.16	0.35	0.07
5	ES020	Raw	NA	NA	Na	8.70	0.79	0.14
5	ES020	RTOT: 1-76	0.48	4.22E-08	2.03E-03	8.70	0.56	0.10
5	ES020	R1: 1-59	0.87	7.85E-08	2.03E-03	8.70	0.31	0.06
5	ES020	R2: 55-76	0.47	-3.92E-08	2.03E-03	8.78	0.32	0.10
6	ES019	Raw	NA	NA	NA	8.70	0.59	0.13
6	ES019	RTOT: 1-56	0.87	5.59E-08	2.03E-03	8.70	0.22	0.05
7	ES025	Raw	NA	NA	NA	8.70	0.12	0.04
7	ES025	RTOT: 1-23	0.16	1.17E-08	2.03E-03	8.70	0.11	0.03
8	ES027	Raw	NA	NA	NA	8.70	0.98	0.15

8	ES027	RTOT: 1-125	0.96	4.65E-08	2.02E-03	8.70	0.20	0.03
9	ES027	Raw	NA	NA	NA	8.82	0.84	0.13
9	ES027	RTOT: 1-128	0.84	3.77E-08	2.02E-03	8.70	0.35	0.05
9	ES027	R1: 5-68	0.94	6.82E-08	2.02E-03	8.70	0.19	0.04
9	ES027	R2: 64-128	0.17	7.80E-09	2.02E-03	8.70	0.19	0.04

Data = the SIMS measurements used to calculate the regression line. SD = standard deviation. SEM = standard error of the mean.

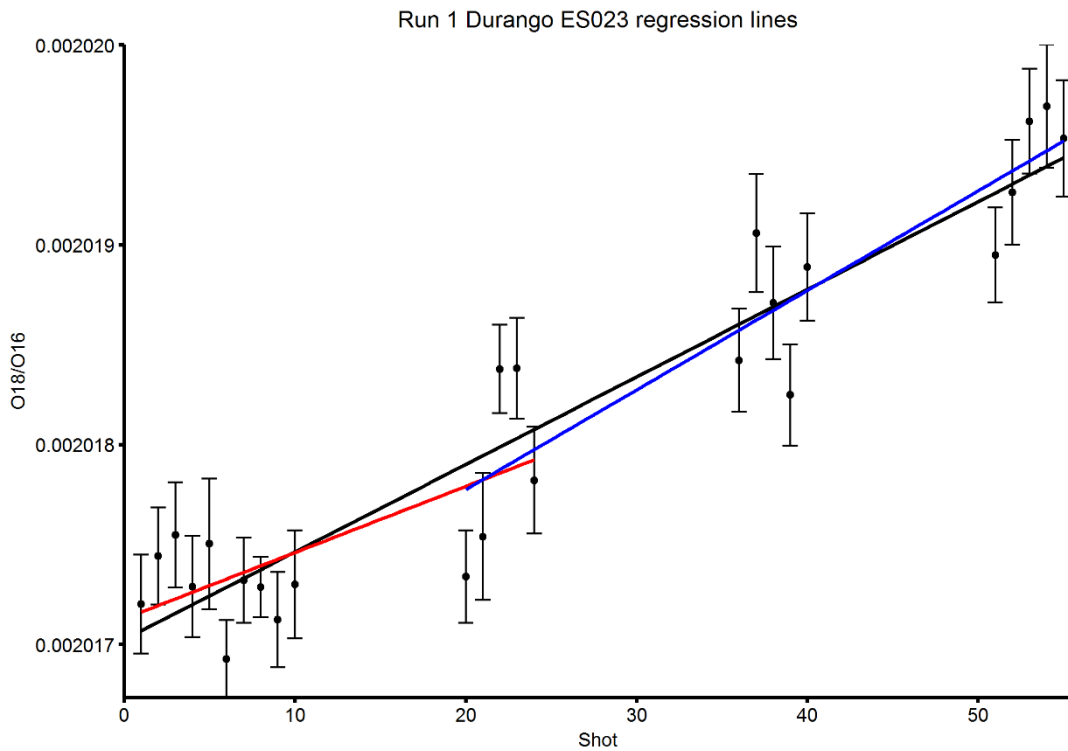


Figure A-C1. Durango analyses from Run 1 on block ES023. Error bars represent one standard deviation. Linear regressions were run through all data points (RTOT, black line), points 1 to 24 (R1, red line), and points 20 to 55 (R2, blue line). RTOT was used to correct the data.

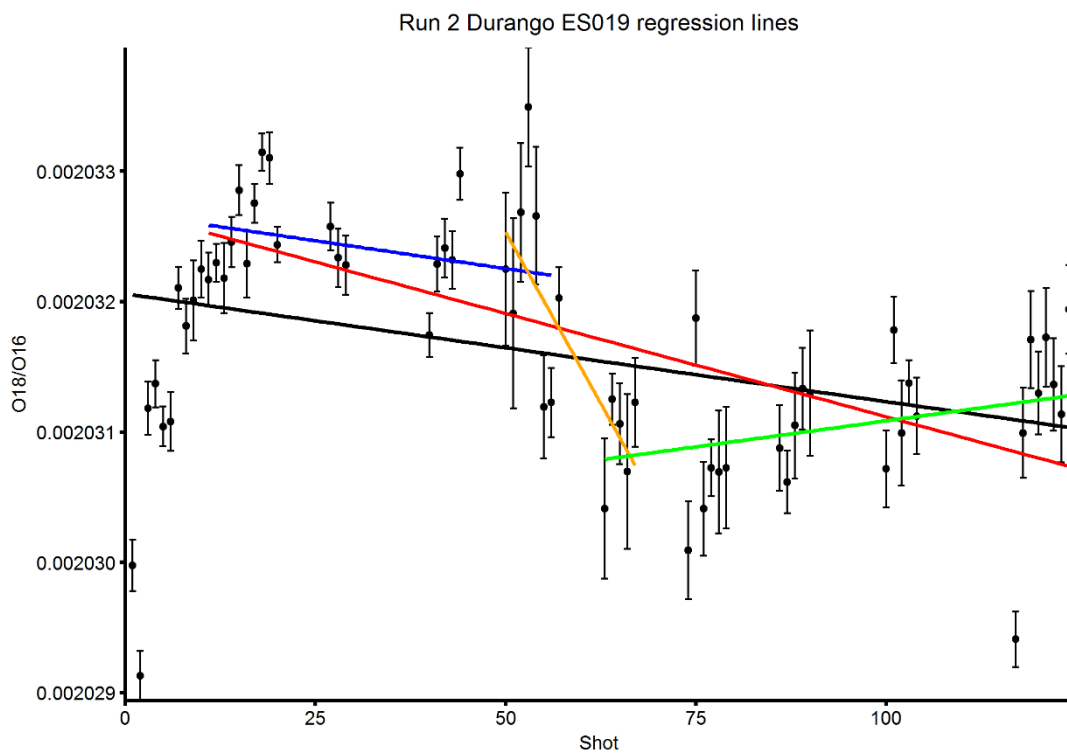


Figure A-C2. Durango analyses from Run 2 on block ES019. Error bars represent one standard deviation. Linear regressions were run through all data points (RTOT, black line), points 11 to 124 (R1, red line), points 11 to 56 (R2, blue line), points 50 to 67 (R3, orange line), and points 63 to 124 (R4, green line).

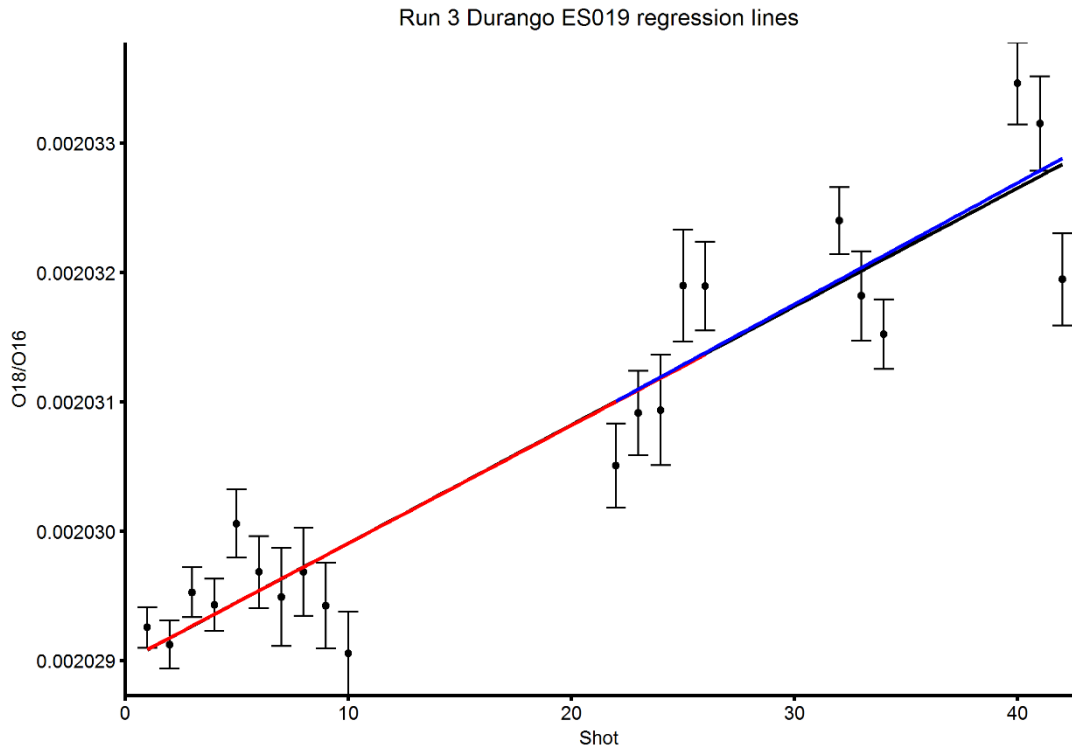


Figure A-C3. Durango analyses from Run 3 on block ES019. Error bars represent one standard deviation. Linear regressions were run through all data points (RTOT, black line), points 1 to 26 (R1, red line), and points 24 to 42 (R2, blue line).

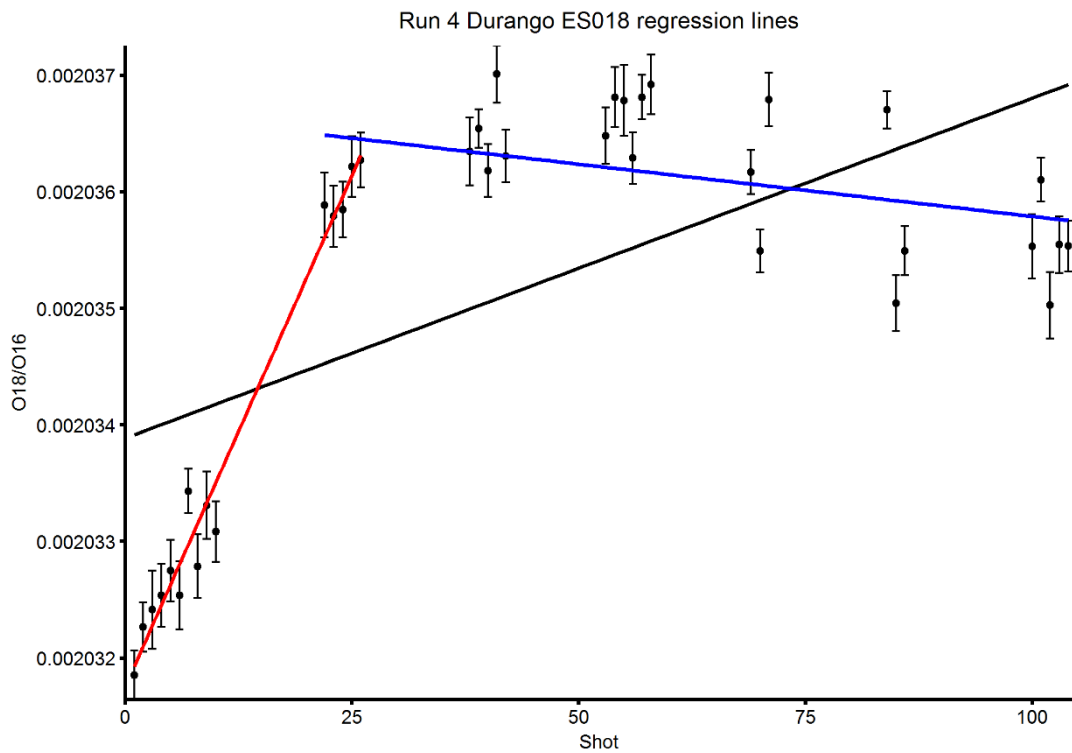


Figure A-C4. Durango analyses from Run 4 on block ES018. Error bars represent one standard deviation. Linear regressions were run through all data points (RTOT, black line), points 1 to 26 (R1, red line), and points 22 to 104 (R2, blue line).

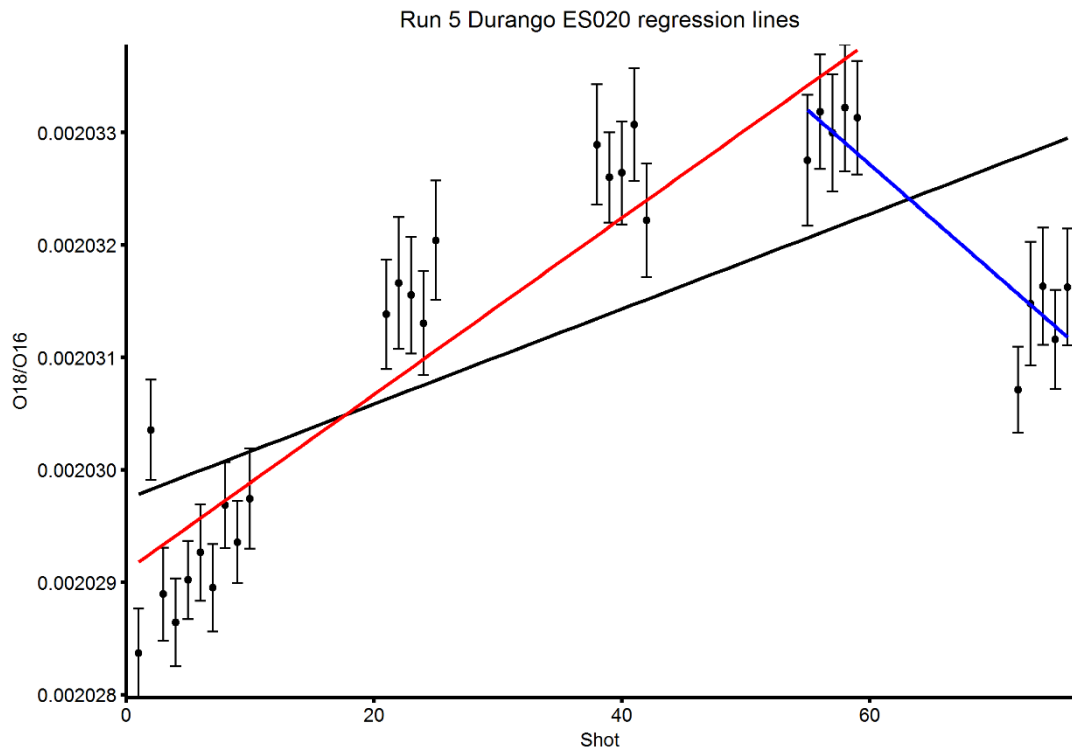


Figure A-C5. Durango analyses from Run 5 on block ES020. Error bars represent one standard deviation. Linear regressions were run through all data points (RTOT, black line), points 1 to 59 (R1, red line), and points 56 to 76 (R2, blue line).

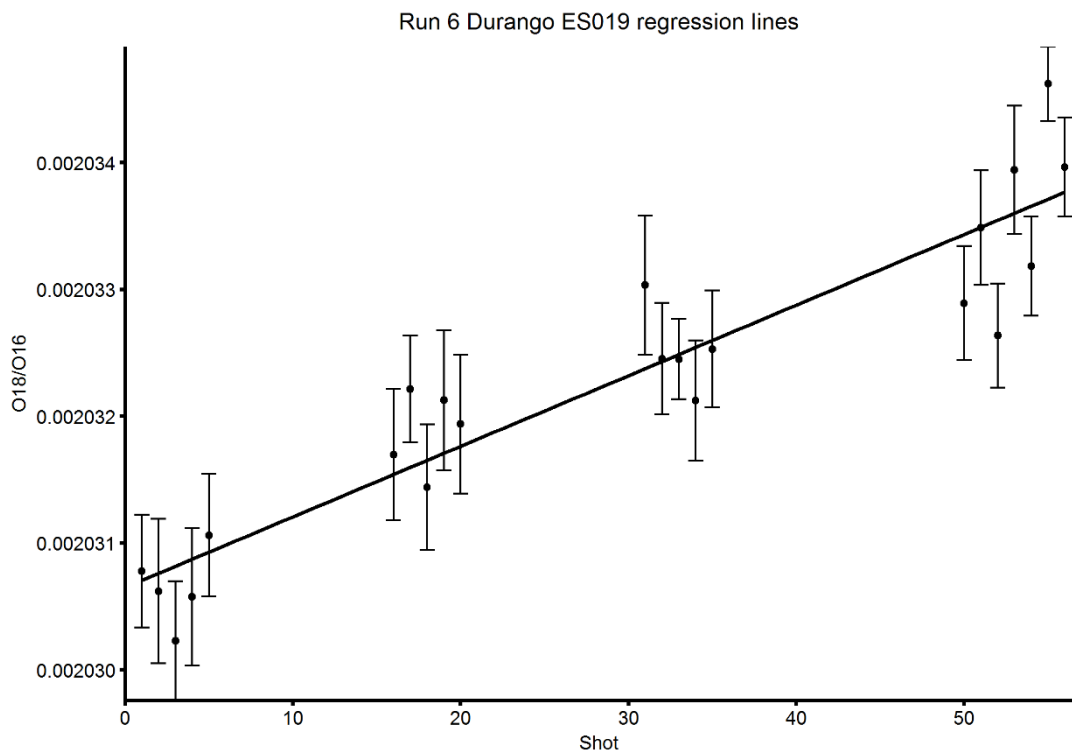


Figure A-C6. Durango analyses from Run 6 on block ES019. Error bars represent one standard deviation. Linear regressions were run through all data points (RTOT, black line).

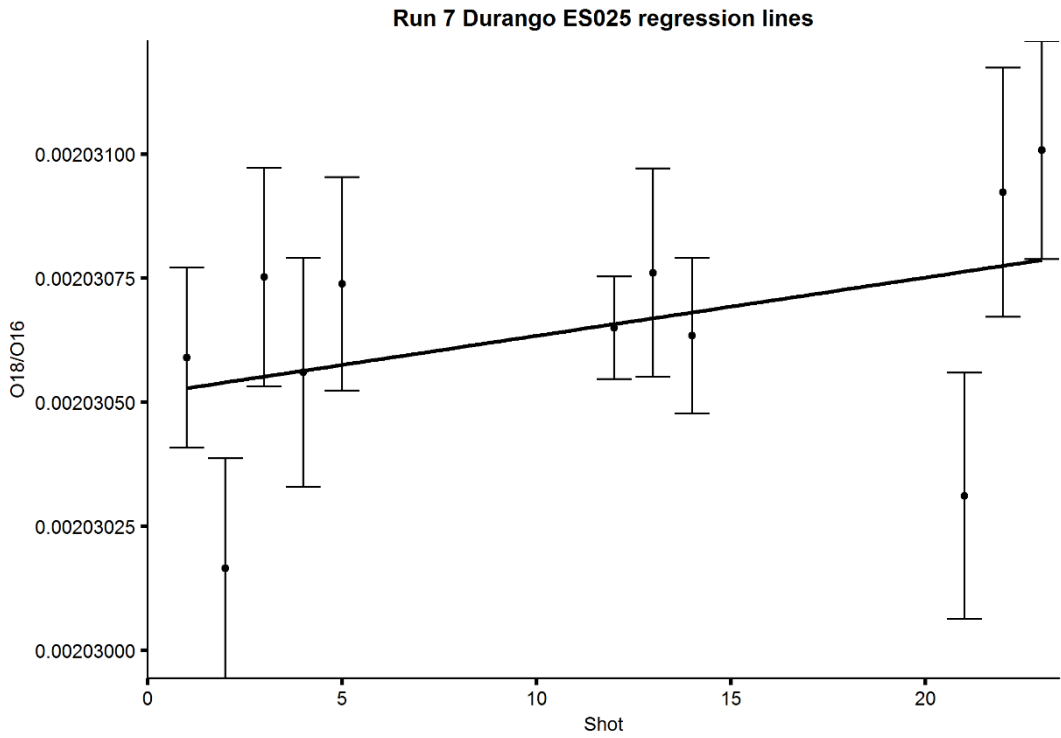


Figure A-C7. Durango analyses from Run 7 on block ES025. Error bars represent one standard deviation. Linear regressions were run through all data points (RTOT, black line).

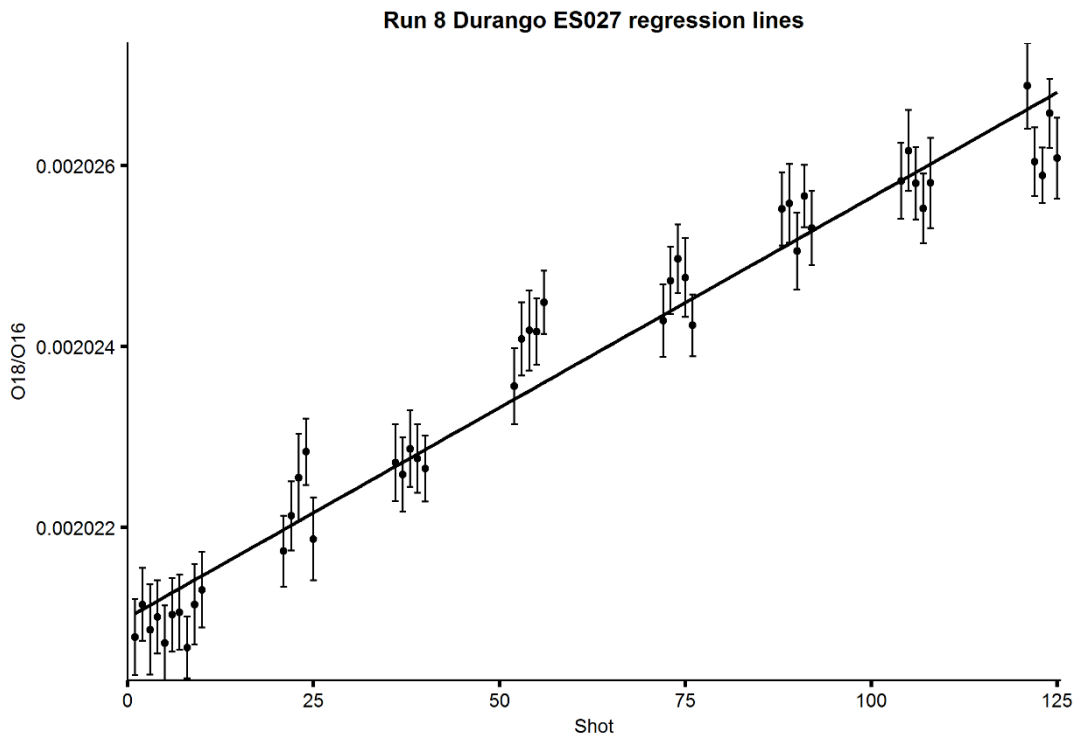


Figure A-C8. Durango analyses from Run 8 on block ES027. Error bars represent one standard deviation. Linear regressions were run through all data points (RTOT, black line).

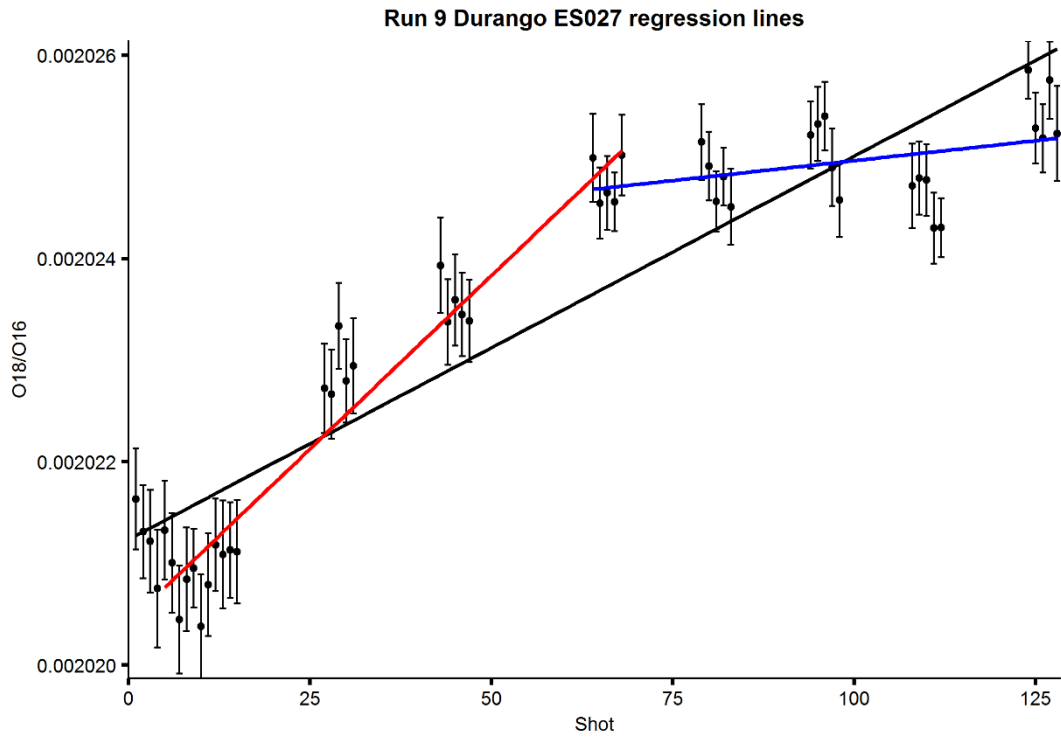


Figure A-C9. Durango analyses from Run 9 on block ES027. Error bars represent one standard deviation. Linear regressions were run through all data points (RTOT, black line), points 5 to 68 (R1, red line), and points 64 to 128 (R2, blue line).

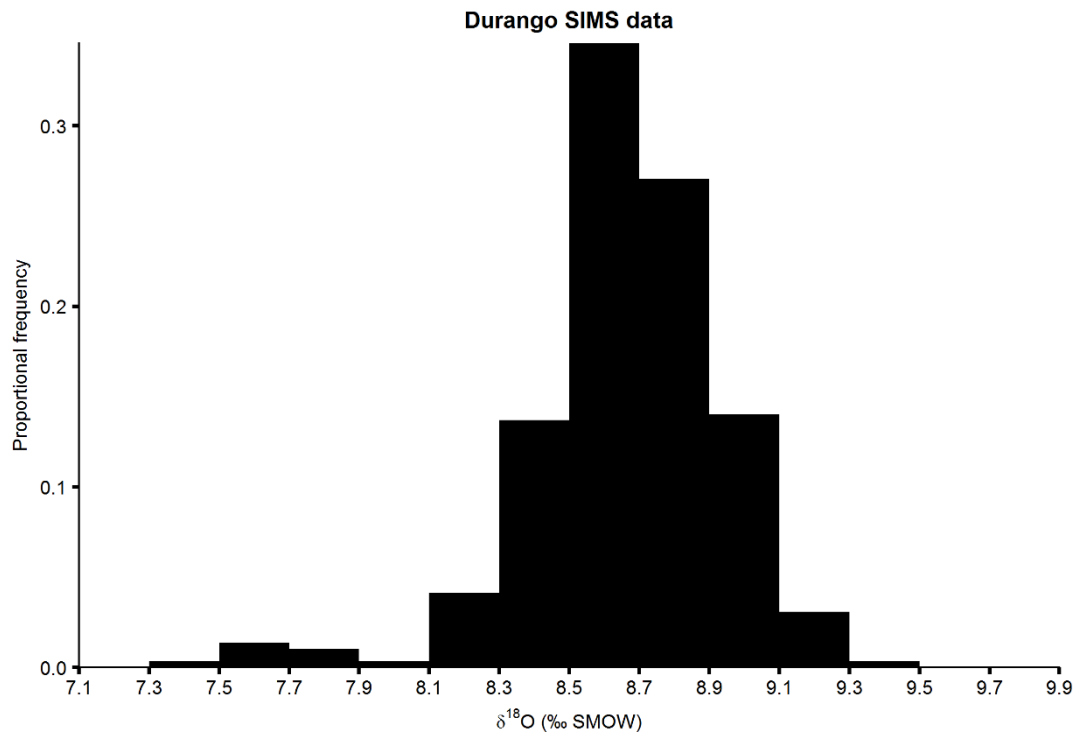


Figure A-C10. Frequency distribution of all Durango analyses in this study. The accepted phosphate $\delta^{18}\text{O}$ value of this Durango crystal is 8.7 ‰.

References cited in Appendix C

Wheeley, J.R., Smith, M.P. & Boomer, I. 2012. Oxygen isotope variability in conodonts: implications for reconstructing Palaeozoic palaeoclimates and palaeoceanography. *Journal of the Geological Society*, 169, 239–250.

Appendix D

SIMS data [electronic]

Appendix D is split into two components. Appendix Da is an Excel spreadsheet of the raw SIMS data, how they were processed, and the final processed data set. Appendix Db is the .csv file of processed SIMS data that was used for analyses in this thesis. Appendix D is available as a digital appendix.

Appendix E

Compilation of Palaeozoic $\delta^{18}\text{O}_{\text{phos}}$ data [electronic]

Appendix E is an Excel spreadsheet of published Palaeozoic $\delta^{18}\text{O}$ data, with full references. This appendix includes the data for and original plot of Figure 5-2. Appendix E is available as a digital appendix.

Appendix F

Greenhouse temperature data [electronic]

Appendix F is an Excel spreadsheet of published greenhouse climate temperature data from the late Mesozoic and early Cenozoic, with full references. This appendix includes the data for Figure 5-5. Appendix F is available as a digital appendix.

Appendix G

Geological data used to compile the climate model base maps [electronic]

Appendix G details the geological data used to make the topographic and bathymetric base maps for the climate models. Appendix G is available as a digital appendix.

Appendix H

Climate model data files [electronic]

Appendix H comprises the .nc files built from the FOAM GCM simulations. There were seven runs of each of the four models, initiated under different greenhouse gas and orbital boundary conditions. Appendix H is available as a digital appendix.

Appendix I

Excel spreadsheet of early Cambrian climatically sensitive lithologies [electronic]

Appendix I is an Excel spreadsheet of early Cambrian climatically sensitive lithologies, with full references. Appendix I is available as a digital appendix.

*All knowledge is precious
whether or not it serves the slightest human use
— A. E. Houseman*